National Library
of Canada

Acquisitions and
Bibliographic Services Branch

395 Wellington Street
Ottawa, Ontario
K1A 0N4

Bibliothèque nationale
du Canada

Direction des acquisitions et
des services bibliographiques

395, rue Wellington
Ottawa (Ontario)
K1A 0N4

Your file Votre référence

Our file Notre référence

NOTICE

The quality of this microform is heavily dependent upon the quality of the original thesis submitted for microfilming. Every effort has been made to ensure the highest quality of reproduction possible.

If pages are missing, contact the university which granted the degree.

Some pages may have indistinct print especially if the original pages were typed with a poor typewriter ribbon or if the university sent us an inferior photocopy.

AVIS

La qualité de cette microforme dépend grandement de la qualité de la thèse soumise au microfilmage. Nous avons tout fait pour assurer une qualité supérieure de reproduction.

S'il manque des pages, veuillez communiquer avec l'université qui a conféré le grade.

La qualité d'impression de certaines pages peut laisser à désirer, surtout si les pages originales ont été dactylographiées à l'aide d'un ruban usé ou si l'université nous a fait parvenir une photocopie de qualité inférieure.

Canada

A Magnetocalorimetric Study of Spin Fluctuations in an Amorphous Metal

by

Andrew LeRossignol Dawson
Department of Physics, McGill University
Montréal, Québec
June 1994

A Thesis submitted to the
Faculty of Graduate Studies and Research
in partial fulfillment of the requirements for the degree of
Doctor of Philosophy

ISBN 0-612-00088-5

to my family

Abstract

Spin fluctuations (SF) are magnetization fluctuations in a metal. They have been proposed as the fundamental origins of the finite temperature properties of transition metals. This thesis presents amorphous iron–zirconium (a–Fe_xZr_{100-x}) as an ideal system in which to study SF. a–Fe_xZr_{100-x} transforms from an exchange–enhanced paramagnet to a weak ferromagnet with increasing x, while the atomic structure remains virtually unchanged. T' enhancement by SF of the effective electron mass has been studied in a–Fe_xZr_{100-} low temperature calorimetry. We report the first observation of the complete quenching or suppression of SF in a metal, achievable by either raising the temperature, or by applying a high magnetic field. This complete quenching allows us to rule out the formation of super–paramagnetic clusters, the only other plausible explanation of the data. a–Fe_xZr_{100-x}, therefore, shows the clearest evidence to date of SF in the electronic properties.

Résumé

Les fluctuations de spin (FS) sont des fluctuations de magnétisation dans un métal. Les FS ont été proposés comme les origines fondamentales des propriétés à températures finies des métaux de transition. Cette thèse présente le fer-zirconium amorphe (a–Fe_xZr_{100-x}) comme système idéal pour étudier les FS. a–Fe_xZr_{100-x} se transforme d'un para–aiment augmenté par un couplage d'échange à un ferro–aiment faible quand la valeur de x augmente, pendant que la structure atomique reste presque inchangée. L'augmentation par FS de la masse effective de l'électron a été étudiée par calorimétrie à basses températures. Ici, nous présentons la première observation du "quenching" ou la suppression des FS dans un métal, qu'on peut faire par augmentation de la température ou par application d'un grand champs magnétique. Ce quenching complet nous permet d'exclure la formation des régions super–paramagnétiques, la seule autre explication des résultats. Donc, a–Fe_xZr_{100-x} montre, jusqu'à maintenant, une preuve la plus claire des FS dans les propriétés électroniques.

Acknowledgments

This work could not have been done without the help of many people, some of whom I would now like to thank.

First of all, I would like to express my sincere gratitude to my supervisor, Dominic Ryan, for his patience and support throughout my degree. His suggestions and critiques were a major directing force behind this work. Secondly, I like to thank John Ström–Olsen, whose technical advice, on at least two occasions, kicked the project out of neutral.

Gratitude is due Zaven Altounian, whose advice on the sample preparation and characterization was very helpful. I would also like to thank Zaven for serving as my acting supervisor. Many thanks also to Dave Baxter, who provided magnetic susceptibility data. These data allowed numerical comparison of the experiment with theory which would otherwise not have been possible. Mark Sutton generously provided his x–ray data acquisition program, which I was easily able to use with my calorimetry subroutines. Many thanks to Glen Poirier for his microprobe work.

I would also like to thank Louis Taillefer for discussions on the subtle theoretical aspects of spin fluctuations. Numerical results of spin fluctuation theory from Oleh Baran were also helpful. For useful suggestions about calorimetry, I would like to thank Brett Ellman and Hank Fischer, both of whom have had experience in this difficult measurement. Thanks also to W. B. Muir for his advice on the construction of electronic circuits. Conversations with Ralf Brüning, Steve Brauer and Abdelhadi Sahnoune were also appreciated.

Gratitude is also due to many people who helped with the hardware. Frank van Gils was indispensable throughout the construction and assembly of the calorimeter, and also provided many solutions throughout the work. Thanks also to Michel Champagne, who machined the cryostat. Many small projects were graciously completed by Robin van Gils. Assistance was also given by nameless hordes of Dutch Boys.

Thanks is due also to undergraduate staff, Steve Godbout, Mark Orchard–Webb, Michel Beauchamp and Savario Biunno who lent much equipment for this project. Thanks also to many who offered gave computer help, notably Mark Sutton, Loki Jorgenson, Martin Lacasse and Eric Dufresne.

This work was graciously supported by a grant from the Walter C. Sumner Memorial Foundation, Halifax, Nova Scotia. I would like to thank my parents, who have given me enormous support throughout the years. I would also like to thank my wife, Carolyn, and son, George, who have made many sacrifices for this work. Finally, I would like to thank God Almighty, without Whom virtually none of this work would have been possible.

Contents

List of Figures

Chapter 1

Introduction

Historically, an understanding of magnetism in solids has been approached from two perspectives. In the *local moment picture*, which applies in magnetic insulators and rare earth f–electron metals, the moments are treated as being completely localized, each associated with one particular atom in a solid. In the completely opposite *itinerant moment picture*, which applies to alkaline, alkaline earth and noble metals in an applied magnetic field, electrons are treated as being completely delocalized and existing in an energy band. Controversy about which picture applies in d–electron transition metals, notably the iron group metals (Fe, Co, Ni), lasted fifty years. While the ground state properties of the iron group metals were finally demonstrated to be explainable within the itinerant model, mean field theory was unable to predict finite temperature properties. The challenge, both to experiment and to modern theories of magnetism is to therefore explain the finite temperature magnetic properties of d–band metals.

The failures of mean field theory can be traced to its neglect of fluctuations. Fluctuations may affect the static mean field in a system whose response is non–linear. Dubbed *spin fluctuations* (*SF*), magnetization fluctuations in an itinerant magnet determine magnetic properties at all finite temperatures, particularly in *weak itinerant ferromagnets.* Modern theories of d–band magnetism incorporating *SF* promise a unified picture of magnetism which reduces to the itinerant or localized picture in

appropriate limits.

Generally, measurement of static magnetic properties cannot unambiguously identify the presence of *SF*. Consequently, experimental evidence for the existence of *SF* has come mainly from observations of the *SF* scattering effects on electronic properties and from neutron scattering results. Many experimental studies have investigated weakly magnetic d-band metals, like Ni_3Al, $ZrZn_2$ and $InSc_3$, often as the composition is varied slightly off that of the stoichiometric crystal. This allows the study of *SF* as the strength of the magnetism is varied through the critical concentration for magnetism. The conclusions of these studies are often weakened, however, by the unfortunate necessity of comparing measurements from a perfect crystal with those from off-stoichiometry crystals containing different numbers of defects.

We present amorphous iron zirconium (a–Fe_xZr_{100-x}) as an ideal system in which to study spin fluctuations. On adding an appropriate amount of iron, this system undergoes a transition from a nearly ferromagnetic metal into a weak itinerant ferromagnet. The advantage of the glassy structure of this system is that the atomic arrangement is virtually unchanged over a wide composition range. We have studied the effect of *SF* scattering on the effective electron mass in a–Fe_xZr_{100-x} by measuring the low temperature specific heat, $C_P(T)$, of a–Fe_xZr_{100-x} at finely spaced intervals of composition x near the critical composition of $x_c \approx 37\%$. These measurements show an enhancement of the effective electron mass at low temperatures (T<5 K) which disappears at higher temperatures (T>7 K). We have identified this mass enhancement as arising due to *SF*. This view is supported by the observation that the mass enhancement is greatest for samples right near the critical concentration.

Since the spin fluctuation temperature, T_{SF}, the characteristic energy scale of *SF*, is very low ($\sim$ 7 K) in a–Fe_xZr_{100-x}, we are able to observe for the first time the vanishing of the *SF* at higher temperatures. We also report the first observation of the *complete* quenching or suppression of *SF* modes by high magnetic fields.

Many authors [1,2] have warned that the effect of magnetic clustering may appear as *SF* effects in $C_P(T)$. Because, however, the *SF* may be completely quenched in

one of our samples, we are able to rule out the existence of magnetic cluster formation in this sample using thermodynamic arguments.

In Chapter 2, we present the Weiss and Stoner theories of magnetic order, and give an account of their successes and failures. Modern theories of magnetism incorporating spin fluctuations are then discussed along with their experimental consequences. Previous experimental work on $a-Fe_xZr_{100-x}$ is also reviewed in Chapter 2. Fabrication of $a-Fe_xZr_{100-x}$ ribbons is discussed in Chapter 3, and a description is given of important sample characterization techniques. Precision absolute calorimetry is necessary to compare *SF* effects in different samples and a discussion of this difficult low temperature measurement is given in Chapter 4. Previous magnetometry results are re-interpreted in Chapter 5, and the results of calorimetry and magnetocalorimetry measurements are presented and discussed. Chapter 6 summarizes the important results of this study and discusses suggestions for future work.

Chapter 2

Background

2.1 Local Magnetism

The simplest picture of magnetism is that of elementary magnetic moments localized on individual atoms in a solid. This picture is found to apply in the vast majority of magnetic solids and many of the concepts introduced here aid in an understanding of itinerant magnetism.

Classically, according to the Bohr–van Leewen theorem [3], magnetic phenomena in solids should not exist at all. Quantum Mechanics is necessary for an understanding of the fundamental origins of the elementary magnetic moments, $\vec{\mu}$, which combine to produce a measurable magnetization, $\vec{M}$. The discrete electronic energy levels of the free atom lead to the formation of an electronic magnetic moment, $\vec{\mu}$, which is given by:

$$\vec{\mu} = -g(J,L,S)\mu_B\vec{J} \tag{2.1}$$

where μ_B is the Bohr magneton. The total, orbital and spin angular momentum of the electrons in the atom (J, L and S respectively) are calculable using Hund's rules. The Landé factor, $g(J,L,S)$, is given by [4]:

$$g(J,L,S) = \frac{3}{2} + \frac{1}{2}\left[\frac{S(S+1) - L(L+1)}{J(J+1)}\right], \tag{2.2}$$

if the electronic g–factor is taken as exactly 2.

2.1.1 Local Paramagnetism

In an applied magnetic field, $\vec{H}$, an atomic moment acquires a magnetostatic energy, $-\vec{\mu}\cdot\vec{H} = g(J,L,S)\mu_B J_z H$. This energy, and simple statistical mechanics, allows us to calculate the volume magnetization, $M(H,T)$, of a gas of N isolated atoms in equilibrium at a temperature, T.

$$M(H,T) \equiv M_0\left(\frac{H}{T}\right) = g(J,L,S)\mu_B J \frac{N}{V} B_J\left(\frac{g(J,L,S)\mu_B H}{k_B T}\right), \qquad (2.3)$$

where $E_J(u)$ is the Brillouin function [4]. For small fields, the magnetic volume susceptibility, $\chi(T)$, can be written in CGS units as:

$$\begin{aligned} \chi(T) = \chi_C(T) &\equiv \frac{dM}{dH} = \frac{g^2(J,L,S)\mu_B^2 J(J+1)}{3k_B T}\frac{N}{V} \qquad \text{if}: \ \frac{\mathrm{g(J,L,S)}\mu_B \mathrm{H}}{\mathrm{k_B T}} \ll 1. \\ \chi_C(T) &\equiv \frac{p_{eff}^2}{3k_B T}\frac{N}{V} \end{aligned} \qquad (2.4)$$

This expression is the *Curie law* which describes paramagnetism in any system of non–interacting local moments at low enough fields. In a solid, if the ionization state of the magnetic atoms is known, the Curie law can be used directly to calculate $\chi(T)$.

In paramagnetic rare earth metals, for instance, the magnetic moment of the f–electron ion calculated by Hund's rules and equation 2.1 agrees well with the magnetic moment determined from the experimentally observed Curie law [5].

In transition metal salts, d–electron wavefunctions centered about the metal ion are extended in space, so that the ion cannot be treated as isolated. Crystal electric fields from neighboring atoms, with sufficient asymmetry, cause L levels to be split such that the ground state has $L = 0$. In this case, $J = S$ for the ion gives Curie moments in good agreement with experimentally observed susceptibilities of transition metal salts [6]. This suppression of the orbital moment, L, in d–electron salts is known as orbital *quenching* [5].

2.1.2 Weiss Theory of Local Magnetic Order

The most obvious manifestation of magnetism is *ferromagnetism*, which refers to the experimental observation of a spontaneous magnetization in a solid in the absence of an applied magnetic field. The earliest theory of ferromagnetism was the phenomenological *Weiss molecular field model* [5]. In this treatment, an elementary moment feels a molecular field, λM, proportional to the overall volume magnetization in addition to the applied field H. The resultant effective field is:

$$H_{EFF} = H + \lambda M,$$

where λ is the dimensionless *molecular field constant.* The magnetization is determined by assuming that the system responds to the effective field just as if it were an externally applied field. The actual origin of the effective field constant, λ, (or for that matter the origin of the elementary moments themselves) was unknown classically. Estimates of λ due to dipole–dipole coupling were 1000 times too small compared with observed values of $\sim 10^4$ [3].

The magnetization, M, of a system of *interacting* local moments can now be determined simply by inserting H_{EFF} into the expression for the magnetization of the non–interacting system. Equation 2.3 becomes:

$$M = M_0\left(\frac{H_{EFF}}{T}\right).$$

If $H = 0$ and we define $u = \lambda M/T$, then this equation becomes:

$$\frac{uT}{\lambda} = M_0(u).$$

In Fig. 2.1, $M_0(u)$ is plotted together with the straight lines, uT/λ, for different values of T/λ. At small values of u, $M_0(u)$ can be approximated by $\chi_C T u$ while at high values of u, $M_0(u)$ curves over and eventually saturates to $g(J,L,S)\mu_B J$. As can be easily seen from the figure, the equation has a non–zero solution, M, for small values of T/λ, or, more precisely, when $uT/\lambda < \chi_C(T)Tu$. The *ferromagnetic ordering temperature* or *Curie temperature*, T_C, below which there is a spontaneous

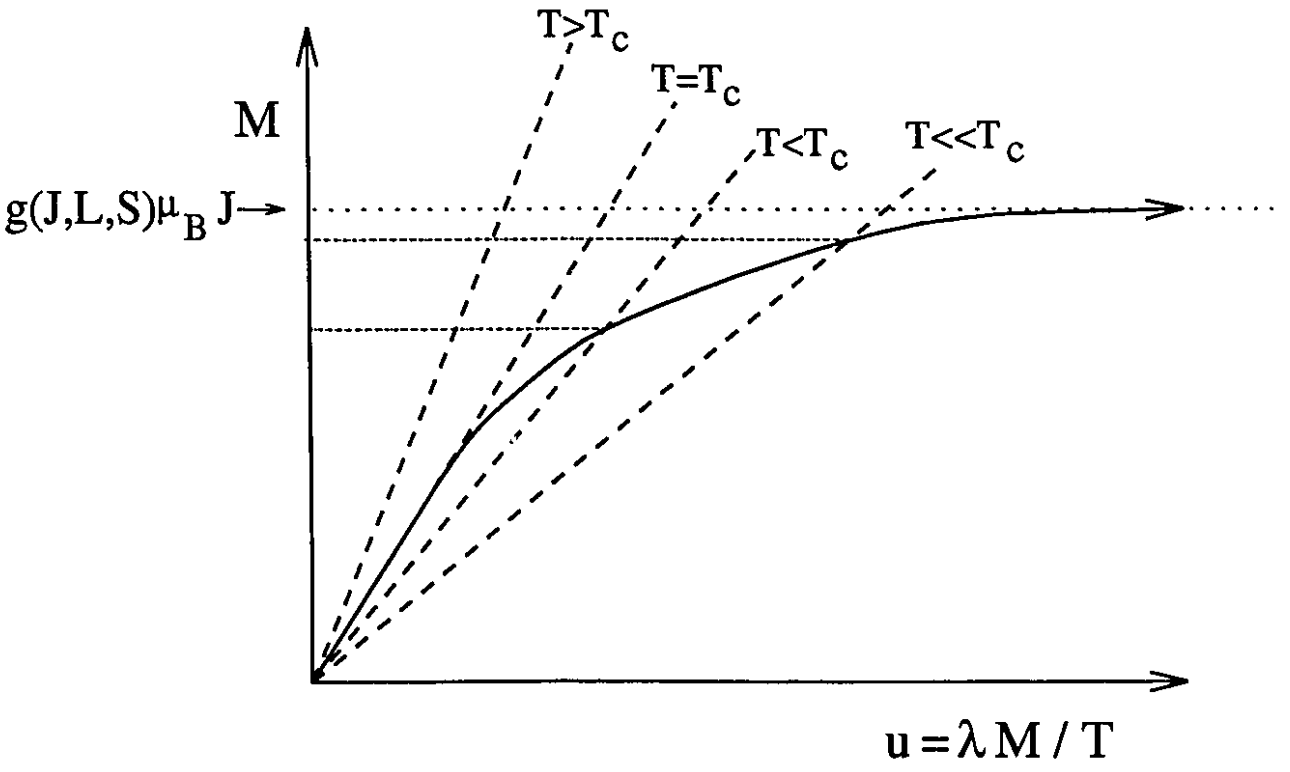

Figure 2.1: Weiss molecular field theory of ferromagnetism in a system of interacting local moments. The solid line is the non–interacting magnetization $M_0(u)$ and the dashed lines are uT/λ for different values of T/λ.

magnetization, is given by:

$$\begin{aligned} \lambda\chi_C(T_C) &= 1 \\ \text{or } T_C &= \lambda\frac{p_{eff}^2}{3k_B}\frac{N}{V}, \end{aligned} \tag{2.5}$$

using the Curie law. At T_C, M=0, but as the temperature decreases, there is a solution for $M \neq 0$ as shown in Fig. 2.1. As $T \rightarrow 0$, $u \rightarrow \infty$ and the magnetization saturates at $g(J,L,S)\mu_B J\frac{N}{V}$ with all moments aligned. *This is a critical test of the Weiss model, i.e. that the spontaneous magnetization at $T = 0$ is directly derivable from J.* At finite temperatures below T_C, the spontaneous magnetization, $M(T)$, can be solved for numerically and compared with experiment.

At high temperatures, there is no spontaneous magnetization, but if $H \neq 0$ then:

$$M = \chi_C(T)H_{EFF} = \chi_C(T)(H + \lambda M)$$

so that:

$$\chi \equiv \frac{dM}{dH} = \chi_C(T)/(1 - \lambda\chi_C(T)) \tag{2.6}$$

This is a more general equation which relates the non–interacting susceptibility, in this case $\chi_C(T)$, to the susceptibility of a paramagnet, $\chi(T)$, in the presence of interactions ($\lambda \neq 0$). Inserting the Curie susceptibility, $\chi_C(T)$ from equation 2.4:

$$\chi = \chi_C(T)/(1 - T_C/T) \tag{2.7}$$

$$\chi = \frac{p_{eff}^2}{3k_B(T - \Theta_{CW})}\frac{N}{V}, \quad \text{where } \Theta_{CW} = T_C. \tag{2.8}$$

This equation, called the *Curie–Weiss (CW) law*, is a first order correction to the Curie law. The Curie–Weiss law accounts for the effect of interactions between local moments on the paramagnetic susceptibility. While it strictly applies only to systems of local moments, *the Curie–Weiss law has been used to parameterize the susceptibility of virtually all magnets above the ordering temperature.* In Weiss theory, $\Theta_{CW} = T_C$, but experiments usually yield different, even negative, values.

Another critical test of the Weiss theory is that the ordered moment, p_s, at $T = 0$ is the same as the high temperature paramagnetic moment, p_c. The ordered moment, p_s, is derived from the magnetization at $T = 0$:

$$p_s \equiv \lim_{T\to 0} M\frac{V}{N}. \tag{2.9}$$

The Curie moment, p_c is determined from the high temperature susceptibility:

$$p_{eff}^2 \equiv 3k_B\left[\frac{d\chi^{-1}}{dT}\right]^{-1} \equiv p_c(p_c + g(J,L,S)\mu_B). \tag{2.10}$$

From these definitions and equations 2.3, 2.4, 2.8, $p_s = p_c = g(J,L,S)\mu_B J$, so that for a Weiss local magnet, the *moment ratio*, p_c/p_s, is unity.

Weiss local moment theory correctly describes virtually all insulating f– and d–electron compounds. By this, we mean that the observed moment ratios are unity and the ordered moments are given by equation 2.1. Weiss theory can also be used to describe many rare earth f–electron metals. Here, the f–electrons, buried deep within the atom and shielded by outer conduction electrons, behave as local moments. Weiss theory is *mean field theory* which, with slight modifications, can be made to describe magnetic ordering in many exotic magnetic structures such as *anti–ferromagnetic*, *ferrimagnetic* or *helimagnetic structures* [5,7].

2.1.3 Deviations from Weiss Theory

Weiss theory qualitatively describes the energetics of the magnetic phase transition in local moment systems. By this, we mean that values of molecular field parameter, λ, taken from different measurements, agree and can be roughly used to calculate the Curie temperature [5]. *This implies that Weiss theory contains all the ingredients necessary to describe the thermodynamics of the phase transition.* On closer examination, however, small deviations of the experimentally observed behaviour of $M(T)$ from the predictions of Weiss theory occur in two temperature regimes: at very low temperatures and at temperatures near T_C.

At low temperatures, the spontaneous magnetization, $M(T)$, is reduced more quickly with increasing temperature than determined by the Weiss model which predicts that $M(T)$ should decay exponentially with temperature according to the Boltzmann factor ($M(T) \propto \exp \Delta E/k_B T$). This is simply because, in Weiss theory, the magnetization decays due to single spin flips ($\downarrow\downarrow\uparrow\downarrow\downarrow$). It can be shown, however, that spreading a single spin–flip sinusoidally over all of the spins with a wavevector, $\vec{q}$, leads to magnetic excitations with a lower magnetic energy:

$$\hbar\omega(\vec{q}) = \mathcal{D}q^2. \tag{2.11}$$

These excitations are called *spin waves* or *magnons*. Equation 2.11 is the *spin wave dispersion relation* and $\mathcal{D}$ is the *spin wave stiffness*. Since $\hbar\omega(\vec{q}) \rightarrow 0$ at $\vec{q} \rightarrow 0$, these

low energy excitations dominate the behaviour of $M(T)$ at low temperatures.

At a temperature, T, spin wave populations are given by the Bose function, $n_B(\varepsilon)$. The magnetization, $M(T)$, and specific heat, $C_P(T)$, resulting from spin wave excitations are calculated as being proportional to the total number of spin waves and the derivative of the total energy respectively.

$$\begin{aligned} M(0) - M(T) &\propto \int_{-\infty}^{\infty} n_B\left(\hbar\omega(\vec{q})\right) d^3q \propto T^{\frac{3}{2}} \\ C_P(T) &\propto \frac{d}{dT}\left[\int_{-\infty}^{\infty} n_B\left(\hbar\omega(\vec{q})\right)\hbar\omega(\vec{q}) d^3q\right] \propto T^{\frac{3}{2}} \\ \text{where : } n_B(\varepsilon) &\equiv \left[-1 + \exp\left(\frac{\varepsilon}{k_B T}\right)\right]^{-1}. \end{aligned} \tag{2.12}$$

The prominence of the spin wave contribution at low temperatures is a consequence of the fact that thermal excitation need not destroy the magnetization by flipping spins completely, but merely by canting them ($\uparrow\nearrow\rightarrow\searrow\downarrow\swarrow\leftarrow\nwarrow\uparrow$). Spin waves are, therefore, *transverse excitations* [8]. The $T^{\frac{3}{2}}$ behaviour in $M(T)$ and $C_P(T)$, characteristic of spin waves, has been observed in many insulating and metallic systems [5].

The second region where the Weiss mean field theory is inapplicable is near the Curie temperature. Weiss theory predicts a second order phase transition. The effect of fluctuations in the magnetization. must be explicitly included in *renormalization group theory*, which is appropriate for a magnet near the critical point. These magnetization fluctuations exhibit *scale invariance* and lead to *power law divergences* of the thermodynamic quantities in temperature. In particular [4]:

$$\begin{aligned} M(T) &\propto (T_C - T)^{\beta} \quad T < T_C \\ \chi(T) &\propto (T - T_C)^{-\gamma} \quad T > T_C \\ C_H(T) &\propto |T - T_C|^{-\alpha}. \end{aligned} \tag{2.13}$$

Weiss theory predicts $\beta = \frac{1}{2}$ and $\gamma = 1$. Experiment, as well as more modern theories, give $\beta \approx \frac{1}{3}$ and $\gamma \approx 1.3$ [4]. The $C_P(T)$ exponent, α, observed to be or order 0.1, is not

definable in Weiss theory, which predicts a characteristic second order discontinuity in $C_P(T)$ at T_C. Finite values of α, above and below T_C, are an indication of how the phase transition is smeared out by fluctuations.

2.1.4 Exchange and Correlation

We now know that the energy which gives rise to magnetic ordering is not magnetic, but electrostatic in origin. The molecular field arises as a subtle consequence of the requirement that electrons must comply with the Pauli exclusion principle which says that: *no two electrons may occupy the same quantum state.* Since electrons are indistinguishable, for a system of N electrons at positions, $\vec{r}_i$, and with spins, $\vec{s}_i$, the square of the N–electron wave function, $|\Psi(\vec{r}_1\vec{s}_1, \vec{r}_2\vec{s}_2, \vec{r}_3\vec{s}_3 ... \vec{r}_N\vec{s}_N)|^2$, must remain unchanged upon the interchange of any two elcctrons. For electrons, the Pauli principle can be restated as : *the total many–electron wavefunction must be antisymmetric with respect to the exchange of any two electrons :*

$$\Psi(\vec{r}_1\vec{s}_1 ... \vec{r}_i\vec{s}_i ... \vec{r}_j\vec{s}_j ... \vec{r}_N\vec{s}_N) = -\Psi(\vec{r}_1\vec{s}_1 ... \vec{r}_j\vec{s}_j ... \vec{r}_i\vec{s}_i ... \vec{r}_N\vec{s}_N).$$

Let us consider the 2–electron wavefunction describing the electrons in the hydrogen molecule (H_2), the simplest "solid". The two electron Hamiltonian for the H_2 molecule may generally be written as:

$$\mathcal{H} = \mathcal{H}_1 + \mathcal{H}_2 + \mathcal{H}_{1,2},$$

where $\mathcal{H}_1$ and $\mathcal{H}_2$ are the Hamiltonians of electrons #1 and #2 in the absence of interactions between them. The ground state solutions to these terms, $\phi_A(\vec{r}_1)$ and $\phi_B(\vec{r}_2)$ are given by :

$$\begin{aligned} \mathcal{H}_1\phi_A(\vec{r}_1) &= E_A\phi_A(\vec{r}_1) \\ \mathcal{H}_2\phi_B(\vec{r}_2) &= E_B\phi_B(\vec{r}_2). \end{aligned}$$

The two simplest approaches to the problem are to use the *Heitler–London model* or the *molecular orbital model.* In the former $\phi_A(\vec{r}_1)$ and $\phi_B(\vec{r}_2)$ are taken as the wavefunctions describing isolated H atoms at points A and B while, in the latter, they are molecular orbital wavefunctions corresponding to the H_2^+ ion with a bond distance $A-B$. These two models correspond to the local and itinerant picture, respectively, in an infinite crystal.

The *interaction Hamiltonian,* $\mathcal{H}_{1,2}$, contains the *Coulomb interaction Hamiltonian,* $e^2/|\vec{r}_2-\vec{r}_1|$, and any (presumably small) 1–electron Hamiltonians which were not included in $\mathcal{H}_1$ and $\mathcal{H}_2$. In order to do perturbation theory and determine the first order effect of $\mathcal{H}_{1,2}$, we must first construct spatially symmetric and antisymmetric 2–electron wave functions. Normalized symmetric and antisymmetric combinations, $\psi_+(\vec{r}_1,\vec{r}_2)$ and $\psi_-(\vec{r}_1,\vec{r}_2)$, are constructed as:

$$\begin{aligned}
\psi_\pm(\vec{r}_1,\vec{r}_2) &\equiv A_\pm\left[\phi_A(\vec{r}_1)\,\phi_B(\vec{r}_2) \pm \phi_A(\vec{r}_2)\,\phi_B(\vec{r}_1)\right] \\
\text{where the normalization, } A_\pm^{-2} &\equiv 2\left[1\pm\alpha\right] \\
\text{and the } \textit{overlap integral}, \quad \alpha &\equiv \int_{-\infty}^{\infty} \phi_A^\dagger(\vec{r}_1)\,\phi_B(\vec{r}_1)\,\phi_B^\dagger(\vec{r}_2)\,\phi_A(\vec{r}_2)\,d^3r_1 d^3r_2.
\end{aligned}$$

The 2–electron spin states are the standard spin parallel and spin antiparallel 2–electron spinor combinations, $\chi_{triplet}$ and $\chi_{singlet}$. The total antisymmetrized wavefunctions may now be written as:

$$\begin{aligned}
\Psi_+(\vec{r}_1\vec{s}_1,\vec{r}_2,\vec{s}_2) &\equiv \psi_+(\vec{r}_1,\vec{r}_2)\,\chi_{singlet}(\vec{s}_1,\vec{s}_2) \\
\Psi_-(\vec{r}_1\vec{s}_1,\vec{r}_2,\vec{s}_2) &\equiv \psi_-(\vec{r}_1,\vec{r}_2)\,\chi_{triplet}(\vec{s}_1,\vec{s}_2).
\end{aligned}$$

We now use the *Hartree–Fock approximation* (HFA), to determine the perturbed energies of these states. The HFA is simply first order perturbation theory applied to the properly antisymmetrized 2–electron wavefunctions. The total energy $E_\pm$ of of the Ψ_- and Ψ_+ in the HFA is therefore;

$$E_\pm = \int_{-\infty}^{\infty} \Psi_\pm^\dagger\,\mathcal{H}\,\Psi_\pm\; d^3r_1 d^3r_2$$

$$
\begin{aligned}
&= \int_{-\infty}^{\infty} \Psi_{\pm}^{\dagger} \left[\mathcal{H}_1 + \mathcal{H}_2 + \mathcal{H}_{1,2}\right] \Psi_{\pm} \, d^3r_1 d^3r_2 \\
&= E_A + E_B + 2A_{\pm}^2(\mathcal{Q} \pm \mathcal{J}), \\
\text{where } : \mathcal{Q} &\equiv \int_{-\infty}^{\infty} \phi_A^{\dagger}(\vec{r}_1)\, \phi_B^{\dagger}(\vec{r}_2)\, \mathcal{H}_{1,2} \phi_A(\vec{r}_1)\, \phi_B(\vec{r}_2)\, d^3r_1 d^3r_2 \\
\text{and } : \mathcal{J} &\equiv \int_{-\infty}^{\infty} \phi_A^{\dagger}(\vec{r}_1)\, \phi_B^{\dagger}(\vec{r}_2)\, \mathcal{H}_{1,2} \phi_B(\vec{r}_1)\, \phi_A(\vec{r}_2)\, d^3r_1 d^3r_2.
\end{aligned}
$$

There are two new terms which appear in the energy as a result of $\mathcal{H}_{1,2}$. The *direct integral* or *Hartree energy*, $\mathcal{Q}$, is simply $\mathcal{H}_{1,2}$ integrated over clouds of the charge density, $e|\phi(\vec{r})|^2$, of the unperturbed basis states. This term would result if we had not antisymmetrized the wavefunctions. The *exchange integral*, $\mathcal{J}$, has no classical analog and occurs as a result of the antisymmetrization of the basis wavefunctions. The energy difference between (Ψ_-), the polarized state, and (Ψ_+), unpolarized spin states, is:

$$\Delta E \equiv E_- - E_+ = -2\left[\mathcal{Q}\left(A_+^2 - A_-^2\right) + \mathcal{J}\left(A_+^2 + A_-^2\right)\right].$$

This allows us to cast as an effective spin–spin Hamiltonian, $\mathcal{H}_{exchange}$:

$$
\begin{aligned}
\mathcal{H}_{exchange} &\equiv -J\left[\frac{1}{2} + 2\frac{\vec{s}_1 \cdot \vec{s}_2}{\hbar^2}\right] \\
\text{if } : J &\equiv \left[\mathcal{Q}\left(A_+^2 - A_-^2\right) + \mathcal{J}\left(A_+^2 + A_-^2\right)\right],
\end{aligned}
$$

where we have defined the *exchange constant*, J, which can be positive or negative. This form of the exchange Hamiltonian is clearly diagonal in the total spin, $\vec{s}_1 + \vec{s}_2$, which means that there is a solution with both spins aligned. This solution is the ground state if $J > 0$. It turns out that $J < 0$ in the hydrogen molecule, which is therefore antiferromagnetic. In materials with high $\mathcal{J}$, however, we may expect $J > 0$ which leads to ferromagnetic alignment of the spins. $\mathcal{H}_{exchange}$ reveals the physical origin of the molecular field as arising from Coulomb interactions between electrons constrained by the Pauli principle. J is proportional to the dimensionless molecular field parameter, λ, which may now be estimated. These estimates agree in order of magnitude with observed values of $\lambda \sim 10^4$ [3].

All additional terms in the correct total energy, not accounted for by the (HFA), we define as the *correlation energy.* Correlation between parallel spins is explicitly included in the HFA and is often called *exchange correlation.* Antisymmetrization of the basis wavefunction explicitly keeps parallel spins spatially separated. This is because the spatial part of Ψ_- is antisymmetric, ($\Psi_-(\vec{r}_1, \vec{r}_2) = -\Psi_-(\vec{r}_2, \vec{r}_1)$), and so there is zero amplitude at $\vec{r}_1 = \vec{r}_2$. The inter-electronic Coulomb energy can thus always be lowered by choosing this ferromagnetically ordered wavefunction. The HFA is, therefore, prejudiced in favour of ferromagnetic order. The correlation energy is so named because it must account the correlations existing between electrons of opposite spin which also avoid each other because of Coulomb repulsion. The inclusion of the correlation energy must correct the prejudice of the HFA. Consequently, the correlation energy must work against ferromagnetic order. The correlation Hamiltonian cannot be cast as we did $\mathcal{H}_{exchange}$, so that the total spin is no longer a good quantum number and the ferro/antiferromagnet wavefunctions are not static solutions. Correlation is largely accounted for in a local Weiss model since the electrons are explicitly confined to sit at separate atomic sites, thus avoiding each other completely. Proper account of the correlation energy in a metal, however, defines the unresolved problem in the theory of itinerant magnetism.

2.2 Itinerant Magnetism

The iron group metals (Fe,Co,Ni) are the only transition elements which are ferromagnetic at room temperature. In these metals, we would expect the orbital angular momentum to be quenched ($L = 0$), so that $J = S$. The expected ordered moment from Weiss theory is, therefore: $-g(J, L, S)|\vec{J}|\mu_B = -g(S, 0, S)S\mu_B = -2S\mu_B$. Since the total spin, S, is always an integer or half integer, this means that *local ordered moments observed in d-electron metals must be in integral multiples of* μ_B.

It is immediately evident that the local moment picture cannot be used for the iron group metals since their ordered moments are non-integral ($\mu_{Fe} = 2.22\mu_B$, $\mu_{Co} =$

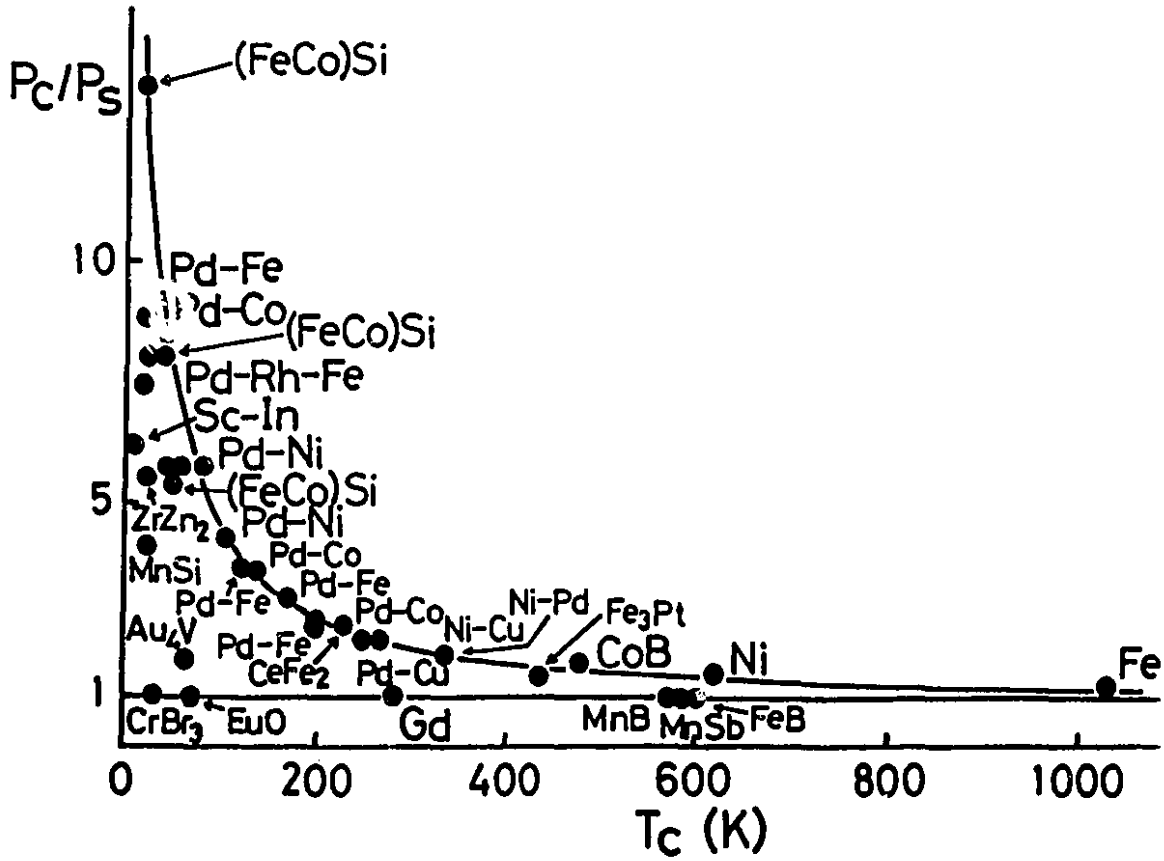

Figure 2.2: Rhodes-Wolfharth Plot for various transition metal elements and alloys taken from ref. [10]. The moments p_c and p_s are defined in equations 2.9 and 2.10.

$1.71\mu_B$, $\mu_{Ni} = 0.61\mu_B$). Also the moment ratios, p_s/p_c, exceed 1 by as much as 40%. *Weak ferro-magnets* (*e.g.* Ni_3Al, Zr_2Zn, Sc_3In) are a class of d-electron magnetic alloys with extremely low ordered moments ($\sim 0.1\mu_B$) and high values of p_c/p_s (up to 10)[9] Clearly the local moment picture is inapplicable in these metals. Values of the moment ratio are displayed in Fig 2.2 for many transition metal elements and alloys. This is referred to as the *Rhodes-Wolfharth* plot.

In the following sections, we discuss the itinerant electron model, which is capable of explaining the existence of non-integral ordered moments and moment ratios different from unity.

2.2.1 Free electron theory

Electrons can always lower their kinetic energy by occupying the entire sample volume instead of only the volume near a particular atomic site. For core electrons which occupy filled inner shells in the atom, the negative atomic binding energy of the electron outweighs the lowering possible due to delocalization. If the binding energy is small, however, as we may expect for electrons in outer partially filled shells, then it may be energetically favourable for the electron to occupy the entire sample volume. This is the case in simple metals, such as sodium, where conduction electrons are not localized on any particular atom and can be treated as being nearly free.

In the Sommerfeld free electron model of a metal, electrons feel no potential except that which confines them to the sample volume, V. The energy of an electron with a wavevector, $\vec{k}$, is then simply its kinetic energy, $\hbar^2\vec{k}^2/2m$, where m is the electron mass. The volume confinement requires that the wave vector conform to the relation:

$$\vec{k} = \frac{2\pi}{\sqrt[3]{V}}\left[n_x\hat{i} + n_y\hat{j} + n_z\hat{k}\right]. \tag{2.14}$$

The *reciprocal lattice vectors*, $\vec{K} = \sqrt[3]{N}\vec{k}$, can be defined as the wavevector states allowed to an electron confined to the unit cell volume, V/N. Each $\vec{k}$ state can accommodate two electrons: one with spin up ($\uparrow$) and one with spin down ($\downarrow$).

In accordance with the Pauli principle, at $T = 0$, N electrons fill N states, starting from that of zero energy, up to the *Fermi energy*, ε_F. In wavevector space the locus of states with energy ε_F is given by $\hbar^2\vec{k}_F^2/2m$, which defines the *Fermi sphere*. The *Fermi wave vector*, k_F, is completely determined by the electron number density, N/V, so that ε_F can easily be calculated and is of order $k_B(10^4\ \mathrm{K})$.

Since the n_i of equation 2.14 are of order 10^7, we can treat the set of allowed wavevectors as a continuum characterized by a density function. From equation 2.14, we can calculate the number of states, $\Delta\mathcal{N}$, in the wavevector space volume element d^3k as :

$$\Delta\mathcal{N} = 2\frac{V}{(2\pi)^3}\Delta k^3 = 2\frac{V}{(2\pi)^3}4\pi k^2\Delta k$$

$$\Delta\mathcal{N} \propto \sqrt{\varepsilon}\Delta\varepsilon$$

The *density of electron energy levels*, $N_0(\varepsilon)$, for a gas of free electrons can thus be written, since, by definition of ε_F, $\int_0^{\varepsilon_F} N_0(\varepsilon)d\varepsilon = N$, as:

$$N_0(\varepsilon) \equiv \lim_{\Delta\varepsilon\to 0}\left(\frac{\Delta\mathcal{N}}{\Delta\varepsilon}\right) = \frac{2N}{3\varepsilon_F}\sqrt{\frac{\varepsilon}{\varepsilon_F}} \quad \text{if } \varepsilon > 0, \quad \text{(zero otherwise).} \tag{2.15}$$

The *Fermi function*, $f_\mu(\varepsilon)$, describes how electron states are populated at a finite temperature, T. It turns out that the only electron states whose occupations are significantly changed from that at $T = 0$ are those with energies within k_BT of ε_F. The density of states at the Fermi level, $N_0(\varepsilon_F)$, is a most important quantity since $N_0(\varepsilon_F)k_BT$ is roughly the number of electrons which can change their energy and therefore contribute to measurable electronic properties. We note in passing that, since $N_0(\varepsilon_F) \propto \varepsilon_F^{-1} = 2m/(\hbar^2\vec{k}_F^2)$ and since $\vec{k}_F$ is only a function of the electron density, $N_0(\varepsilon_F)$ is proportional to the electron mass, m. Sommerfeld free electron theory works surprisingly well, considering its crudeness, and gives good order of magnitude estimates for almost all electronic properties.

We can derive the specific heat, $C_P(T)$, of a gas of non–interacting electrons [4,11] by noting that the total energy at a temperature T is:

$$\varepsilon = \int_{-\infty}^{\infty} f_\mu(\varepsilon)N_0(\varepsilon)\varepsilon d\varepsilon \tag{2.16}$$

$$\text{where : N} = \int_{-\infty}^{\infty} f_\mu(\varepsilon)N_0(\varepsilon)d\varepsilon \tag{2.17}$$

$$f_\mu(\varepsilon) \equiv \left[1 + \exp\left(\frac{\varepsilon - \mu}{k_BT}\right)\right]^{-1},$$

where μ is the chemical potential and $f_\mu(\varepsilon)$ is the Fermi function. To simplify this calculation, we make use of the Sommerfeld expansion [4] which, for any function, $H(\varepsilon)$, is:

$$\int_{-\infty}^{\infty} f_\mu(\varepsilon)H(\varepsilon)d\varepsilon = \int_{-\infty}^{\mu} H(\varepsilon)d\varepsilon + \frac{\pi^2}{6}(k_BT)^2 H'(\mu) + O(T^4). \tag{2.18}$$

The energy now becomes:

$$\varepsilon = \int_{-\infty}^{\mu} N_0(\varepsilon)\varepsilon d\varepsilon - \frac{\pi^2}{6}(k_B T)^2 [N_0(\varepsilon)\varepsilon]'_{\varepsilon=\mu}. \tag{2.19}$$

The conservation requirement of equation 2.17 allows us to calculate the first order shift in the chemical potential, μ, [4] at a temperature, T, from its value of ε_F at $T = 0$;

$$\mu = \varepsilon_F - \frac{\pi^2}{6}(k_B T)^2 \left[\frac{N_0'(\varepsilon_F)}{N_0(\varepsilon_F)}\right]. \tag{2.20}$$

Inserting this into equation 2.19 gives:

$$\begin{aligned} \varepsilon &= \int_{-\infty}^{\mu} N_0(\varepsilon)\varepsilon d\varepsilon + \frac{\pi^2}{6}(k_B T)^2 N_0(\varepsilon_F), \\ \text{therefore} : C_P(T) &\equiv \frac{d\varepsilon}{dT} = \frac{\pi^2}{3} k_B^2 T N_0(\varepsilon_F) \equiv \gamma_0 T. \end{aligned} \tag{2.21}$$

This important relation tells us that $C_P(T)$ is given by the classical value of $3k_B$, times $N_0(\varepsilon_F)k_B T$, the number of electron states which have their occupations significantly different from that at $T = 0$, times some constants of order unity. Since , as discussed, $N_0(\varepsilon_F) \propto m$, the ratio of the measured linear coefficient, γ, of the low temperature $C_P(T)$ to that of a free electron gas, γ_0, is universally referred to as the *effective electron mass*, $m^* \equiv \gamma/\gamma_0$.

In a crystalline system an electron feels a potential which has the periodicity of the lattice. In this periodic potential, the free electron wave functions combine to form *Bloch states* which are still itinerant and can still be characterized by a wavevector, $\vec{k}$. In this *nearly free electron model* [4], it can be shown that electron state energies are significantly modified from their free electron values only where the electron wavevector is near Brillouin zone boundaries of the reciprocal lattice corresponding to the crystal. The resulting energy dispersion curve, $\varepsilon(\vec{k})$, has *forbidden energy gaps* near Brillouin zone boundaries and so is broken up into *energy bands.* For Fermi wavevectors near Brillouin zone boundaries, the potential can have a profound effect on the Fermi sphere, distorting it in some cases beyond all recognition into the general

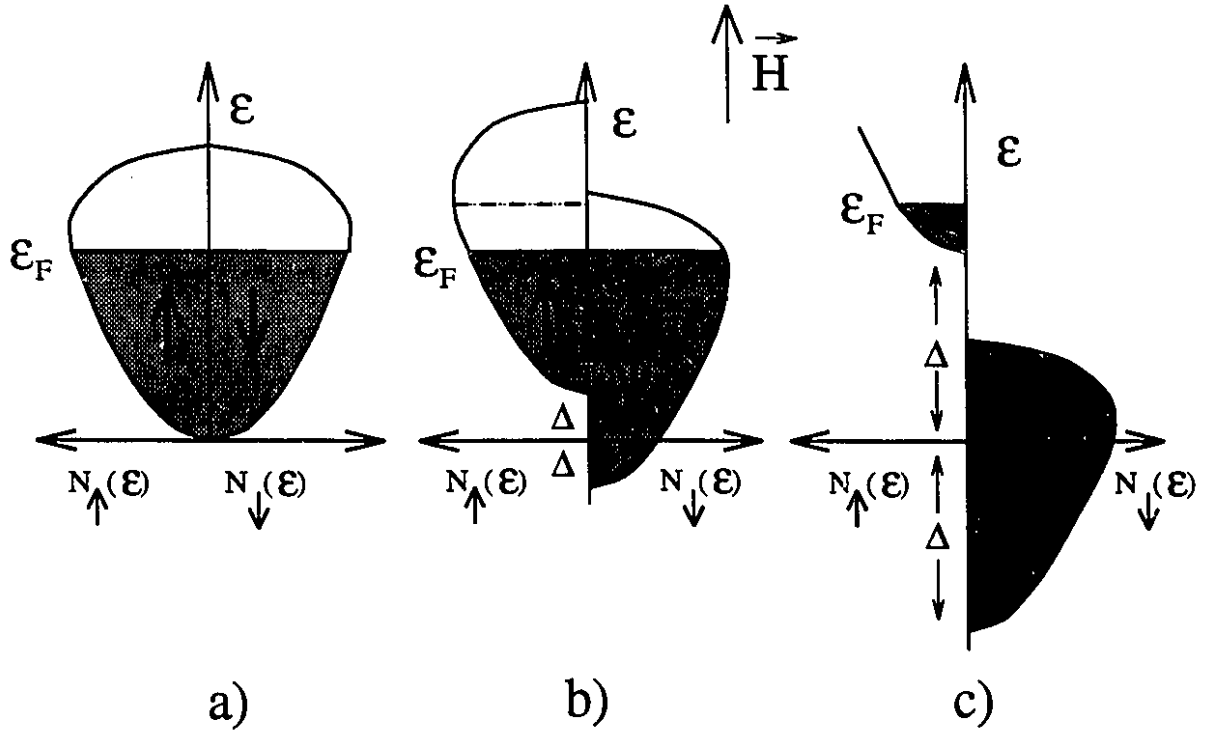

Figure 2.3: Energy level scheme describing the magnetic splitting of electron density of states a) of an unmagnetic metal, b) of an paramagnetic or weakly ferromagnetic metal and c) of a strongly ferromagnetic metal.

Fermi surface. The equations of free electron theory can be salvaged if we define an effective band mass, $m^* \equiv \hbar^2 \left[\frac{d^2\epsilon}{dk^2}\right]^{-1}$, and an effective Fermi velocity, $\vec{v}_F \equiv \frac{1}{\hbar}\frac{d\epsilon}{dk}$.

2.2.2 Pauli Paramagnetism

A metal can show paramagnetism without a local moment. Fig. 2.3a shows an *energy level scheme* corresponding to a partially filled electron band. If we choose to distinguish spin, then the density of ↑ and ↓ spins in each *spin sub-band*, $N_\uparrow(\varepsilon)$ and $N_\downarrow(\varepsilon)$, are both $\frac{1}{2}N_0(\varepsilon)$. Occupying the band with N electrons then gives each sub-band $N/2$ electrons. If we now apply a small magnetic field, H, then the energy of the spin sub-bands is *split* by an energy 2Δ. From equation 2.1, each free electron has a moment $-g(J,L,S)|\vec{J}|\mu_B = -g(\frac{1}{2},0,\frac{1}{2})\left(\frac{1}{2}\right)\mu_B = -1\mu_B$, so that Δ is simply *the Zeeman splitting*, $\mu_B H$. The ↑ electron thus acquires an additional magnetic energy $+\Delta$ and likewise the ↓ electron acquires $-\Delta$. The densities of states in the presence

of Δ can be written:

$$\begin{aligned} N_\uparrow(\varepsilon) &= \frac{1}{2}N_0(\varepsilon-\Delta) \approx \frac{1}{2}\left[N_0(\varepsilon) - N_0'(\varepsilon)\Delta\right] \quad \text{if } \Delta \ll \varepsilon \\ N_\downarrow(\varepsilon) &= \frac{1}{2}N_0(\varepsilon+\Delta) \approx \frac{1}{2}\left[N_0(\varepsilon) + N_0'(\varepsilon)\Delta\right] \quad \text{if } \Delta \ll \varepsilon \end{aligned}$$

Since $\Delta \ll \varepsilon_F$ for the highest experimentally accessible fields, the approximations are valid for ε near ε_F. These energies are the only ones for which electron occupation changes significantly so that other energies are irrelevant to the problem.

The resulting situation is displayed in Fig. 2.3b, which shows that some of the electrons in the $\uparrow$ sub–band spill into the $\downarrow$ sub–band. The number of electrons in each sub–band ($n_\uparrow$ and $n_\downarrow$) are now given by :

$$\begin{aligned} n_\downarrow &= \frac{1}{2}\int_{-\infty}^{\infty} f_\mu(\varepsilon)N_0(\varepsilon+\Delta)d\varepsilon \\ n_\uparrow &= \frac{1}{2}\int_{-\infty}^{\infty} f_\mu(\varepsilon)N_0(\varepsilon-\Delta)d\varepsilon \qquad (2.22) \\ \text{with : } \mathrm{N} &= n_\uparrow + n_\downarrow. \qquad (2.23) \end{aligned}$$

Given the temperature T, equations 2.22 and 2.23, the splitting Δ, $N_0(\varepsilon)$ and the number of electrons N determine the three unknowns $n_\uparrow, n_\downarrow$ and μ which completely describe the paramagnetism. The *relative magnetization*;

$$\zeta \equiv (n_\downarrow - n_\uparrow)/N = MV/\mu_B N, \qquad (2.24)$$

can now be calculated by using equations 2.22 simplified by the Sommerfeld expansion;

$$\zeta = \Delta\left[\int_{-\infty}^{\mu} N_0'(\varepsilon)d\varepsilon - \frac{\pi^2}{6}(k_BT)^2 N_0''(\mu)\Delta\right].$$

This equation is correct to order T^2 and Δ. Using the chemical potential (equation 2.20) gives an expression for the relative magnetization:

$$N\zeta = N_0(\varepsilon_F)\left(1-\alpha_0 T^2\right)\Delta \qquad (2.25)$$

$$\text{where} : \alpha_0 \equiv \frac{\pi^2}{6}(k_B)^2\left[\left(\frac{N_0'(\varepsilon_F)}{N_0(\varepsilon_F)}\right)^2 - \left(\frac{N_0''(\varepsilon_F)}{N_0(\varepsilon_F)}\right)\right]$$
$$\equiv \frac{\pi^2}{12T_F^2}. \tag{2.26}$$

Here we have implicitly defined T_F, which is the *effective Fermi temperature.* T_F is equal to the actual degeneracy temperature, ε_F/k_B, for a parabolic free electron band.

The Pauli magnetic susceptibility of a gas of non–interacting itinerant electrons can now be calculated from equation 2.25 as:

$$\chi_P(T) \equiv \frac{dM}{dH} = \mu_B^2 \frac{N}{V}\frac{d\zeta}{d\Delta}$$
$$\chi_P(T) = \mu_B^2 \frac{N_0(\varepsilon_F)}{V}(1 - \alpha_0 T^2). \tag{2.27}$$

This susceptibility can be derived directly from $N_0(\varepsilon_F)$ and gives agreement within ~50% or so with the observed susceptibilities of all simple sp–band metals (alkali, alkaline earth and noble metals). The discrepancy is due to neglect of electron–electron repulsion [4]. Since $T_F \sim 10^4$ K, the temperature dependence of $\chi_P(T)$ is only a few percent over the whole accessible temperature range.

2.2.3 Stoner Theory of Itinerant Magnetic Order

The application of molecular field theory to a system of interacting itinerant electrons is called *Stoner theory*[12]. While Stoner first applied it to free electrons in a parabolic band[12], the theory can be used describe magnetic order occurring amongst electrons associated with any arbitrary Fermi surface[13].

In order to cast Stoner theory as a mean field theory, we consider the Hubbard Hamiltonian which is written:

$$\mathcal{H}_{HUBBARD} = \sum_{\vec{k}\sigma} \hat{n}_{\vec{k}\sigma}\varepsilon(\vec{k}) + I\sum_i \hat{n}_{i\uparrow}\hat{n}_{i\downarrow} + \mu_B H(n_\uparrow - n_\downarrow),$$

where the $\hat{n}$ are number operators [14]. The first term describes the electron energy bands of a non–magnetic metal and the third term is the normal Zeeman energy. The second term favours magnetism, since it keeps compensating pairs of $\uparrow\downarrow$ spins away from the same lattice site, i. In Stoner theory, electron correlations are neglected and the second term is approximated by: $In_\uparrow n_\downarrow$[15]. This is equivalent to a Hartree–Fock approximation which also neglects correlations as discussed in section 2.1.4. Noting that $4n_\uparrow n_\downarrow = N^2 - N^2\zeta^2$, the Hubbard Hamiltonian may be simplified:

$$\mathcal{H}_{HUBBARD} = \sum_{\vec{k}\sigma} \hat{n}_{\vec{k}\sigma}\varepsilon(\vec{k}) + \frac{IN^2}{4}\left(1-\zeta^2\right) - \mu_B H N\zeta.$$

We can now define an effective field;

$$H_{EFF} \equiv -\frac{\frac{1}{V}d\mathcal{H}_{HUBBARD}}{dM} = -\frac{\frac{1}{V}d\mathcal{H}_{HUBBARD}}{(\mu_B\frac{N}{V})d\zeta} = H + \frac{IN}{2\mu_B}\zeta,$$

where I plays the role of the molecular field constant λ. The two are related by $\lambda = \frac{1}{2}IV/\mu_B^2$. The effective field leads to a splitting:

$$\Delta = \mu_B H_{EFF} = \mu_B H + \frac{1}{2}IN\zeta.$$

Let us now assume that Δ is small compared to ε_F. In this case we can use Δ as an expansion parameter as we did in the paramagnetic case. Equation 2.25 can be improved using the Sommerfeld expansion so that it is correct to order Δ^2. The effect of Δ^2 terms on μ must also be considered, and the calculation is similar to the introducing the shift in μ due to finite T (equation 2.20). Equation 2.25 becomes [13]:

$$\begin{aligned}(1+\alpha_0 T^2)\zeta + \gamma\zeta^3 &= \frac{N_0(\varepsilon_F)}{N}\Delta = \frac{N_0(\varepsilon_F)}{N}(\mu_B H + \frac{1}{2}IN\zeta) \qquad (2.28)\\ \text{where : } \gamma &= \frac{1}{2}\left(\frac{N}{N_0(\varepsilon_F)}\right)^2\left[\left(\frac{N_0'(\varepsilon_F)}{N_0(\varepsilon_F)}\right)^2 - \frac{1}{3}\left(\frac{N_0''(\varepsilon_F)}{N_0(\varepsilon_F)}\right)\right]\\ &= \frac{3}{16} \quad \text{for free electrons(equation 2.15).}\end{aligned}$$

In zero applied field, then;

$$(1 - \frac{1}{2}IN_0(\varepsilon_F) + \alpha_0 T^2)\zeta + \gamma\zeta^3 = 0. \qquad (2.29)$$

At $T = 0$, we can see right away that since $\gamma > 0$, this equation has a non-zero solution ζ only if:

$$\overline{I} \equiv \frac{1}{2} I N_0(\varepsilon_F) > 1. \tag{2.30}$$

Equation 2.30 is referred to as the *Stoner criterion for magnetic order.* The Stoner criterion determines when the magnetic potential energy decrease becomes greater than the subsequent kinetic energy increase introduced by preferentially occupying $\downarrow$ states. At this point, the metal become unstable against the formation of a magnetic moment. The Stoner criterion has no analog in Weiss theory in which any finite molecular field constant λ will lead to magnetic order at a finite temperature. For a given I, the criterion is realized by a high $N_0(\varepsilon_F)$. This explains why magnetic order occurs in transition metals, since d-bands are less broadened in energy by the effect of the crystalline environment than s- and p-bands and so have a higher $N_0(\varepsilon_F)$.

If the Stoner criterion is satisfied, then equation 2.29 can be solved for the spontaneous relative magnetization ζ;

$$\zeta^2 = \frac{\overline{I} - 1 - \alpha_0 T^2}{\gamma}, \tag{2.31}$$

which is valid for values of ζ small enough such that $\Delta/\varepsilon_F \ll 1$. The ordered moment at $T = 0$, p_s, can be now be written:

$$\begin{aligned} p_s &= \mu_B \zeta_0 = \mu_B \sqrt{\frac{\overline{I} - 1}{\gamma}} \\ p_s &= \mu_B \sqrt{\frac{16}{3}(\overline{I} - 1)} \text{ for free electrons.} \end{aligned} \tag{2.32}$$

We notice here that for sufficiently small values of $\overline{I} - 1$, p_s can be made arbitrarily small. Stoner theory therefore, through the introduction of an additional parameter ($N_0(\varepsilon_F)$) has no trouble explaining the existence of non-integral ordered moments [5]. Metallic systems with $p_c \ll \mu_B$ ($\zeta_0 \ll 1$) are called *unsaturated* or *weak ferromagnets* and the band splitting is schematically illustrated in Fig. 2.3b. This picture applies to pure Fe, in which both spin bands are only partially occupied, however because of its large value of $\overline{I}$, Fe has been classed as a *nearly strong ferromagnet* [1].

The application of a magnetic field to a weak ferromagnet increases the magnetization further since the splitting, Δ, is increased. This result of Stoner theory, therefore, explains the observation of finite susceptibilities in metallic ferromagnets at $T = 0$[16]. This observation is inexplicable by Weiss theory, where the local moments are already completely saturated.

In parabolic free electron band with no gaps, Stoner theory says that as $\overline{I} \rightarrow \infty$, the splitting becomes sufficient to completely empty the $\uparrow$ band of electrons and we say that we have a *saturated* or *strong ferromagnet.* The ordered moment takes its Weiss value for $S = \frac{1}{2}$ of $p_s = \mu_B$. In a real metal the $\downarrow$ band may have limited capacity and some electrons are left in the $\uparrow$ band, as illustrated in Fig. 2.3c. This actually corresponds to the situation in pure Ni and the ordered moment of $0.6\mu_B$ is commonly stated to result from 0.6 holes left in the d–band.

From equation 2.31 the ordering temperature, T_C, can be determined as the temperature at which $\zeta^2 = 0$:

$$\begin{aligned} 0 &= 1 - \overline{I} + \alpha_0 T_C^2 \\ T_C &= \sqrt{\frac{\overline{I} - 1}{\alpha_0}} \\ \text{and from eqn. 2.26, } \mathrm{T_C} &\approx T_F\sqrt{\overline{I} - 1}. \end{aligned} \tag{2.33}$$

In a paramagnet ($\overline{I} < 1$) and in an applied field $H \neq 0$, the magnetic susceptibility can be determined from the non–interacting susceptibility, $\chi_0(T)$, as in the local model (equation 2.6):

$$\chi(T) = \chi_0(T)/(1 - \lambda\chi_0(T)) \tag{2.34}$$

$$\chi = \frac{\chi_P(T)}{1 - \overline{I}} \equiv S\chi_P(T), \tag{2.35}$$

where we have taken $\chi_P(T)$ as $\chi_0(T)$ and derived the simple relation $\lambda\chi_P(T) \approx \lambda\chi_P(0) = \overline{I}$. We have also defined the *Stoner enhancement factor* $S \equiv (1 - \overline{I})^{-1}$. The

itinerant *exchange enhanced* Pauli paramagnet does not order at a finite temperature and so these metals are often called *nearly ferromagnetic metals.* The simplest near ferromagnet is pure Pd which has a Stoner factor $\mathcal{S} \sim 10$ [2].

Consider now a metallic alloy system containing a concentration, x, of magnetically active atoms which becomes ferromagnetic at $T = 0$ when x exceeds a *critical concentration*, x_c. If the magnetism is itinerant, then $\overline{I}= 1$ at x_c and may be linearly expanded about x_c, that is:

$$\overline{I} - 1 \propto (x - x_c).$$

Combining this relation with previous results (equations 2.32, 2.33 and 2.35), allows us to summarize the predictions of Stoner theory for an itinerant magnet near a ferromagnetic instability.

$$\left[T_C^2\right] \propto \left[M^2(T=0)\right] \propto \left[\chi^{-1}(T=0)\right] \propto \left[x - x_c\right] \propto \left[\overline{I} - 1\right]. \qquad (2.36)$$

At x_c then, the system undergoes a transition from a nearly ferromagnetic metal to a weak ferromagnet. Presumably, I is roughly constant over a small range of x, and $\overline{I}$ increases predominantly due to a rising $N_0(\varepsilon_F)$. Relations 2.36 are quite well obeyed by the nearly-/weakly-ferromagnetic Ni_3Al alloys, which are magnetically ordered for Ni contents greater than 75%. These relations are neatly displayed as a *Mathon plot* (Fig. 2.4).

We note in passing that the application of sufficient external pressure to an itinerant ferromagnet destroys the magnetic order. This is simply because the resulting volume contraction leads to an expansion of the Fermi surface. The kinetic energy is, therefore, increased, eventually to the point where the Stoner criterion is no longer satisfied [1,17].

There is general agreement that the Stoner picture provides a complete picture of d-band magnetism at T=0. Fermi surfaces topologies can be predicted from band structure calculations and compared with extremal Fermi surface areas measured by the de Haas-van Alphen (dHvA) effect [15]. A knowledge of the Fermi surface determines $N_0(\varepsilon)$ and its derivatives at ε_F. These values, together with an independent

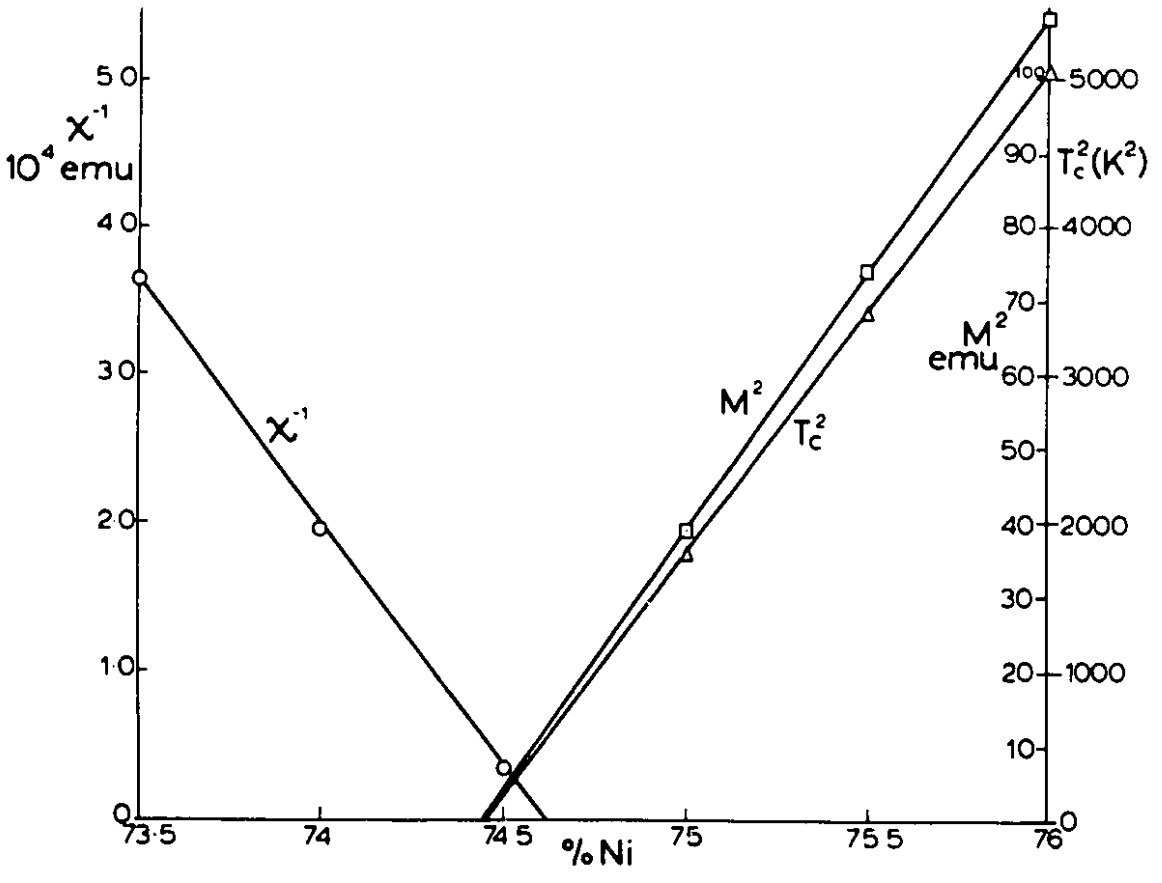

Figure 2.4: Mathon plot for Ni_3Al alloys: taken from ref. [1]. M and χ are the ground state magnetisation and susceptibility, respectively. The points are measured data and the solid straight line are consistent with Stoner theory.

measure of I (which may also be obtained by dHvA measurements), allow a theoretical value of the ordered moment, p_s, to be calculated from equation 2.32. *State of the art band-structure measurements can now completely explain the ground state ordered moments of the iron group metals using Stoner theory* [18].

2.2.4 Failures of Stoner Theory

While Stoner theory succeeds in explaining many aspects of d-band magnetism (*e.g.* Fig 2.4), it fails to correctly predict the energy scale of the phenomenon. From equation 2.33, T_C may be predicted by Stoner theory with the same information used to calculate p_c as discussed in the previous section. These predictions yield a T_C

which is a factor of two or more too big compared with observed values for the Fe group elements [17,18]. In weak ferromagnets, T_C^{STONER} may exceed the measured T_C by more than an order of magnitude. We conclude that the essential energetic ingredients of the phase transition are not in Stoner theory [18]

In Stoner theory, the spontaneous magnetization at $T = 0$ is destroyed with rising temperature by *Stoner excitations*. These are simply the thermal excitations of electrons from the spin down ($\downarrow$) band with a wavevector $\vec{k}$ into the spin up ($\uparrow$) band with a wavevector $\vec{k} + \vec{q}$. The energy of these spin–flip excitations, $\omega(\vec{q})$, is given for free electrons with a splitting, Δ, by:

$$\begin{aligned} \hbar\omega(\vec{q}) &= 2\Delta + \frac{\hbar^2}{2m}(\vec{k}+\vec{q})^2 - \frac{\hbar^2}{2m}(\vec{k})^2 \\ \hbar\omega(\vec{q}) &= 2\Delta + \frac{\hbar^2}{2m}(2\vec{k}\cdot\vec{q} + \vec{q}^2). \end{aligned} \tag{2.37}$$

The region of *phase space* (the energy–wavevector plane $\{\omega, |\vec{q}|\}$) available to these *single particle excitations* is limited, since $\omega = 0$ excitations from the $\downarrow$ Fermi surface to the $\uparrow$ Fermi surface require a minimum change of the electron wavevector $|\vec{q}| = |\vec{k}_{F\downarrow} - \vec{k}_{F\uparrow}|$. Also if an electron's wavevector does not change, then its energy must change by 2Δ. The phase space available to single particle excitations is called the *Stoner continuum* and is illustrated in Fig 2.5. Representations of excitations on the two axes in the level scheme of Fig 2.3b are also shown.

In Stoner theory, as the temperature increases from zero, Stoner excitations deplete the $\downarrow$ band of electrons and fill up the $\uparrow$ band until the two bands are equally occupied at T_C and the spontaneous magnetization vanishes. If this were the case, we would expect the wavevector space volumes of the $\uparrow$ and $\downarrow$ Fermi surfaces to be different at $T = 0$. With increasing temperature, this difference should shrink progressively until the two Fermi surfaces are identical at T_C. The extremal areas of the two Fermi surfaces may be measured directly by the de Haas–van Alphen (dHvA) effect. dHvA studies on pure Ni have shown that the relative area difference between the two Fermi surfaces does not decrease quickly enough with temperature to account

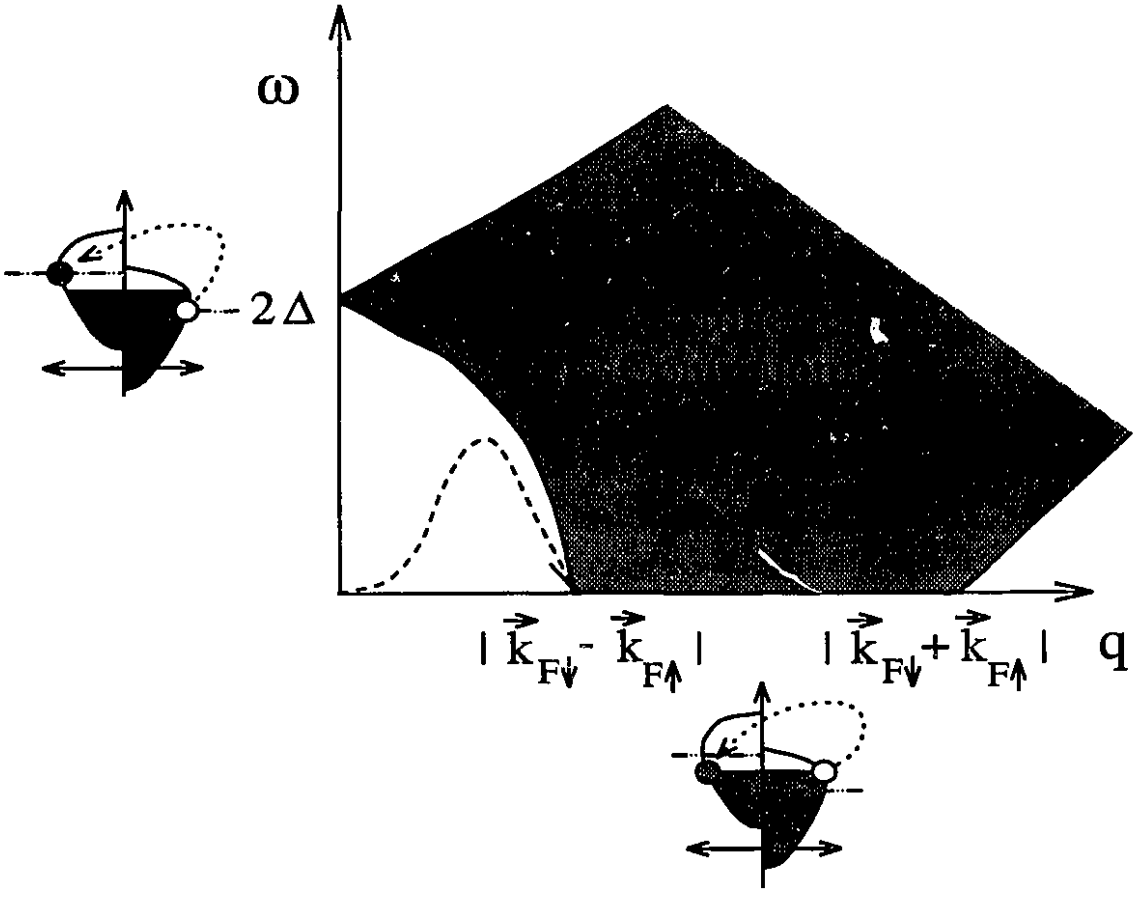

Figure 2.5: Phase space for magnetic excitations in a ferromagnet. The shaded region represents the Stoner continuum of single particle excitations. The unshaded region is inaccessible to these excitations and a well defined dispersion curve for lightly damped spin waves may exist (illustrated here as a dashed line). Also shown are representations of Stoner excitations on the two axes as illustrated in the level scheme of Fig 2.3b.

for the observed decay of the magnetization [15]. This confirms that the decay of the spontaneous magnetization does not occur primarily through Stoner excitations.

Stoner theory also fails at high temperatures where it predicts that the paramagnetic susceptibility should change quadratically with temperature. In contrast, a Curie–Weiss law (equation 2.8) is observed in virtually all magnetically ordered metals in the paramagnetic regime. The law is even obeyed by enhanced Pauli paramagnets at high temperatures. This manifestation of local moment behaviour by an itinerant metal was at the heart of the controversy over the origins of d–band magnetism.

2.3 Spin Fluctuations: Fundamental Considerations

2.3.1 Definition and Discussion

The failures of Stoner theory arise because it is a *mean field theory* which neglects electron correlations in the sense discussed in section 2.1.4. Correlations are accounted for by *spin fluctuations* or *paramagnons*, which we now define in *two ways*, with reference to the two limiting pictures: itinerant and local magnets.

First, in Stoner theory, the motion of the excited electron in the $\uparrow$ band and the hole in the $\downarrow$ band which comprise the Stoner excitation are uncorrelated and move completely independently of one another. In theories accounting for electron correlations, electron–electron interactions lead single particle excitations to behave collectively. These collective excitations of electron–hole pairs are called *spin fluctuations* .

For the second definition, we consider the phase space region about $q = 0$, excluded from the Stoner continuum (Fig. 2.5). Here, spin waves are observed to propagate with a well defined dispersion curve. Observations of spin waves in the Fe group metals were once taken as evidence that they were local magnets [19]. The existence of spin waves in an itinerant model, however, was demonstrated [19], and their presence in metals indicates the importance of electron correlations. In the spin wave region of phase space, the particle and hole which make up the Stoner excitation can be thought of as being *so correlated*, that they sit on the same atom and the picture of local moments applies [20]. From these local moments, spin wave states may be constructed as before (see section 2.1.3). As q increases, the spin wave dispersion curves cross into the Stoner continuum (Fig. 2.5), where they are then free to exchange energy with Stoner excitations and rapidly become over–damped, non–propagating *SF* modes.

We now have two alternate ways of defining spin fluctuations in either the local or the itinerant picture, that is: *as over–damped spin waves* or *as highly correlated Stoner*

excitations. SF are described by a characteristic energy, $k_B T_{SF}$, where T_{SF} is the *spin fluctuation temperature.* We shall see that T_{SF} occurs in the mathematical description of the effect of *SF* on any measured property. It is roughly the temperature above which all *SF* modes are thermally excited, in the same way as the Debye temperature, Θ_D, is the temperature above which all phonon modes are excited in a crystal.

In a strong magnet ($\overline{I} \gg 1$), the splitting Δ is large. The spin wave region of phase space is therefore large (see Fig. 2.5) and we expect the metal to behave as a local magnet. This is the situation in rare–earth metals, such as gadolinium. We might expect *SF* to be important in *weak magnets* ($\overline{I} \sim 1$) simply because of their small splitting, Δ, which places the boundary of the Stoner continuum (Fig 2.5) very close to $q = 0$. More phase space is therefore available for *SF* which then become the important low energy excitations. In a *near ferromagnet*, the excluded region of the Stoner continuum vanishes, and there are no spin waves, only *SF*.

It is now believed that the spontaneous magnetization in transition metals is destroyed by transverse *SF*, in which the number of $\uparrow$ and $\downarrow$ electrons is not changed, but the moments are transversely canted ($\uparrow\nearrow\rightarrow\searrow\downarrow\swarrow\leftarrow\nwarrow\uparrow$) reducing the total magnetization. This is similar to the way in which the magnetization is destroyed near $T = 0$ in a local magnet by spin waves, which are sinusoidal transverse excitations. The difference, however, is that Weiss theory, in the absence of spin waves, can be used to calculate T_C in a local magnet. By contrast, in an itinerant magnet, *spin fluctuations completely determine the finite temperature properties, including* T_C [14].

In a mean field theory, *SF* are assumed to have no effect on the static mean field and, therefore, on the static magnetic properties. However, this is not valid in a system whose response is non–linear as a sinusoidal field at one frequency may then generate responses at other frequencies, notably at zero frequency. We have shown (equation 2.28) that the response, here the magnetization, M, of a near/weak magnet is, in fact, non–linear in H. This is a more general result of the *Ginzburg–Landau expansion* in which, for small M, the free energy, $F(M)$, may be expanded in powers

of M^2;

$$F(M) = F_0 + \frac{1}{2}aM^2 + \frac{1}{4}bM^4 - MH,$$

$$\text{in equilibrium } \frac{\mathrm{dF}}{\mathrm{dM}} = 0, \text{ so that : H} = aM + bM^3. \tag{2.38}$$

In a paramagnet, the coefficient, a, is simply the inverse non–interacting susceptibility, $\chi_0^{-1}(T)$. In a local paramagnet, $\chi_0^{-1}(T)$ is the inverse Curie susceptibility which grows linearly with T, so that the relative importance of the non–linear term, bM^3, decreases with increasing temperature. By contrast, in an itinerant paramagnet, the inverse Stoner susceptibility is nearly temperature independent. This suggests the importance of considering non–linearity, and thus *SF*, at all temperatures in an itinerant magnet.

The static response arising due to *SF* works to reduce the susceptibility of a paramagnet. A simple way of understanding this is to consider a small region of a paramagnet in which a large amplitude *SF* occurs. This may lead the region to have a magnetization near saturation and a huge local effective field. The region would therefore be virtually unaffected by a small applied field, so that it acts like "magnetically dead" volume. The overall susceptibility is therefore reduced by this dead volume fraction.

2.3.2 Modern *SF* Theories

The general approach taken to rectify the failures of Stoner theory is to include the effect of long wavelength *SF* on the magnetization. We will touch on four separate schools of *SF* theories. The first and simplest theory of *SF* [17,18], due to Wohlfarth and others, considers the effect of *SF* as introducing an effective pressure. The second work, Moriya's microscopic theory of *SF* [10,21], uses techniques similar to those employed by the third school of theories, which we will refer to as *paramagnon theory* [22–25]. Being more developed in its predictions of electronic properties, paramagnon theory has been used to describe the vast majority of experimental work on

SF properties, and so is used exclusively in our data analysis. The derivations of paramagnon theory are complicated, so that we will use the work of a fourth school, the phenomenological *SF* theory of Lonzarich and Taillefer, in order to obtain a physical understanding of its predictions.

The simplest theories of *SF* [17,18] consider the effect of *SF* as renormalizing the Ginzburg–Landau coefficient, a (equation 2.38), by a small constant $\alpha(T)$. We can simply think of $\alpha(T)$ as the dead volume fraction discussed in the last section. In this treatment, the effect of *SF* equivalently can be viewed as introducing an effective pressure [17], which similarly renormalizes the Ginzburg–Landau coefficients. The renormalized susceptibility, $\overline{\chi_0}(T)$, is written as [8]:

$$\overline{\chi_0}(T) = \frac{\chi_0(T)}{1+\alpha(T)}.$$

If we neglect the temperature dependence of the Pauli susceptibility, so that $\chi_0(T) \approx \chi_P(T=0)$, then we can rewrite the susceptibility of an itinerant paramagnet as (*c.f.* equation 2.34):

$$\chi(T) = \frac{\overline{\chi_0}(T)}{1-\lambda\overline{\chi_0}(T)} = \frac{\chi_P(T=0)}{1-\bar{I}+\alpha(T)},$$

since $\bar{I} = \lambda\chi_P(T=0)$. We would expect $\alpha(T)$ to be proportional to the number of *SF* occupying each *SF* mode due to thermal activation. This is proportional to the Bose factor which, at high temperatures ($T \gg T_{SF}$), is simply T/T_{SF}. Writing $\alpha = cT/T_{SF}$, we have:

$$\chi(T) = \frac{T_{SF}\chi_P(T=0)/c}{T - T_{SF}(\bar{I}-1)/c}. \tag{2.39}$$

This is exactly the form of the Curie–Weiss (CW) law (equation 2.8) with $\Theta_{CW} = T_{SF}(\bar{I}-1)/c$. Θ_{CW} has the sign of $\bar{I}-1$ and so is positive for weak ferromagnets and negative for near ferromagnets. We have therefore demonstrated how *SF* lead to a CW law in an itinerant magnet. This is just one of many manifestations of *SF* that make an itinerant magnet appear to behave as a local magnet.

Including the effects of *SF*, we can generally determine the interacting susceptibility, $\chi(T)$, as the non–interacting susceptibility, $\chi_0(T)$, divided by $(1-\lambda\chi_0+\alpha(T))$. In a local magnet, $\chi_0(T)$ is just the Curie susceptibility, $\chi_C(T)$. If α is assumed to

be small, then it only has a small effect on $\chi(T)$, except near T_C, where $1-\lambda\chi_0 \rightarrow 0$. This leads to the conclusion that *while SF are important in determining the* behaviour *of static quantities near T_C in a local magnet, they are not important in determining the* value *of T_C*. In a near/weak system, however, $\lambda\chi_0(T=0) \equiv \overline{I} \sim 1$. This means that $1-\lambda\chi_0(T)$ is *always* close to zero and has a very weak temperature dependence. A small value of α then has a dramatic effect in determining $\chi(T)$ *at all temperatures* and in reducing the value of T_C.

The high temperature linear form of $\alpha(T)$ actually violates the third law of thermodynamics at low temperatures [17], so that $\chi(T)$ cannot be so easily determined. Mohn and Wolfarth [18] have derived a universal equation for determining T_C from T_{SF} and the ordering temperature calculated by Stoner theory, T_C^{STONER}:

$$\frac{T_C^2}{(T_C^{STONER})^2} + \frac{T_C}{T_{SF}} - 1 = 0.$$

This equation gives good agreement with observed values of T_C for the iron group metals as well as for various intermetallic compounds [18].

Modern theories of itinerant magnetism [10,14] consider the detailed form of the magnetic excitation spectrum. In *linear response theory* [8], the response $\vec{M}(\vec{q},\omega)$ to the application of an infinitesimal field $\vec{H}(\vec{q},\omega)$ with a wave vector $\vec{q}$ and at frequency ω is given by:

$$\vec{M}(\vec{q},\omega) = \overline{\overline{\chi}}(\vec{q},\omega)\vec{H}(\vec{q},\omega),$$

where $\overline{\overline{\chi}}(\vec{q},\omega)$ is the generalized dynamical susceptibility which is a complex tensor. For an isotropic magnet the components of $\overline{\overline{\chi}}(\vec{q},\omega)$ can be summarized as:

$$\chi_\nu(\vec{q},\omega) \equiv \chi'_\nu(\vec{q},\omega) + i\chi''_\nu(\vec{q},\omega)$$

where $\nu = \perp, \parallel$. The imaginary part, $\chi''_\nu(\vec{q},\omega)$, is proportional to the energy absorption, and gives the distribution spectrum of magnetic excitations. The general form of $\chi''_\nu(\vec{q},\omega)$ in the spin wave and SF regions of phase space may be summarized as [14]:

$$\chi''_\perp(\vec{q},\omega) = \frac{1}{2}\pi\omega\chi_\perp(q)\left[\delta(\omega-\omega(\vec{q})) + \delta(\omega+\omega(\vec{q}))\right] \quad \text{for spin waves} \qquad (2.40)$$

$$\chi''(q,\omega) = \chi(q)\frac{\omega\Gamma(q)}{\omega^2+\Gamma(q)^2,} \text{ for } SF. \tag{2.41}$$

$\chi(q)$ is the static susceptibility, which may be written to lowest order in q as [14]:

$$\chi^{-1}(q) \approx \chi^{-1}(0)\left[1+\frac{q^2}{q_c^2}\right]. \tag{2.42}$$

The *correlation wave vector*, q_c, is the inverse of the distance over which a localized disturbance affects the magnetization of neighbouring regions.

Spin waves are *monodispersive*, which means that for a given q, there is only one excitation energy, $\omega(q)$, which defines the *dispersion relation* for the spin waves. This is reflected by the delta functions in equation 2.40. The Lorentzian form of equation 2.41 shows that *SF* are non–monodispersive, which means that for a given wavevector, q, the excitations possess a distribution of energies. $\Gamma(q)$ is the *damping frequency* or the *inverse lifetime of a SF*. The Lorentzian is peaked at the energy $\Gamma(q)$, which is therefore also taken to define the *quasi–dispersion relation* for the *SF*. Like a spin wave, which is a spin flip sinusoidally distributed over localized moments, a *SF* is also a spin flip excitation. It is, however, distributed non–monodispersively over itinerant moments.

$\chi''_\nu(q,\omega)$ is measurable directly by inelastic neutron scattering. Measuring the energy and wavevector change of the neutron gives the dispersion curves of the excitations directly. In a magnetic crystal, sharp inelastic peaks are observed just off Bragg angles, corresponding to gains or losses of neutron energy to spin waves. In a local magnet, spin wave dispersion curves are found to be rigid, that is the spin wave stiffness, $\mathcal{D}$, does not change much with temperature [26]. In Ni_3Al , however, the spin wave stiffness $\mathcal{D}$ was found to decrease with increasing temperature, vanishing at T_C [27]. This "mode–softening" is reminiscent of the rapid decrease of Θ_D in a crystal near the temperature of a structural ordering transition. The Lorentzian form (equation 2.41) has been observed directly by small angle neutron scattering in Ni_3Al just above T_C [27].

In the paramagnet, we can generalize mean field theory for the dynamic susceptibility and include the effect of *SF* renormalization The interacting susceptibility, $\chi(\vec{q},\omega)$, is directly obtained from the the non–interacting susceptibility, $\chi_0(\vec{q},\omega)$, by:

$$\chi(\vec{q},\omega) = \frac{\chi_0(\vec{q},\omega)}{1 - \lambda(\vec{q},\omega)\chi_0(\vec{q},\omega) + \alpha(\vec{q},\omega)} \tag{2.43}$$

where $\lambda(\vec{q},\omega)$ and $\alpha(\vec{q},\omega)$ are the *dynamic* molecular field and *SF* renormalization constant, respectively [8,14]. If $\alpha(\vec{q},\omega) = 0$ then we can construct an independent Stoner theory at each $\{\vec{q},\omega\}$ mode. The effect of *mode–mode coupling* is accounted for by $\alpha(\vec{q},\omega)$, which, in general, depends on $\chi_0(\vec{q},\omega)$ at all $\{\vec{q},\omega\}$ and on the number of excited modes. This enormous complication has been treated only in the simplest ways [8], which we will only briefly outline.

If we ignore zero–point energies then there are no *SF* at $T = 0$ and $\alpha \rightarrow 0$ as $T \rightarrow 0$. This is satisfactory since we know from experiment that Stoner theory is valid at $T = 0$. The dynamic susceptibility, $\chi(\vec{q},\omega)$, determines the *SF* quasi–dispersion, which in turn affects $\chi(\vec{q},\omega)$, through $\alpha(\vec{q},\omega)$. Modern theories, therefore, determine $\chi(\vec{q},\omega)$ and $\alpha(\vec{q},\omega)$ *self–consistently.*

The *self–consistent renormalization* (SCR) theory of magnetism, due to Moriya and others [10,21] is a microscopic theory which takes $\alpha(\vec{q},\omega)$ as a constant for all $\{\vec{q},\omega\}$. Here $\overline{\overline{\chi}}(\vec{q},\omega)$ is calculated microscopically using Feynman diagram techniques. SCR theory is acknowledged as the first theory which was able to calculate a high temperature Curie–Weiss law due to the new mechanism of *SF* [21,28,29].

Lonzarich and Taillefer [14,30] have treated the problem phenomenologically in their *self–consistent Ginsburg–Landau theory.* In this treatment, the local free energy is expanded in a Ginzburg–Landau expansion in the static magnetization, M, and zero–average fluctuating components $< m_q^2 >$ for small q. The theory is cast in terms of four experimentally meaningful parameters; a, b, determined from the measured magnetization (equation 2.38) and c, γ, determined from neutron scattering data. This theory and the well known parameters for Ni_3Al , determine values of T_C and the moment ratio, p_c/p_s, in good agreement with experiment, using no adjustable parameters.

The quasi–dispersion relation, $\Gamma(q)$, can be written as [14]:

$$\Gamma(q) = \gamma\chi^{-1}q\left[1+\left(\frac{q}{q_c}\right)^2\right]. \tag{2.44}$$

This result shows that near the critical point ($\chi^{-1} \to 0$), $\Gamma(q) \to 0$, and *SF* become important low energy excitations as argued previously.

2.3.3 *SF* Quasi–dispersion

Paramagnon theory [22–25], which was first applied to liquid ^{3}He, casts its predictions for the electronic properties in terms of T_{SF}, the characteristic energy of spin fluctuations, given as T_F/S [2]. In order to understand the meaning of T_{SF}, we determine its interpretation in Lonzarich and Taillefers' theory [14,30].

In what follows, we ignore the temperature dependence of $\Gamma(q)$, which enters through $\chi(T)$ in equation 2.44. The temperature dependence of the *SF* quasi–dispersion arises largely as a consequence of self–consistency requirements [8,14], and is most marked near the critical point. The assumption of a temperature independent $\Gamma(q)$, while incorrect, is not unreasonable, however, in interpreting our data, which are taken over a temperature range where χ, and thus $\Gamma(q)$, change little with temperature.

Taking the Lonzarich and Taillefer expressions for $q_c \equiv l_c^{-1} = 1/\sqrt{c\chi}$ [14] and $T_{SF} \equiv T^* = \hbar\gamma/k_B\sqrt{c\chi^3}$ [14], we can rewrite equation 2.44 as:

$$\Gamma(q) = \frac{k_B T_{SF}}{\hbar}\frac{q}{q_c}\left[1+\left(\frac{q}{q_c}\right)^2\right]. \tag{2.45}$$

If we ignore fundamental constants, $2T_{SF}$ is the damping frequency $\Gamma(q)$ at the correlation wavevector, q_c. If we look along the path in phase space $\omega(q) = \Gamma(q)$ which is roughly the locus of maxima in $\chi''(q,\omega)$, then, from equation 2.41, $\chi''(q,\omega)$ is simply $\chi(q)/2$. Since $\chi(q)$ is reduced by one half at q_c (equation 2.42), $2T_{SF}$ is, therefore, the energy at which the dynamic susceptibility is diminished to half its value at $q = 0$. *T_{SF} is the characteristic energy of the SF*, above which the spectral weight of the *SF* modes rapidly diminishes.

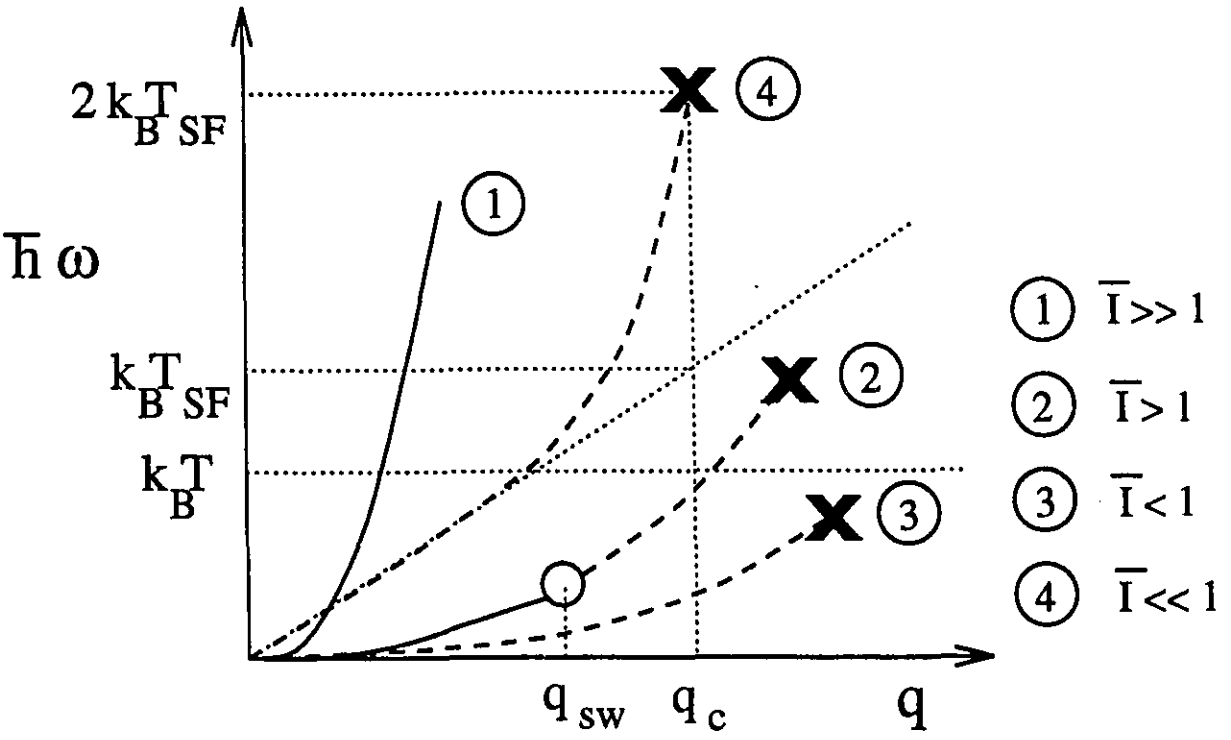

Figure 2.6: Dispersion curves for spin waves (solid lines) and quasi–dispersion curves *SF* (dashed lines) for magnets with various values of $\bar{I}$. The wavevector q_{SW} separates the spin wave and *SF* regions of phase space. Modes which are thermally excited below a temperature T fall below the dotted line. The *SF* curves are truncated at the phase space point $\{q_c, 2T_{SF}\}$ by an **X**. This **X** gives the point where the generalised susceptibility is down to half its value at $q = \omega = 0$.

The elementary excitations of an itinerant ferromagnet are illustrated in Fig 2.6 which shows the spin wave dispersion curves and the *SF* quasi–dispersion curves for samples with various values of $\bar{I}$. We have simplified the *SF* quasi–dispersion curves by *truncating* them at q_c. Since the linear term in $\Gamma(q)$ is proportional to the susceptibility, $\chi^{-1}(q = 0)$ (equation 2.44), we expect the *SF* quasi–dispersion curves to be highly dependant on $\bar{I}$ near the critical point ($\bar{I}$= 1). Here the *SF* become most important since the dispersion curves are moved to lower energies and many more *SF* are thermally excited. The spin wave and *SF* regions of phase space are divided by a wavevector, q_{SW}, which roughly corresponds to the boundary of the Stoner continuum.

Consider a strongly exchange enhanced itinerant paramagnet with $\bar{I}$ slightly less than 1 (curve #3 in Fig. 2.6). Since the curve is at low energies, many *SF* are excited and they have a marked effect on the electronic properties. If we increase the energy

scale of the curve, we reduce the occupation and thus effect of *SF*. We can achieve this effect in two ways. First, we can move farther away from the critical concentration and thus reduce $\overline{I}$, so that χ^{-1} and thus $\Gamma(q)$ is increased. A second method is the application of a magnetic field H. Since *SF* are excitations corresponding to a single spin flip, the application of a magnetic field increases the energy of a *SF* by twice the Zeeman splitting, $\mu_B H$. When this energy is comparable to T_{SF} , the dispersion curve would be moved up in energy by a significant amount. Eliminating the effect of *SF* through the application of a magnetic field, $H \approx k_B T_{SF}/\mu_B$, is referred to as *field quenching of SF* [2].

2.4 Spin Fluctuations: Effects on Electronic Properties

The effects of spin fluctuations on the finite temperature properties are expected to be most important in nearly ferromagnetic ($\mathcal{S} \gg 1$) and weakly ferromagnetic ($p_c/\mu_B \ll 1$) metals, where $\overline{I} \sim 1$. Magnetization measurements therefore provide a direct measure of $\overline{I}$ and thus a check as to whether we should look for *SF*. Fitting the results of *SF* theory to magnetization measurements, however, is rarely conclusive. Consequently, experimental evidence for the presence of *SF* has been sought mainly by *neutron scattering*, and by studying the effects of *SF* on the *electronic properties.*

Ni_3Al is probably the most extensively studied weak ferromagnet. It has a cubic crystal structure which is very much like that of pure, fcc Ni (a strong ferromagnet) [31]. Ni_3Al simple cubic structure results if the corner Ni atoms in the standard fcc Ni unit cell are replaced by Al. Ni_3Ga is a similar metal, but $N_0(\epsilon_F)$ is slightly smaller so that the alloy is nearly–ferromagnetic. As noted before, *SF* have been observed by neutron scattering in Ni_3Al [27] and *SF* theory has been successful in describing the thermodynamics of the magnetic ordering [14]. Studies have also been done on the Ni_3Al alloy system which becomes ferromagnetically ordered for Ni contents more than 75% [32]. The value of $\overline{I}$ can thus be tuned by changing the amount

of Ni.

2.4.1 Fermi Liquid Theory

The existence of strong Coulomb interactions between electrons in a metal suggests that any treatment of conduction electrons as free is dubious. The free electron model, however, is overwhelmingly successful considering its simplicity. The reason for the success of the free electron model is that at low temperatures, the Pauli exclusion principle puts even more stringent requirements on the motion of the electron that does consideration of Coulomb interactions.

Developed to describe ^{3}He, Landau's *Fermi liquid theory* [33–37] first suggested that a metal may be treated as a gas of free *quasi–particles*. While not identifying what these quasi–particles are, he stated that they were fermions, and so must also obey the Pauli principle and are occupied according to the Fermi function.

In Fermi liquid theory, it is postulated that there is a one–to–one correspondence between the quasi–particle states of an interacting system and the states of the free electron gas. The interaction is turned on *adiabatically*, and an electron state with an energy $\varepsilon(\vec{k})$ and an occupation $n(\vec{k})$ becomes a quasi–particle state whose energy and occupation are changed by $\delta\varepsilon(\vec{k})$ and $\delta n(\vec{k})$ respectively. The low lying excitations out of this quasi–particle Fermi surface must be symmetric under the inversion, $\vec{q} \rightarrow -\vec{q}$, so that the excitation energy can be expanded as:

$$\varepsilon(q) \approx \frac{\hbar^2}{2m^*}q^2 + O(q^4) + ..., \tag{2.46}$$

where we have defined the *effective mass* m^* by analogy with the free electron gas. The energy band distortion resulting from the interactions occurs only in the vicinity of ε_F, and the subsequent shift in $N_0(\varepsilon_F)$ is accounted for to first order by renormalizing the electron mass. In going beyond this approximation to next order, one writes the free energy of the system as [33]:

$$F = F_0 + \sum_{\vec{k}\sigma}(\varepsilon_{\vec{k}} - \mu)\delta n_{\vec{k}\sigma} \sum_{\vec{k}\vec{k}'\sigma\sigma'} f(\vec{k}\sigma, \vec{k}\sigma')\delta n(\vec{k}\sigma)\delta n(\vec{k}'\sigma'), \tag{2.47}$$

where f is the *effective interaction.*

In the case of electron–phonon coupling, the change in electron energy due to lattice distortions couples electrons and phonons. The linear dispersion curve ($\omega(k) = ck$) extends to infinite energies. The *electron–phonon mass renormalization constant*, λ_{e-p}, is defined by $1 + \lambda_{e-p} \equiv m^*/m$. Experimentally, λ_{e-p} is usually found to be of order, but usually less than, 1.

In our case, at low temperatures, we consider the electron mass renormalization due to *SF*. At low temperatures, the *SF* quasi–dispersion is linear, like the phonon dispersion. We would therefore expect a similar mass renormalization constant, λ_{SF}. At temperatures high compared to T_{SF}, however, we expect that the truncated *SF* quasi–dispersion will not affect m^*. This is because the electronic excitations have a mean energy k_BT, and in this region of phase space there are effectively no *SF* modes and the *SF* quasi–dispersion is irrelevant. λ_{SF} is therefore expected to tend to zero at temperatures well above T_{SF}.

2.4.2 Specific Heat

The low temperature electron specific heat, $C_P(T)$, of a free electron gas was determined in equation 2.21. In the presence of the electron–phonon interaction, the electron $C_P(T)$ is determined directly by replacing the electron mass, m, by an effective mass, m^*, determined from Fermi liquid theory.

$$\frac{C_P}{T} = \frac{m^*}{m}\gamma_0 \equiv (1 + \lambda_{e-p})\,\gamma_0$$

We have argued that the effective mass is expected to be renormalized due to the presence of *SF* at low temperatures, but not at temperatures high compared to T_{SF}. Fermi liquid theory gives that the electron $C_P(T)$ is renormalized as follows [2]

$$\frac{C_P(T)}{T} = \gamma_0(1 + \lambda_{e-p} + \lambda_{SF}) + DT^2 \ln(\frac{T}{T_{SF}}) \qquad T \ll T_{SF}. \tag{2.48}$$

Now, in addition to a new mass enhancement factor, λ_{SF}, there is a new temperature dependant term in the electron $C_P(T)$ which is actually negative. This negative term reflects the fact that the mass enhancement must decrease as T increases to towards T_{SF}. The parameters of this expression were determined to be [2]:

$$\begin{aligned} D &= \frac{6\pi^2}{5}\frac{(|\mathcal{S}|-1)^2}{T_{SF}^2|\mathcal{S}|}\gamma_0 \\ \lambda_{SF} &= \frac{9}{2}\ln|\mathcal{S}|. \end{aligned} \tag{2.49}$$

T_{SF} is the spin fluctuation temperature discussed previously and given by $T_{SF} = T_F/\mathcal{S}$. Experimental $C_P(T)$ data has verified that both D and λ_{SF} increase with $\mathcal{S}$, so that there is qualitative agreement with predictions [2]. Quantitative agreement with equations 2.49 has not been demonstrated by experiment and the predicted amplitude of the effect is typically an order of magnitude too big compared with experiment [2].

The $T^3 \ln T$ form of $C_P(T)$ in equation 2.48 was first derived for and successfully applied to liquid ^{3}He, the most obvious Fermi liquid [22,23,38]. It can be derived using only the fact that the effective interaction defined in equation 2.47 only depends on $\left(\vec{k}\cdot\vec{k}'\right)^2$ [39]. This equation has been applied to many d–band metals [2,40–42] as well as to complex f–electron metals [43,44] and heavy fermion metals [45,46].

The $C_P(T)$ arising from SF can be reduced or *quenched* upon the application of a large magnetic field ($H \sim k_B T_{SF}/\mu_B$). This is due to the increase of the SF energy by $2\mu_B H$, as discussed previously. When this energy is greater than T_{SF}, we expect the SF to be completely quenched ($\lambda_{SF} \to 0, D \to 0$). The correct form of the SF quenching of $C_P(T)$ is [2,47]:

$$\frac{\gamma(H)-\gamma(H=0)}{\gamma(H=0)} = -0.1\ \frac{\mathcal{S}}{\ln\mathcal{S}}\left(\frac{\mu_B H}{k_B T_{SF}}\right)^2 \tag{2.50}$$

This equation was first experimentally verified in the heavy fermion metal UAl_2 [43] and has since been verified in only a small number of systems [2,44,48].

Ikeda et. al. [2] have given an extensive experimental review of the effect of SF on the specific heat and resistivity. A recent magnetocalorimetric study of SF in

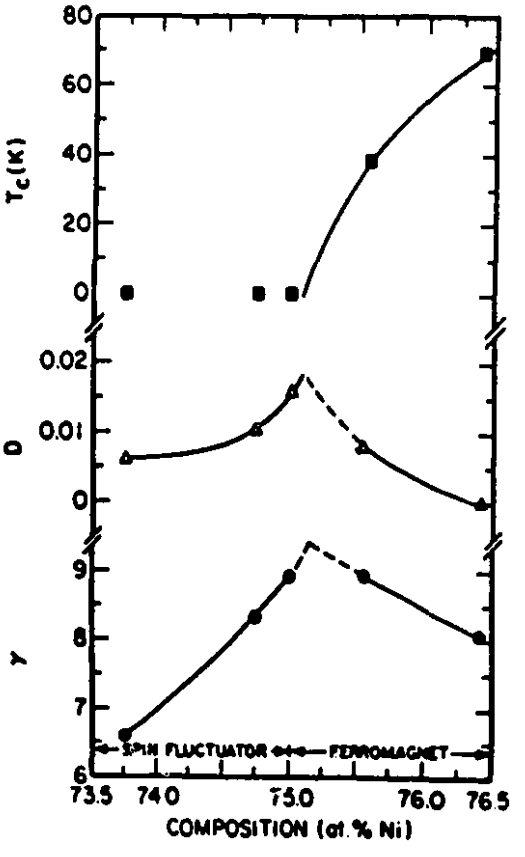

Figure 2.7: Low temperature $C_P(T)$ of Ni_xAl alloys: The Curie temperature, T_C, the coefficient D from equation 2.48 and the coefficient γ of the linear term in $C_P(T)$. The data is taken from ref. [2]. Note the compositions are based on chemically analyzed alloys.

Ni_xAl_{100-x} [41,42,49] reported observations of a small $T^3 \ln T$ term in $C_P(T)$. Fits of expression 2.48 to the data yielded values of D and γ which are displayed in Fig 2.7. These values were found to increase to a maximum at the critical concentration of 75% Ni, as expected from the theory (equation 2.50). The same study found that the SF term did not change appreciably upon the application of a 2.5 Tesla magnetic field. The authors took this as evidence that the anomalous $C_P(T)$ signal was not a result of the formation of *super–paramagnetic clusters*, since a cluster signal is usually substantially altered at fields an order of magnitude smaller [50]. The application of a 10 Tesla field changed the observed value of γ by $\sim 10\%$ which was roughly consistent with equation 2.50, using values of S and T_{SF} determined

from the magnetic susceptibility and the zero field specific heat.

2.4.3 Resistivity

The electrical resistivity due to *SF* scattering has been derived using Fermi liquid theory. From very general considerations, the resistivity can be shown to behave as T^2 as $T \rightarrow 0$ [4,51,52]. Roughly speaking, the only electrons capable of scattering are those with an energy within k_BT of ε_F. These electrons number $N_0(\varepsilon_F)k_BT$, so that the probability of a scattering event is proportional to the square of this number. The resistivity is thus proportional to T^2.

The complete Fermi liquid theory result for the resistivity *SF* is proportional to $(T/T_{SF})^2$ at low temperatures [51,53]. This behaviour has been seen in Ni_3Al alloys [54,55] and other weak–/near– magnets [2]. Evidence for the presence of *SF* requires studying the changes in the resistivity as the sample composition is varied [53,56] or detailed fitting of the complete Fermi liquid theory expression to the resistivity. Furthermore, in high magnetic fields such that $\mu_B H \geq k_B T_{SF}$, the T^2 term is reduced to zero as the *SF* are *quenched* [2].

2.5 Amorphous Fe–Zr

Amorphous iron zirconium (a–Fe_xZr_{100-x}) is an *early transition metal–late transition metal* system which may be readily made amorphous by melt–spinning. It is an interesting system at low temperatures, as it exhibits three distinct phases; superconducting, paramagnetic and ferromagnetic. These phases are illustrated in (Fig 2.8) which is the low temperature phase diagram of a–Fe_xZr_{100-x} [57]. The critical concentration for the onset of magnetic order was found to be $x_c \approx 37\%$ Fe. At higher Fe concentrations ($x \approx 90\%$), a–Fe_xZr_{100-x} becomes a frustrated ferromagnet which exhibits transverse spin freezing [58,59].

a–Fe_xZr_{100-x} is believed to be an itinerant magnet for many reasons [59]. First, dilute amounts of Fe do not exhibit local paramagnetic moments in Zr [37]. That Fe

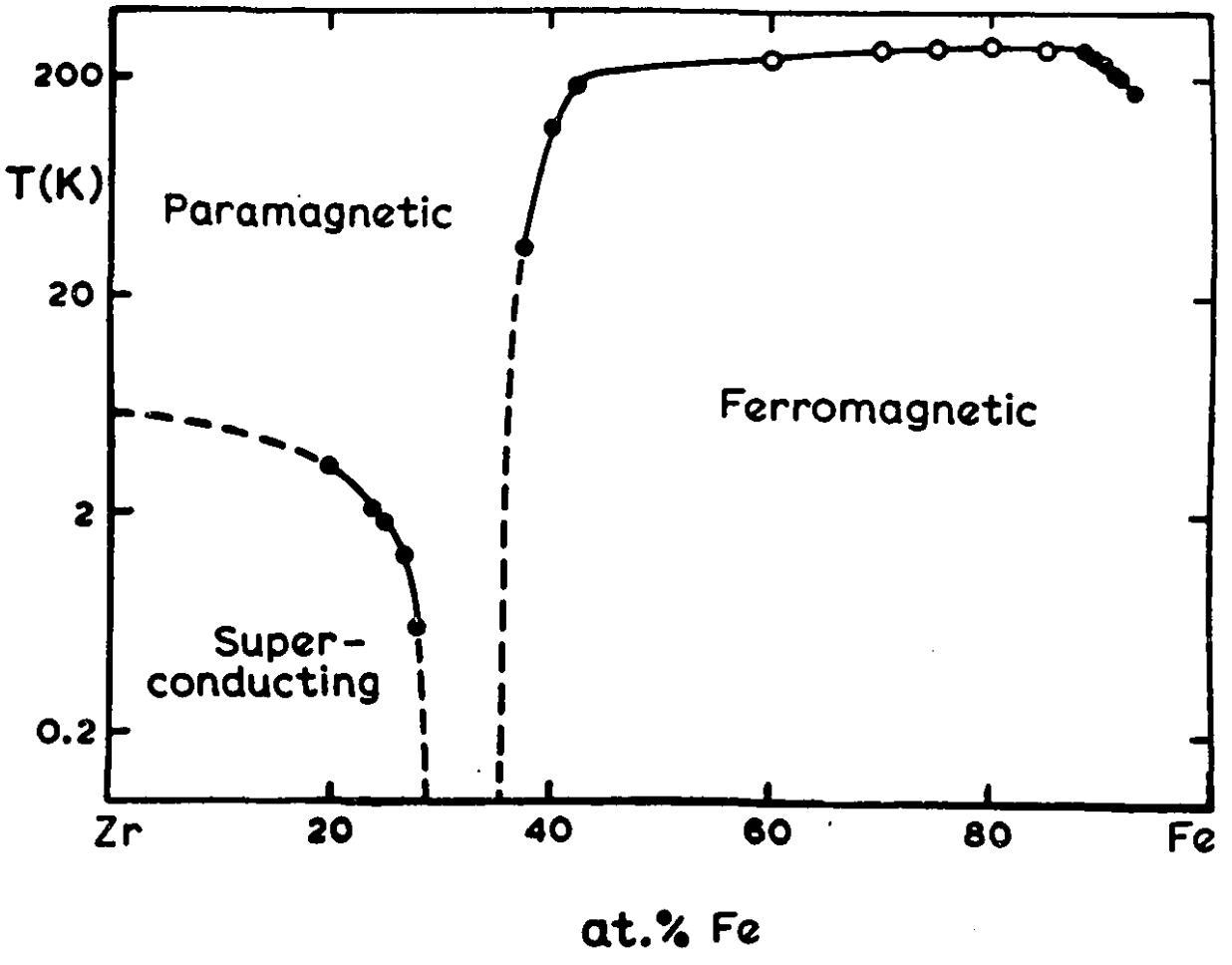

Figure 2.8: Low temperature phase diagram of $a-Fe_xZr_{100-x}$, adapted from ref. [57]. The closed symbols are for melt spun samples and the open symbols are for sputtered films.

does display a local moment in some d–electron metals and not in others (notably itself) illustrates the whole local/itinerant moment problem. Secondly, it is unlikely that the superconducting phase could coexist in a system with local Fe moments. Thirdly, in a local moment system, magnetic order should appear once an unbroken chain of nearest neighbor Fe atoms is established. This is referred to as the *percolation threshold* and can be calculated for simple packing models to be ~20% Fe. The fact that ordering only occurs at around 40% Fe strongly suggests that the order is itinerant and that the formation of the moment and the magnetic order occur together.

Magnetometry measurements confirm that $a-Fe_xZr_{100-x}$ is a near/weak ferromagnet. Susceptibility studies in paramagnetic $a-Fe_xZr_{100-x}$ samples at room temperature [57] suggested that $a-Fe_xZr_{100-x}$ is a strongly exchanged enhanced paramagnet for $x < 37\%$ with a Stoner factor, S, approaching 10. Further, measurement of the ordered moments of the ferromagnetic alloys showed the values to be non–integral [57].

Various experimental works have suggested the presence of spin fluctuations in $a-Fe_xZr_{100-x}$. A low temperature study of alloys near $x = 37$ showed a strong T^2 temperature dependence in the resistivity which could be analyzed using a model including scattering by *SF*[56]. This analysis yielded rough estimates for T_{SF} which went through a minimum near x_c, where T_{SF} was found to be as low as 20 K. A more detailed study [53] of the isostructural system a-$(Fe_yNi_{100-y})_{33.3}Zr_{66.7}$ determined T_{SF} = 15 K for $a-Fe_{33.3}Zr_{66.7}$. A study of superconductivity in $a-Fe_xZr_{100-x}$ [60] suggested that spin fluctuations modified the Cooper pair coupling.

Some other experimental studies on $a-Fe_xZr_{100-x}$ are worth mentioning. Ultraviolet photoelectron spectroscopy (UPS) has shown that there are open d–bands in $a-Fe_xZr_{100-x}$ [61]. Mössbauer spectroscopy [62] and also small angle neutron scattering [63] have shown $a-Fe_xZr_{100-x}$ to be a highly compositionally uniform material. Measurements of the Hall coefficient of $a-Fe_xZr_{100-x}$ [64] showed it to be proportional to the susceptibility.

Specific heat studies have been done on $a-Fe_xZr_{100-x}$ samples with spacing in x of 5% [65–67]. One study found a vanishing phonon contribution [67]. Both studies (probably done on the same samples) found anomalous behaviour in $C_P(T)/T$ at temperatures below 3 K and both groups attributed this behaviour to the formation of super–paramagnetic clusters.

Chapter 3

Amorphous Fe–Zr Ribbons

The equilibrium phase diagram [68,69] of iron–zirconium (Fe–Zr) is displayed in Fig. 3.1. A deep eutectic exists at 24% Fe about which amorphous alloys may be formed by rapid quenching in the range of 20~43% Fe. $a-Fe_xZr_{100-x}$ ribbons with Fe contents between 26% and 40% were fabricated by melt–spinning. Characterization of these ribbons is essential and included the determination of their elemental concentration by electron microprobe, and the verification of their amorphous structure by x–ray diffraction. As a further check of both composition and structure, the crystallization characteristics of the ribbons were studied using differential scanning calorimetry.

3.1 Sample Preparation

Starting elements were 99.98% pure Fe flakes [70] and a 99.94% pure Zr bar[71]. The Zr bar was cut into ~1 gram pieces which were etched in a solution of 20:1:1 (distilled water):(HNO_3):(H_2O_2). The pieces were repeatedly etched until they had a silvery finish. Fe flakes were not etched, as this led to further surface contamination. The elements were then degreased using acetone followed by isopropyl alcohol.

Appropriate amounts of Fe and Zr were then placed (Zr on top) in a water–cooled copper depression in an arc–furnace. The chamber was flushed three times with

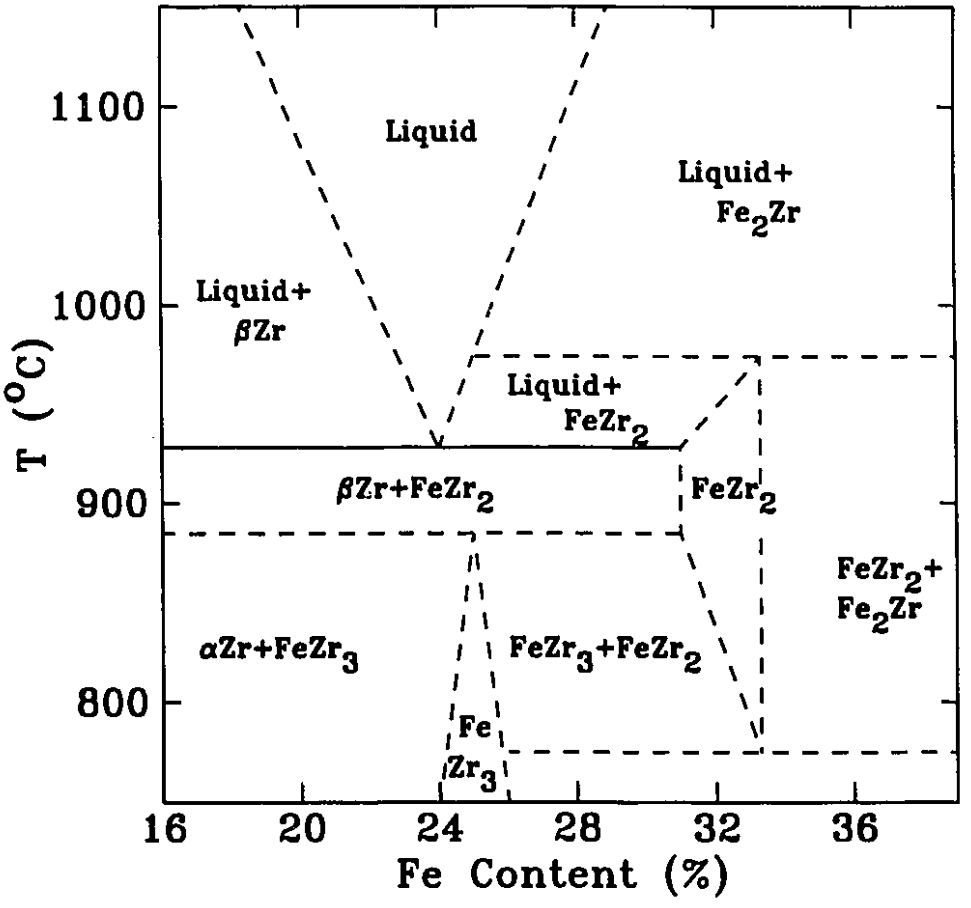

Figure 3.1: Structural phase diagram of Fe–Zr about the eutectic at 24% Fe (reproduced from ref. [69]). The positions of the dashed lines is not precisely known.

99.998% pure argon gas which was then further purified by melting a titanium boule (oxygen getter). After the elements were mixed in the first melt, the resulting ingot was twice flipped and remelted to ensure homogeneity. The final ~5 gram ingots were found in all cases to exhibit mass changes of less than 0.05% from the masses of the starting elements.

From these ingots, amorphous ribbons were formed by melt-spinning. Pieces of ingot totaling ~ 0.5 gram composed a *charge* which was placed into a quartz tube crucible with a ~ 0.5mm hole at one end. The crucible was placed in a sealed chamber and ~ $\frac{1}{2}$ atmosphere environment of 99.995% pure helium was established. The charge was heated by radio frequency induction to melting for a few seconds, after which a ~2 atmosphere pressure of argon was suddenly introduced into the

crucible. This over-pressure ejected the molten alloy through the hole and onto a copper wheel spinning with a tangential speed of ~50m/sec. The rapid cooling (~10^6 K/sec) undergone by the molten alloy on hitting the wheel inhibits crystallization. The result was that meter length amorphous ribbons were ejected from the wheel with a width of ~1 mm and thicknesses varying between 15 and 20 μm.

3.2 Sample Characterization

3.2.1 Electron Microprobe

Electron microprobe analysis was used to determine the elemental compositions of all the amorphous ribbons studied. Polished and electrically grounded metal samples are bombarded with a collimated ~15keV electron beam. Metal atoms within a few thousand angstroms of the surface become electronically excited and emit characteristic 0.3~5keV x-rays which are detected and analyzed. The resulting x-ray energy spectra are then compared with those from reference oxides, so that, if suitable corrections are made for varying x-ray and electron absorption depths, the elemental concentration of the sample may be determined to within 0.5%.

Fig. 3.2 shows the microprobe determined Fe concentration of several $a-Fe_xZr_{100-x}$ ribbons plotted as a function of the targeted concentration which was weighed out in starting elements. Since very little mass change was measured after arc-melting, the targeted concentration is taken as the concentration of the arc-melted alloy ingots.

The severe relative iron loss (in some cases as much as $\frac{1}{4}$ of the amount in the ingot) evident in Fig. 3.2 probably results from insufficient heating of the charge during the melt-spinning process. The 30-40% Fe charges were not heated quite to the liquidus temperature, and in equilibrium would reside in the top-right region of Fig. 3.1, (liquid plus Fe_2Zr crystals). Within the melted ingot, therefore, Fe_2Zr crystals formed, probably predominantly on the cooler surface of the charge. These crystals leached Fe from the remaining liquid. The Fe poor liquid was then ejected

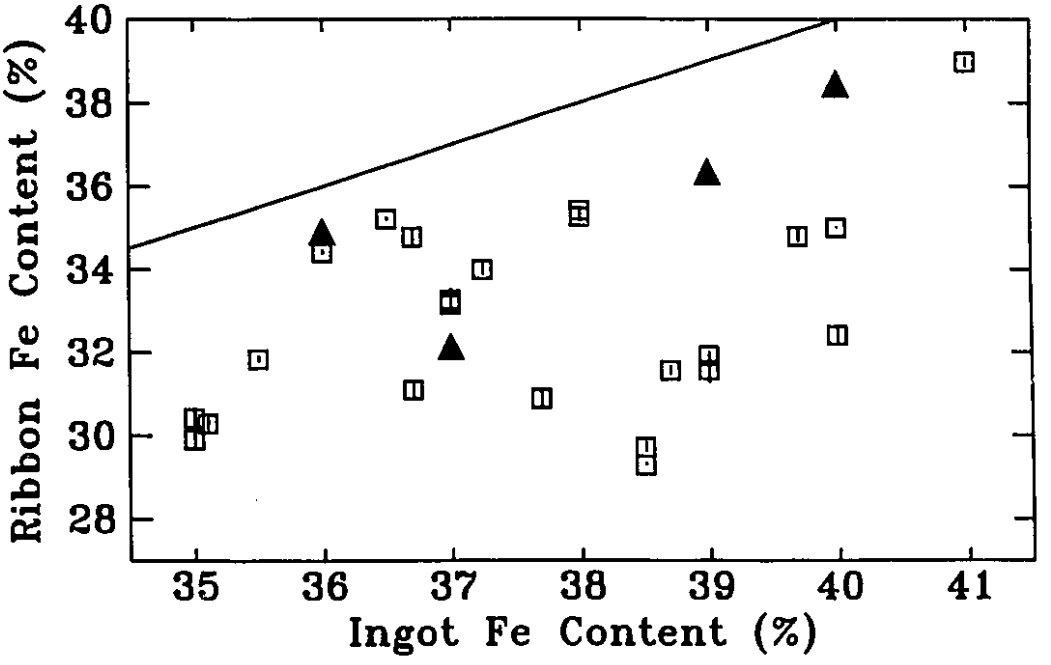

Figure 3.2: Electron microprobe determination of $a-Fe_xZr_{100-x}$ ribbon concentrations: (□) samples made by the author; (△) samples made by another worker [72]. The solid x=y line would result if there were no Fe loss on melt–spinning.

to form Fe poor ribbons while most of the Fe_2Zr was left behind in the solid shell which remained in the crucible. All studied ribbons were found to be amorphous by x–ray diffraction, but small blobs were visible embedded in some ribbons. One of these blobs was microprobed and verified to be rich in Fe compared to the amorphous background.

Efforts made to reduce Fe leaching by heating the charge to higher temperatures were largely unsuccessful. These efforts included heating the charge faster, using more induction heating power and using larger (>1 gram) charges to increase their surface to volume ratios, and so reduce relative heat loss. The temperature of the melting ingot can only be determined by fast optical pyrometry, which was not performed. Ribbons of 31% and 35% Fe were melt–spun from charges taken from the same 36.7% Fe ingot. This confirms that the Fe loss occured during the melt–spinning process. Fig. 3.2 shows that initially the Fe loss increases with Fe content as expected due to a rising liquidus temperature, but then seems to decrease at higher Fe contents.

Some ribbons were analyzed for oxygen content. The results are plotted in Fig. 3.3

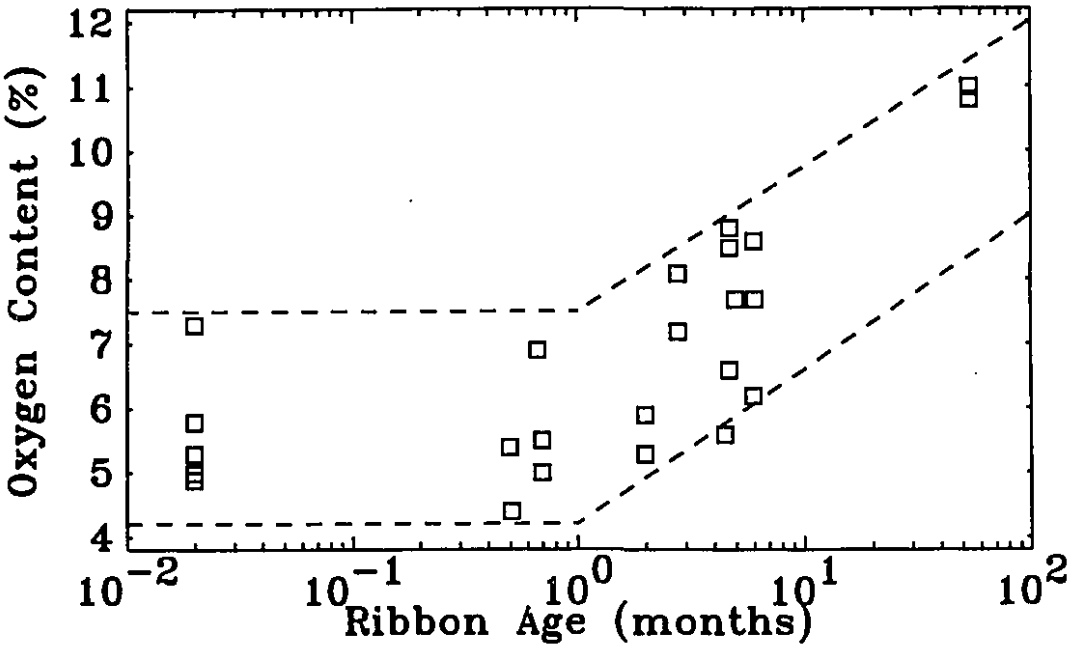

Figure 3.3: Oxidation of $a-Fe_xZr_{100-x}$ ribbons with time; oxygen concentrations were deduced by electron microprobe. The dashed lines are guides to the eye.

against the age of the samples. The evident correlation and the fact that the probe depth is known to be only 0.6μm, leads to the conclusion that the measured oxygen exists only on the sample surface. A certain amount of oxide is formed initially and gradually increases with time, doubling over five years.

3.2.2 X-ray Diffraction

The structure of all ribbons was verified to be amorphous by CuK_α x-ray diffraction using an automated Nicolet-Stöe powder diffractometer. Typical diffraction scans, displayed in Fig. 3.4, show two broad peaks characteristic of glasses and are devoid of sharp crystal spikes. The area of the minimum observable crystal spike divided by the total area of the diffraction scan gives a maximum possible crystallinity fraction of ~0.1%, assuming no texturing. This fraction is normally far too small to be observable in the specific heat.

The *free* side of a ribbon is that which was not in contact with the wheel during melt-spinning and so cooled slower than any other part of the ribbon. Crystallization

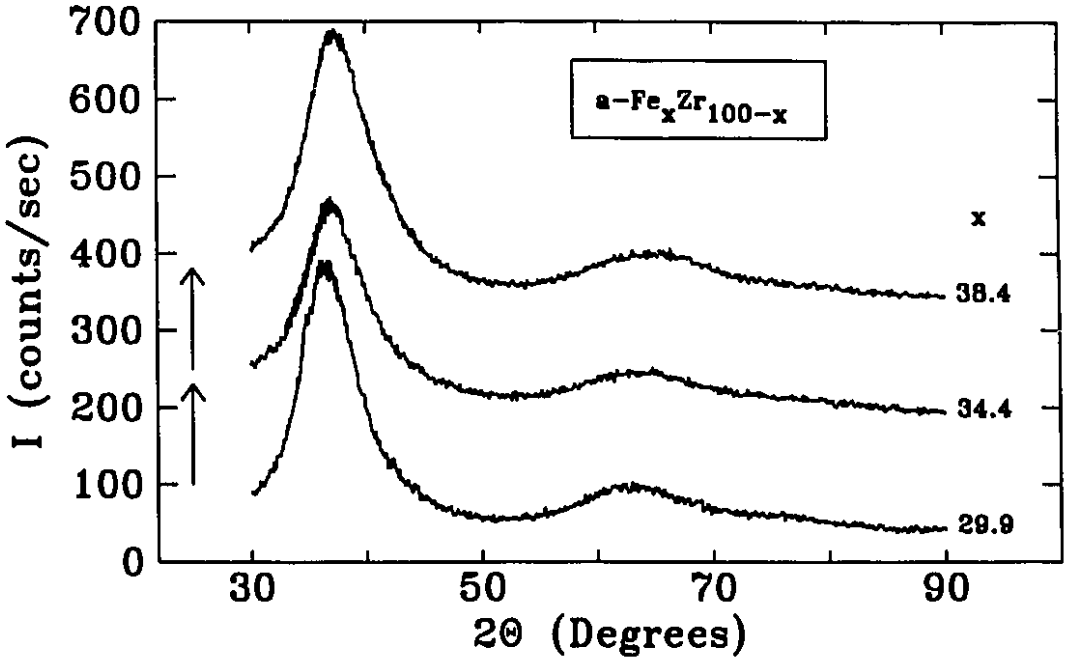

Figure 3.4: Powder x-ray diffraction patterns of the free sides of various $a-Fe_xZr_{100-x}$ ribbons. Offsets have been used to separate the data.

due to insufficiently fast quench rates should therefore have occurred preferentially on the free side. Diffraction scans were therefore normally done on the free side of the ribbon. Scans of only the free side of some ribbons with x near 30% displayed small spikes in the first amorphous peak at $2\Theta \approx 37°$. These spikes could be completely removed from the diffraction patterns by lightly sanding the free side of the ribbon. This confirms that the spikes resulted from crystallizations which occurred only on the surface.

Fig. 3.4 also shows that there is a small shift of the amorphous peaks to higher angles with increasing Fe content. A Gaussian function plus a constant background were fit to the first peak and the scattering angle, $2\Theta_{MAX}$, at which the peak occurs was determined. Displayed in Fig. 3.5, $2\Theta_{MAX}$ is an average of scattering from many bond distances, and so it is expected to be simply related to the measured density. From ref. [73], the density of $a-Fe_xZr_{100-x}$ for $20\% < x < 40\%$ is well represented by the straight line: $\rho(\mathrm{gm/cm^3})=6.392+1.65(x/100\%)$. If M is the average atomic

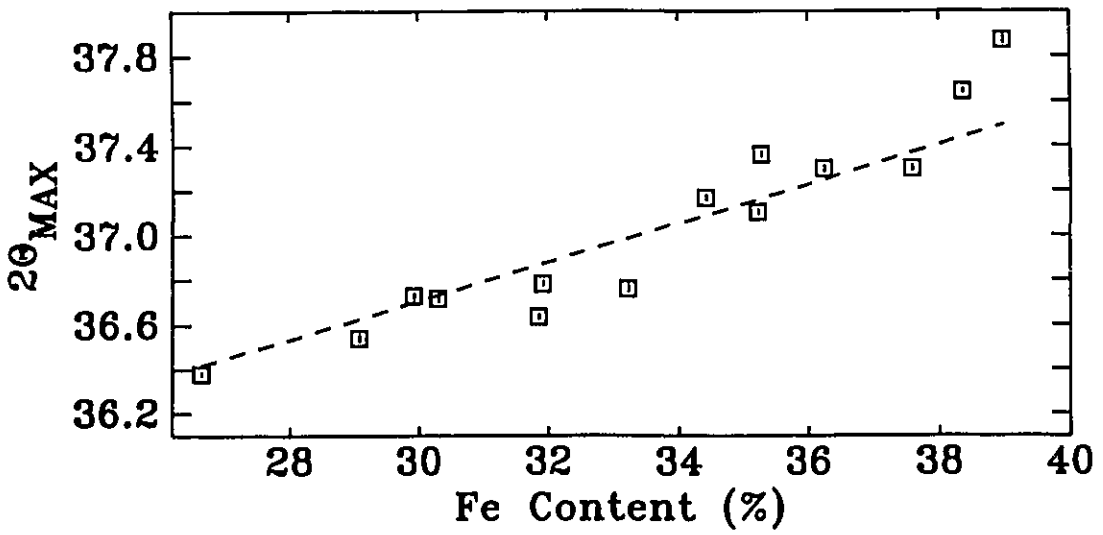

Figure 3.5: Composition dependence of first x-ray diffraction peak position in a–Fe_xZr_{100-x}. The dashed line is derived from the measured density as described in the text. The error bars were determined by the fitting program.

mass, then a mean lattice spacing, $\overline{a}$, for a close-packed structure may be defined by:

$$\rho = \frac{M}{0.74\overline{a}^3}.$$

The momentum transfer corresponding to the first peak, $\overline{q}$, is inversely proportional to the average lattice spacing:

$$\overline{q} = \frac{2\pi f}{\overline{a}} = \frac{4\pi}{\lambda_{CuK_\alpha}} \sin\Theta_{MAX}.$$

The factor f is 1 for Bragg's law and is given by 1.23 for simple glasses [74]. Using a value of f=1.23 gives a good fit to the data, which is shown in Fig. 3.5.

3.2.3 Differential Scanning Calorimetry

As another means of characterizing the ribbons, their behaviour during crystallization was studied. In a Perkin-Elmer differential scanning calorimeter (DSC), ~10mg of ribbon was heated at a constant rate of 40 K/minute. The heating power was monitored and exhibited a minimum when the ribbon crystallized (initially into the metastable $FeZr_2^*$ phase [73] for all of the ribbons studied). The temperature where

the minimum occurs is the crystallization temperature, T_X, and the total energy released by the sample is the crystallization enthalpy, ΔH_C. Zinc was used as a melting point standard (T_M=690 K) and was heated in the DSC at 40 K/minute. The melting peak was found to be shifted up to 693 K due to thermal lag of the sample. A thermal lag correction of 3 K was therefore subtracted from all measured values of T_X. T_X is shown for all ribbons in Fig. 3.6 and is in agreement with the results of ref. [73]. The value of T_X shows a peak at x=37.5%. This may indicate the existence of a eutectic at that composition not accounted for by available phase diagrams [73]. In fact, the isomorphous system Fe–Hf does show a eutectic at 36.1% Fe. The behaviour of T_X agrees well with the previous work and provides a further check on the Fe concentration measured by microprobe.

Also displayed in Fig. 3.6 is the half width of the crystallization peak, σ_{T_X}, defined as the difference between T_X and the onset temperature of the peak. σ_{T_X} grows monotonically with increasing Fe content.

The area under the crystallization peak yields the crystallization enthalpy, ΔH_C, which is also shown in Fig. 3.6. The values of ΔH_C uniformly decrease with Fe content in agreement with those of ref. [73]. The discrepancy between the results is due to the nonequivalent conventions used by different workers in determining the temperature limits of the crystallization peak. The enthalpy results provide a double check of the uniform amorphous quality of the ribbons.

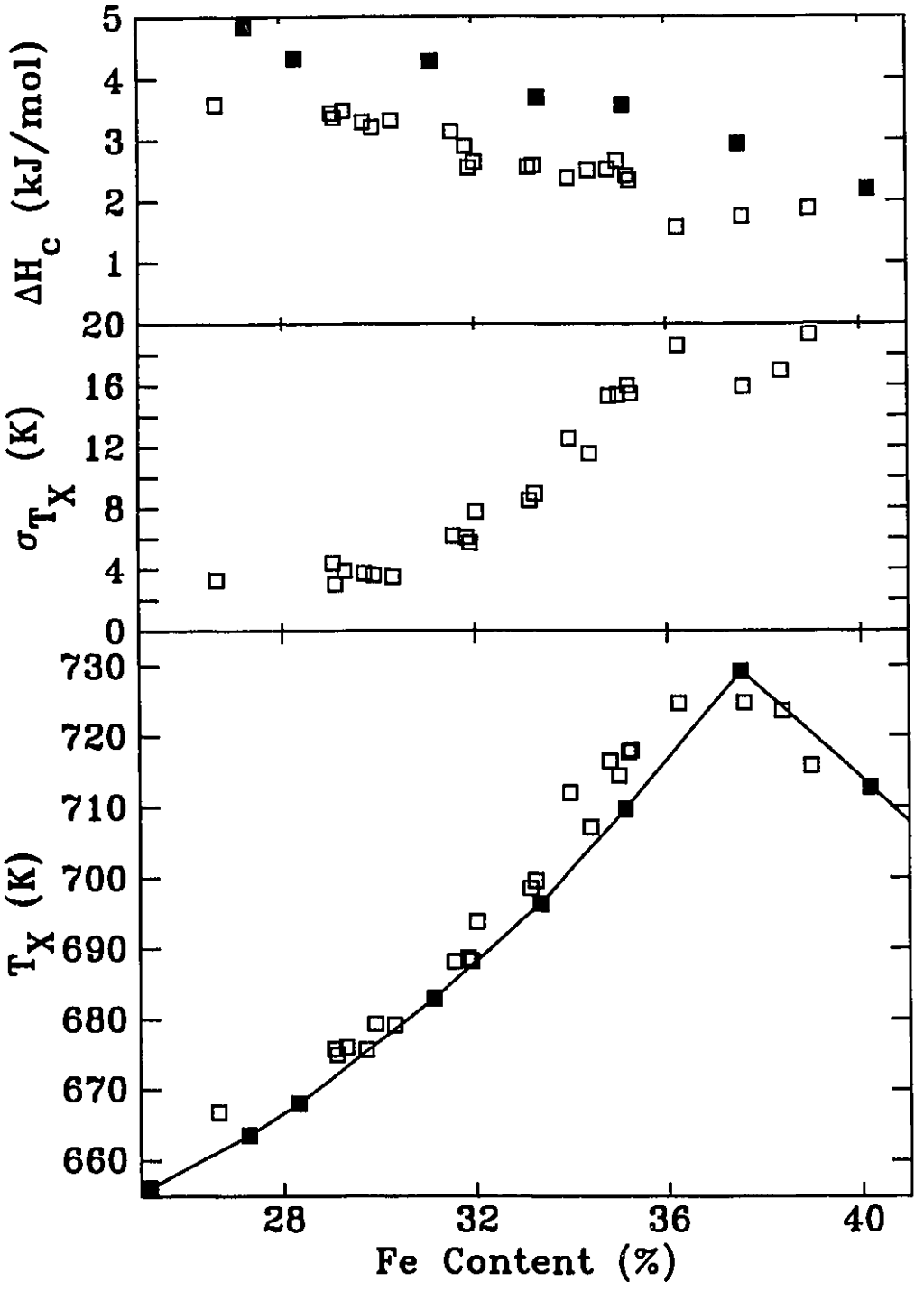

Figure 3.6: Crystallization characteristics of a–Fe_xZr_{100-x} at a heating rate of 40 K/minute. Displayed are the crystallization temperature T_X, crystallization peak half width σ_{T_X}, and the crystallization enthalpy ΔH_C. The solid line and filled symbols are the results of ref. [73].

Chapter 4

Absolute Calorimetry

4.1 General Considerations

The *specific heat capacity*, C_P, of a given amount of sample measured at constant pressure and at a temperature, T, is defined as:

$$C_P(T) \equiv \lim_{\Delta T \to 0} \left(\frac{\Delta Q}{\Delta T} \right)_{P,T} \tag{4.1}$$

where ΔQ is an infinitesimal amount of heat input to the sample and ΔT, is the resulting temperature rise. Since theories modeling the specific heat usually implicitly assume that the volume, V, of the sample is fixed, they yield C_V, the specific heat at constant volume. The difference between C_P and C_V can be written [75]:

$$C_P - C_V = \frac{VT(\frac{1}{V}(\frac{dV}{dT})_P)^2}{\frac{1}{V}(\frac{dV}{dP})_T}.$$

This difference rapidly decreases with lowering temperature and is generally less than 1% below 100 K [75]. Since our study is restricted to such low temperatures, we will not distinguish between C_P and C_V. Measurement of C_P is referred to as *absolute calorimetry*, as opposed to *relative calorimetry* which follows the ratio $C_P(T)/C_P(T_{REF})$ for some T_{REF} and is typically used in studying phase transitions.

Absolute calorimetry is a difficult measurement. The main reason for this is that a calorimetry measurement cannot be done in thermal equilibrium. While other measurements may be done at a fixed temperature, measurement of $C_P(T)$, by definition

(equation 4.1), requires the sample to change temperature during the experiment. Since calorimetry is usually done in systems where $C_P(T)$ changes significantly with temperature, great pains must be taken to keep ΔT as small as possible. This means that the sample temperature must be measured to a high precision, since the operation of subtraction, involved in calculating ΔT, leaves it with a high relative error.

Another feature that makes calorimetry difficult, is that all calorimeters have a specific heat of their own, generally referred to as the *addenda*. The addenda specific heat must be measured separately, without a sample, and subtracted off the measured sample+addenda specific heat to yield that of the sample alone. This requires the calorimeter to be reproducible to within the accuracy desired. Calorimetry on small samples (<100mg) is generally referred to as *micro-calorimetry* [76].

4.2 Time Relaxation Calorimetry

The electrical analog of the ideal *time relaxation* (TR) calorimeter [76–80] is illustrated as a circuit diagram in Fig. 4.1. This representation can be used if electrical currents, voltages, resistances and capacitances are interpreted as heat currents, temperatures, thermal resistances and heat capacities respectively.

The measurement procedure is as follows: The temperature of the thermal reservoir is brought to equilibrium at a temperature T_0, represented by the electrical ground in Fig. 4.1. A fixed power, P, represented as a current source, is then applied to the sample (C_S) and addenda (C_A). The power flows into the thermal reservoir through a thermal *link* resistance, $R \equiv 1/K$. The sample+addenda heats up until it reaches equilibrium at a temperature $T_0 + \Delta T$. The link resistance, R, may now be determined from Newton's law of cooling (Ohm's law) as:

$$R \equiv \frac{1}{K} = \frac{\Delta T}{P}.$$

The power, P, is then instantaneously switched off and the sample temperature, T, is measured as a function of time. By differentiating the definition of C_P with respect

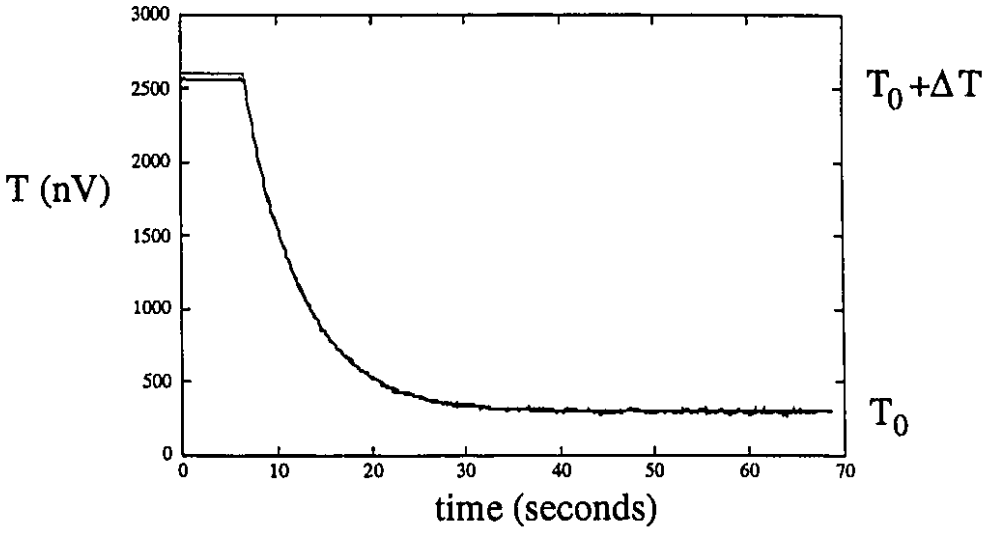

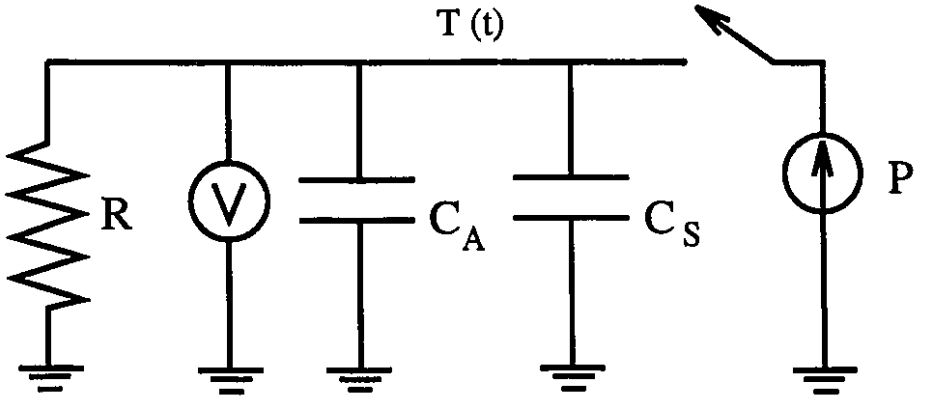

Figure 4.1: Electrical circuit representing thermal circuitry of the idealized calorimeter. Also shown is an actual temperature drop taken on a ribbon sample at 6.5 K. The temperature axis is in nanovolts of thermocouple signal. The data and the best fit simple exponential (equation 4.2) are both displayed as solid lines.

to time, and combining the result with Newton's law of cooling, the heat flow out of the sample+addenda is:

$$-C_P\frac{a}{dt}(T-T_0)=\frac{1}{R}(T-T_0)$$

$$\frac{d}{dt}(T-T_0)+\frac{1}{RC_P}(T-T_0)=0$$

$$\text{where : } C_P = C_A + C_S.$$

This differential equation has the solution:

$$T = T_0 + \Delta T \exp(-\frac{t}{\tau}) \tag{4.2}$$

$$\text{where : } \tau = RC_P = R(C_A + C_S).$$

So the monitored *temperature drop* with time, t, is fitted with an exponential decay and C_P is determined by $C_P = \tau/R = \tau K$. This is the governing equation of the TR technique.

4.3 The ^{4}He Cryostat

We are interested in C_P at low temperatures which are achieved in a ^{4}He cryostat immersed in a bath of liquid ^{4}He at 4.2 K.

4.3.1 Cryostat Construction

The cryostat, illustrated in Fig. 4.2, is composed of a copper block suspended by three stainless steel tubes. The copper block functions as the thermal reservoir and is enclosed in a radiation shield. The shield ensures that everything within it is exposed to thermal radiation only from surfaces at the reservoir temperature. The two outer tubes are used to pump out the sample space with a diffusion pump to pressures below 10^{-4} millibar. The space is enclosed in a copper can machined with a 5° taper at its opening so that it mates with a copper cone supported by the two outer tubes. When coated with vacuum grease, this forms an easily remountable vacuum tight seal which may be cooled in a bath of ^{4}He with out breaching.

Twisted bunches of 75μm manganin wires [81], each with a total resistance of $\sim$250Ω, run down the two outer tubes from room temperature above. These wires are wound onto two copper rods which extend into the liquid ^{4}He bath with GE 7031 varnish. A layer of cigarette paper under the wires ensures electrical isolation. This *thermal anchoring* ensures that there is no significant heat flow from room temperature into the copper block through the wires. Copper wires were originally used, but, because of their high thermal conductivity [82], they were found to heat up the absolute thermometer so that it measured a temperature higher than that of the copper block. Since C_P is measured at the copper block temperature, this effect led to a

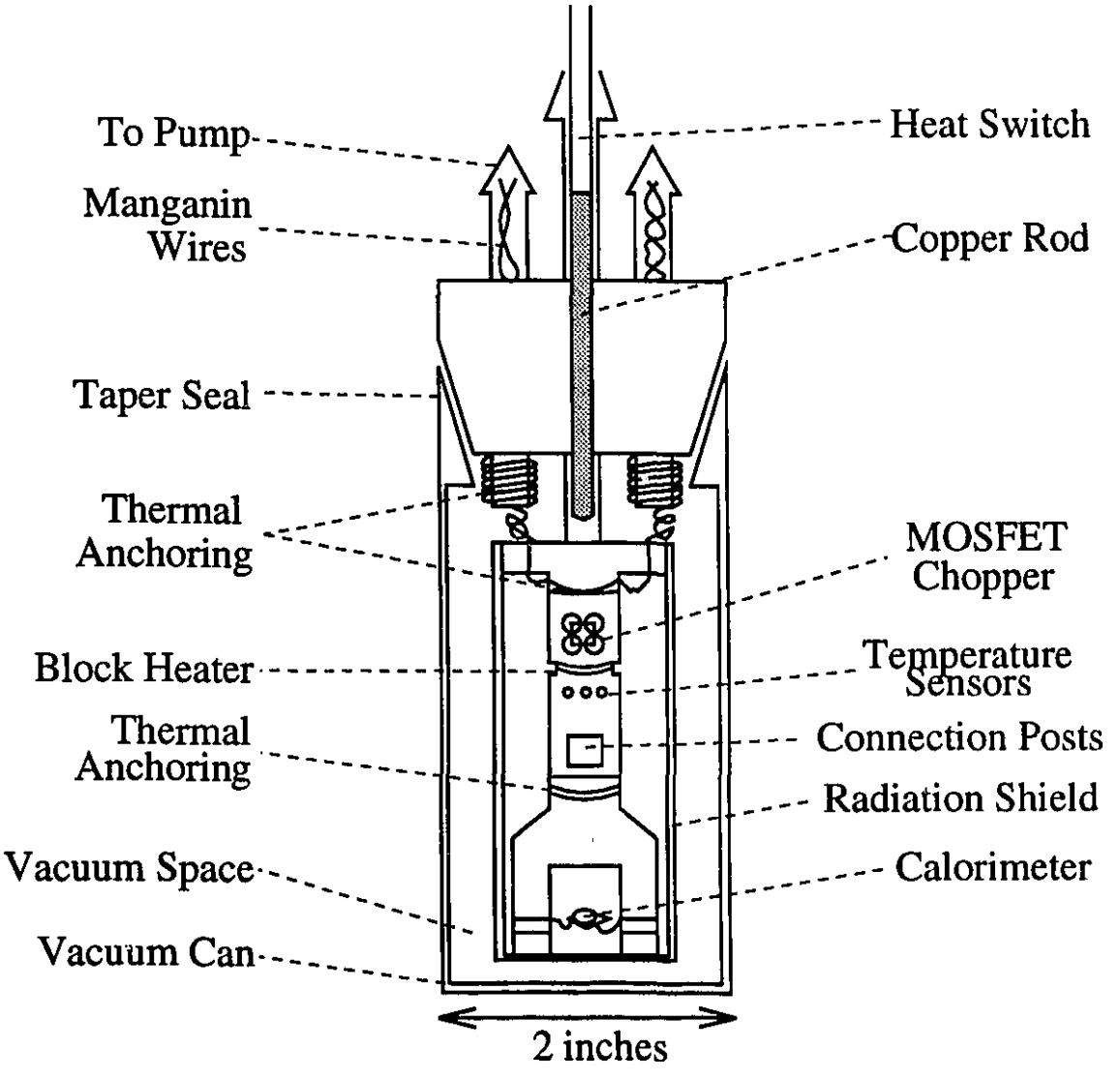

Figure 4.2: Diagram of Cryostat

systematically low measured C_P for the standards. The low thermal conductivity [82] manganin wires are then attached to the copper block where they are again thermally anchored to guard against stray temperature gradients.

The removable calorimeter stage is a copper prong with a surface which mates with the copper block. The two may be tightly screwed together, with a layer of vacuum grease between them, to ensure good thermal contact. In this way, the prong and the main block are effectively made into a single unit and the two will not be distinguished.

4.3.2 Temperature Control

Before discussing the operation of the calorimeter and the various thermometers, we discuss how the necessary precise temperature control of the copper block reservoir is achieved. The central stainless steel tube supports the copper block and is the dominant thermal contact between it and the 4.2 K liquid ^{4}He bath. Within the central tube is a copper rod which may be raised or lowered to contact the copper block. The tube may also be filled with a low pressure of He gas, so that it acts as a *heat switch*, allowing the cooling power to the copper block to be varied over a wide range. Further, the copper rod may be raised and 1 atm. of ^{4}He may be introduced for $\sim$20 minutes to condense liquid helium in the switch. The switch may then be pumped, lowering the temperature of the block below 4.2 K. With careful pumping, the block may be brought to as low as 1.7 K for $\sim$2 hours before all the liquid ^{4}He is consumed.

Precise temperature control of the copper block is achieved with a commercial temperature controller (Lakeshore^{TM} DRC-91C)[83]. This device stabilizes temperature by measuring the resistance of a 10kΩ carbon composite resistor [84] used as a control sensor and controlling the power to a 40Ω heater wire non–inductively wound on the copper block [85], *above all of the sensors.* All major heat flows and temperature gradients therefore occur between the block heater and the heat switch. In this way, all of the sensors are embedded in a near thermally isolated isothermal block all at the same temperature.

Power to the 40Ω heater wire is controlled to be proportional to the temperature error, its time derivative and integral in different programmable amounts. Temperature may be stabilized within 1 mK indefinitely for temperatures between 1.7 K and 20 K. This high stability is necessary, since while the reservoir temperature does not need to be measured this precisely, instabilities in its temperature appear at the calorimeter.

The system is controlled and the data are collected by a IBM–PC clone (XT)

configured with VENIX^{TM}, a UNIX type operating system and programmed[1] in C. The PC is equipped with an IEEE interface [86] used to communicate with various voltmeters and the temperature controller. Also installed is a general purpose Labmaster^{TM} computer board [86], which contains an analog–to–digital converter (ADC), a digital–to–analog converter (DAC), a high precision quartz crystal oscillator/timer and digital logic input/output. These devices are used to interface and control all the homemade electronic circuits. The system can be run completely automatically. The computer changes and stabilizes block temperature, then performs and monitors temperature drops which ultimately yield C_P.

4.4 The Calorimeter

Fig. 4.3 is an illustration of our time relaxation micro–calorimeter. We define "calorimeter" to refer only to the small assembly comprised of the addenda and the sample. Since the addenda C_P is always measured with that of the sample, choice of materials with low specific heats for the construction of the calorimeter is essential. The main body of the micro–calorimeter is a $8 \times 8 \times 1$ mm^3 single crystal of sapphire (Al_2O_3) [87]. Sapphire has the useful property that it has a high Debye temperature (>900 K)[88], so that the low temperature C_P is small. Also, the thermal conductivity of sapphire is large [89], so that compared to all other thermal conductances, the sapphire substrate may be considered as a thermal short circuit.

One side of the sapphire is scored with a diamond saw. This facilitates the deposition in a belljar evaporator of a $\sim 100\Omega$ constantan film (Cu:Ni) in a strip along the diagonal. This film is used to heat the calorimeter by running a constant current through it. Current leads are 75μm diameter Au–7%Cu wires [90] fixed to the heater film with silver loaded epoxy [91].

The calorimeter is equipped with two *secondary thermometers.* One is a Au–

[1] Mark Sutton's *hkl* x–ray data acquisition program was generously provided and modified for our purposes.

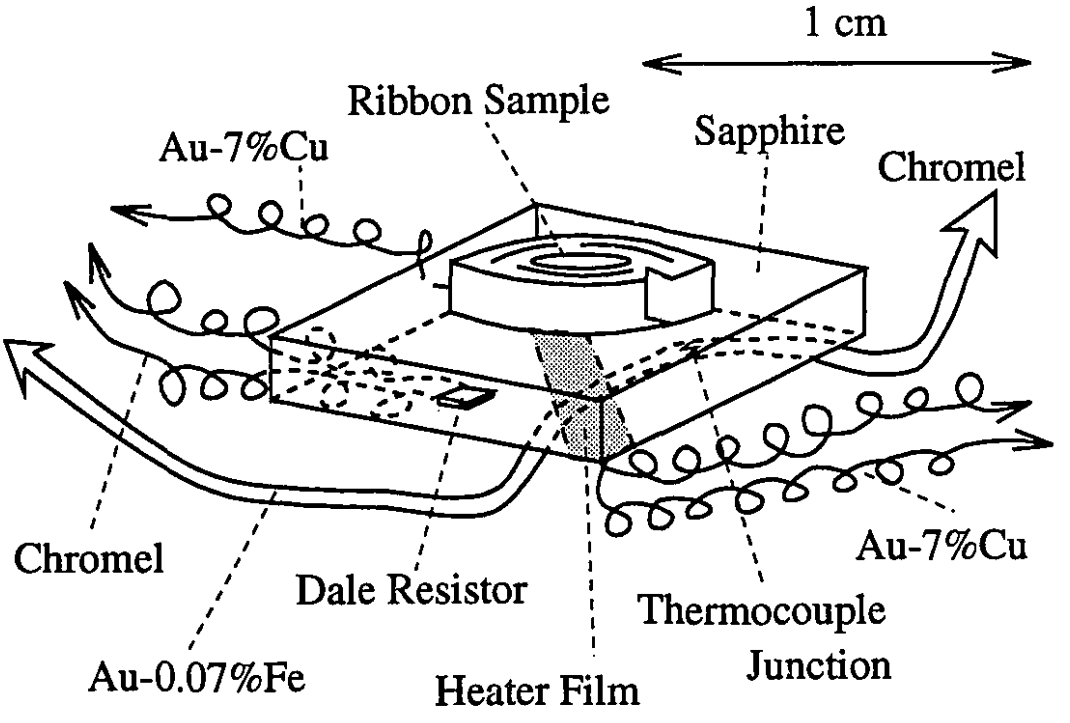

Figure 4.3: Illustration of calorimeter shown mounted with a coiled metallic ribbon sample.

0.07%Fe/chromel thermocouple junction, used as a fast relative thermometer to follow the temperature drops. The other is a *Dale* thick film resistor [92] which is used as a slow, *in situ* calibrated thermometer to measure ΔT.

The thermocouple junction is formed by spark–welding between 125 μm diameter chromel [93] and Au–0.07%Fe wires [93]. This junction is then fixed to the sapphire substrate with electrically insulating epoxy [94]. The $1 \times 1 \times \frac{1}{2}$mm^3 commercial *Dale* 150kΩ thick film ruthenium–oxide resistor [92] comes mounted on a sapphire substrate with pre–soldered terminals, onto which are soldered to two 75μm chromel wires. The Dale is epoxyed onto the now completed addenda. All wires attached to the addenda are then thermally anchored with GE7031 varnish through cigarette paper to four copper pads extending from the copper prong which is the thermal reservoir.

Since the calorimeter operates in high vacuum, the only heat flow paths are radiation and conduction through the link wires. Since blackbody radiation is insignificant at low temperatures, the wires coming from the addenda form the only significant

thermal link to the thermal reservoir and so have been chosen carefully. Suppose that the Dale thermometer is not perfectly attached to the sapphire substrate, but through a small thermal resistance r. The Dale would then be at a colder temperature than the sapphire substrate, since r forms a voltage divider with R_W, the thermal resistance of the Dale wires. The resulting error in the measurement of K and thus of C_P will be r/R_W. The correction is identical if the heater is badly connected. The thermal resistance of the heater and Dale wires must therefore be kept as large as possible, to minimize the error, r/R_W. The calorimeter is designed, therefore, so that most of the heat flow is through the $\sim$ 1 cm of thicker Au–0.07%Fe thermocouple wire.

Thermal and electrical conductivities of metals are roughly related through the Wiedemann–Franz law [4] and increase together. Approximate estimates give the ratio of the thermal conductivities of (Au–0.07%Fe):(Au–7%Cu):(chromel) as 100:10:1 [82]. Au–7%Cu was chosen because it has a thermal conductivity substantially lower than that of Au–0.07%Fe, while still having the low electrical resistivity which is necessary for the measurement of the power in the 100Ω heater film. The Dale resistor has a resistance always greater than 150 kΩ, so that we connected it using chromel, a worse conductor. The thinner high resistance wires are wound in 2mm diameter coils to increase their length to ~4cm.

4.5 Instrumentation

The governing equation of the relaxation calorimeter is:

$$C_P(T_0) = \tau K = \tau \frac{P}{\Delta T} \tag{4.3}$$

We will discuss separately the measurement of each of the four quantities which determine $C_P(T_0)$, namely : T_0, P, ΔT and τ. The dominant sources of uncertainty are the measurements of ΔT and τ which each contribute roughly $\frac{1}{2}$%, leading to an absolute uncertainty of 1% on the total sample+addenda C_P. This means, for

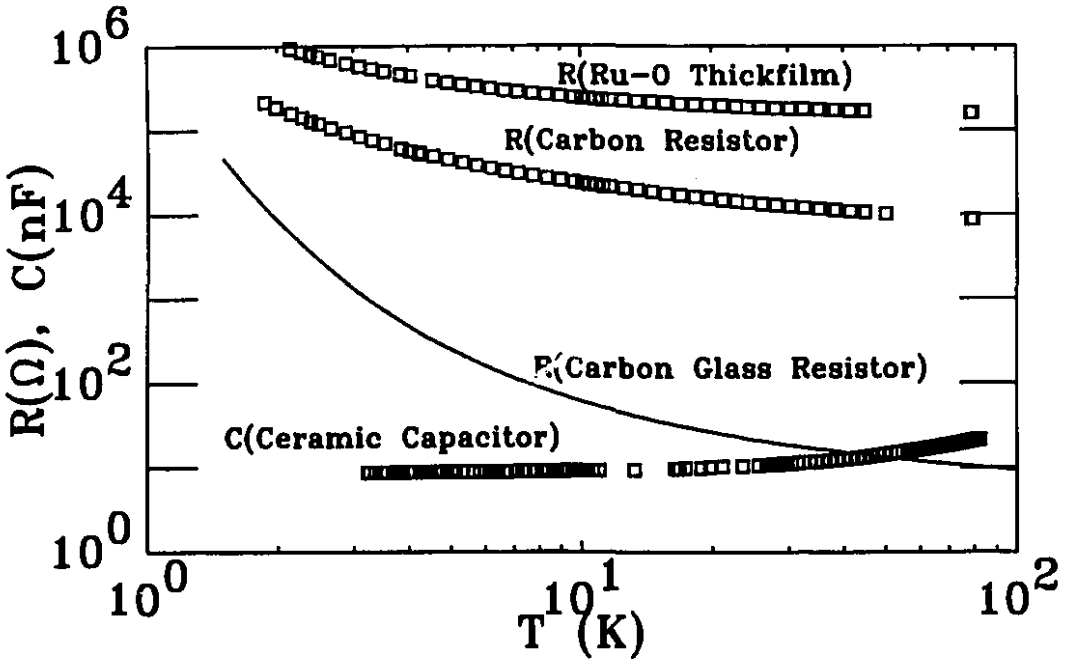

Figure 4.4: Behavior of various temperature sensors used at low temperatures.

example, that the C_P of a sample equal to that of the addenda can be determined with an absolute uncertainty of ~2%.

4.5.1 Absolute Thermometry (Measurement of T_0)

The most important measurement is that of temperature. Absolute thermometry was done with a commercial *carbon glass resistance* thermometer (CGR) calibrated between 1.5 K and 80 K by the manufacturer [83]. CGRs are probably the best sensor for the temperature range 1 K – 100 K due to their high sensitivity, reproducibility after repeated thermal cycling and the small sensitivity of their calibration to an applied magnetic field [95]. Worst case errors due to all factors are documented to be under 5 mK at temperatures below 10 K [83]. The resistance of the CGR is measured with a high sensitivity AC Potentiometric Conductance Bridge [96] to an accuracy approaching 1 part in 10^5.

The low temperature characteristics of the various temperature sensors used (Carbon glass thermometer, Dale thick film Ru–O resistor, carbon composite resistor and capacitance sensor) are displayed in Fig. 4.4. A useful quantity is the *sensitivity*, S_X,

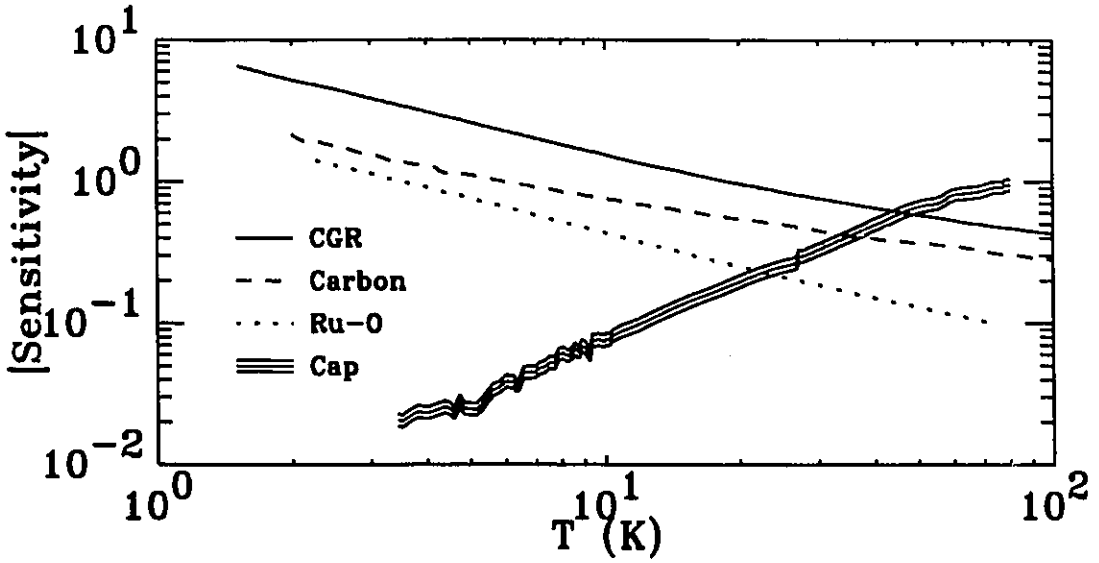

Figure 4.5: Absolute value of the sensitivity of various thermometers. The sensitivity, S_X, is defined by $S_X \equiv d\ln X/d\ln T$, where X is the property used as a thermometer.

defined as:

$$S_X = \frac{d\ln X}{d\ln T} = \frac{dX}{X}/\frac{dT}{T}.$$

Since it gives the fractional change of X due to a fractional change of T, the absolute value of the sensitivity is a "figure of merit" for the usefulness of the quantity X as a thermometer. The sensitivity of the various sensors (X = resistance or capacitance) is displayed in Fig. 4.5. All resistive sensors used have $\mid S_X \mid > 1$ at 4.2 K.

All of the secondary thermometers are calibrated against the CGR by measuring X and T_{CGR} when the sensor and CGR are at the same temperature. These calibrations must be done for each He run, since none of the secondary sensors maintained their calibration on thermally cycling up to room temperature and back.

AC four point measurements of all sensors were done, unless otherwise stated, to eliminate the effects of the 250Ω lead wires. AC measurements eliminate the effect of μV level DC differential thermal emfs generated by the 300 K temperature gradient across the manganin lead wires. The different AC frequencies must be "detuned" off integral multiples of each other so that pickup of one signal by another is avoided. All

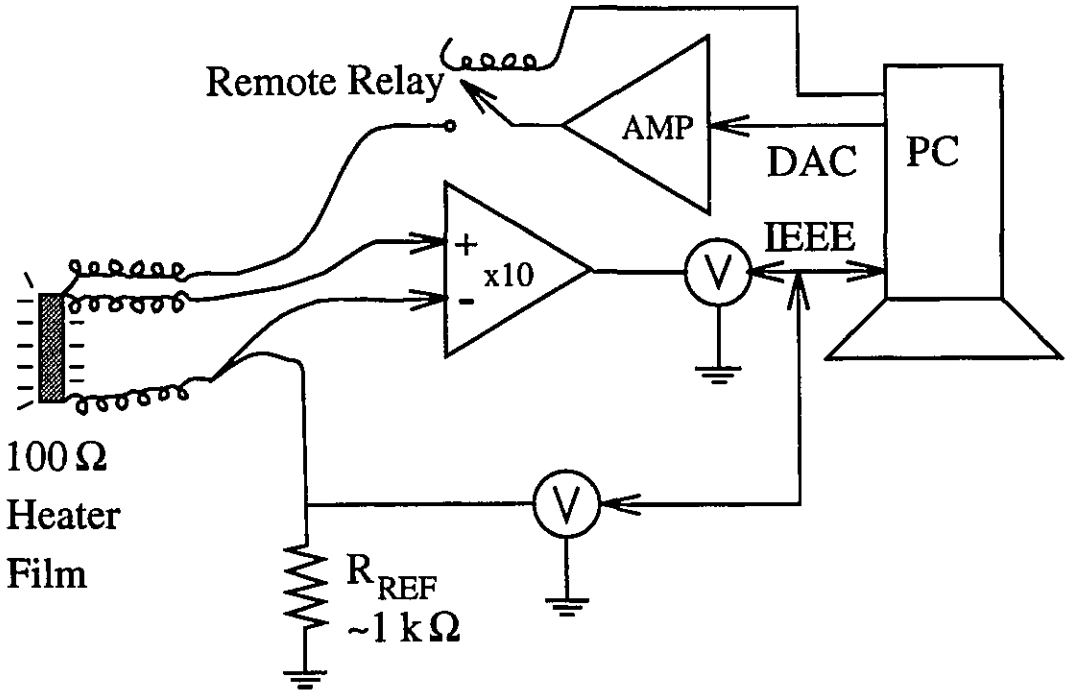

Figure 4.6: Diagram of heater circuit.

sensor circuits and wiring were extensively shielded and referenced to a single ground. Electrically floating circuits were always found to be more susceptible to crosstalk.

4.5.2 Measurement of the Heater Power, P

The heater circuit, shown in Fig. 4.6, generates and measures the power, P, applied to the 100Ω constantan heater film, which raises the sample temperature. The computer generates a DC voltage which is buffered and applied to the heater circuit. The subsequent voltage drop, V, across the heater is amplified by an instrumentation amplifier (Analog Devices AD524) and measured with a Keithley 199 digital voltmeter. The current, I, is determined by measuring the voltage across a ~1kΩ reference resistor. The heater may be remotely turned off within 1 msec with a simple relay. Three link wires join the heater to the copper block. This wiring scheme measures half of the heat generated in the wires. This is the amount of heat which flows into the calorimeter and so is the desired measurement. The power measurement is taken

as:

$$P = (V_{ON} - V_{OFF})(I_{ON} - I_{OFF}).$$

This procedure minimizes the effect of differential thermal emfs, which are measured in the OFF state and then subtracted. Measurement of the power is easily done to an accuracy of 0.1%, which is more than sufficient.

4.5.3 Measurement of the Temperature Rise, ΔT

The Dale ruthenium–oxide thermometer [92] is a CERMET or ceramic metal thick film [97,98]. The film is composed of small particles of metal suspended in an insulating oxide matrix. Electrical conduction occurs by variable range hopping [99] of electrons between metal particles which freezes out at low temperatures according to the relation [97,98]:

$$R = R_0 \exp\left[\left(\frac{T_D}{T}\right)^d\right] \qquad \frac{1}{4} \leq d \leq \frac{1}{2}.$$

The Dales are actually sold as compact resistors and since the films all have the same dimensions, resistance values are controlled by varying the metal content of the films. At dilution fridge temperatures (<100 mK), 1kΩ Dales have sufficiently large sensitivity to be useful as thermometers [97,98]. We needed lower metal contents so that the conductivity freezes out at our higher temperatures. Therefore we have chosen a 150kΩ Dale whose resistance increases by a factor of three upon cooling to 4.2 K.

In order to measure this resistance, we have constructed an AC Wheatstone bridge circuit with a computer controlled reference resistor. The circuit, illustrated in Fig. 4.7, is excited by a 10Hz sine wave generated by the computer's DAC. This excitation, typically 10mV, is chosen so that the power on the Dale (V^2/R) equals one thousandth of the power applied to the film heater. The reference resistor is an array of precision resistors in series with relays wired in parallel to them, so that they may be individually shorted out. The resistors have values 1Ω,2Ω,4Ω,8Ω,etc so that the control signal which opens the relays is equal to the total value of the reference

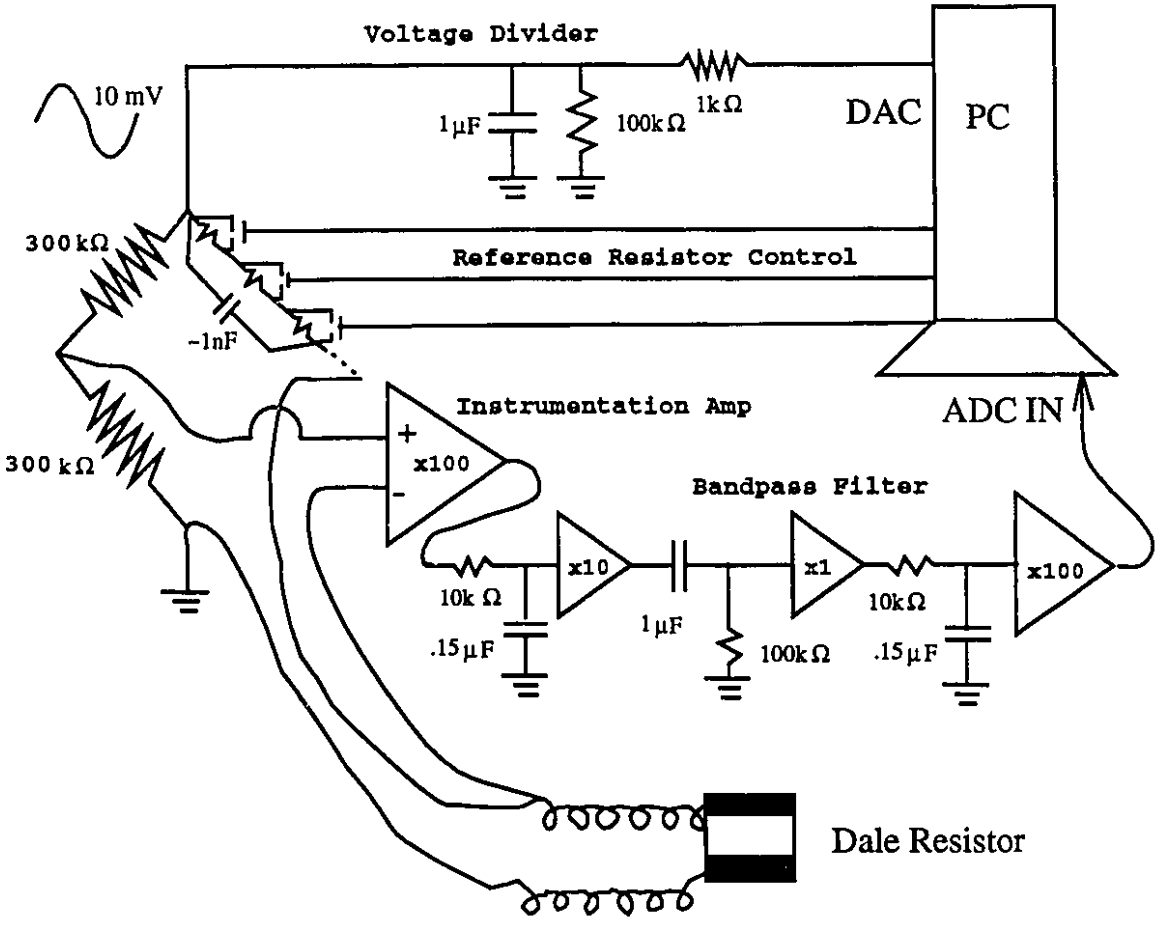

Figure 4.7: Block Diagram of High Impedance Bridge Circuit

resistor in binary. A three point measurement is done on the Dale which cancels out measurement of the lead resistance to the degree that the 250Ω leads are matched (~5%). This leads to an insignificant error in the measurement of the 150kΩ Dale. When the reference resistor has the same value as the Dale resistor, the bridge output is zero and we say that the bridge is *balanced.*

Measurement of the high 150kΩ Dale resistance requires careful consideration. Since it is in parallel with a lead capacitance of order 100pF, a large quadrature signal, 90° out of phase with the driving signal, appears at the output of the bridge, along with the ~10μV imbalance signal. This quadrature signal may be mostly balanced out by placing a ~1nF compensating capacitor in parallel with the reference resistor.

The modulation frequency must still be kept low (10Hz), however, to minimize the quadrature signal.

The output of the bridge is input to a four stage differential amplifier with a total gain of 10^5 and a 3dB pass band between 2 and 70Hz. The heavily shielded amplifier is battery powered [100], to minimize the residual 60Hz pickup. The amplified output is input to an ADC which monitors the signal as a function of time. The resultant trace is then chopped by the computer program with a square wave at 10Hz. This yields a rectified signal which is averaged to give a DC voltage proportional to the imbalance of the bridge. In this way, the computer acts as a digital lock–in amplifier which rejects noise [101,102]. The relative phase between the output and input signal is automatically held constant since the excitation signal is generated within the same computer subroutine loop that chops the input.

The imbalance signal is monitored as the computer controlled reference resistor is varied. These data are then interpolated to determine the reference resistance in the balanced (zero output) state which is the Dale resistance. In 15 seconds and with an excitation of 10mV, the bridge is capable of determining a 100 – 1000kΩ resistance with a precision of 2 parts in 10^4.

The Dale is calibrated at thermal equilibration with no power supplied to the sample heater film. The Dale resistor is then at the same temperature as the reservoir, measured by the CGR. This gives us an in situ calibration of the Dale resistance versus temperature. The resistance of the Dale is then fitted to a polynomial of the form:

$$R_{DALE}(T) = R_0 \exp\left[\sum_{n=1}^{N} A_n (\frac{T_R}{T})^{dn}\right] \tag{4.4}$$

$R_{DALE}(T)$ may be inverted to determine the function $T_{DALE}(R) = R^{-1}_{DALE}(R)$, so that we may determine the temperature rise when the power, P, is on. ΔT is thus determined as:

$$\Delta T = T_{DALE}(R_{ON}) - T_{DALE}(R_{OFF}). \tag{4.5}$$

At 4.2 K, the Dale sensitivity is about 1. This means that the relative uncertainty on the determined Dale temperature, $\frac{\sigma_T}{T}$, is the same as $\frac{\sigma_R}{R}$ *i.e.* 2×10^{-4}. The un-

certainty $\sigma_{\Delta T} = \sqrt{2}\sigma_T$, and since $\frac{\Delta T}{T} \approx 5\%$, we obtain a relative uncertainty on ΔT of:

$$\frac{\sigma_{\Delta T}}{\Delta T} = \sqrt{2}\frac{\sigma_T}{T}/(\frac{\Delta T}{T})$$

$$\frac{\sigma_{\Delta T}}{\Delta T} = \sqrt{2} \times 2 \times 10^{-4}/(.05) \approx \frac{1}{2}\%.$$

4.5.4 Measurement of τ

Since it takes 15 sec to measure, the Dale resistance is useless for following the temperature drops which occur over ~10 seconds. A [Au – 0.07%Fe]–[chromel] thermocouple [103] was used as a fast thermometer to measure the drop of the sample temperature in time. [Au – 0.07%Fe]–[chromel] was chosen for its high sensitivity ($\sim 15\mu$V/K) and high linearity at low temperatures [103].

The DC thermocouple voltage cannot be directly measured since differential thermal emfs totally dominate the signal [104]. For this reason, an electrical chopper [105] was mounted directly on the cold copper block. This circuit, shown in Fig. 4.8, modulates the thermocouple signal at a frequency of ~1kHz. The modulated signal is not affected by DC thermal emfs which largely occur after the chopper, along the wires between the copper block and room temperature.

The low temperature chopper[105] consists of four MOSFETS[2] [105] used as on/off switches, arranged in a bridge. At 1kHz, the gates of alternate pairs of MOSFETS are positively biased at 12V and the thermocouple signal is reversed. This modulated output goes through a shielded transformer and into an Ithaco lock–in amplifier [107]. The lock–in amplifier acts essentially an inverse chopper that rejects unwanted signals

[2]Whether or not a MOSFET functions at 4.2 K is largely dependant on its architecture. We tested three members of an older MOSFET family; the MFE3002, 2N4351 and 3N171, and found them all to function normally at 4.2 K. We also tested the 2N7000 and the VQ1004P, two modern power MOSFETS (known as VMOS or TMOS), and found that they both function at 77 K, but not at 4.2 K. Since most manufacturers are switching all their production to power MOS, which all have similar architecture, our results suggest that MOSFETS which function at 4.2 K could soon become a thing of the past. For an extensive review entitled "Cold Electronics", see ref. [106].

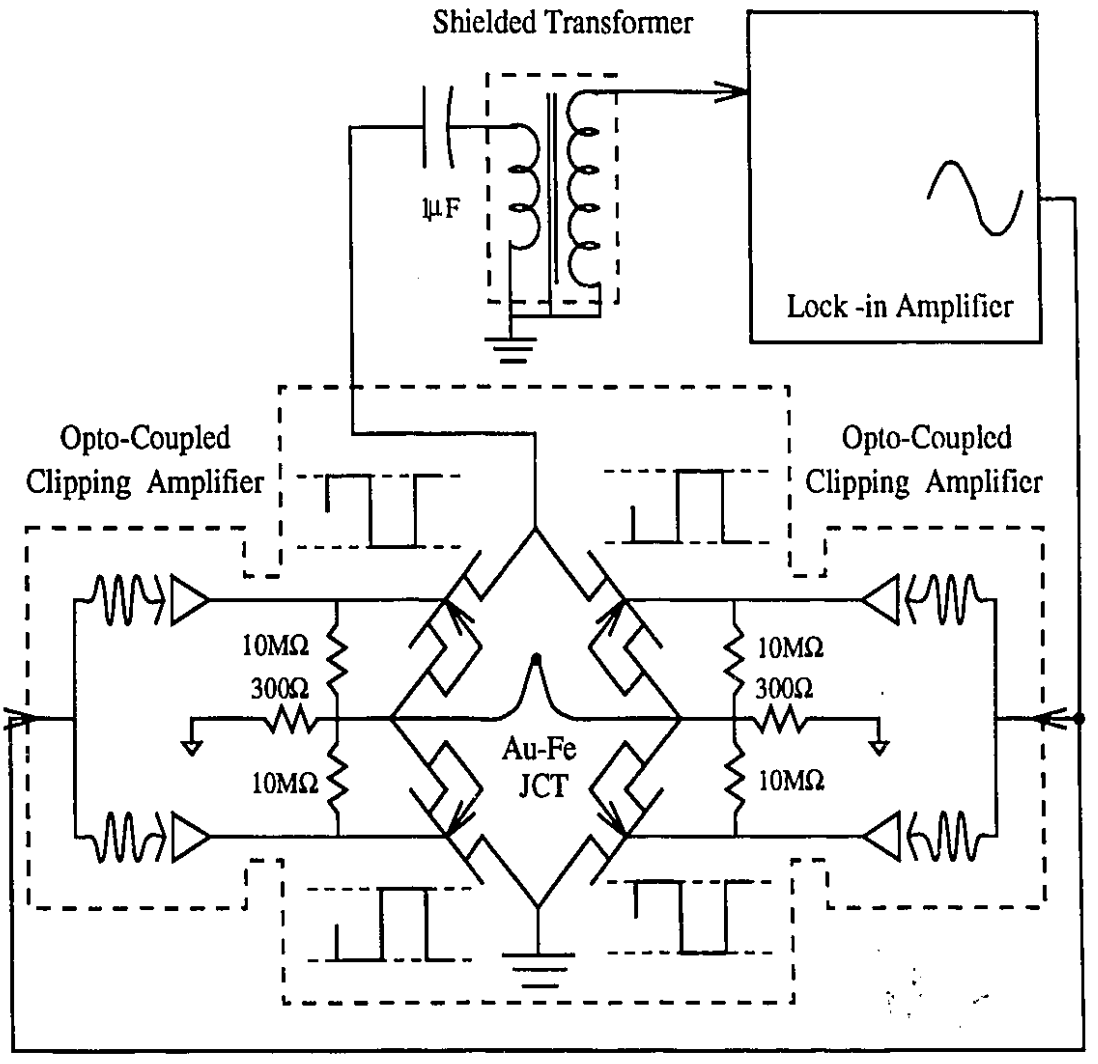

Figure 4.8: Block Diagram of Low Temperature MOSFET Chopper Circuit

so that only those near the modulation frequency are coherently rectified and filtered. Simpler variations of this circuit using only one or two MOSFETS were found to be ineffective since the chopped thermocouple signal was accompanied by a much larger offset. This offset was probably due to capacitative feedthrough of the MOSFET gate signals. The symmetry of the MOSFET bridge design balances out this offset to an acceptable level, comparable to the $\sim 1\mu$V thermocouple signal.

The 1kHz reference output generated by the lock–in amplifier is optocoupled to two sets of clipping amplifiers which provide 0 – 12V square waves that bias the MOSFET gates. The square waves must be referenced to two separate electrically

floating commons so that these amplifiers must be powered by isolated supplies. Since transformer isolated power supplies led to an unacceptable level of 60Hz feedthrough, the clipping amplifiers are powered by rechargeable batteries [100].

The location of the calorimeter in the McGill physics building is within line of site of a Megawatt transmitter which provides all radio and television signals in Montréal. Being composed of long wires and semiconductors, the chopper circuit was found to act like a crystal radio set. Radio frequency (RF) above 50MHz was picked up by the long wires, rectified by the MOSFETS onto the DC thermocouple voltage and then was chopped along with it. Even though the circuitry was heavily shielded, movement of the wires, like the adjustment of a TV antenna, caused the lock–in amplifier output to change sporadically. The antenna effect was totally absent when the circuit was transported to the basement. As a permanent solution, the entire workstation was enclosed in a low cost 2m× 2m× 3m aluminum screen Faraday cage which sufficiently attenuated the RF.

The output of the lock–in amplifier is filtered with a time constant, τ_{FILTER}, kept always less then 1% of the exponential decay time constant, τ. With a filter bandwidth of 25Hz, we could measure the thermocouple signal with a residual noise approaching 5nV. The thermocouple signal is monitored during temperature drops for roughly ten time constants by the quartz timer triggered analog-to-digital converter (ADC). Simple exponentials (equation 4.2) were fitted to these ADC traces and the decay time constant, τ, was extracted to within an uncertainty of typically $\frac{1}{2}$%. The almost perfect fit of an exponential to the measured traces (see Fig. 4.1) is testament to the high linearity of the thermocouple.

4.6 Determination of C_P

4.6.1 Corrections for Finite ΔT

The calorimeter measures $K = \frac{P}{\Delta T}$ and τ at each temperature, yielding in principle an independent absolute $C_P = \tau K$ at each temperature, T_0. Until now, however,

we have not introduced complications arising from the finite ΔT. Roughly speaking, C_P is measured at the average temperature, $T_0 + \frac{\Delta T}{2}$ so that $C_P(T_0)$ is measured high by a fraction $3(\Delta T/2T)$ for $C_P \propto T^3$. As ΔT is lowered, this systematic error is reduced, but the signal–to–noise ratio for C_P goes down proportionately. As a compromise between these two considerations, we have chosen $\Delta T/T \sim 5\%$, so that $C_P(T_0)$ is measured high by $\sim 8\%$. We must therefore correct for this non–negligible systematic error. In the following paragraphs, we describe separately how the $\Delta T = 0$ values of K and τ are extracted from K_{MEAS} and τ_{FIT}, their values measured with a finite ΔT. C_P is then determined by $C_P = \tau K$ as before.

Since the temperature gradient exists over the length of the wire, the measured link conductance $K_{MEAS}(T_0)$ is equal to $K(T)$ integrated over ΔT. We have approximated this integral by introducing a shift of the temperature to the average temperature, that is:

$$K_{MEAS}(T_0) = \frac{P}{\Delta T} = \int_{T_0}^{T_0+\Delta T} K(T)dT \approx K(T_0 + \frac{\Delta T}{2}).$$

This approximation is well justified since $K(T)$ is nearly linear in temperature, as is clear from Fig. 4.9, which shows the determined link conductance, plotted as K/T. SPLINE–LIKE functions[3] fitted to K/T are also displayed. Curves measured during different runs indicate that K/T changes between ^{4}He runs, but its general temperature dependence is maintained. In fact, subtracting off the SPLINE–LIKE function fitted to the $K(T)/T$ data of one run from the data of any other run yields a curve which is very nearly a constant within the noise. Consequently, we have used the value of the SPLINE–LIKE function fitted to the $K(T)$ data, rather that some corrected form of the actual pointwise measurement of $K(T)$. This procedure reduces noise introduced to C_P by fluctuations in the measurement of K.

The corrections to τ are more subtle, since they must account for the changes

[3]The SPLINE–LINE function is composed of four piece–wise polynomials of order five or less. The separate polynomials are constrained so that their values and derivatives are continuous at the points where they meet. The position of these points is optimised by a non–linear fitting program. SPLINE–LINE functions are useful in fitting $C_P(T)$ and $K(T)$ data, since they give a good representation of the data, without following sharp features which usually result from noise.

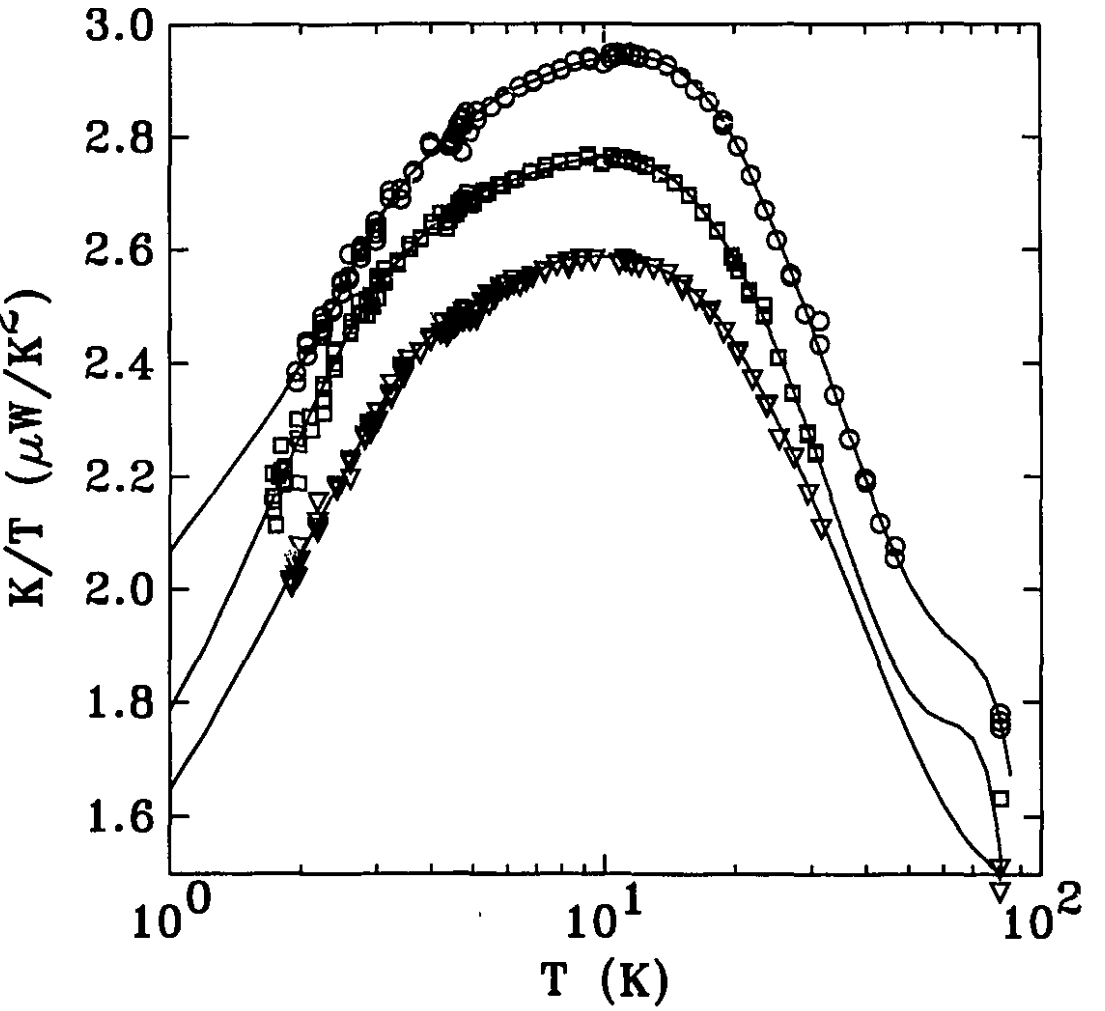

Figure 4.9: Thermal conductance, K, of calorimeter wires plotted as K/T for three separate helium runs. The solid lines are SPLINE–LIKE functions fitted to the data.

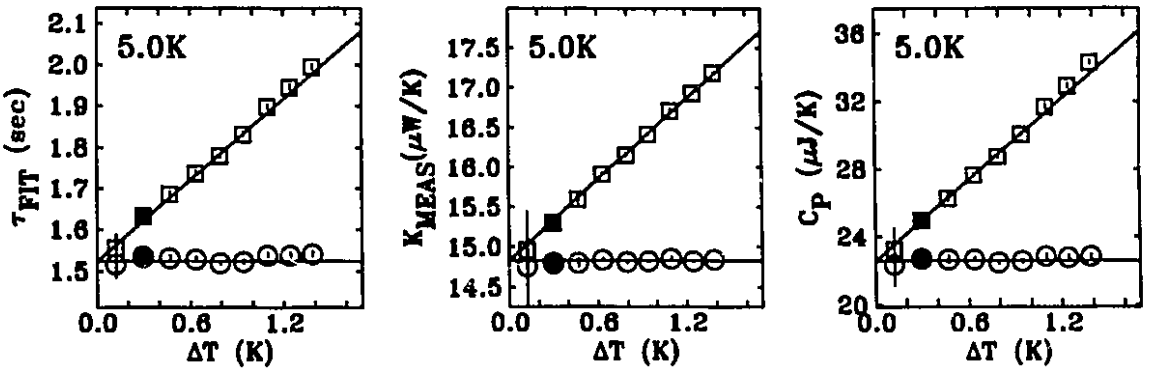

Figure 4.10: Power Scan. The values τ,K and $C_P = \tau K$ at $\Delta T = 0$ (o) are calculated from K_{MEAS} and τ_{FIT}, their values measured with a finite ΔT (□), using the solid lines independently determined from the whole data set with $\Delta T/T \sim 5\%$. This normal operating point is indicated by filled symbols.

in both C_P and K, during the drop. To lowest order, the effect of a changing C_P and K can be modeled by introducing a second short transient to the exponential drop. Care must be taken in this calculation, since the entire sample+addenda is heated to $T_0 + \Delta T$, while the conductance link temperature is distributed across ΔT. Consideration is given to how a least squares fit to a single exponential will fit this now double exponential. The following expression linking $\tau_{FIT}(\Delta T)$ and $\tau \equiv \tau_{FIT}(\Delta T \rightarrow 0)$ is found to apply:

$$\tau_{FIT}(\Delta T) = \tau \left[1 + \frac{4}{9}\left(\frac{d\ln\tau}{d\ln T} + \frac{1}{2}\frac{d\ln K}{d\ln T}\right)\frac{\Delta T}{T_0}\right]. \tag{4.6}$$

The value of τ is determined by the requirement of self consistency. Once roughly determined, the values of $\tau(T_0)$ are fitted to a low order polynomial in temperature which is differentiated to yield $\frac{d\ln\tau}{d\ln T}$. Equation 4.6, $\frac{d\ln\tau}{d\ln T}$, the SPLINE–LIKE function representing $K(T)$ and τ_{FIT} are then used to redetermine τ. This process is repeated until it converges on a value of τ, usually after 20 iterations or so.

The accuracy of the correction procedure has been independently tested by performing a number of temperature drops with different ΔTs but at the same T_0. Results of these *power scans* are shown in Fig. 4.10. The directly measured values K_{MEAS} and τ_{FIT}, are plotted as points and the solid lines give the dependence of these quantities predicted independently by the correction procedure. The excellent

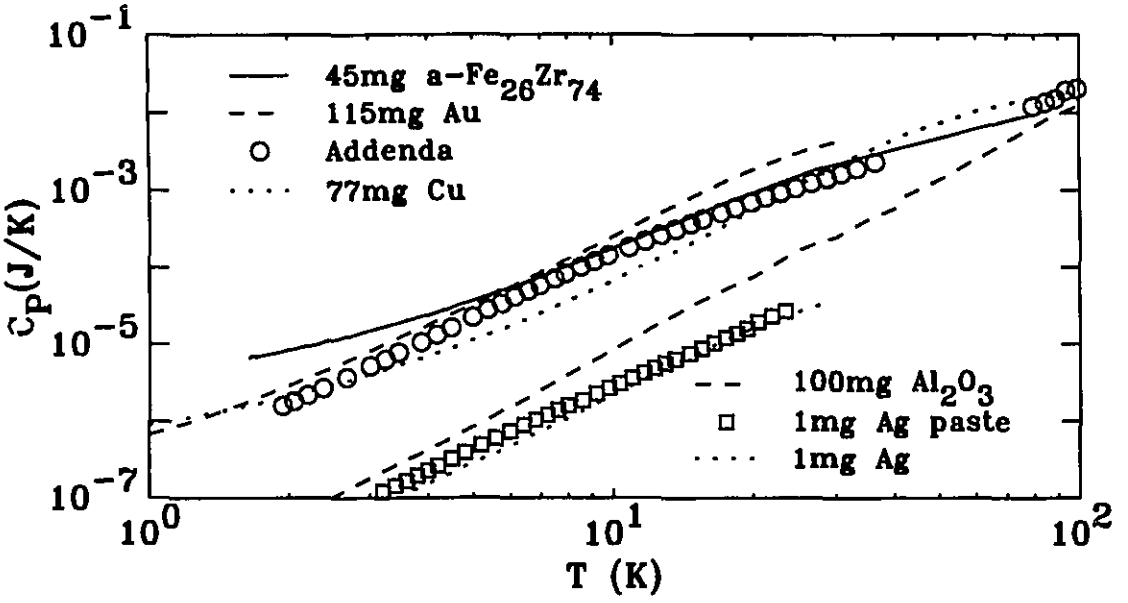

Figure 4.11: The C_P of various masses of various materials.

agreement demonstrates the effectiveness of the procedure.

4.6.2 The Addenda C_P

The specific heats of the addenda, the standard samples and various other materials are plotted in Fig. 4.11. The bare addenda was run three separate times and C_P was found to be identical within 1%. The measured C_P from these addenda runs is fitted to a SPLINE–LIKE function. This function is subtracted from all sample+addenda runs to yield only the C_P of the sample.

At high temperatures near those of liquid nitrogen (77 K), C_P of the addenda is almost completely accounted for by the 100mg of sapphire, which makes up most of its mass. At low temperatures, however, the C_P of the hard (high Debye temperature, Θ_D [88]) sapphire is insignificant and the addenda C_P is composed of that of the epoxy and $\frac{1}{3}$ of the link wires [76]. These have high C_P at low temperature[108]) because of their low Θ_D and high electronic C_P respectively. The C_Ps of metallic ribbons studied are actually easier to measure than the C_P of the copper and gold standard samples, since they have a large linear electronic C_P and thus a less rapid variation of C_P with temperature than the mostly cubic C_P of copper and gold.

Samples are fixed to the polished top face of the addenda with about 5mg of silver paste [109], a conductive adhesive dispensed reproducibly with a 10μL syringe. This amount of silver paste was also added to the bare addenda, so it is also subtracted off with $C_{ADDENDA}$. Silver paste has the advantage that it conducts heat well, can be removed easily with acetone and has a low C_P which was measured (Fig. 4.11) as slightly more than that of pure silver [108,110]. This indicates that the binder in the paste evaporates away leaving mostly silver. Commonly used insulating Apiezon N grease [111] has more than 10 times the gram specific heat, so that more silver paste may be used to thermally bond the sample.

4.6.3 Sample Mounting

The samples studied are all metallic a–Fe–Zr ribbons. Sample masses must be chosen to provide a high ratio of C_{SAMPLE}:$C_{ADDENDA}$, preferably at least 1, so that the operation of subtracting $C_{ADDENDA}$ increases the relative uncertainty by only a factor of 2 or less. At the lowest temperatures, this corresponds to at least 10mg as shown in Fig. 4.11. Since only a few milligrams of metallic ribbon could be laid flat on the addenda, attempts were made to increase the mass of ribbon, by hanging 5mm over either side, increasing the sample mass by a factor of three. In this case non–exponential drops were observed, and were discussed extensively in ref. [112]. These non–exponential drops were determined to result from the fact that when the sample overhangs by 5mm, the internal relaxation time of the overhanging part becomes significant. When there are significant thermal resistances other than the main thermal link in the calorimeter then the simple representation of the calorimeter in Fig. 4.1 does not apply. Consider what happens if C_A and C_S are not perfectly thermally connected, but coupled through a second link, R_2. In this case, illustrated in Fig. 4.12, elementary circuit analysis tells us that a double exponential decay should occur which has the following form [112]:

$$T = T_0 + A_+ \exp(-\frac{t}{\tau_+}) + A_- \exp(-\frac{t}{\tau_-}) \tag{4.7}$$

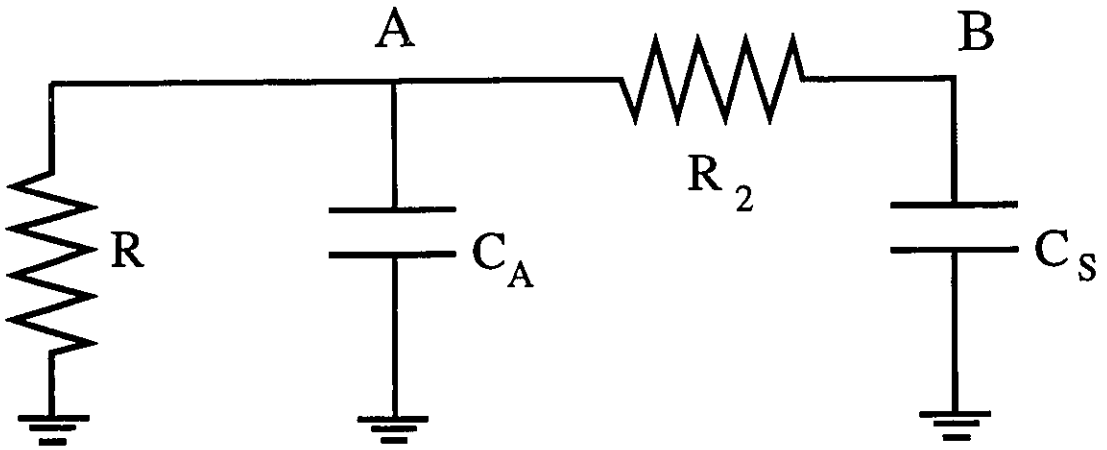

Figure 4.12: A circuit illustrating the electrical representation of bad thermal contact between the addenda, C_A, and the sample, C_S.

where:

$$\tau_{\pm} = \frac{2h\tau_0}{(\lambda + h + 1) \mp \sqrt{(\lambda + h + 1)^2 - 4h\lambda}}$$

$$\begin{aligned} \tau_0 &= C_A R \\ h &= \frac{R_2}{R} \qquad \text{(conductance ratio)}, \\ \lambda &= \frac{C_A}{C_S} \qquad \text{(specific heat ratio)}. \end{aligned}$$

In the limit of small R_2, the two time constants can be written:

$$\tau_+ \approx \frac{1+\lambda}{\lambda}\tau_0 = R(C_A + C_S) \equiv \tau$$

$$\tau_- \equiv \tau_2 \approx \frac{h}{1+\lambda}\tau_0 = R_2\left(\frac{1}{C_A} + \frac{1}{C_S}\right)^{-1}.$$

In ref. [112] the temperature drops were modeled with equation 4.7 as well as with a more realistic series solution to the heat conduction equation. Values of C_P derived using this techniques agreed well with those determined from runs where the ribbons were all in good thermal contact with the addenda. Consistent estimates of the thermal conductivity of the ribbons could also be extracted. While analysis of

double exponentials was satisfactory in this case, *the strategy generally employed in the time relaxation technique is to require single exponential relaxation and thus that* $\tau_2 \ll \tau$.

The complex relaxation associated with the overhanging sample led us to devise an effective way of mounting even more ribbon with no significant internal relaxation times. Half meter lengths of ribbon were neatly coiled by hand into a bundle like a roll of tape which was closed with a tiny dab of Krazy Glue^{TM}. The roll was then silver pasted [109] to the addenda. Work on the overhanging ribbons [112] showed that if the ribbons extend over the edge of the addenda by 5mm, there is a measurable internal τ_2 problem. Since the roll height is only 1mm, both the ribbon's thermal conductance and its total specific heat are reduced by a factor of 5. The internal time constant is, therefore, reduced by a factor of $5^2 = 25$, *i.e.* into insignificance. Examination of the early time behavior of the temperature drops taken on such rolls indicates directly that there are no significant short time constants. One such drop is displayed in Fig. 4.1 and is well fitted by an exponential. Small discrepancies at early times are completely accounted for by effect of low pass filtering. The roll method allows the maximum amount of ribbon to be mounted with the added advantage that any possible demagnetization fields resulting from an applied vertical magnetic field are minimized.

Considerations of the internal sample relaxation time reveal the real power of the time relaxation (TR) technique. The other common method of absolute calorimetry is the *heat pulse* (HP) or *quasi-adiabatic* technique [76–80,113,114]. Here, the experimental setup is the same as in Fig. 4.1 except now the power, P, is only applied for a short time, Δt, depositing an amount of heat $\Delta Q = P\Delta t$ into the sample. C_P then is calculated directly from equation 4.1. This technique is used to do the most accurate measurements of C_P on gram size samples. In the HP technique, however, the requirement on τ_2 is that: $\tau_2 \ll \Delta t \ll \tau$ [76]. This means that for small samples (<100 mg) [76], where τ_2 becomes significant, τ can be made much shorter in the TR technique than in the HP technique. Since τ determines how long it takes to reach

equilibrium after changing reservoir temperature, a shorter τ means that more data points can be taken in a given time using the TR technique than in the HP technique.

Attempts were made to reduce $C_{ADDENDA}$ and so further increase the ratio of C_{SAMPLE} to $C_{ADDENDA}$. Addendas constructed using less epoxy, however always resulted in calorimeters which measured high C_Ps of the standards. Errors arose from a significant τ_2, which could be directly observed in the early time behavior of bare addenda drops. τ_2 must therefore result from bad thermal contact between various parts of the addenda. The coefficients $A_\pm$ from equation 4.7 depend on the four possible sets of boundary conditions (heat input or temperature measured at either point A or B in Fig. 4.12). Unless one is sure which set applies, equation 4.7 cannot easily be used to fit non–exponential drops. An older, heavier addenda was the only one which yielded correct standard C_Ps and no measurable τ_2. It survived and was used for the entire study.

We conclude generally that epoxy has too low a thermal diffusivity to be used in constructing addendas. Attempts should be made to use only thin films elements deposited directly on the addenda [115,116], preferably with metal film contact pads so that wire leads may be attached with solder.

4.6.4 C_P Standards

Due to the number of things which can go wrong in an absolute calorimetry measurement, many of which have been described above, *measurement of C_P for established standards is imperative in establishing the integrity of the measurement.*

Our absolute measurement of the gram specific heat of 99.999% pure copper and 99.9999% pure gold pellet-like samples are plotted as C_P/T versus T^2 in Fig. 4.13. This method of plotting the data is used since C_P is proportional to a linear plus a cubic term in T as $T \rightarrow 0$ in a normal metal, so that the data yield a straight line. Also displayed are the extremely accurate results of D. L. Martin [110,117,118] determined using a heat pulse calorimeter on gram size samples.

In Fig. 4.14 the data of Fig. 4.13 are replotted as a percent deviation from the

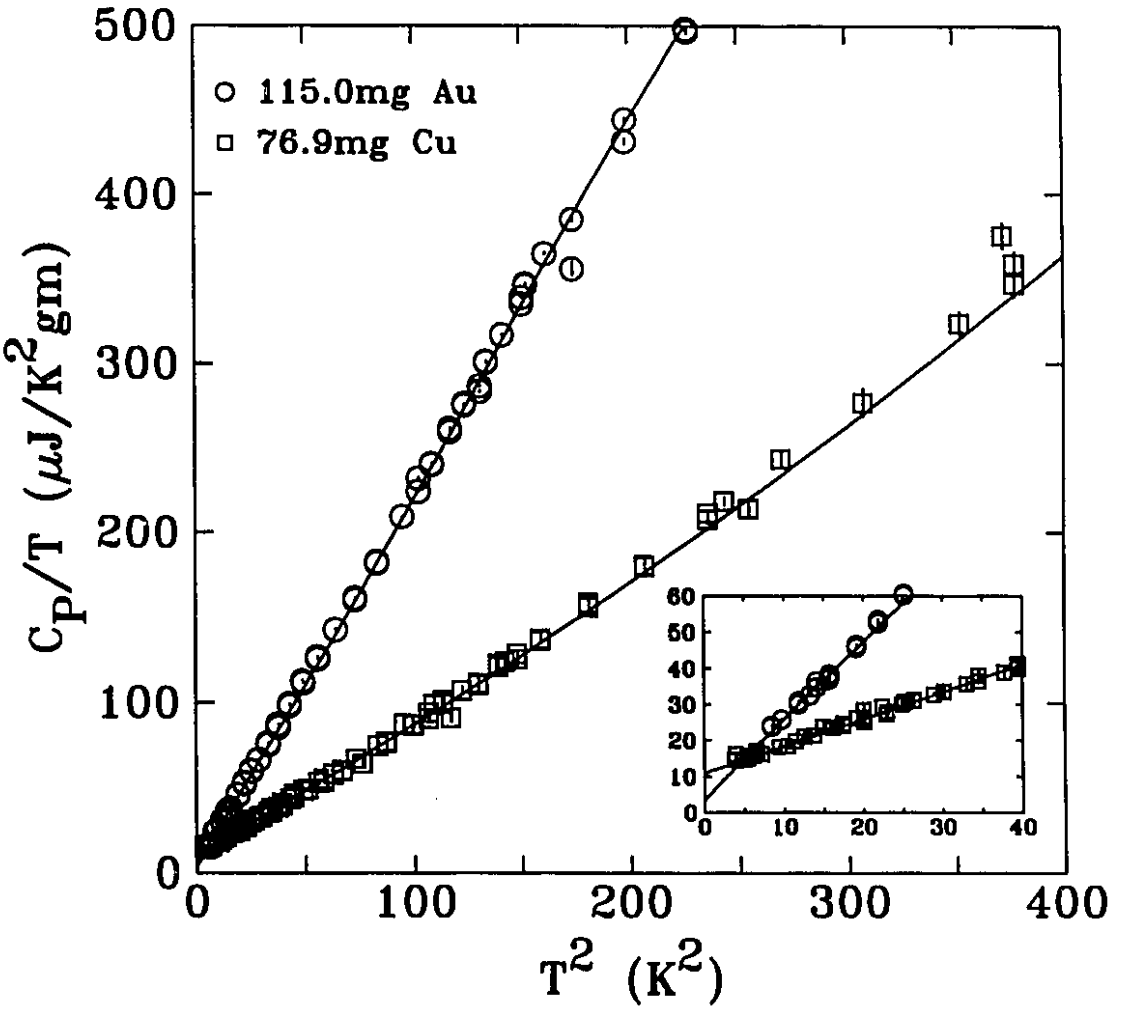

Figure 4.13: Measured absolute gram specific heat of copper (Cu) and Gold (Au). The solid lines are the data of D. L. Martin [110,117,118].

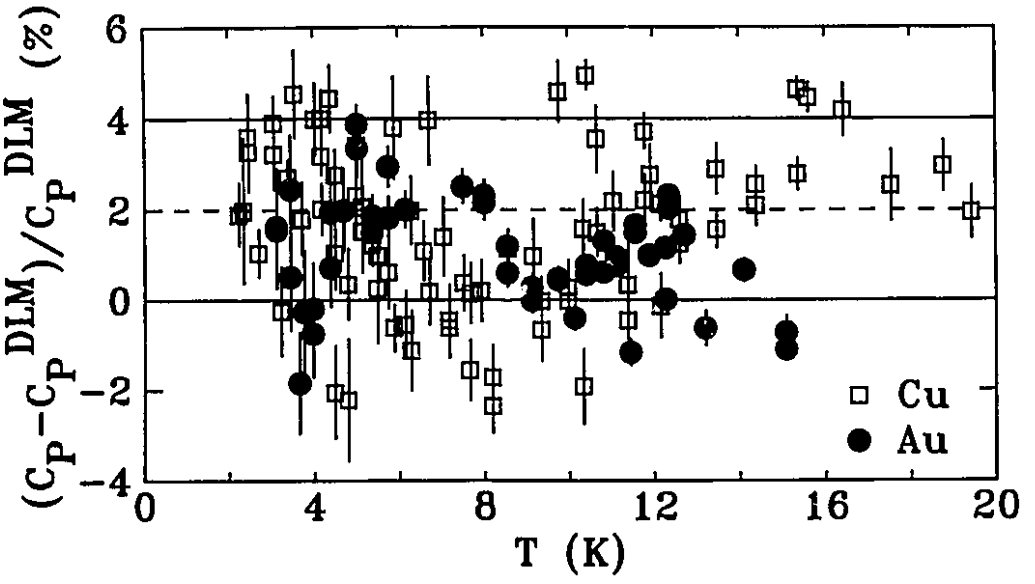

Figure 4.14: Accuracy of Specific Heat Measurement: the data of Fig. 4.13 are shown as a percent deviation from the data of D. L. Martin [110,117,118]. The dashed line is the quoted accuracy of 2% and the solid lines are separated by twice the quoted precision of 2%.

data of D. L. Martin. We can see that the C_P error is roughly a curve with a scatter of 2% offset by less that 2% at all temperatures. We therefore quote the absolute accuracy and precision of the calorimeter each as 2%.

4.7 Magnetocalorimetry

The cryostat can be placed into the 5cm bore of a 5 Tesla superconducting solenoid [119], so that the addenda sits in the maximum field. The field is constant to within 1% over the whole addenda. The magnetic field intensity is determined as the measured ~80 Amp current through the solenoid multiplied by the field–to–current ratio supplied by the manufacturer.

A problem arose on the first application of a magnetic field to the calorimeter. An intermittent microvolt level signal of a frequency of around 100Hz appeared on the thermocouple signal. This was found to be due to mechanical vibrations of the addenda in the field. A simple calculation shows that 1μm amplitude vibrations at 100Hz of 1cm wire in a plane perpendicular to a 5 Tesla field lead to a 30μV induced signal across the wire. An addenda was designed with holes in it which were used

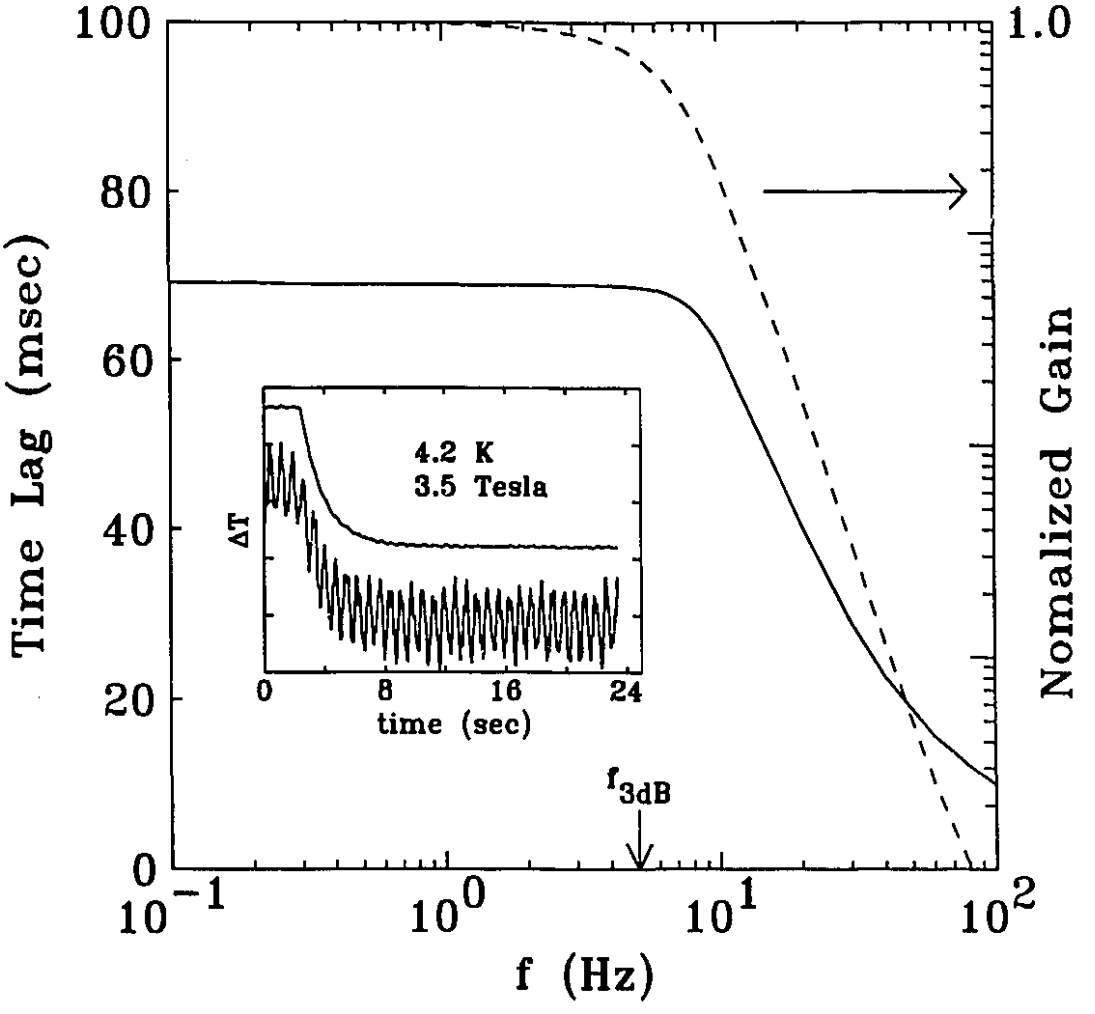

Figure 4.15: Measured attenuation characteristics of the constructed 5Hz, 4–pole Bessel filter. The dashed line shows the gain and the solid line shows the time lag introduced by the filter. The inset shows the effect of the filter on two drops taken under otherwise identical conditions.

to tightly bind the addenda with thin nylon fishing line. This eliminated the 100Hz oscillations from the signal, however a smaller amount of just as troublesome 20Hz oscillations was found to persist. The problem was solved by the construction a 5Hz 4–pole Bessel filter [120], the measured attenuation characteristics of which are shown in Fig. 4.15. This filter is designed so that the *time lag* experienced by a signal on going through the filter is constant up to frequencies well above f_{3dB}, while still providing a 24dB/octave attenuation at high frequencies. The filter has the effect, therefore, of attenuating the unwanted high frequency components, while merely delaying the slowly varying exponential part by a fixed lag, without distorting it. The dramatic

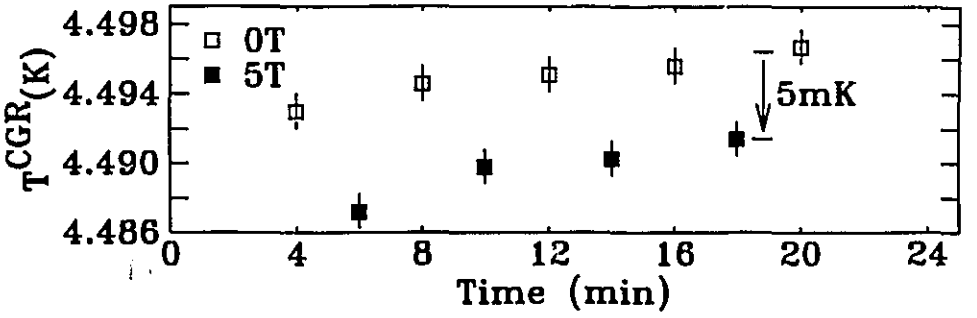

Figure 4.16: Absolute thermometry calibration in magnetic field. The temperature of the carbon glass thermometer (T_{CGR}) is measured as a 5 Tesla magnetic field is turned on and off while temperature is controlled using a field independent capacitance sensor. The arrow shows the determined apparent temperature shift of -5 mK resulting from the field.

effect of the Bessel filter is illustrated in Fig. 4.15 which shows a drop taken in a 3.5 Tesla field with and without the Bessel filter.

All of the resistive sensors used have a significant magnetoresistance necessitating the use of a field independent capacitance thermometer [83]. A commercial capacitance card for the temperature controller [83] measures a capacitance by letting it integrate current pulses. A standard 56nF ceramic capacitor was found to have the same temperature sensitivity and drift with time as commercial capacitance thermometers [83]. Initially, attempts were made to calibrate the capacitor with the CGR in zero field and then use it to determine temperature with the field on. However, internal strain relief causes the capacitance to drift at a rate corresponding to ~10 mK/hour, too rapidly for the sensor to be used as a long term reference thermometer. The strategy employed, therefore, was to control temperature with the capacitance sensor, and monitor the CGR temperature as the field is turned on and off as quickly as possible. The resulting measurement of T_{CGR} is shown in Fig. 4.16 as a function of time. Here, we can see that the effect of the 5 Tesla field can be expressed as an apparent temperature shift, which is, in this case, -5 mK. Even unaccounted for, this shift would correspond to a shift in C_P of at most 2%.

Apparent temperature shifts due to the fringes of a 5 Tesla field were determined in this way for several temperatures. Five times the relative temperature shift ($\Delta T/T$) is displayed in Fig. 4.17. Also plotted are apparent temperature shifts in 2.5T, deter-

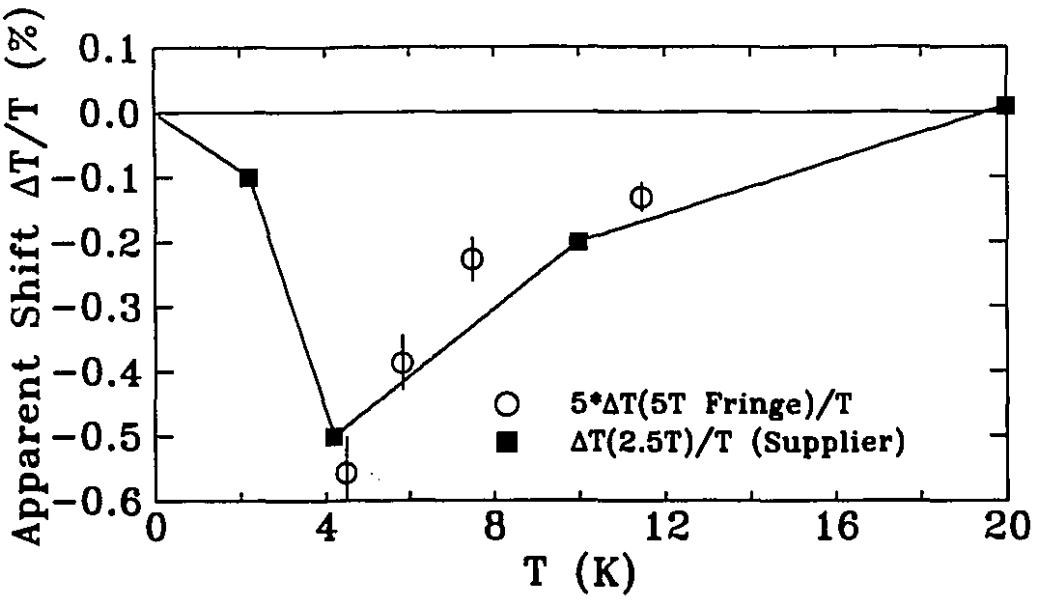

Figure 4.17: Field Calibration of Thermometer: Five times the apparent temperature shifts, determined from data like those of Fig. 4.16, due to a fringing 5 Tesla fields are plotted versus temperature. Apparent temperature shifts typical of CGRs published by the supplier [121] are also shown.

mined by the supplier for a typical CGR. The agreement between these data suggests that the CGR sits in a field one tenth of that at the center of the solenoid. This is consistent with 15% which is an estimate of fringing field fraction at the CGR position. We have therefore used 1/10 of the published curve to shift the measured temperature in a field, which amounts to a maximum shift of -5mK in 5 Tesla .

Since the effect of a magnetic field on the CGR could now be corrected for, the measurement of C_P was done completely independently at fixed field values over a wide temperature range. The link conductance was found to increase with an applied field at low temperatures, probably due to magnetic alignment of the Fe in the Au–0.07%Fe wire and associated reduction of electron scattering. The conductance was found to increase by at most 10% in 5 Tesla at 2 K.

The results of standard sample runs are shown in Fig. 4.18. No field dependence to the C_P of either the addenda or a copper standard was observed to within 2%, as expected. This gives us great confidence in our absolute magnetocalorimetry measurement.

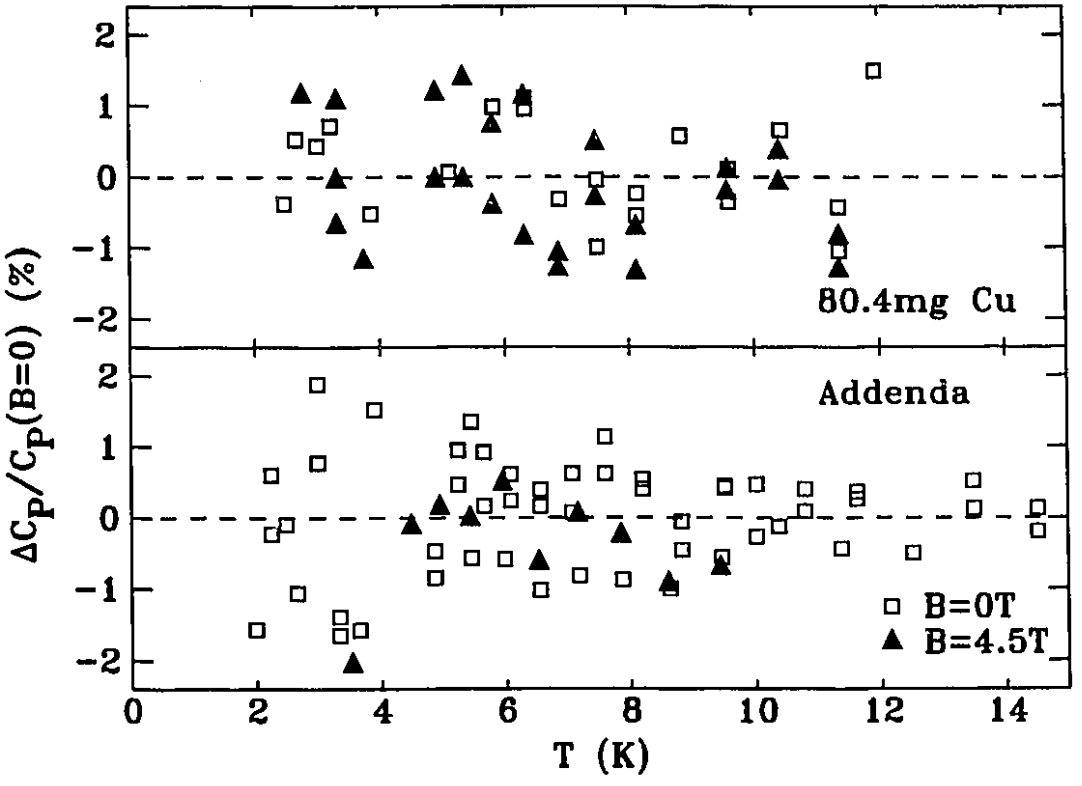

Figure 4.18: The specific heats of the bare addenda and a copper sample in and out of a magnetic field of 4.5 Tesla. The data are presented as a percent deviation from a SPLINE–LIKE function fitted to the zero field data.

Chapter 5

Results and Discussion

5.1 Magnetometry Results

Measurement of magnetic properties by magnetometry is important generally as a means of understanding the behaviour of magnetic contributions to the specific heat. Specifically, we will want to know how big the *Stoner exchange enhancement factor*, S, is in a–Fe_xZr_{100-x}. This will allow us to predict the strength of the spin fluctuation (SF) contribution to the electronic specific heat. SF are expected to have the largest effect for nearly ferromagnetic ($S \rightarrow \infty$) and weakly ferromagnetic (ordered moment, $p_s \rightarrow 0$) samples.

Dr. D. V. Baxter supplied magnetization data on five paramagnetic a–Fe_xZr_{100-x} samples which were presented in ref. [64]. The magnetization, M, in magnetic fields, H, was measured at temperatures between 4.2 K and room temperature and for $0 < \mu_0 H < 1.5$ Tesla, using an alternating gradient force magnetometer [64]. In their original analysis, straight lines were fitted to the high field ($\mu_0 H > 0.5$ Tesla) M *vs.* H data and the slope was taken as the magnetic susceptibility, χ. Following the work of ref. [57], we re–analyse the data above 0.5 Tesla in a manner more appropriate for near/weak ferromagnets. Our susceptibility values are higher than those of ref [64], in particular for the Fe rich alloys, where our χ values are a factor of ~ 2 higher. Nonetheless, the same trends in temperature and Fe content are observed in

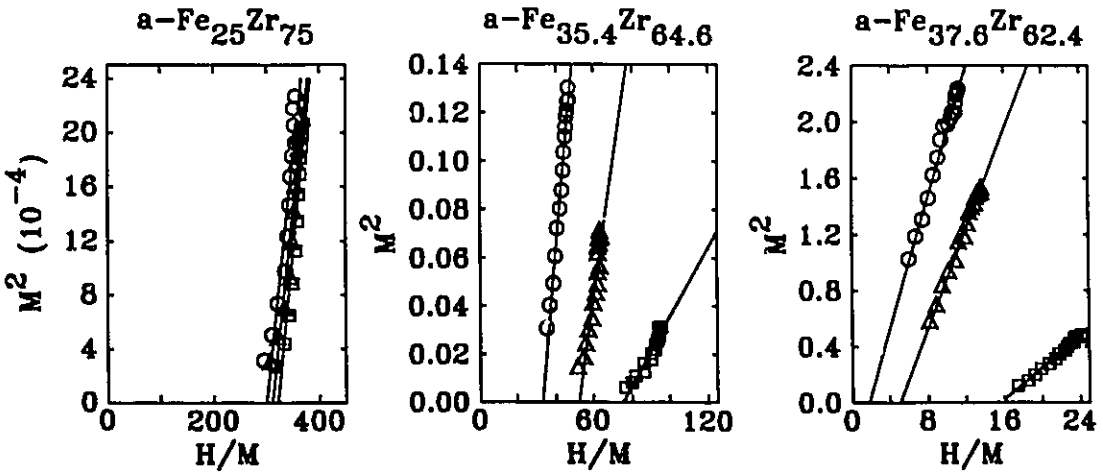

Figure 5.1: Arrott plots for $a-Fe_xZr_{100-x}$. The magnetization data was supplied by Dr. D.V. Baxter and was originally presented in ref. [64]. The units for the x- and y-axes are the standard CGS units; KOe gram/emu and (emu)^2 respectively. The data are shown for three of the five samples at temperatures of 5.5 K(○), 11.5 K(△) and 40 K(□) and for magnetic fields between 0.5 and 1.5 Tesla. Solid lines are the best linear fits whose x-axis intercepts are taken as the inverse susceptibility, χ^{-1}.

χ, irrespective of the method of data analysis.

In a system with a small uniform magnetization, M, the free energy can always be expanded in a Ginzburg–Landau expansion (equation 2.38). As discussed in Chapter 2, the result is that the applied magnetic field, H, and the magnetization, M are related by:

$$\frac{H}{M} = a + bM^2. \tag{5.1}$$

From this equation, we can see that in an *Arrott plot* of H/M *vs.* M^2, the data should follow straight lines. In a paramagnetic sample, both a and b are greater than zero and the straight lines should cut the x-axis at a point corresponding to the inverse magnetic susceptibility, χ^{-1}.

In Fig. 5.1, we have displayed representative Arrott plots for three samples at various temperatures. The data follow straight lines and we have determined the inverse paramagnetic susceptibilities, χ^{-1}, by simply reading off the $M^2 = 0$ intercepts on the H/M axes. The CGS units of χ are emu/Oe gram, which are equivalent to cm^3/gram. These units are widely, though incorrectly, stated as emu/gram. The values of χ are displayed in Fig. 5.2 for all five samples as a function of temperature.

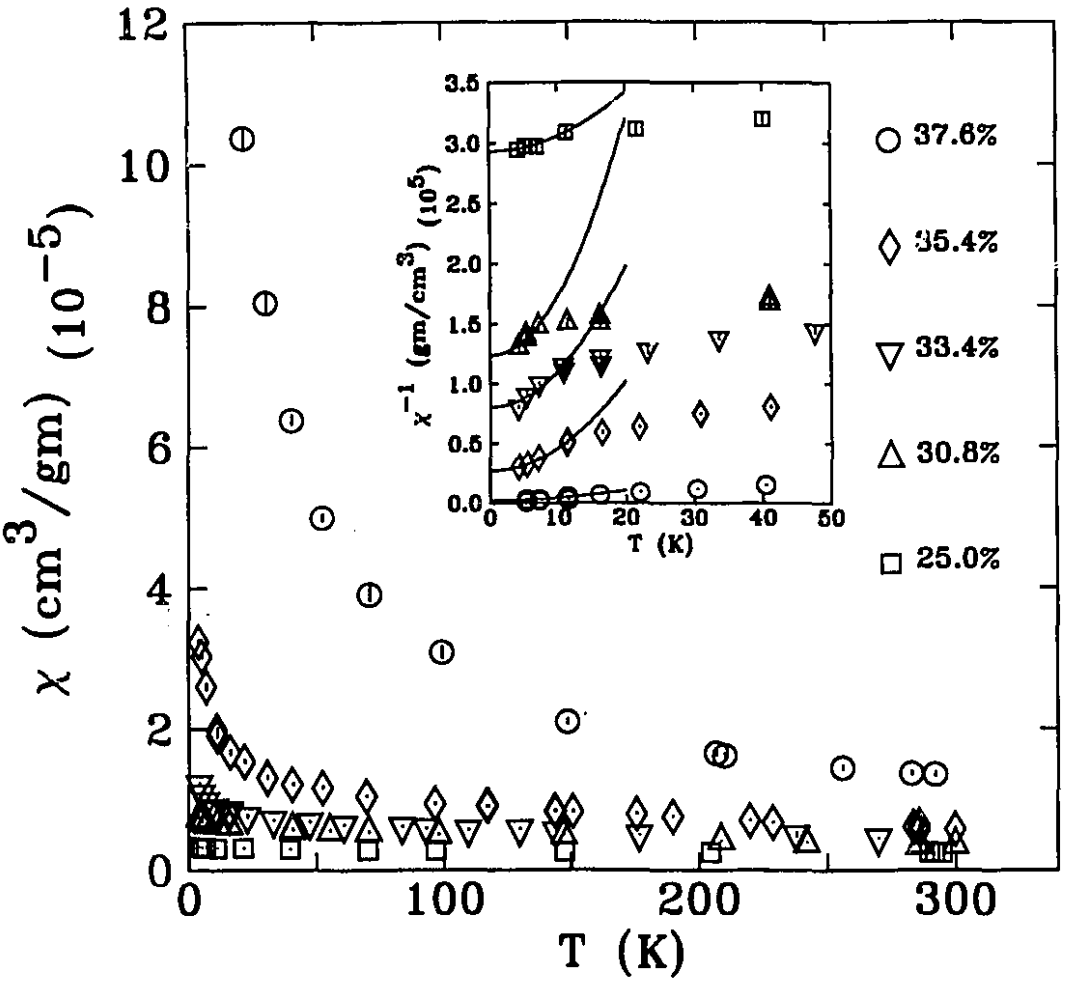

Figure 5.2: Magnetic Susceptibility of Paramagnetic $a-Fe_xZr_{100-x}$. The measured $\chi(T)$ is displayed for five paramagnetic samples. The inset shows the inverse susceptibility, $\chi^{-1}(T)$, at low temperatures. The solid lines are parabolas used to determine $\chi^{-1}(T=0)$.

Stoner theory predicts that the susceptibility of a nearly ferromagnetic metal should be weakly, quadratically dependant on temperature (equation 2.35). Clearly, this nearly temperature independent, quadratic function is not a correct description of the highly temperature dependant measured susceptibility of $a-Fe_xZr_{100-x}$. Nonetheless, following previous work on nearly magnetic Ni_3Ga [32], we have used a parabola of the form: $\chi^{-1}(T) = \chi^{-1}(T=0) + [const.]T^2$, as an extrapolation scheme to extract $\chi(T=0)$, the ground state susceptibility. Our extrapolated ground state susceptibilities are not much different from those measured at 4.2 K, so that the exact nature of the extrapolation scheme is not important.

We should add here that a previous study [57] noted that Zr has a high Van-Vleck susceptibility ($\sim 1.3\times10^{-6}$ cm^3/gm). They subtracted estimates of this, and of the Larmor diamagnetic contribution due to core electrons ($\sim -0.2\times10^{-6}$ cm^3/gm), from the measured susceptibility. This allowed them to extract the *valence susceptibility* of a–Fe_xZr_{100-x}. Since our susceptibilities were measured at lower temperatures and were much larger than their room temperature values, we have ignored these corrections. We have also ignored the small Landau diamagnetic contribution ($-\frac{1}{3}\chi_P(T=0)$) of the conduction electrons to χ. Furthermore, we have found, by calorimetry, that an a–$Fe_{37.6}Zr_{62.4}$ sample from the same batch as that of Fig. 5.2 actually exhibits a magnetic transition at temperatures just below 4.2 K. This sample has, therefore, been omitted in estimating the Stoner factor.

The ground state susceptibilities, $\chi(T=0)$, have been determined directly as the $T=0$ intercept of the parabolas from the inset of Fig. 5.2. Together with the data on the ferromagnetic a–Fe_xZr_{100-x} samples of ref. [57], we attempt to construct a *Mathon plot* like Fig. 2.4 for a–Fe_xZr_{100-x}. The ordered magnetic moment, p_s, grows rapidly from zero as the Fe content increases from the critical concentration of $x \sim$37%. Because of this, p_s covers a broad range of values within the precision of the x value. Consequently, the 37.6% Fe sample of Fig. 5.2 and ref. [64] appears as less magnetic than the 37.5% Fe sample of ref. [57]. We present in Fig. 5.3, the determined ground state susceptibility, $\chi(T=0)$, for the samples of Fig. 5.2, and a plot of T_C *vs.* p_s derived from ref. [57] and from our calorimetry result.

The values of $\chi^{-1}(T=0)$ correspond to susceptipilities far larger than those expected for a simple metal ($\sim10^{-6}$cm^3/mole) [4]. We have interpreted these high values of $\chi(T=0)$ to mean that non-magnetic a-Fe_xZr_{100-x} samples are strongly exchange-enhanced paramagnets or near ferromagnets. The behaviour of $\chi^{-1}(T=0)$ is linear in composition, x, as expected for a near ferromagnet. This linear relationship will be used later to estimate values of $\chi^{-1}(T=0)$ for the actual a–Fe_xZr_{100-x} samples used in this study. These estimates, together with the bare densities of states at the Fermi level ($N_0(\varepsilon_F)$) determined by calorimetry, will be used to estimate

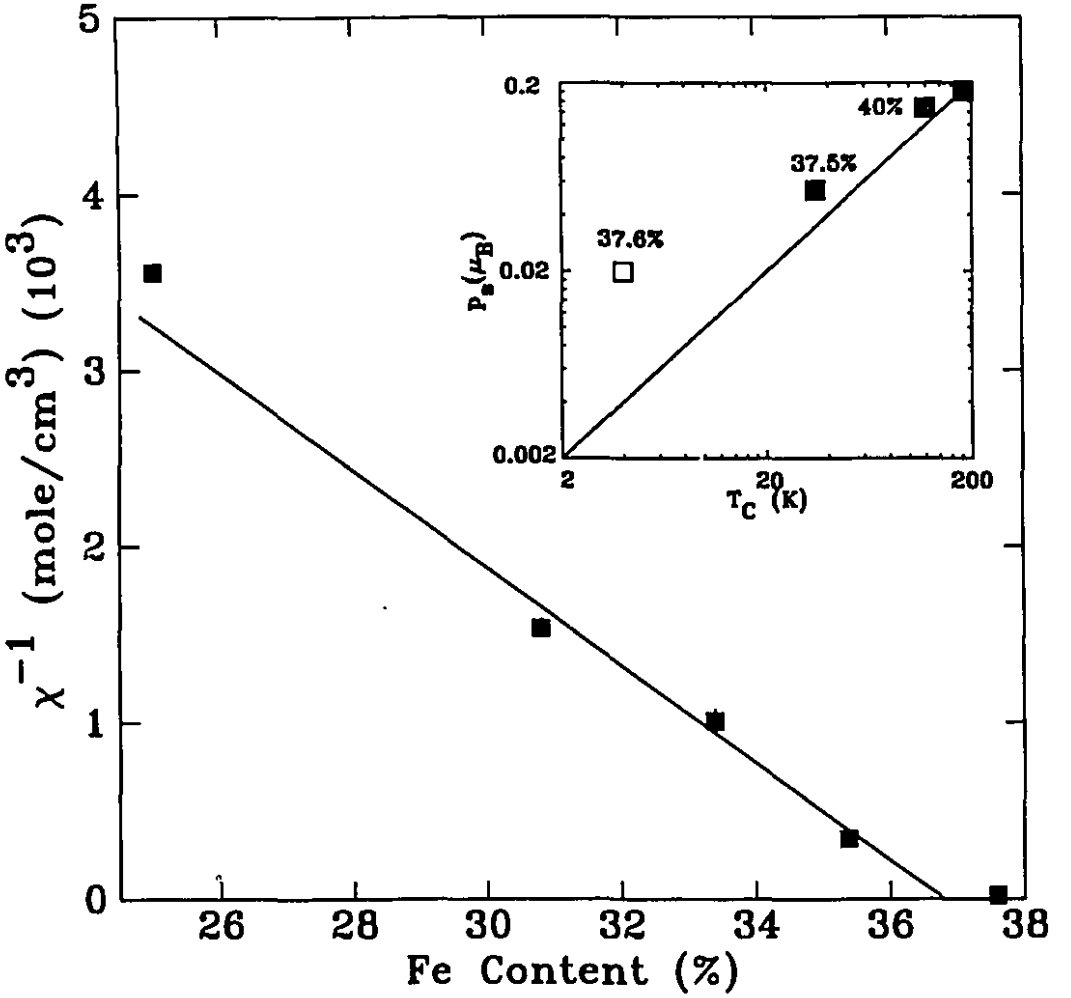

Figure 5.3: Ground State Susceptibility of a–Fe_xZr_{100-x}. The values were determined directly from the $T = 0$ intercepts of parabolas of Fig. 5.2. The inset shows the relation between p_s and T_C, taken from ref. [57]. The values for the a–$Fe_{37.6}Zr_{62.4}$ sample were determined by calorimetry. The solid lines are consistent with Stoner theory.

the Stoner enhancement factors, $\mathcal{S}$, for our samples.

The inset of Fig. 5.3. displays the relationship between p_s and T_C for the ferromagnetic samples of ref [57] and for the 37.6% Fe sample determined later in Fig 5.10, by calorimetry. The values of p_s are a small fraction of a μ_B (<20%). If we insist on identifying these moments with local Fe moments, p_s is at most $0.6\mu_B$/Fe atom. The Weiss local moment model is clearly unable to explain these small ordered moments. Since the Stoner model predicts such *weak ferromagnetism*, the small observed ordered moments give further evidence that a–Fe_xZr_{100-x} is an itinerant near/weak ferromagnet. The plot also shows that both p_s and T_C increase together and a linear

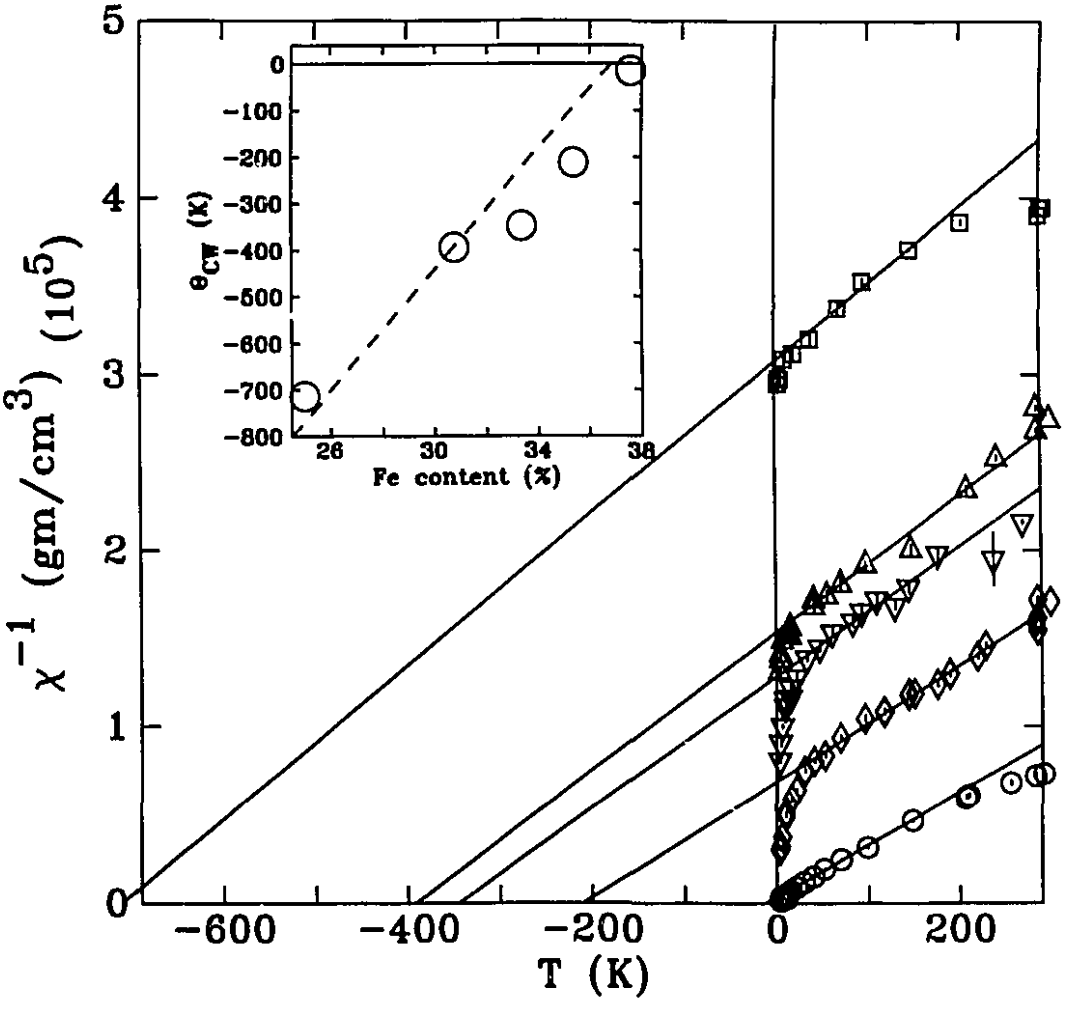

Figure 5.4: Magnetic Susceptibility of a−Fe_xZr_{100-x}: Straight solid lines are fits to a Curie-Weiss law (equation 5.2). The samples are indicated by the same symbols used in Fig. 5.2. The inset shows the values of Θ_{CW} determined from the straight lines. The dashed line is a guide to the eye.

relationship, consistent with Stoner theory, is also displayed.

Fig. 5.4 shows an analysis of the high temperature inverse susceptibility. At higher temperatures, the curves are well fit by straight lines. Deviation only occurs for the sample with the least Fe at the highest temperatures. This deviation results from the Van–Vleck contribution, which we have not subtracted off.

Solid straight lines in the figure represent a Curie–Weiss(CW) law:

$$\chi(T) = \frac{C_{CW}}{T - \Theta_{CW}} = \frac{p_{eff}^2 N_A}{3k_B(T - \Theta_{CW})} \tag{5.2}$$

The inset of Fig. 5.4 shows that all Θ_{CW} values are negative with absolute values that decrease with increasing Fe content, vanishing at x_c. Negative Θ_{CW} values

from high temperature Curie–Weiss fits are typical of nearly ferromagnetic metals such as pure Palladium [52] and Ni_3Ga [32]. The determined CW constant, $C_{CW} \equiv \lim_{T\to\infty}(d\chi^{-1}/dT)^{-1}$, increases monotonically with Fe content from 0.19 K cm^3/mole to 0.26 K cm^3/mole. C_{CW} can be used to calculate effective high temperature Curie moments ranging from $p_c = 0.58\mu_B$ to $0.76\mu_B$. Taking only the measured ordered moments, p_s, from ref. [57], we can estimate a maximum, measured value of the moment ratio, p_c/p_s, which approaches 10.

Although traditionally taken as an indication of local moments, a CW law has recently been derived using spin fluctuation models which apply to itinerant magnets [10,14,21]. Roughly speaking, the CW law, normally the prediction for an interacting local paramagnet, indicates local or correlated behaviour being displayed by itinerant electrons. We derived an expression with the form of a CW law (equation 2.39), by assuming simply that all *SF* modes are thermally excited ($T \gg T_{SF}$). This expression predicts that the observed Θ_{CW} should be proportional to $(\bar{I}-1)T_{SF}$. For these paramagnetic samples, therefore, Θ_{CW} should be negative and increase monotonically to zero at the critical composition. This is exactly what is observed in Fig. 5.4. At low temperatures $T<T_{SF}$, the CW law breaks down since the *SF* modes are not all excited. $\chi(T=0)$ should be bigger than the value extrapolated from the CW law. This behaviour is also observed.

In summary, we have shown that the ground state susceptibilities of the non-magnetic a–Fe_xZr_{100-x} samples of ref. [64] are consistent with the Stoner theory of nearly ferromagnetic metals. The ferromagnetic samples ($x>x_c$) show very small values for both the ordered moment, p_c, and the ordering temperature, T_C which increase with x. All of these results, establish that a–Fe_xZr_{100-x} *is a near/weak itinerant ferromagnet with a critical concentration of* $\sim$*37%*. At high temperatures, in the paramagnetic samples, the susceptibility is reduced, following a Curie–Weiss law with $\Theta_{CW}<0$. This is consistent with the reduction of $\chi(T)$ by thermally activated *SF*. The apparent local moment behaviour at high temperature, as manifested by the observation of a Curie–Weiss law, strongly suggests the presence of spin fluctuations.

5.2 Absolute Calorimetry Results

The complete sets of absolute calorimetry data for the fifteen different $a-Fe_xZr_{100-x}$ samples studied are tabulated in the appendices. Fig. 5.5 shows measurements of the molar specific heat, $C_P(T)$, for several of our $a-Fe_xZr_{100-x}$ samples between ~2 K and 7 K, displayed as C_P/T *vs.* T^2. For a normal metal we expect :

$$C_P(T) = \gamma T + \beta T^3, \tag{5.3}$$

$$\text{where : } \gamma = (1+\lambda_{e-p})\gamma_0 \equiv \frac{m^*}{m}\gamma_0,$$

$$\gamma_0 \equiv \frac{1}{3}\pi^2 k_B^2 N_0(\varepsilon_F) = N_0(\varepsilon_F)\left(425\frac{\text{mole K}^2}{\text{eV J atom}}\right)^{-1}, \tag{5.4}$$

$$\text{and : } \beta = \frac{(1.944\times 10^6 \text{ mJ/mole K})}{\Theta_D^3}.$$

The electron mass enhancement factor, λ_{e-p}, arises through the electron–phonon interaction and βT^3 is the standard low temperature limiting form of the specific heat due to phonons. Approximating the Debye function by βT^3 is accurate to better than 1% at temperatures below $\Theta_D/20$, where Θ_D is the *Debye temperature* which characterizes the phonon energy spectrum. Since Θ_D~200 K for $a-Fe_xZr_{100-x}$ [65,66], we would expect all of the data sets in Fig 5.5 to follow straight lines with slopes β and $T^2 = 0$ intercept $\gamma \equiv \lim_{T\to 0}(C_P/T)$.

We can see immediately that while the data for the most Fe rich (x =39.0%) and Fe poor (x =26.7%) samples roughly follow a straight line, there is a clear *upturn* in the other curves at the lowest temperatures (T^2<10 K^2). These *upturns* grow slowly as the Fe content increases from x~32% and then quickly disappear by x=39.0% Fe. Since the upturns are most prominent in samples with Fe contents right near the critical composition (x_c ~37%), they must be related, somehow, to the magnetic ordering. *We attribute these upturns to an electron mass enhancement arising due to spin fluctuations (SF).*

As discussed in Chapter 2, the expression for the specific heat of an itinerant

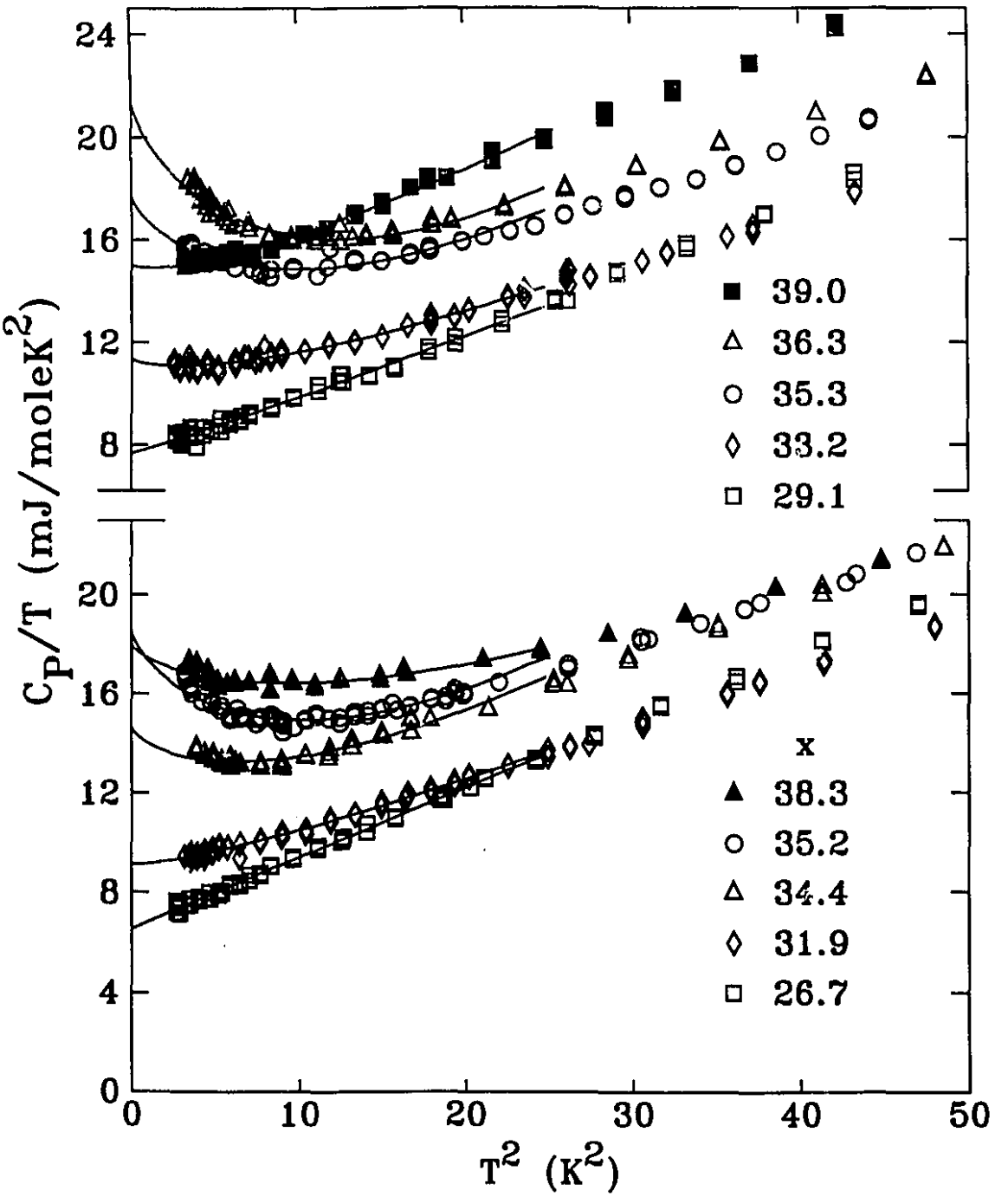

Figure 5.5: Low temperature specific heat of various a–Fe_xZr_{100-x} samples. Samples with Fe concentrations greater than the critical concentration (~37%) are displayed as filled symbols. The solid line are fits to the equation 5.7 below $T = 5$ K. For clarity, samples with adjacent Fe contents have been plotted alternately in the top and bottom regions.

electron magnet in the presence of *SF* is:

$$C_P(T) = \gamma T + \beta T^3 + DT^3 \ln\left(\frac{T}{T_{SF}}\right) \quad T << T_{SF} \tag{5.5}$$

$$\text{where : } \frac{\gamma}{\gamma_0} \equiv \frac{m^*}{m} \equiv (1 + \lambda_{e-p} + \lambda_{SF}).$$

The first two terms of equation 5.5 are just the normal expression (equation 5.3). Predictions for γ include an electron mass enhancement factor due to spin fluctuations, λ_{SF}, as well as the normal electron–phonon enhancement, λ_{e-p}. The third term has the temperature dependence which is the signature of *SF*. It valid only at temperatures far below T_{SF}, where it is *negative*. As $T \rightarrow 0$, the function $T^3 \ln T \rightarrow 0$ faster than T, so that it vanishes at $T = 0$. Consequently, γ can still be identified with $\lim_{T\rightarrow 0}(C_P/T)$.

We have argued in Chapter 2 that equation 5.5 describes a temperature dependant electron mass enhancement factor, $\Lambda_{SF}(T) \equiv C_P^{SF}(T)/\gamma_0 T$, which we now write as:

$$\Lambda_{SF}(T) = \lambda_{SF} + \frac{D}{\gamma_0} T^2 \ln\left(\frac{T}{T_{SF}}\right) \text{ for } T \ll T_{SF}. \tag{5.6}$$

The second term of this relation vanishes at $T = 0$, where $d(T^2 \ln T)/d(T^2)$ has a negative divergence. With rising temperature, $\Lambda_{SF}(T)$ decreases to a negative minimum at $T = T_{SF}/\sqrt{e} \sim 0.6T_{SF}$. At temperatures above $0.6T_{SF}$, the second term increases to zero at T_{SF} and then diverges rapidly for $T>T_{SF}$.

The physical reason for the decrease of $\Lambda_{SF}(T)$ is that, as discussed in Chapter 2, the *SF* quasi–dispersion curve can be thought of as being truncated at an energy $2T_{SF}$ (Fig. 2.6). At $T = 0$, there is a mass enhancement due to *SF* ($\Lambda_{SF}(0) = \lambda_{SF}$). At temperatures $T \gg T_{SF}$, electron excitations have a mean energy ($k_B T$) at which there is effectively no *SF* dispersion curve, and, therefore, no *SF* mass enhancement ($\Lambda_{SF} = 0$). In view of this, we argue that the *SF* electron mass enhancement, $\Lambda_{SF}(T)$, must decrease monotonically to zero with increasing temperature ($d\Lambda_{SF}(T)/dT<0 \ \forall T$). The monotonic decrease of $\Lambda_{SF}(T)$ has been confirmed by numerical integration of an exact expression [30] for the *SF* $C_P(T)$ of $Ni_{3+x}Al_{1-x}$. This calculation determined values of $\Lambda_{SF}(T)$ which always decreased with temperature [122].

Equation 5.5, therefore, becomes completely unphysical for $T>0.6T_{SF}$, where it predicts that $\lambda_{SF}(T)$ increases with temperature, eventually diverging. Fitting the expression to data at too high temperatures will therefore force the fitted value of T_{SF} to high values, so that the $T^3 \ln(T/T_{SF})$ term does not get too big. We have therefore imposed the constraint on our fitting that *equation 5.5 has only been applied to $C_P(T)$ data at temperatures, $T<0.6T_{SF}$.*

For many systems, such as Pd ($T_{SF}\approx$250 K) [48], T_{SF} is so large that the $T^3 \ln T/T_{SF}$ term is negligible at low temperatures and only λ_{SF} is observed. In most other systems [2], T_{SF} is large enough that the low temperature data, where the electron C_P is observable, is all below $0.6T_{SF}$. Preliminary fits to our data, however, gave values of T_{SF} around 8 K, so that *in all of our analysis, the $T^3 \ln T$ term has only been applied to $C_P(T)$ data at temperatures below 5 K.*

The logarithm term in equation 5.5 can be split in two. The part from the denominator is proportional to T^3 and is therefore *indistinguishable* from the phonon term. Equation 5.5 has therefore been more conveniently written as:

$$C_P(T) = \gamma T + BT^3 + DT^3 \ln T, \tag{5.7}$$

$$\text{where : B} = \beta - D\ln(T_{SF}). \tag{5.8}$$

Fits of equation 5.7 to $C_P(T)$ of all samples have been performed for $T<5$K, using a non–linear χ^2 minimization routine, which determines optimum values of the parameters and estimates of their uncertainties. These fits are displayed as the solid lines in Fig. 5.5, where they are seen to give a good description of the data.

5.2.1 Phonons and T_{SF}

Before continuing with the analysis of the spin fluctuation model, we deal with the phonon $C_P(T)$, which is straightforward. In Fig. 5.6, it may be observed that the $C_P(T)$ data from *all* our a–Fe_xZr_{100-x} samples at high temperatures (between 7 K and 10 K) may be well fitted by equation 5.3, which describes normal metallic

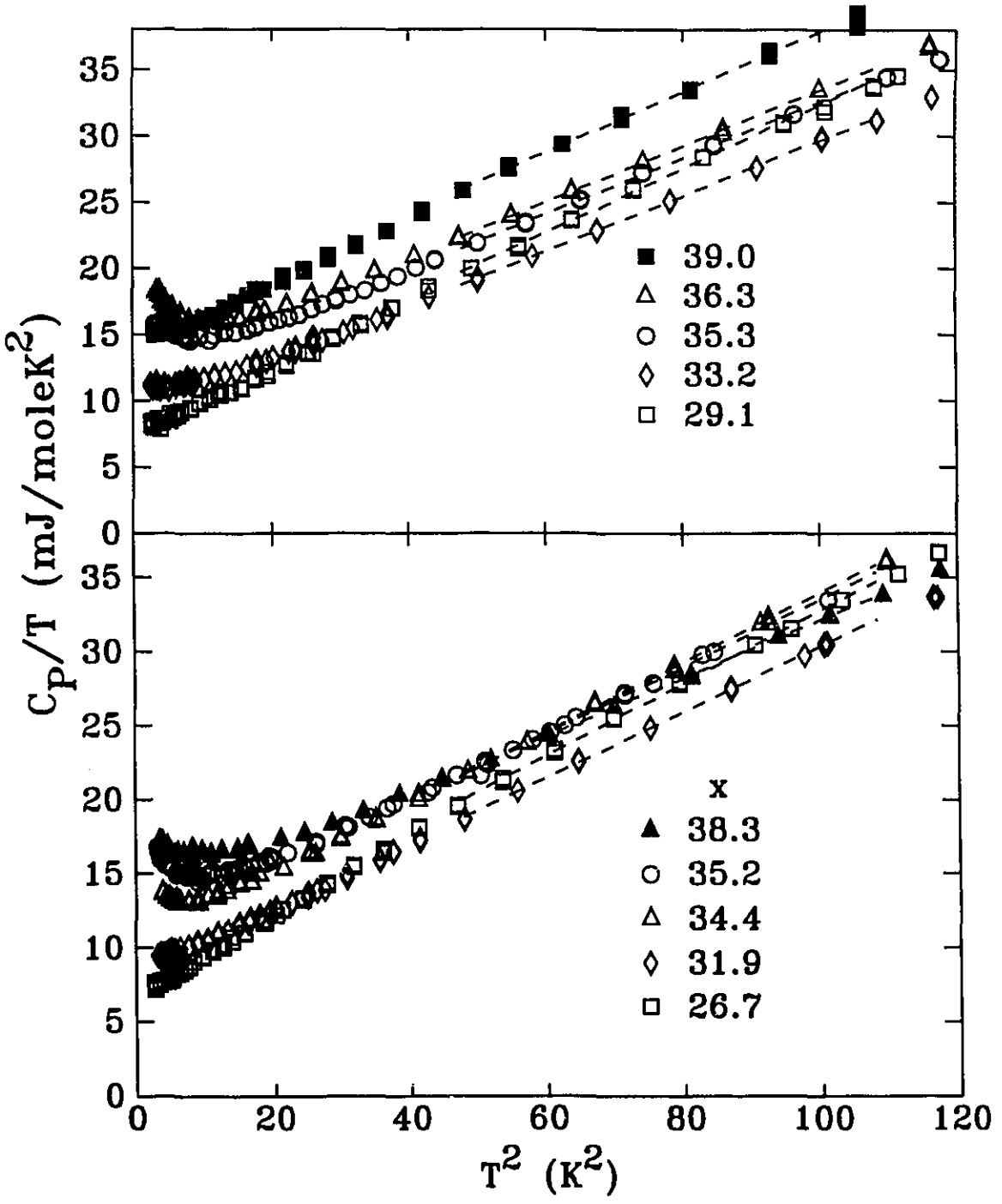

Figure 5.6: Higher temperature specific heat of various a–Fe_xZr_{100-x} samples. Samples with Fe concentrations greater than the critical concentration (~37%) are displayed as filled symbols. The dashed line are fits to the equation 5.3 between $T = 7$ K and $T = 10$ K. For clarity, samples with adjacent Fe contents have been plotted alternately in the top and bottom regions.

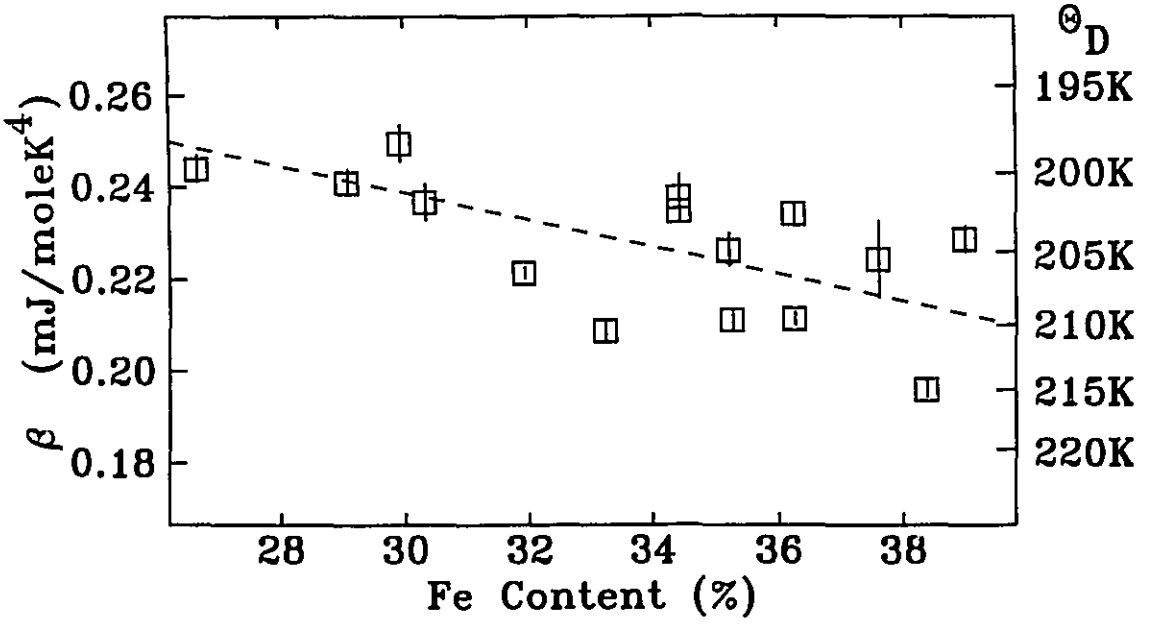

Figure 5.7: Phonon Specific Heat coefficient, β, of a–Fe_xZr_{100-x} derived from fits of $C_P(T)$ to equation 5.3 between 7 K and 10 K. The right hand axis shows corresponding values of Θ_D. The dashed line is a guide to the eye.

behaviour at temperatures $T<\Theta_D/20$. Since $\Theta_D \approx 200$ K [65,66], this condition is satisfied below 10 K. Observation of normal behaviour in all of the samples suggests that the *SF* contribution to $C_P(T)$ is negligible in this temperature range. We have therefore taken the values of β from these fits between 7 K and 10 K as determining the phonon $C_P(T)$ for all temperatures below 10 K. These β values are displayed in Fig. 5.7.

The large scatter in the data arise because the phonon C_P is of the same order as the electron C_P in this temperature range. Both of these contributions are $\sim \frac{1}{2}$ the C_P of the addenda, which is also measured and subtracted off. Also, variations in the ~5mg of silver paste used to mount the sample add to the scatter. The scatter corresponds to roughly 2mg of silver paste. The phonon $C_P(T)$ is, however, seen to be well behaved in concentration, with no unusual features at the critical concentration of 37%Fe. The Debye temperature is determined to be roughly 200 K and increases slightly with increasing Fe content, in agreement with refs [65,66]. We did not observe the divergence in Θ_D reported by another group [67]. If a normal fit is performed at temperatures above 15 K, the fitted value of β begins to decrease slightly. This

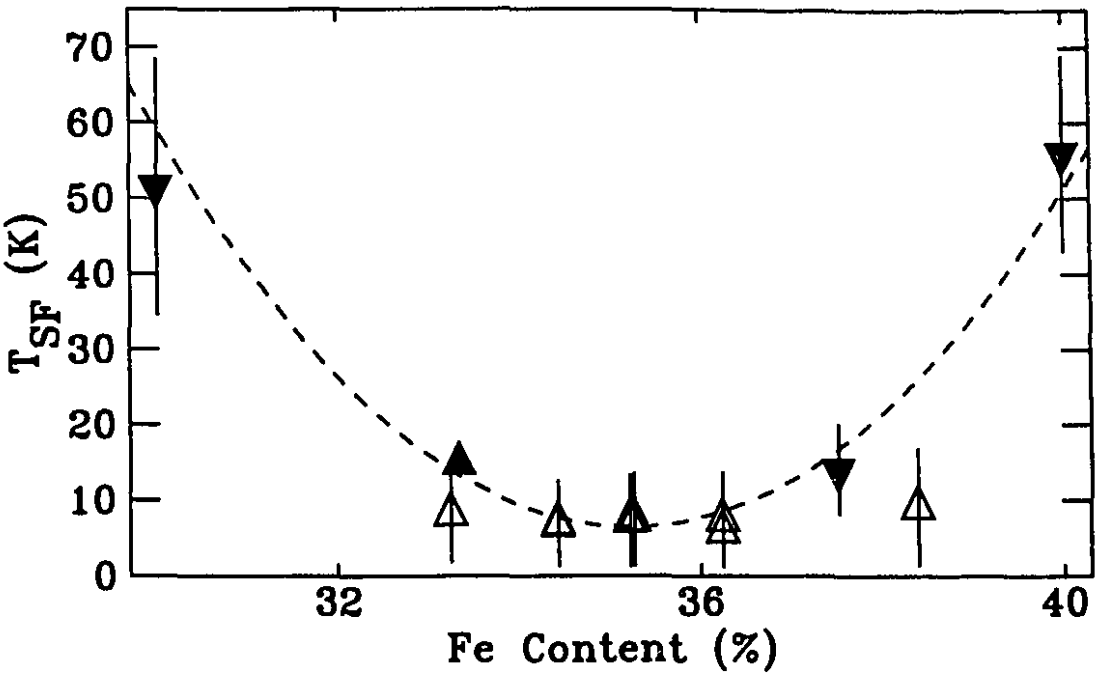

Figure 5.8: Spin fluctuation temperature T_{SF} of a–Fe_xZr_{100-x} (△), determined from the parameters γ, D and β and equation 5.8. Data taken from resistivity studies of ref. [56] (▼) and ref. [53] (▲) are also shown for comparison. The dashed line is a guide to the eye from ref. [56]

decrease is, however, much larger than that predicted by the Debye function. These observations are consistent with previous work on a–Fe_xZr_{100-x} [123], which reported that the effective Debye temperature, $\Theta_D(T)$, increases above 20 K.

In principle, we may now determine T_{SF} from equation 5.8, using the *SF* fitted parameters, γ and D, and the phonon coefficient, β. The uncertainty on all these parameters, particularly β, combine to yeld a very uncertain value of T_{SF}. Furthermore, as discussed, we have liberally interpreted the restriction $T \ll T_{SF}$ as $T<0.6T_{SF}$. Nonetheless, we display these values of T_{SF} in Fig. 5.8, only for the samples which show a clear upturn in their low temperature $C_P(T)/T$. We have also displayed rough values of T_{SF} determined from a resistivity study of a–Fe_xZr_{100-x} [56]. This study identified T_{SF} with the temperature where the resistivity due to *SF* crosses over from a quadratic temperature dependence at low temperatures to a linear dependence at higher temperatures. Altounian et al. [53] have recently done a more detailed determination of T_{SF} through a study of the system a–$(Fe_yNi_{100-y})_{33.3}Zr_{66.7}$. Since Fe and

Ni atoms have virtually the same mass and atomic radius and have similar chemical properties, we may expect that the amorphous structure of this system is simply that of a–$Fe_{33.3}Zr_{66.7}$, with appropriate numbers of Ni atoms randomly replacing Fe atoms. The further assumption that electron–phonon scattering is the same for all metallic glasses of this isostructural system, allowed separation of the resistivity due to *SF* scattering from that due to electron–phonon scattering since for y<40%, the latter process dominates. Applying the complete analysis due to Rivier and Zlatic [51] to the determined *SF* resistivity, the study found $T_{SF} = 15 \pm 1$ K for a–$Fe_{33.3}Zr_{66.7}$, which is also shown in Fig. 5.8.

General agreement occurs between our calorimetrically determined values of T_{SF} and those of the resistivity measurements. We take this agreement between T_{SF} derived from these two very different measurements as support for the *SF* model. From the theory [2], $T_{SF} = T_F/\mathcal{S}$. We would therefore expect T_{SF} to increase sharply from zero as x moves away from $x_c \approx 37\%$, where $\mathcal{S}$ diverges. This behaviour is consistent with the resistivity results. Our values of $T_{SF} \approx 7$ K, however, seem to be almost independent of sample composition. Indeed, a quick look at the data of Fig. 5.5 confirms that all the upturns occur near the same temperature (~3.5 K), so that the energy scale of the phenomena must be of the same order for all the samples. This near sample independence of T_{SF} measured by $C_P(T)$ is probably an artifact of the inadequacy of the theoretical expression (5.5) at all but the lowest temperatures. Further theoretical work describing how $\Lambda_{SF}(T)$ of equation 5.6 decays to zero at high temperatures would be needed to further comment on the value of T_{SF}.

5.2.2 Electronic $C_P(T)$

Since the phonon specific heat, βT^3, of all our samples has been determined. and since we are using the *SF* model, we can take the values $(C_P(T) - \beta T^3)$ as the *electronic* $C_P(T)$, which is displayed in Fig. 5.9. Also shown as horizontal dashed lines are values of γ_{HT}, which we define as the value of γ determined from the high temperature fits to the normal $C_P(T)$ expression (5.3).

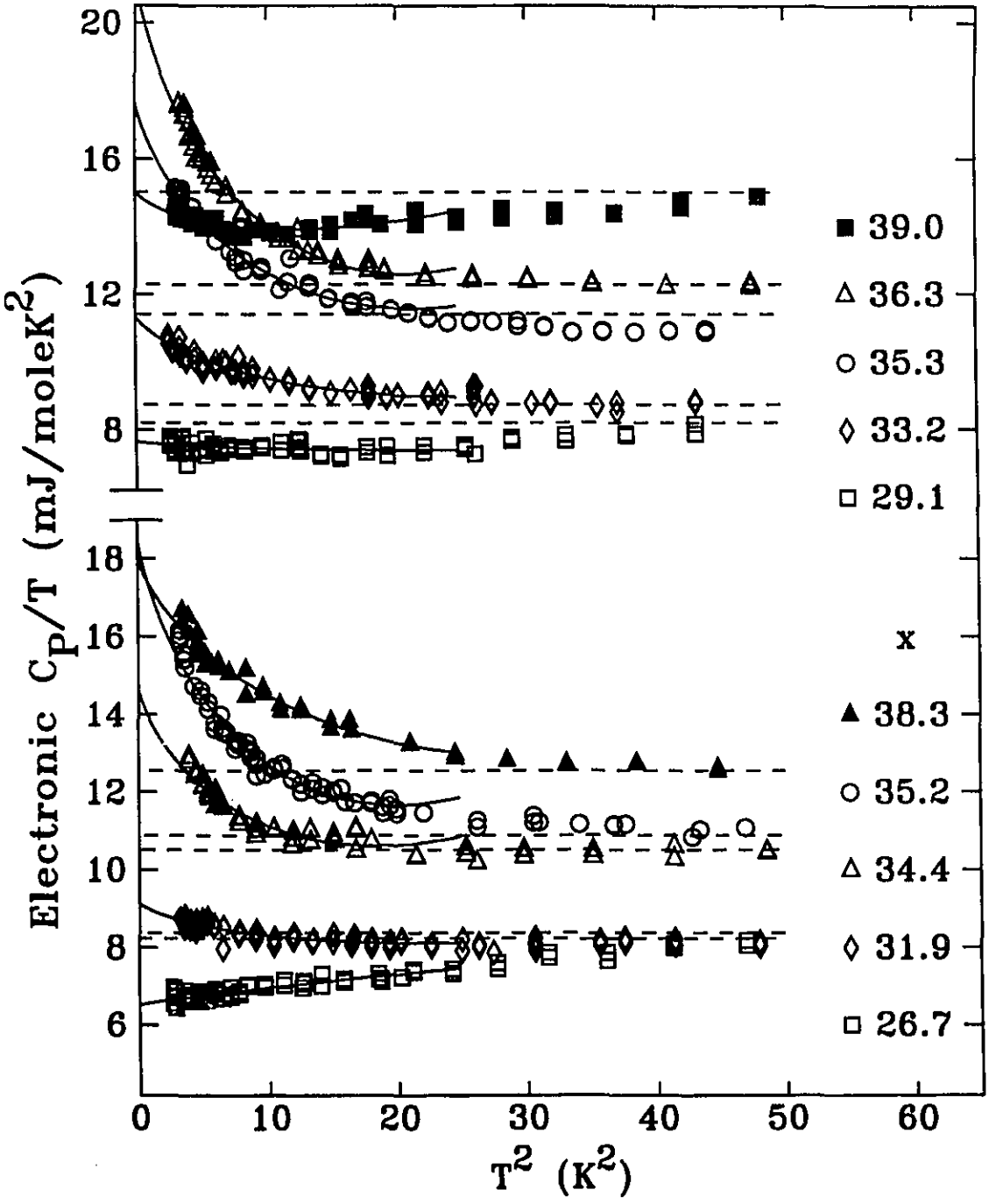

Figure 5.9: Electronic Specific Heat of $a-Fe_xZr_{100-x}$. The purely electronic specific heat has been determined by subtracting the phonon term, βT^3, from $C_P(T)$. Displayed in Fig. 5.7, values of β were determined from fits of the normal expression, $\gamma_{HT}T + \beta T^3$, to $C_P(T)$ between 7 K and 10 K. The dashed lines are the values of γ_{HT}. Samples with Fe concentrations greater than the critical concentration (~37%) are shown with filled symbols and the solid line are fits to the equation 5.7 below $T = 5$ K.

Fig. 5.9 clearly shows the important features of the *SF* signal. As temperature increases from the lowest temperatures, the electronic $C_P(T)/T$ decreases rapidly. At temperatures around 5 K, this decrease has largely disappeared and by 7 K, the linear term attains a value of γ_{HT} which is maintained up to 10 K. The meaning of the three *SF* parameters, γ, D and T_{SF}, becomes clear in Fig. 5.9. The ground state $\gamma \equiv \lim_{[T\to 0 C_P(T)/T]}$ is determined by extrapolating the value of $C_P(T)/T$ to $T = 0$, in our case using equation 5.7 as an extrapolation scheme. D gives a measure of the total change of $C_P(T)/T$ at infinite temperature $(\gamma - \gamma_{HT})$. T_{SF} is a measure of the temperature above which the suppression is complete.

Conveniently, the ordering temperature, T_C, increases rapidly from 0 K to above 100 K on increasing x from 37% to 40%. This means that we can study most ferromagnetic samples at low temperatures without worrying about interference from the magnetic phase transition cusp in $C_P(T)$ which occurs at T_C. This is actually a problem in weakly ferromagnetic Sc_3In, where the $C_P(T)$ cusp occurs in the same low temperature range as the *SF* mass enhancement [2]. A magnetic $C_P(T)$ cusp was observed, in fact, for a sample with $x = 37.6\%$ that was taken from the same batch on which the magnetometry measurements were done [64]. Fig. 5.10 shows $C_P(T)$ of $a{-}Fe_{37.6}Zr_{62.4}$ in which a small bump is clearly visible around 4 K.

In order to separate the low temperature spin fluctuation $C_P(T)$ from the magnetic ordering cusp, we have constructed a composite function $F(T)$. This function is defined as:

$$\begin{aligned} F(T) &= \gamma T + \beta T^3 + DT^3 \ln\left(\frac{T}{T_{SF}}\right) \quad \text{for : T} < \frac{\text{T}_{\text{SF}}}{\sqrt{\text{e}}} \\ F(T) &= \gamma T + \beta T^3 - \frac{DT_{SF}^2}{2e} T \quad \text{for : T} > \frac{\text{T}_{\text{SF}}}{\sqrt{\text{e}}}. \end{aligned} \tag{5.9}$$

While it distorts the fitted value of T_{SF} and likely the other parameters, $F(T)$ has the advantage that it is a smooth function which can be used to fit an entire $C_P(T)$ data set for a given sample below 10 K. Data at temperatures within 1 K of the transition at 4 K were dropped and the rest of the $a{-}Fe_{37.6}Zr_{62.4}$ data set was fitted to $F(T)$.

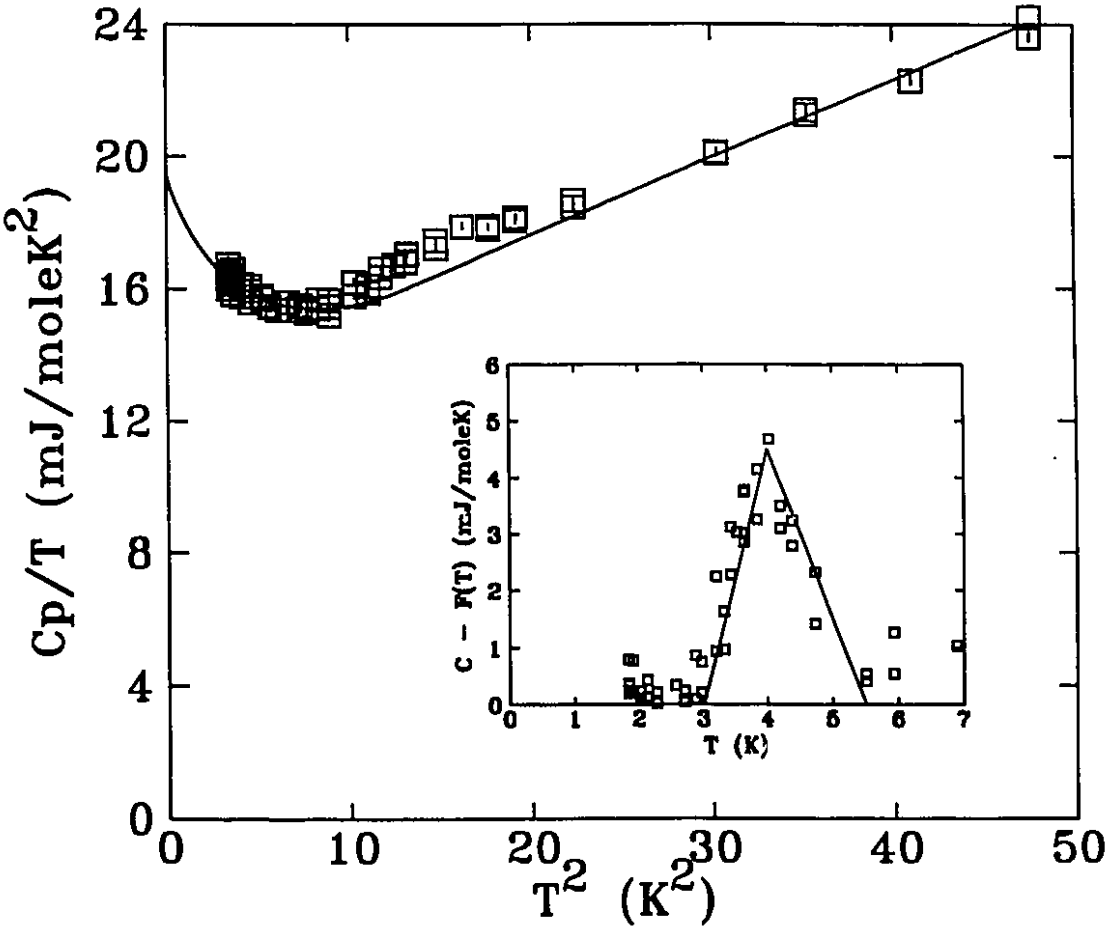

Figure 5.10: Specific Heat of a–$Fe_{37.6}Zr_{62.4}$. The solid line are fits to the function $F(T)$, discussed in the text. The inset shows the result of subtracting $F(T)$ from $C_P(T)$.

The fit, displayed in Fig. 5.10, allowed values of γ and D to be determined for this sample.

The inset to Fig. 5.10 shows the magnetic ordering cusp in $C_P(T)$ determined by subtracting $F(T)$, from the $C_P(T)$ data. The total entropy under this curve is equal to the entropy difference between the $T = 0$ weakly ordered state and the totally disordered state at $T = \infty$, that is:

$$\Delta S = \int_0^\infty \frac{C_P(T)dT}{T} \approx 1.4 \text{ mJ/mole K}.$$

If $\zeta \equiv (n_\downarrow - n_\uparrow)/N$ is the relative magnetization, then we can write the entropy of a system of N electrons, divided into $n_\uparrow \equiv N/2(1-\zeta)$ and $n_\downarrow \equiv N/2(1+\zeta)$ as:

$$S = k_B \ln\left(\frac{N!}{n_\uparrow! n_\downarrow!}\right) \approx k_B \left[N \ln N - n_\uparrow \ln n_\uparrow - n_\downarrow \ln n_\downarrow\right]$$

$$\begin{aligned} S &= Nk_B\left[\ln 2 - \frac{1}{2}(1+\zeta)\ln(1+\zeta) - \frac{1}{2}(1-\zeta)\ln(1-\zeta)\right] \\ &\approx Nk_B\left[\ln 2 - \zeta^2\right] \quad \text{if the relative magnetization, } \zeta \ll 1. \end{aligned}$$

The entropy of the magnet at infinite temperature is $Nk_B \ln 2$, so that the entropy change, $\Delta S = S_{T=\infty} - S_{T=0} \approx Nk_B\zeta_0^2$. Assuming that the saturation moment is that of a–$Fe_{90}Zr_{10}$ ($p_{max} \approx 1.5\mu_B$), we can estimate the ordered moment, p_s, of this sample to be:

$$\begin{aligned} \zeta_0 &= \sqrt{\frac{1.4 \text{ mJ/mole K}}{8.314 \text{ J/mole K}}} = 0.013, \\ \text{so that : } p_s &= p_{max}\zeta_0 = 0.02\mu_B. \end{aligned}$$

This value, $p_s = 0.02\mu_B$, together with T_C of 4 K, is shown in Fig. 5.3.

5.2.3 Spin Fluctuation Parameters

Values of γ and D, derived from fits of equation 5.7 to the $C_P(T)$ data below 5 K, are displayed in Fig. 5.11. The parameters for a–$Fe_{37.6}Zr_{62.4}$ were derived using a modified composite function (equation 5.9), as discussed in the previous section. Also shown are values of γ_{HT} from fits of equation 5.3 to $C_P(T)$ in the range 7 K$<T<$10 K. From this figure, we can see that both γ and D rise to a maximum right at the critical concentration, x_c, determined to be 36.8% from the extrapolation of the γ curves above and below x_c. This is near conclusive evidence that the upturn in $C_P(T)/T$ is magnetic in origin.

We interpret these results to mean that at very low iron concentrations, $C_P(T)$ has no enhancement due to SF, ($\lambda_{SF} = D = 0$) and $C_P(T)$ obeys the normal expression(5.3). As the Fe content is increased, we see the influence of SF on the effective electron mass as an increase in D and λ_{SF} (or γ). These parameters reach a maximum at the critical concentration and then die out with further increase in Fe content as the magnetism becomes firmly established. Qualitatively, this is just what

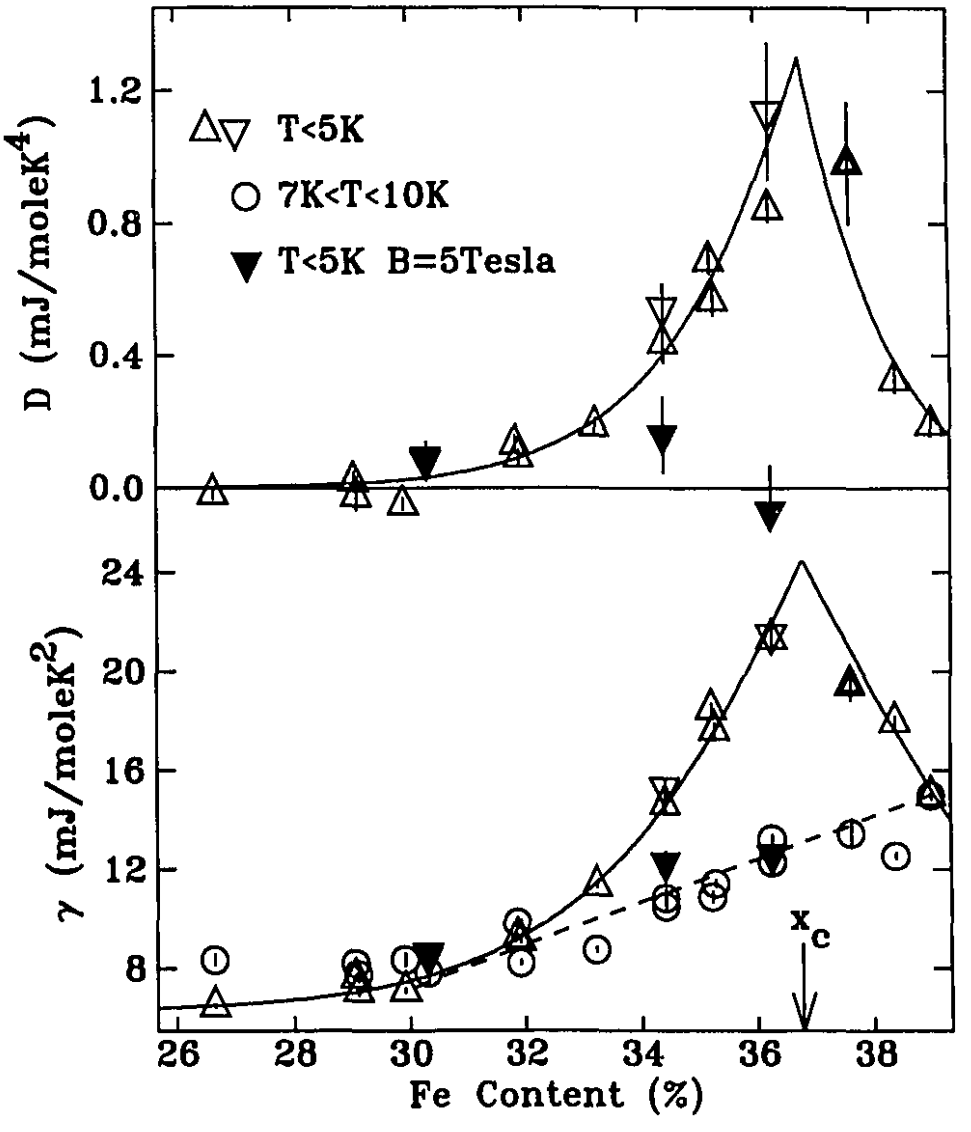

Figure 5.11: Specific Heat: Spin Fluctuation Parameters. The parameters γ and D ($\triangle$, $\triangledown$) derived from fits of the data to equation 5.7 are displayed. Also shown are values of γ_{HT} from normal fits to $C_P(T)$ in the range 7 K<T<10 K(○), as well as parameter values measured when the sample was in a magnetic field of 5 Tesla (filled symbols). Downward pointing triangles refer to measurements taken during magnetocalorimetry runs. The solid and dashed lines are guides to the eye.

is expected from the *SF* model. The absolute value of $S(x)$ has a positive divergence at $x = x_c$, and then monotonically decreases as x moves away from x_c. Since theoretical expressions for both D and γ increase monotonically with S (equations 2.49, 5.10), *SF* theory predicts uniform increases in both D and γ as $x \rightarrow x_c$ from above or below. This is exactly what is observed. The results shown in Fig. 5.11 are very similar to those obtained for $Ni_{3+x}Al_{1-x}$ [2,42], another proposed spin fluctuator (Fig. 2.7).

Also evident in Fig. 5.11, is that the high temperature linear coefficient of $C_P(T)$, γ_{HT}, shows no structure at x_c and simply increases monotonically with x, becoming equal to γ for samples with $x<32\%$ and $x = 39.0\%$. This arises because for $T>T_{SF}\approx 7$ K, electronic excitations have energies $\sim k_B T$, where the *SF* quasi–dispersion curve effectively disappears (Fig 2.6). For these electrons, then, there is effectively no quasi–dispersion curve and therefore no mass enhancement factor due to *SF*. The complete disappearance of the *SF* enhancement in $a-Fe_xZr_{100-x}$ is observable *solely due to its low* T_{SF}. The enhancement vanishes in a temperature range where the electronic $C_P(T)$ is still a significant fraction of the total $C_P(T)$. In a system with higher T_{SF}, the electronic $C_P(T)$ would be only a small fraction of the total by the time the *SF* enhancement reduced to zero. Because of the good normal fits to the data in the temperature range 7 K$<T<$10 K, we can believe that this is *the first observation of the complete reduction of the effective electron mass* m^* *from its low temperature SF+phonon enhanced value to its high temperature normal phonon enhanced value.* We can also see from Fig. 5.11 that in a 5 Tesla magnetic field, $\gamma \rightarrow \gamma_{HT}$ for the $a-Fe_{36.3}Zr_{63.7}$ sample, a result that will be discussed later.

We now assume that γ_{HT} contains no contribution from *SF* and is simply given by the normal expression (5.3). This will allow us to determine the *bare electron density of states at the Fermi level,* $N_0(\varepsilon_F)$. This value, together with the previously determined values of the ground state susceptibility, $\chi(T = 0)$, will permit a determination of the Stoner enhancement factor, S, which can then be used to make a numerical comparison between *SF* theory and our experimental results.

Onn et. al. [66] have determined the electron–phonon mass enhancement fac-

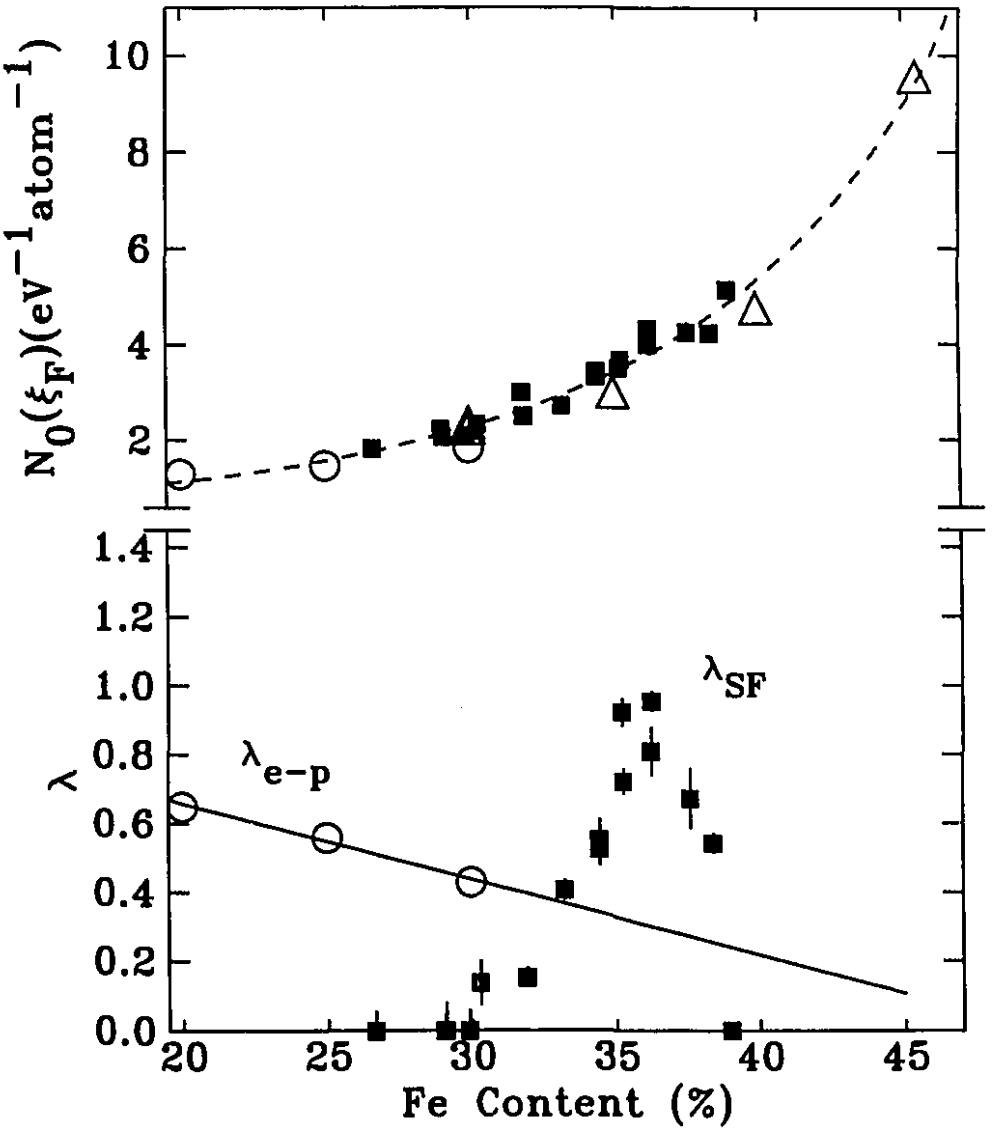

Figure 5.12: Electron Density of states, $N_0(\varepsilon_F)$. Determinations of (○)λ_{e-p} from ref. [66] are shown together with our linear extrapolation (solid line). The filled symbols are our values of λ_{SF} and $N_0(\varepsilon_F)$ whose determination is discussed in the text. Values of $N_0(\varepsilon_F)$ determined in ref. [66](○) are shown along with $N_0(\varepsilon_F)$ similarly derived from the γ given in ref [67] for melt-spun ribbons and thin sputtered films of a–Fe_xZr_{100-x} (△). The dashed line is a guide to the eye.

tor for superconducting samples (x<30% Fe) by using the McMillan equation. This equation relates the superconducting transition temperature and λ_{e-p} which must increase together since superconductivity usually results from a strong electron–phonon interaction. We have linearly extrapolated the λ_{e-p} values of Onn et. al. [65,66] to higher Fe contents, as shown in Fig. 5.12, to get a crude estimate of $\lambda_{e-p}(x)$.

We have determined $N_0(\varepsilon_F)$ and λ_{SF} from the relations:

$$\gamma_{HT} = \frac{1}{3}\pi^2 k_B^2 N_0(\varepsilon_F)(1+\lambda_{e-p}) = (425\frac{\text{mole K}^2}{\text{eV J atom}})^{-1} N_0(\varepsilon_F)(1+\lambda_{e-p})$$

$$\gamma = (425\frac{\text{mole K}^2}{\text{eV J atom}})^{-1} N_0(\varepsilon_F)(1+\lambda_{e-p}+\lambda_{SF})$$

These values are shown in Fig. 5.12, along with values of $N_0(\varepsilon_F)$ given by a previous $C_P(T)$ study of a–Fe_xZr_{100-x} [66]. Values of γ from another $C_P(T)$ study [67] of melt–spun ribbons and amorphous sputtered samples of a–Fe_xZr_{100-x}, made at compositions inaccessible by melt–spinning, were also considered. These values were analyzed in the same way as our γ_{HT} values to yield another set of $N_0(\varepsilon_F)$ values which are also displayed.

There is very good agreement between our $N_0(\varepsilon_F)$ values and those of the other studies. Further, these studies were done on samples richer and poorer in Fe than ours and bracket our data nicely, confirming the monotonic rise of $N_0(\varepsilon_F)$ with x. These results give us great confidence in our identification of γ_{HT} as the normal non–magnetic electron–phonon enhanced γ. The values of λ_{SF} are seen to show a peak at x_c where the value reaches a maximum of 1. The values of $T_{SF}\approx$7 K and of λ_{SF}<1 are similar to those for $Ni_{3+x}Al_{1-x}$, so that a–Fe_xZr_{100-x} can probably be classified as the same type of spin fluctuator [2].

Now that we have $N_0(\varepsilon_F)$, we can determine the Stoner enhancement factor, $\mathcal{S}$, from:

$$\chi(T=0) = \mathcal{S}\mu_B^2 N_0(\varepsilon_F).$$

Taking $\chi^{-1}(T=0) = (27600\ \text{gm/cm}^3)(36.8\% - x)/100\%$ which is the straight line displayed in Fig. 5.3, and using $\mu_B^2 = 32.32\times10^{-6}\text{cm}^3\,\text{eV atom/mole}$, we have calcu-

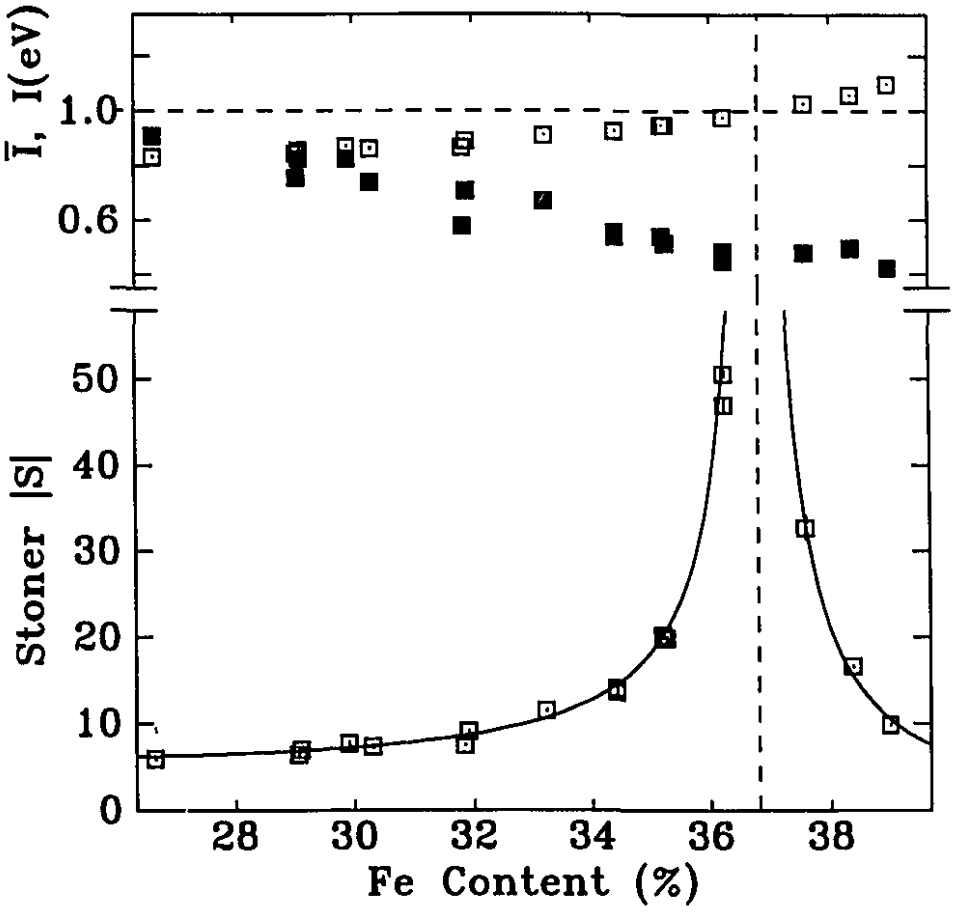

Figure 5.13: Absolute value of Stoner enhancement factor, S, of a–Fe_xZr_{100-x}. Displayed in the upper portion are determined values of $\overline{I}$(□) and the interaction energy I in eV (filled symbols). The vertical dashed line is drawn through the critical composition $x_c \approx 37\%$. The solid line is a guide to the eye.

lated S values for all of our paramagnetic samples which are displayed in Fig. 5.13. We have continued this scheme to obtain values for S in the ferromagnetic samples. S is negative for $x > x_c$ and $\mid S \mid$ values are also displayed in Fig. 5.13. This extrapolation is appropriate in the Stoner model and amounts to assuming a linear variation of $\overline{I}$ in x about x_c. Also shown are values of $\overline{I}$, obtained from $S^{-1} \equiv 1 - \overline{I}$, and the interaction energy I from $\overline{I} \equiv \frac{1}{2} I N_0(\epsilon_F)$.

Fig. 5.12 shows that a–Fe_xZr_{100-x} is indeed a strongly exchange enhanced paramagnet for $x < 37\%$ Fe, with a Stoner factor rising to $S \approx 50$ for our most extreme sample. Even samples with less than 30% Fe still show values of $S > 5$. The figure also suggests that the interaction energy I actually *decreases* with x and that the

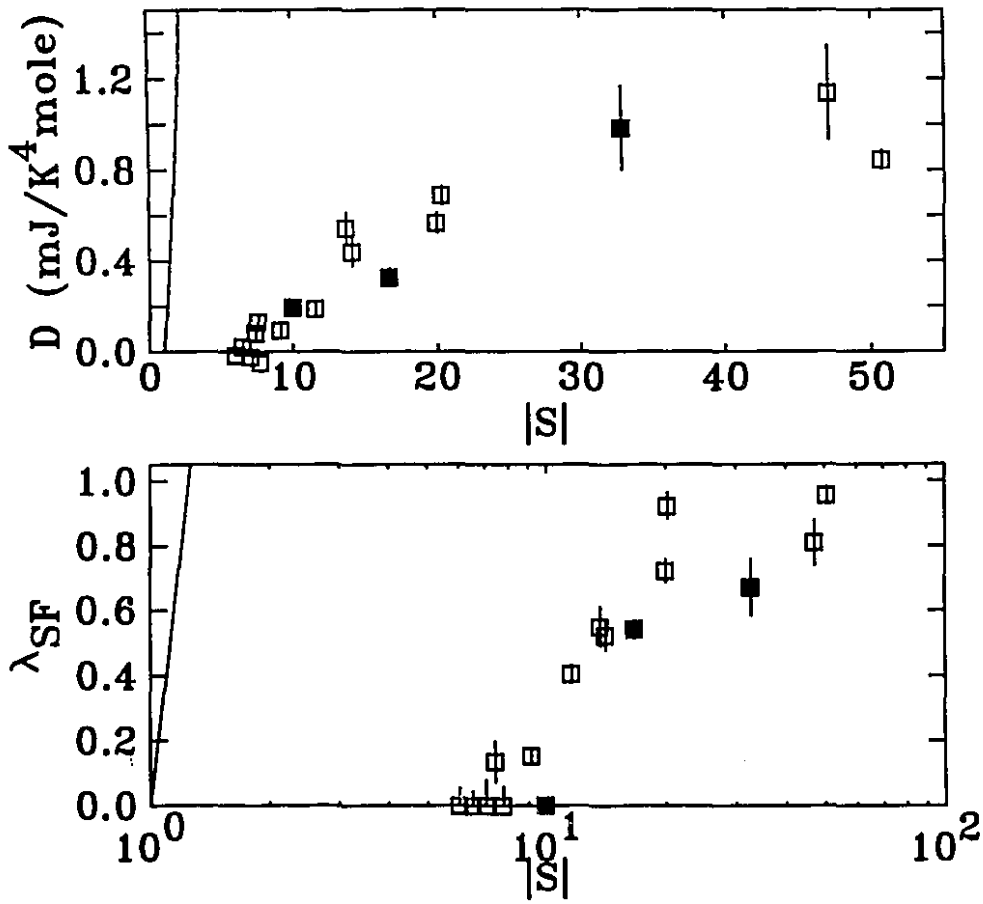

Figure 5.14: Absolute predictions for spin fluctuation parameters. The values of λ_{SF} and D are plotted against $\mathcal{S}$ for all our a–Fe_xZr_{100-x} samples. Ferromagnetic samples are denoted by filled symbols. The solid line are the predictions of equations 5.10.

ferromagnetism develops in spite of this, driven by the strong increase of $N_0(\varepsilon_F)$ with x.

We are now in a position position to test the predictions of SF theory regarding the absolute magnitude of the C_P enhancement. These relations are:

$$\begin{aligned} D &= \frac{6\pi^2}{5}\frac{(|\mathcal{S}|-1)^2}{T_{SF}^2|\mathcal{S}|}\gamma_0 \\ \lambda_{SF} &= \frac{9}{2}\ln|\mathcal{S}|. \end{aligned} \tag{5.10}$$

The values of λ_{SF} and D are appropriately plotted against $\mathcal{S}$ in Fig. 5.14. The theoretical predictions for D were made using the values of T_{SF}= 7 K and γ_0 =

9mJ/mole K^2. Predictions for λ_{SF} and D are found to be too high by factors of 10 and 100 respectively compared to the data, as shown in the figure. Gross overestimation of the parameters by the theory has been observed before, if not always explicitly pointed out [2,40–42]. As plotted, both the predictions and the fitted parameter values are roughly linear, suggesting that the theory is at least consistent with the dependence of the parameters on $\mathcal{S}$. Other predictions for λ_{SF} do exist [57,60] but have not been considered here.

5.2.4 Summary

The results of the calorimetry study were that upturns in $C_P(T)/T$ of $a-Fe_xZr_{100-x}$ were observed at temperatures below 4 K. These upturns were most pronounced in samples near the critical composition for ferromagnetism, $x_c \approx 37\%$. This feature disappears if the low temperature data ($T<7$ K) is dropped. For $T>7$ K, $C_P(T)$ follows behaviour typical of a normal metal, with no distinguishable feature at x_c.

The upturns in $C_P(T)/T$ could be described using a model accounting for enhancement of the electron mass due to the presence of spin fluctuations. We stress that we have not verified temperature dependence predicted by this model, which is not even expected to be valid in our temperature range ($T/T_{SF} \geq 25\%$). Of The three parameters of the model; D and λ_{SF} were shown to depend on Fe content according to the trend predicted by *SF* theory. Both show a peak value at the critical concentration of $\sim$37% Fe. T_{SF} was found to be in agreement with values determined from the measured resistivity. Absolute agreement of the parameters with predictions was not achieved.

We have observed, for the first time, the complete disappearance of the electron mass enhancement due to *SF* at temperatures above 7 K. Above 7 K, we observe only the normal electron–phonon enhancement of the electron mass. This observation was only possible because of the low T_{SF} of $a-Fe_xZr_{100-x}$, which leads the *SF* enhancement to vanish at low enough temperatures that the electron $C_P(T)$ is still a sizable fraction of the total $C_P(T)$, and the phonon $C_P(T)$ can still be simply represented by its low

temperature limiting form.

5.3 Magnetocalorimetry Results

Fig. 5.15 summarizes measurements of the electronic $C_P(T)$ for three paramagnetic $a-Fe_xZr_{100-x}$ samples independently determined in various fixed magnetic fields between 0 and 5 Tesla (and tabulated in Appendix B). The data are all displayed on the same axes with no offsets. The electronic $C_P(T)$ was determined, as before, by subtracting off βT^3, where β was obtained from fits of $C_P(T)$ to the normal expression(5.3), between 7 K and 10 K. The high temperature linear coefficient, γ_{HT}, determined from these same fits is also shown.

The magnetocalorimetric behaviour of the three samples is quite different. For the $a-Fe_{30.3}Zr_{69.7}$ sample, which shows no upturn in $C_P(T)$ at $H = 0$, the application of fields up to 5 Tesla has no measurable effect on $C_P(T)$. In the most nearly ferromagnetic sample, $a-Fe_{36.3}Zr_{63.7}$, which shows the biggest upturn at $H = 0$ of any of our samples, the application of a 1 Tesla field has virtually no effect on $C_P(T)$. In contrast, *the application of a 5 Tesla field completely removes the upturn in the electronic* $C_P(T)/T$ *for* $a-Fe_{36.3}Zr_{63.7}$. Furthermore, $C_P(T)/T$ *is reduced to* γ_{HT}, *a continuation of its high temperature,* $H = 0$ *behaviour, extrapolated to lower temperatures.* In $a-Fe_{34.4}Zr_{65.6}$, a sample which shows a modest upturn at $H = 0$, the application of $\mu_0 H = 5$ Tesla has a marked effect on the upturn, *but does not completely suppress it.*

These results can be explained in terms of spin fluctuation theory which expresses the change in $C_P(T)$ in an applied field as a change in the linear coefficient of $C_P(T)$. The linear part of $C_P(T)$, $\gamma(H)$, should decrease in a field, H, as:

$$\frac{\gamma(\mathrm{H}) - \gamma(\mathrm{H} = 0)}{\gamma(\mathrm{H} = 0)} = -0.1 \frac{\mathcal{S}}{\ln \mathcal{S}} \left(\frac{\mu_B \mathrm{H}}{k_B T_{SF}} \right)^2. \tag{5.11}$$

The decrease in γ, referred to as the *quenching* of *SF*, describes how the energy gap, $\mu_B H$, which opens up in the *SF* quasi–dispersion curve decrease the effect of *SF* on the electron mass enhancement, λ_{SF}.

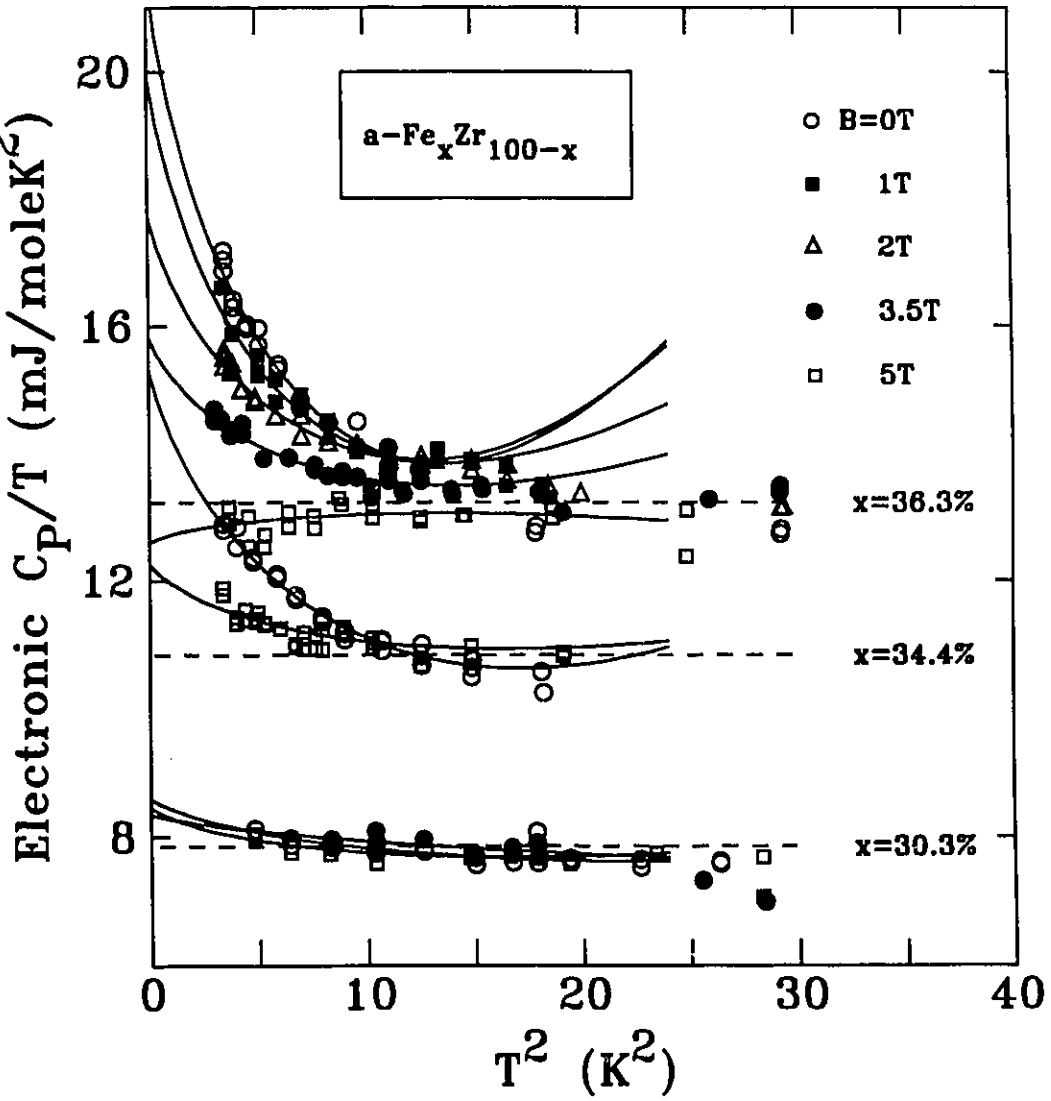

Figure 5.15: Magnetic field dependence of the electronic $C_P(T)$ of three paramagnetic samples; a–$Fe_{36.3}Zr_{63.7}$,a–$Fe_{34.4}Zr_{65.6}$ and a–$Fe_{30.3}Zr_{69.7}$. The solid lines are fits to equation 5.7 below 5 K. The dashed lines are values of γ_{HT}, the high temperature linear coefficient of $C_P(T)$ in zero field.

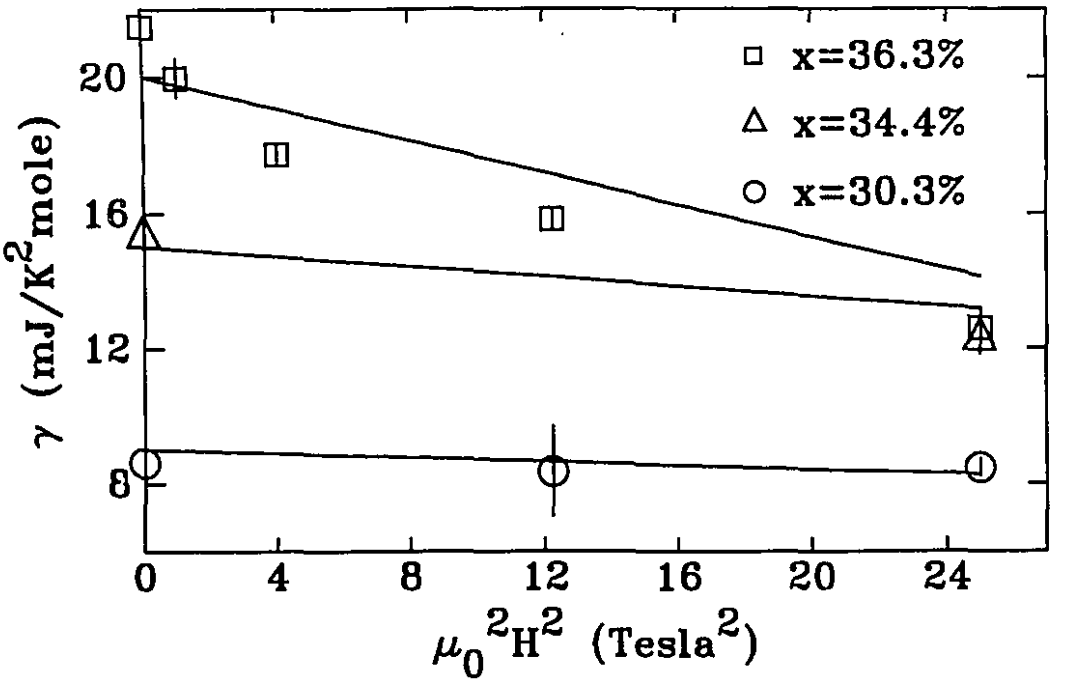

Figure 5.16: Magnetic field dependence of the linear $C_P(T)$ of $a-Fe_xZr_{100-x}$, displayed for the three samples, $a-Fe_{36.3}Zr_{63.7}$,$a-Fe_{34.4}Zr_{65.6}$ and $a-Fe_{30.3}Zr_{69.7}$. The values of γ were determined from the *SF* fits to $C_P(T)$, displayed in Fig. 5.15. The solid lines are determined from the independently calculated values of the quench rates (equation 5.11) and an arbitrary optimum value of $\gamma(H=0)$.

Qualitatively, we can see that equation 5.11 explains our data. For the most Fe rich sample, $a-Fe_{36.3}Zr_{63.7}$, with the largest Stoner factor, $S\approx 50$, the quenching factor is large and *a field of 5 Tesla completely quenches the SF.* The small S of $a-Fe_{30.3}Zr_{69.7}$ leads to a negligible change in γ in 5 Tesla. For the intermediate sample, $a-Fe_{34.4}Zr_{65.6}$, the *SF* are significantly, but not completely, quenched in 5 Tesla, where a small upturn remains and $C_P(T)/T$ is still larger than γ_{HT}.

Fits of the total $C_P(T)$ to the *SF* expression (5.7) at all values of H have been preformed below 5 K, as before. Ikeda et. al. have noted that upon application of a magnetic field, H, to a metal in the presence of *SF* a small cubic term may appear, which vanishes at $H=0$. This term has been observed in some spin fluctuators, but it has been completely ignored here, since the *SF* expression is not strictly valid in our temperature range. The fitted values of γ and D in $H=0$ and $H=5$T have been displayed in Fig 5.11 ($\bigtriangledown$ and filled symbols).

The values of γ determined from the fits are displayed as a function of H^2 for all three samples in Fig. 5.16. The data for $a-Fe_{36.3}Zr_{63.7}$ do not follow the predicted

straight line, however. This is mostly due to the slight difference between $\gamma(H = 0)$ and $\gamma(\mu_0 H = 1T)$. As the $H = 0$ and $\mu_0 H = 1T$ data sets are indistinguishable except for the spacing of the data points, we believe that the difference in the values of γ extracted from these two curves is an artifact of the fitting procedure. Furthermore, because of the scarcity of the field data for $a-Fe_{34.4}Zr_{65.6}$ and $a-Fe_{30.3}Zr_{69.7}$, we cannot establish the functional form of quenching in field.

Table 5.1: Summary of field quenching results. The experimental and theoretical quench rates $(d(\Delta\gamma(H)/\gamma(H = 0))/(dH^2))$ are tabulated. The theoretical quench rate results were calculated from equation 5.11, using $T_{SF} = 7$ K, $\mu_B = 0.672$ K/T and the values of S determined previously from the susceptibility (Fig. 5.13). The experimental quench rates were determined from the slopes of linear fits to the data displayed in Fig. 5.15.

$a-Fe_xZr_{100-x}$ Sample	Stoner S	Experimental Quench rate	Theoretical Quench rate
$a-Fe_{30.3}Zr_{69.7}$	7	$-0.07\%/T^2$	$-0.33\%/T^2$
$a-Fe_{34.4}Zr_{65.6}$	14	$-0.80\%/T^2$	$-0.49\%/T^2$
$a-Fe_{36.3}Zr_{63.7}$	50	$-1.5\%/T^2$	$-1.2\%/T^2$

To calculate the magnitude of the field quenching we have used $T_{SF} = 7$ K, $\mu_B = 0.672$ K/T and the values of S determined previously from the susceptibility (Fig. 5.13). The experimental and theoretical *quench rates*, $d[\Delta\gamma(H)/\gamma(H = 0)]/d[\mu_0 H^2]$, are tabulated in Table 5.1. Choosing an arbitrary value of $\gamma(H = 0)$ which optimizes agreement with the data, we have plotted the predictions for the field quenching of γ and displayed them as solid lines in Fig. 5.15.

The approximate agreement between the measured and independently predicted quench rates is our strongest quantitative evidence that the upturn in the electronic $C_P(T)/T$ arises from spin fluctuations. The field dependence of the electronic $C_P(T)/T$ data for $a-Fe_{36.3}Zr_{63.7}$ comprises the first known observation of the complete quenching of spin fluctuations. These data, coupled with the observation of only partial quenching in $a-Fe_{34.4}Zr_{65.6}$ under similar conditions, are perhaps the most convincing calorimetric evidence for the presence of spin fluctuations in any

metal.

5.4 Alternative Explanations of the Data

If the upturned $C_P(T)/T$ signal is not due to spin fluctuations, then an alternative explanation must account for the observed dependence of the zero field $C_P(T)/T$ upturn on temperature and on Fe composition. It must also fully describe the magnetometry results and do a better job than the *SF* model of relating the zero field calorimetry to the susceptibility. This model must also explain the magnetocalorimetry results, which are in numerical agreement with the predicted quenching of *SF*. The magnetocalorimetry results conclusively establish the magnetic origins of the upturns, so that we may restrict our considerations to magnetic models.

We note in passing that a linear term in $C_P(T)$ arises in the phonon $C_P(T)$ of any structural glass, attributable to the formation of two-level systems. The coefficient of this linear term has a near universal value for all amorphous metallic alloys and is of order 0.1 mJ/mole K [124]. We have ignored this contribution, which is small and is expected to be composition and magnetic field independent.

Enhanced linear $C_P(T)$ values have been observed in systems which exhibit spin glass ordering [123]. These enhancements only occur, however, at temperatures below the spin freezing temperature, T_F. If this is the explanation of the upturns, then the characteristic cusp in the susceptibility at T_F [125] should have been observed by magnetometry. Since no cusps were observed, we rule out the explanation that $a-Fe_xZr_{100-x}$ is a spin glass.

An explanation that is harder to rule out is that the $C_P(T)/T$ upturns occur due to the formation of super–paramagnetic clusters within the samples. The necessity of considering this explanation as an alternative to spin fluctuations has been stressed by other authors [1,41,42].

Super-paramagnetism [126] occurs in solids containing small ($\sim$20Å) ferromagnetic regions or clusters. Such a material is super–paramagnetic at a given temper-

ature, if the thermal energy, k_BT, is larger than the magnetic energy, $\mu_{CLUS}H_{LOC}$. Here, μ_{CLUS} is the total magnetic moment of all the atoms in the cluster, and H_{LOC} is the average local effective magnetic field at the cluster which may arise, for example, from demagnetizing fields due, for example, to particle shape or anisotropic crystal fields. If $\mu_{CLUS}H_{LOC}/k_BT \ll 1$, then the magnetic cluster system may achieve thermal equilibrium and behaves exactly like a paramagnet composed of elementary moments, μ_{CLUS}. As the temperature is lowered below the *blocking temperature*, $T_B \approx \mu_{CLUS}H_{LOC}/k_B$, then the system gets trapped in meta-stable states and can no longer equilibrate in a reasonable time. This is the case for coercive ferromagnets, which have T_B higher than room temperature. These solids manifest hysteresis, which results from long-lived metastable states of fixed orientation of the $\sim 1\mu$m domains. For super-paramagnets, T_B, can be much lower than room temperature.

In order to understand the consequences of super-paramagnetism, consider an isolated atom with total electron angular momentum, J, leading to a magnetic moment, $\mu = g(J,L,S)\mu_B J$. If we apply a magnetic field, H, then we have a system of $N = 2J+1$ levels and we can write down the partition function:

$$\mathcal{Z} = \sum_{j=-J}^{J} e^{-j\Theta_s/T}, \tag{5.12}$$

where the *splitting* between the levels:

$$\Theta_s \equiv \frac{g(J,L,S)\mu_B H}{k_B}.$$

$\mathcal{Z}$ may be summed and appropriately differentiated to yield the magnetization:

$$M(T) = g(J,L,S)\mu_B J B_J(\frac{\Theta_s}{T}) \tag{5.13}$$

$$B_J(u) \equiv \frac{2J+1}{2J}\coth\frac{2J+1}{2J} - \frac{1}{2J}\coth\frac{1}{2J},$$

and the specific heat at constant field,

$$C_H(T) = K_B\left(\mathcal{E}(\frac{\Theta_s}{T}) - \mathcal{E}(\frac{\Theta_s}{NT})\right). \tag{5.14}$$

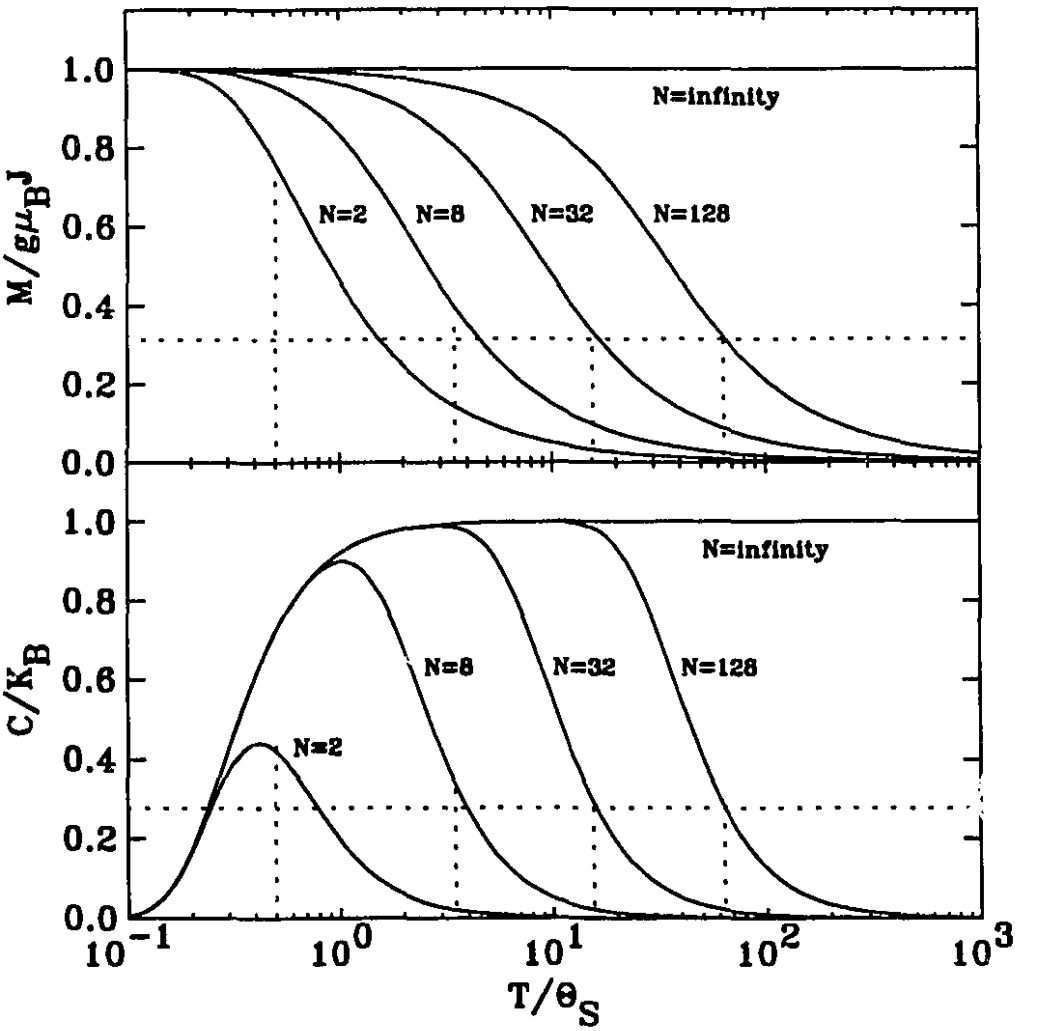

Figure 5.17: Specific heat and magnetization of a paramagnetic atom for various of N (or $J \equiv (N-1)/2$). Vertical dotted lines indicate the values $T/\Theta_s = J$ and horizontal dotted lines indicate the y values expected at T/Θ_s as J goes to infinity.

The Einstein function, $\mathcal{E}(u)$ is given by:

$$\mathcal{E}(u) = \frac{(u/2)^2}{\sinh^2(u/2)}.$$

$C_H(T)$ is simply the temperature derivative of the magnetic energy, $M(T)H$. Equations 5.13 and 5.14 have been plotted against T/Θ_s in Fig. 5.17 for various number of levels $N = 2J + 1$. If we look at the specific heat at high N, we can roughly describe it as a peak with a maximum value of k_B (the Dulong-Petit value for two degrees of freedom) which occurs between the temperatures Θ_S and Θ_S/N. The en-

tropy contained under this peak is $k_B \ln J$. As N goes to infinity, the specific heat is given by a single Einstein function $\mathcal{E}(\Theta_*/T)$. From this figure and the equations we can see that, for a given N (or J) both the specific heat and magnetization of a paramagnet depend only on the ratio H/T. *This is a fundamental defining feature of any paramagnet.*

If we now look at a paramagnetic cluster, things are more complicated than for the isolated atom. First of all, the degeneracy of each $2J+1$ level is no longer necessarily 1. The degeneracy scheme can be modeled, however, by considering the cluster as an appropriate combination of systems with different numbers of *non-degenerate* levels. The specific heat peaks resulting from summing contributions from the different subsystems is generally referred to as a *Schottky peak* [11,36,50]. In a real super-paramagnet, determining the values of the three unknown quantities; the local field, H_{LOC}, the number of levels, N, (or the cluster moment μ) and the actual cluster density is difficult [50], even without the complication of distributions in the values of μ and H_{LOC}. However, we can still rigorously say that M and C_H must only depend on the ratio $\overline{(H+H_{LOC})}/T$, where we have taken an appropriate average sum of the applied and local fields.

We might expect that our upturn signals result from the formation of small super-paramagnetic crystals in our amorphous samples. The most likely candidate for these crystals is Fe_2Zr.

Attempts to collapse the measured magnetization data onto one universal curve for the a–Fe_xZr_{100-x} samples were partially successful only for the a–$Fe_{37.6}Zr_{62.4}$ sample. This is a simple consequence of the fact that it has a low Curie–Weiss temperature, Θ_{CW}, as discussed before, so that it nearly follows a Curie law. The plot of the proposed universal curve is displayed in Fig. 5.18. The data have been fitted to :

$$M = C_1 B_J(C_2 \frac{H}{T})$$

for $J = \frac{1}{2}$ and $J = \infty$. Taking the C_1, C_2 values for $J = \infty$, we get 4×10^{-4} clusters/mole and a cluster moment of $61\mu_B$. We have assumed here that H_{LOC}=0. Since the magnetization is beginning to saturate around 1 Tesla, however, $\mu_0 H_{LOC}$ must

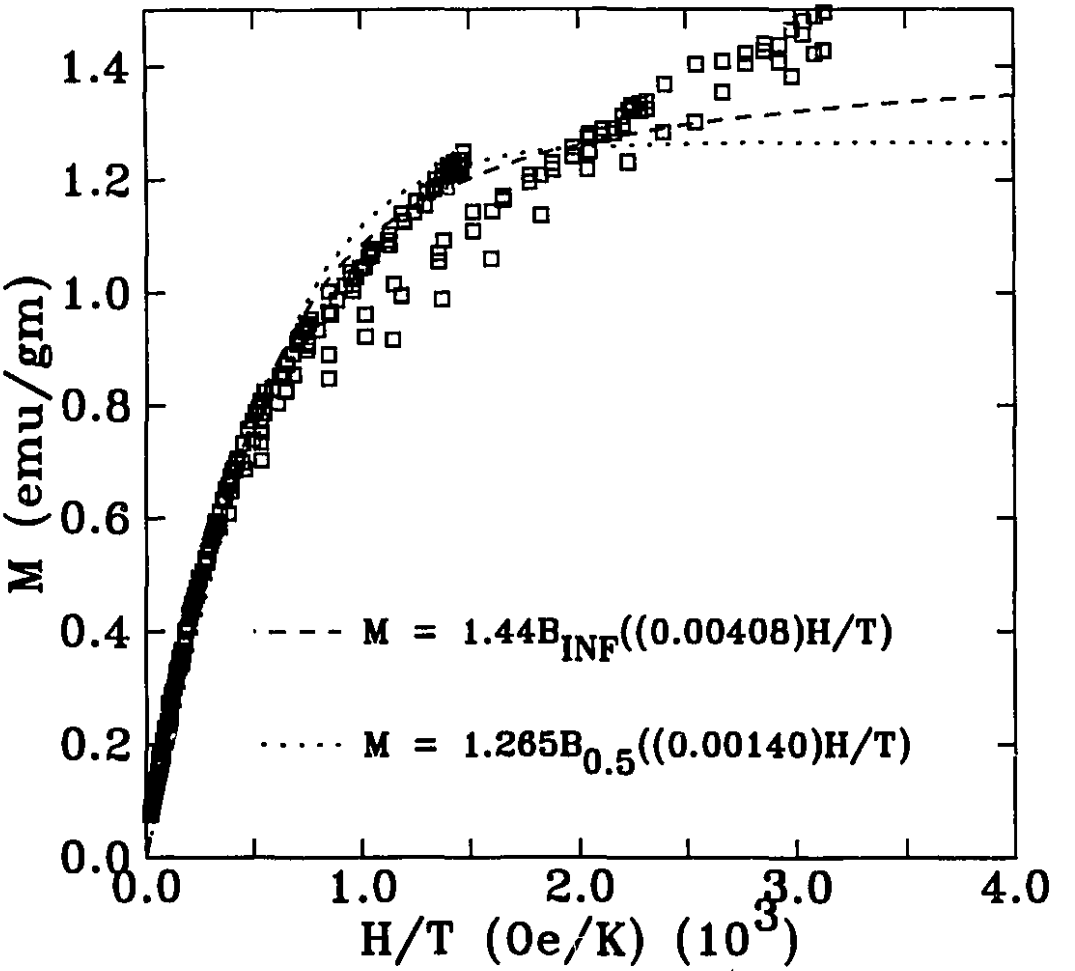

Figure 5.18: Magnetization of a–$Fe_{37.6}Zr_{62.4}$. The solid lines are fits to the Brillouin function $C_1 B_J(C_2 H/T)$ for $J = \frac{1}{2}$ and $J = \frac{1}{2}$. The data below 0.5 Tesla has been dropped.

be much less than 1 Tesla. Overall, universal magnetization curves could not be established for most of the samples. Furthermore, we already established that the susceptibility followed the predictions of Stoner theory. *The magnetometry results, therefore, do not support a super–paramagnetic cluster model.*

In ref. [127], careful consideration was given to the applications of the cluster model to the a–Fe_xZr_{100-x} $C_P(T)$ data. Here, $C_P(T)$ was considered to be a Schottky peak resulting from cluster moments in a non–zero local field, H_{LOC}. Simply approximating

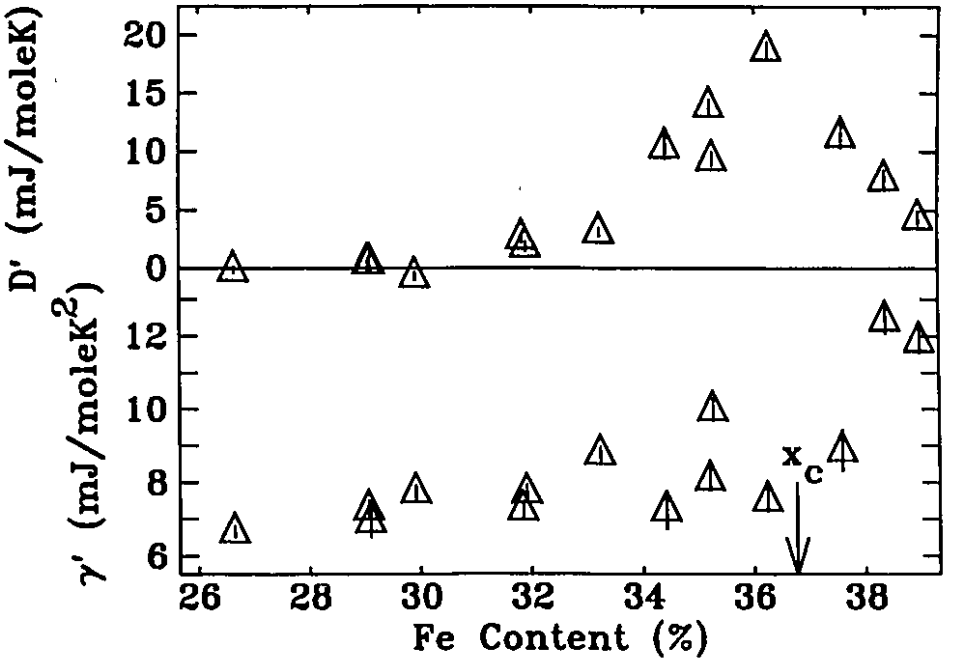

Figure 5.19: Super-paramagnetic Cluster Parameters for a–Fe_xZr_{100-x}. The parameters γ' and D' were determined by fitting equation 5.15 to the $C_P(T)$ data below 5 K.

the Schottky peak by a constant and fitting the data with the function:

$$C_P(T) = \gamma' T + \beta' T^3 + D' \tag{5.15}$$

gives as good fits to the C_P data as the *SF* fit, but with one less parameter. The values of γ' and D', shown in Fig 5.19, behave smoothly in composition [127]. This smooth behaviour in composition seems an unlikely result of magnetic clusters, whose formation and characteristics are expected to be highly dependant on sample preparation conditions, notably ribbon quench rate, which were quite variable. Associating D' with k_B times the number of clusters per mole yields $\sim 10^{-3}$ clusters per Fe atom. This is similar to the results obtained for the cluster moment by magnetometry (Fig. 5.18). The good fits of this simple cluster model (equation 5.15) to the data lead us to conclusion that *we cannot rule out the cluster model on the basis of the zero field $C_P(T)$ data.*

Recalling that the agreement between the high and low temperature data in 5 Tesla provided convincing evidence that $C_P(T)$ in a field of 5 Tesla is completely non–

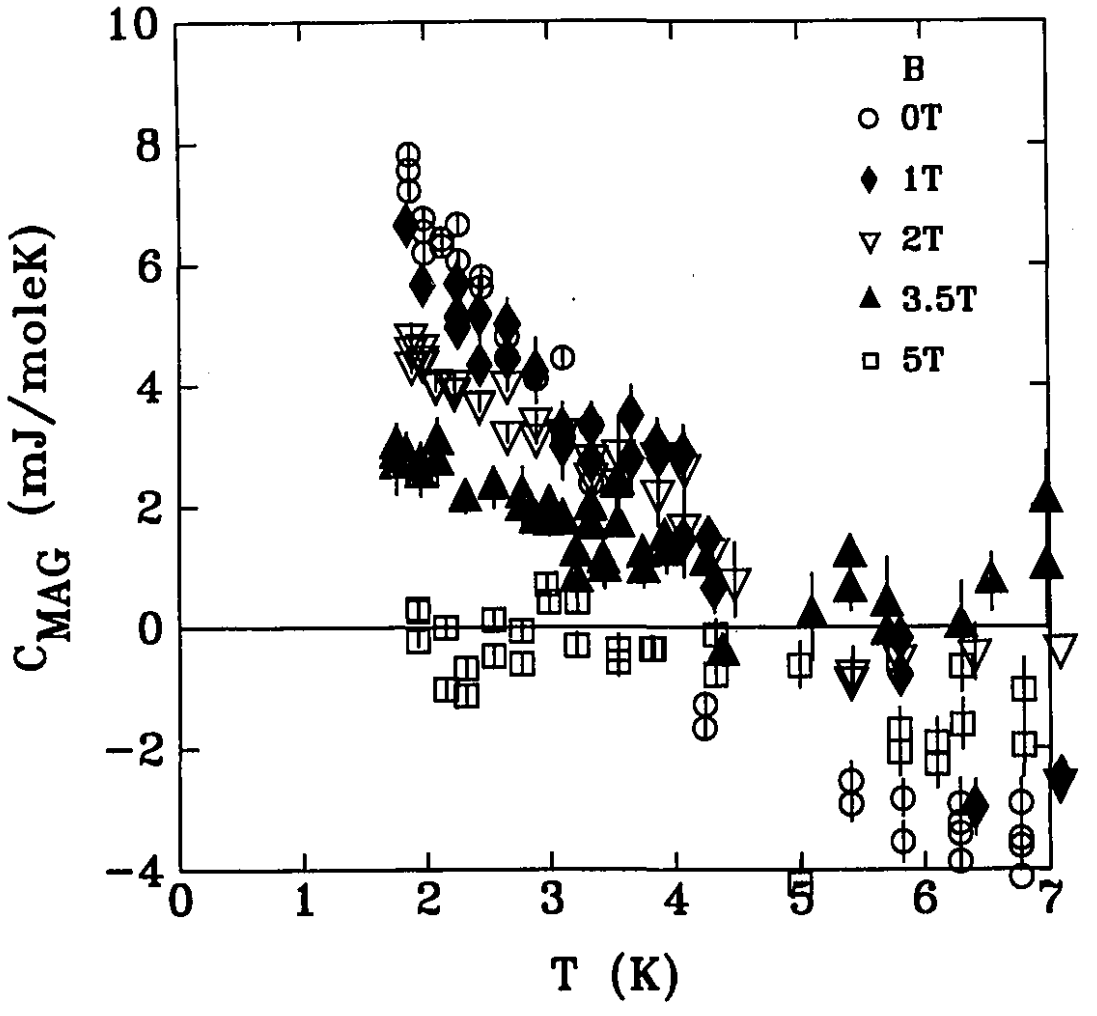

Figure 5.20: Magnetic specific heat of a–$Fe_{36.3}Zr_{63.7}$ determined by subtracting fits of the high temperature $H = 0$ data from the data at each field.

magnetic for this sample, we now look at the $C_P(T)$ data for a–$Fe_{36.3}Zr_{63.7}$. Fig. 5.20 shows the results of subtracting off an extrapolation of the high temperature, $H = 0$ fit ($\gamma_{HT} + \beta T^3$) from all the rest of the data which we can thus assume is the *magnetic specific heat*, $C^{\downarrow}_{MAG}(T)$. First of all we remark that the data are almost identical in $H = 0$ and $\mu_0 H = 1$ Tesla. This implies that H_{LOC}, which is responsible for C_{MAG} at $H = 0$, must be of order 1 Tesla, or more. This value is huge compared to those for typical cluster systems where C_{MAG} is markedly affected by $H \sim 0.1$ Tesla [50]. Furthermore, we ruled out such large values of H_{LOC} with the magnetometry results.

More basic considerations reveal an even more fundamental criticism of the cluster model. Predictions of the cluster model are that C_{MAG} only depends on $\overline{(H_{LOC}+H)}/T$. This means that increasing H and increasing T should affect C_{MAG} in the opposite sense. Quick inspection of the Fig. 5.20, however, reveals that at any field, H, and temperature, T, C_{MAG} always decreases upon increasing either the magnetic field or the temperature. *Experimental observations are, therefore, in complete contrast with the predictions of super–paramagnetism.*

The objection may be raised that the subtraction of γT was incorrect. However, in order to make the cluster model tenable, we would need to construct a C_{MAG} such that $dC_{MAG}/dT > 0$ at all temperatures. Simple consideration of Fig. 5.20, however, shows that this would require γ to be reduced by more than half its value of $\sim$12mJ/K^{2}mole, for a–$Fe_{36.3}Zr_{63.7}$. This would lead γ to show a substantial negative dip at concentrations near the critical concentration, which is unphysical.

In summary, from magnetocalorimetry data of Fig 5.20, we have completely ruled out the formation of magnetic clusters as being the origin of the upturn $C_P(T)/T$ signal from fundamental thermodynamic arguments. The only remaining explanation of the data, therefore, is spin fluctuations.

Chapter 6

Conclusions

In this thesis, the low temperature specific heat, $C_P(T)$, of amorphous Fe–Zr samples near the critical composition for ferromagnetism has been studied in and out of high magnetic fields. Taken together with low temperature resistivity and susceptibility measurements, these measurements provide the most convincing evidence to date for the presence of *SF* in the measurement of electronic properties.

The main conclusions of the magnetometry results are:

- The magnetization data of ref. [64] on paramagnetic a–Fe_xZr_{100-x} samples was reanalyzed using Arrott plots. In agreement with a previous study [57], the determined ground state paramagnetic susceptibilities were found to be consistent with the large values expected for exchange–enhanced Pauli paramagnets.

- The inverse ground state susceptibility of a–Fe_xZr_{100-x} was found to be linear in Fe content, being zero at the critical concentration for ferromagnetism. This result is consistent with Stoner theory.

- The ground state susceptibility, measured by magnetometry, was combined with the density of electron states at the Fermi level, measured by calorimetry, to yield values of the Stoner enhancement factor approaching 50 for paramagnetic a–Fe_xZr_{100-x}.

- Low ordered moments in ferromagnetic a–Fe_xZr_{100-x}, measured in ref. [57], were combined with an ordered moment, measured by calorimetry, to study the relationship between the ordered moment and the ordering temperature. These results were found to be consistent with Stoner theory.

- The above conclusions, combined with previous work, all combine to strongly support the view that a–Fe_xZr_{100-x} is a near/weak itinerant ferromagnetic metal with a critical concentration of ~37% Fe.

- A Curie–Weiss law was observed at high temperatures in the susceptibility of paramagnetic a–Fe_xZr_{100-x} samples. The Curie–Weiss magnetic moment was roughly constant for all paramagnetic samples studied, while the Cure–Weiss temperature was found to increase from –700 K to near zero on increasing Fe content. These results were found to be consistent with the Curie–Weiss law predicted by spin fluctuation theory.

The main conclusions of the calorimetry results are:

- Upturns were observed in the values of $C_P(T)/T$ of some a–Fe_xZr_{100-x} samples, for T<4 K, where $C_P(T)$ is the specific heat. These upturns were found to be most pronounced in samples nearest to the critical concentration for ferromagnetism.

- The upturns in $C_P(T)/T$ were analysed as resulting from an electron mass enhancement due to spin fluctuations (*SF*). The *SF* expression, carefully implemented, was found to fit the $C_P(T)$ data. The composition dependence of the parameters was found to be consistent with the predictions of *SF* theory.

- The phonon $C_P(T)$ was determined from the high temperature data, which was found to follow the predicted behaviour for a normal metal. The phonon contribution was found to be only weakly dependant on Fe content.

- Subtracting the determined phonon contributions from $C_P(T)$, we were able to estimate the spin fluctuation temperature, T_{SF}, which were consistent with

previous values determined from resistivity measurements. The near composition independent value of $T_{SF} \approx 7$ K probably indicates the inadequacy of the *SF* expression in our temperature range.

- The high temperature $C_P(T)$ data also yielded values of the effective electron mass which were reduced from the ground state values by as much as 50%. These high temperature values were found to display no anomalous features at the critical composition and their composition dependance was found to be in good agreement with previous work on $a-Fe_xZr_{100-x}$ samples outside our composition range.

- The previous conclusion suggests that, because of the low T_{SF} of our system ($\sim$7 K), we have observed, for the first time, the complete reduction of the *SF* and phonon enhanced electron mass to its high temperature phonon enhanced value.

- Assuming that the high temperature electron mass is enhanced only by phonons and estimating the electron–phonon contribution from a previous study, we have determined experimental values of the bare electron densities of states at the Fermi level, which agree well with previous work. These estimates were used to determine the Stoner enhancement factors of all of our samples. We were also able to estimate the electron mass enhancement factor due to *SF* for our samples, which approaches 100%.

- Using the estimated Stoner factors, the predictions for the *SF* parameters were compared with experimental values. As observed in other systems, the predictions are high by a factor of at least 10 compared with experiment.

The main conclusions of the magnetocalorimetry results are:

- The application of a magnetic field to our samples was found to affect only the upturns in $C_P(T)/T$, which conclusively demonstrates the magnetic origin of this feature.

- We observed the first known instance of the *complete* quenching of the *SF* contribution to $C_P(T)$. This occurred in our a–$Fe_{36.3}Zr_{63.7}$ sample in a field of 5 Tesla.

- The $C_P(T)$ of the normally behaved a–$Fe_{30.3}Zr_{69.7}$ sample was unaffected by a 5 Tesla field. The moderate upturns in $C_P(T)/T$ of a–$Fe_{34.4}Zr_{65.6}$ were substantially, *but not completely*, reduced in a 5 Tesla field. This result gives further strong support for the *SF* model, which predicts that both the upturn strength and the field quench rate should increase with the Stoner enhancement factor.

- The measured Stoner factor and the *SF* quenching expression were combined to yield predictions which were in very good agreement with the observed quench rates. This is as conclusive as any previous numerical evidence for the existance of a *SF* contribution to the specific heat.

- The most plausible alternative explanation of the data is the formation of super–paramagnetic clusters in our samples. This was ruled out using a fundamental thermodynamic argument on data from the a–$Fe_{36.3}Zr_{63.7}$ sample. This was the sample in which we claim to have observed the complete quenching of *SF*, and the normal metallic behaviour of the sample in a 5 Tesla field was a key part of the argument. This strong argument against super–paramagnetism is, therefore, inaccessible in other systems, where complete field quenching has not been observed.

Virtually all of our results confirm that a–Fe_xZr_{100-x} is a spin–fluctuator. Unlike studies on off–stoichiometry crystalline systems whose structure becomes progressively defect ridden upon moving away from the perfect crystal, our conclusions are not weakened upon consideration of defect formation. As shown, for instance, by our x–ray diffraction data or our Debye temperature measurements, the atomic arrangement in all of our samples is virtually identical. Our samples, therefore, comprise a system in which only the strength of the magnetism is varied. Furthermore, because of the low $T_{SF}\approx$7 K of this system, the influence of spin fluctuations can be *completely*

removed by either raising the temperature to the comparatively low value of 7 K, or by applying only moderate magnetic fields of order 5 Tesla.

Further experimental and theoretical work need to be done, in order to fully understand the behaviour of spin fluctuations in this unique system. We propose the following measurements on $a-Fe_xZr_{100-x}$ samples, closely spaced in Fe content near $x = 37\%$, like the samples used in this study.

- Small angle neutron scattering studies on $a-Fe_xZr_{100-x}$ may observe the Lorentzian form of the generalized susceptibility and provide another measure of T_{SF}.

- Magnetic susceptibility measurements should be performed over a wider temperature range, particularly on ferromagnetic samples.

- Magnetoresistance measurements may observe the quenching of the *SF* scattering in high magnetic fields. This quenching should occur at the same field as the quenching observed in this work.

- Very low temperature calorimetry measurements (<1 K) may verify the functional form of the low temperature electron mass enhancement. This work would, by itself, rule out magnetic cluster formation and may allow more unambiguous fitting of the *SF* expression (equation 5.5) to the data.

- Low temperature calorimetry measurements in higher magnetic fields ($\sim$ 10 Tesla) would allow a more detailed study of the *SF* quenching in $a-Fe_xZr_{100-x}$.

The numerical interpretation of these measurements could be unified under a *SF* theory like that of Lonzarich and Taillefer. We believe that our study justifies further theoretical work on the predictions of spin fluctuation theory, since amorphous iron-zirconium provides the controlled environment necessary for a detailed study of spin fluctuations.

Appendix A

Zero Field Calorimetry Data for a–Fe–Zr

The low temperature specific heat of our a–Fe_xZr_{100-x} samples is tabulated below. The data are given as three columns. The columns are: temperature (T, given in Kelvin), molar specific heat (C_P, given in milliJoules/moleK) and an instrumental uncertainty estimate ($\sigma[C_P]$, given in milliJoules/moleK). The instrumental uncertainty estimate is probably not rigourously correct in an absolute sense, but it may be used to compare the relative accuracy of different data points (except near T = 77 K). Sample compositions were determined by electron microprobe and are quoted to an extra decimal place compared with those given in the text.

The absolute calorimetry data, for a given sample, were all taken on the same day in zero applied magnetic field. Typically, rough data were taken near 77 K, with the dewar filled with liquid nitrogen, then below 4.2 K, with the dewar filled with pumped liquid helium. Finally, data were taken above 4.2 K, up to temperatures where the helium bath was depleted (usually between 20 K and 40 K).

Table A.1: Zero Field Calorimetry Data for a-Fe[26.65]Zr[73.35]

Temperature [K]	C_P $[\frac{\text{mJoule}}{\text{moleK}}]$	$\sigma[C_P]$ $[\frac{\text{mJoule}}{\text{moleK}}]$	Temperature [K]	C_P $[\frac{\text{mJoule}}{\text{moleK}}]$	$\sigma[C_P]$ $[\frac{\text{mJoule}}{\text{moleK}}]$	Temperature [K]	C_P $[\frac{\text{mJoule}}{\text{moleK}}]$	$\sigma[C_P]$ $[\frac{\text{mJoule}}{\text{moleK}}]$
1.645	11.87	0.11	1.646	12.58	0.14	1.705	12.76	0.09
1.705	12.21	0.08	1.705	12.96	0.11	1.705	12.65	0.09
1.882	14.18	0.10	1.882	14.11	0.09	1.882	14.60	0.10
2.024	15.78	0.13	2.024	15.56	0.13	2.024	15.60	0.13
2.024	15.53	0.14	2.173	17.41	0.13	2.173	17.39	0.13
2.173	16.88	0.13	2.284	18.06	0.15	2.321	18.56	0.13
2.321	18.75	0.13	2.321	18.70	0.12	2.432	20.35	0.14
2.433	20.10	0.15	2.434	20.30	0.13	2.551	21.42	0.14
2.552	21.16	0.13	2.666	23.24	0.29	2.666	22.61	0.24
2.782	24.40	0.15	2.784	24.21	0.15	2.894	26.28	0.30
2.894	26.30	0.30	2.894	26.25	0.31	3.110	29.10	0.31
3.110	29.33	0.29	3.340	33.02	0.32	3.341	32.65	0.31
3.549	35.67	0.33	3.556	36.14	0.33	3.560	36.43	0.31
3.744	39.11	0.33	3.749	40.33	0.34	3.973	43.89	0.34
3.975	43.66	0.38	4.300	50.33	0.23	4.301	51.01	0.22
4.325	50.89	0.40	4.327	50.65	0.43	4.507	55.08	0.38
4.603	57.83	0.24	4.603	58.07	0.26	4.924	65.39	0.32
4.924	65.90	0.30	5.266	75.75	0.32	5.267	75.04	0.31
5.629	87.22	0.38	5.629	87.82	0.36	6.016	100.6	0.4
6.016	99.34	0.38	6.429	117.0	0.4	6.430	116.4	0.5
6.858	134.1	0.4	6.859	134.9	0.5	7.325	155.6	0.6
7.325	157.1	0.5	7.823	181.7	0.6	7.823	183.2	0.6
8.354	212.3	0.6	8.354	213.2	0.6	8.908	249.1	0.8
8.908	248.1	0.7	9.514	289.9	0.8	9.514	290.3	0.8
9.790	308.8	0.9	9.790	309.1	0.9	10.162	340.6	1.0
10.162	340.7	0.9	10.556	372.6	1.1	10.556	372.4	1.0
10.837	397.5	1.1	10.838	398.3	1.1	11.362	445.0	1.2
11.363	443.1	1.3	11.571	468.7	1.2	11.571	469.3	1.2
12.246	535.8	1.5	12.251	535.7	1.4	13.193	645.0	1.5
13.193	647.1	1.5	14.203	775.0	1.8	14.207	772.2	1.9
15.326	923.9	2.3	15.331	923.0	2.2	16.503	1103	2
16.503	1107	2	17.772	1316	3	17.777	1317	3
19.172	1560	3	19.172	1562	3	20.650	1830	4
20.650	1834	4	22.231	2174	4	22.254	2166	4
23.992	2574	5	24.004	2579	5	24.460	2687	6
24.460	2688	5	26.334	3139	6	26.341	3135	6
28.396	3681	7	28.410	3677	7	79.663	17369	18
79.663	17798	16	79.680	17502	28			

Table A.2: Zero Field Calorimetry Data for a-Fe[29.07]Zr[70.93]

Temperature [K]	C_P $[\frac{\text{mJoule}}{\text{moleK}}]$	$\sigma[C_P]$ $[\frac{\text{mJoule}}{\text{moleK}}]$	Temperature [K]	C_P $[\frac{\text{mJoule}}{\text{moleK}}]$	$\sigma[C_P]$ $[\frac{\text{mJoule}}{\text{moleK}}]$	Temperature [K]	C_P $[\frac{\text{mJoule}}{\text{moleK}}]$	$\sigma[C_P]$ $[\frac{\text{mJoule}}{\text{moleK}}]$
1.638	13.53	0.16	1.638	13.65	0.22	1.638	13.75	0.24
1.638	13.42	0.16	1.638	13.86	0.17	1.733	14.32	0.20
1.733	14.48	0.22	1.733	14.12	0.18	1.733	14.77	0.18
1.734	13.94	0.21	1.896	16.08	0.23	1.896	16.47	0.23
1.896	15.75	0.22	1.896	16.40	0.24	1.992	15.81	0.23
1.992	16.68	0.21	1.992	16.65	0.22	2.083	17.48	0.22
2.083	18.10	0.23	2.197	18.85	0.26	2.197	18.82	0.24
2.197	18.83	0.24	2.323	21.03	0.28	2.323	20.36	0.30
2.323	19.86	0.27	2.434	21.78	0.24	2.435	22.00	0.23
2.435	21.46	0.22	2.561	23.39	0.29	2.561	22.88	0.29
2.561	23.04	0.28	2.661	24.34	0.23	2.662	24.65	0.25
2.896	27.56	0.25	2.896	27.28	0.24	3.115	30.83	0.27
3.116	30.64	0.28	3.341	33.79	0.23	3.343	34.59	0.23
3.525	37.01	0.35	3.536	38.02	0.41	3.554	38.14	0.42
3.561	37.22	0.40	3.770	40.41	0.37	3.771	40.23	0.38
3.964	43.84	0.41	3.972	43.59	0.43	4.219	49.10	0.50
4.219	49.80	0.73	4.409	52.66	0.35	4.409	53.82	0.40
4.717	59.94	0.42	4.717	60.87	0.42	5.046	68.63	0.46
5.046	69.21	0.50	5.120	69.70	0.74	5.396	79.40	0.51
5.396	79.93	0.52	5.769	91.63	0.59	5.769	90.60	0.51
6.158	104.6	0.6	6.158	105.0	0.5	6.580	120.7	0.6
6.580	122.6	0.6	7.028	141.0	0.8	7.028	140.7	0.7
7.506	163.8	0.9	7.507	161.9	0.9	8.007	190.4	0.9
8.007	189.4	1.0	8.550	223.1	1.0	8.551	222.2	1.0
9.131	259.6	1.1	9.131	259.8	1.2	9.753	301.5	1.4
9.753	302.8	1.3	10.051	324.6	1.8	10.056	320.8	5.8
10.404	350.7	1.4	10.404	352.4	1.4	10.569	365.4	1.4
10.569	365.3	1.5	11.111	409.8	1.4	11.111	413.8	1.3
11.269	425.3	1.4	11.269	429.8	1.6	11.847	485.2	1.6
11.847	486.3	1.5	11.984	494.9	1.6	11.984	499.1	1.7
12.922	596.8	1.8	12.922	597.4	1.7	13.920	714.5	2.0
13.920	720.6	2.1	14.991	856.3	2.7	16.178	1024	3
16.178	1029	3	17.424	1215	3	17.424	1218	3
18.765	1438	3	18.770	1432	3	20.207	1687	4
20.207	1693	4	21.799	2015	4	21.799	2020	4
23.477	2390	5	23.488	2296	5	24.473	2615	5
24.485	2626	5	26.374	3076	5	26.380	3074	6
28.452	3592	6	28.466	3586	6	30.976	4396	11
79.838	13097	51	79.856	13400	31			

Table A.3: Zero Field Calorimetry Data for a-Fe[29.11]Zr[70.89]

Temperature [K]	C_P $[\frac{\text{mJoule}}{\text{moleK}}]$	$\sigma[C_P]$ $[\frac{\text{mJoule}}{\text{moleK}}]$	Temperature [K]	C_P $[\frac{\text{mJoule}}{\text{moleK}}]$	$\sigma[C_P]$ $[\frac{\text{mJoule}}{\text{moleK}}]$	Temperature [K]	C_P $[\frac{\text{mJoule}}{\text{moleK}}]$	$\sigma[C_P]$ $[\frac{\text{mJoule}}{\text{moleK}}]$
1.854	16.46	0.28	1.854	15.54	0.19	1.854	15.82	0.28
1.854	15.64	0.22	1.891	16.04	0.17	1.891	16.16	0.19
1.891	15.86	0.33	1.891	15.72	0.24	1.947	16.42	0.24
1.947	16.02	0.22	1.986	16.71	0.19	1.986	16.74	0.19
1.987	16.93	0.29	1.987	17.25	0.30	2.089	17.86	0.29
2.089	17.50	0.28	2.089	17.54	0.19	2.089	17.34	0.19
2.189	18.80	0.27	2.189	18.77	0.29	2.189	18.97	0.28
2.276	19.80	0.22	2.299	20.14	0.28	2.299	19.84	0.27
2.300	20.12	0.26	2.378	20.40	0.29	2.496	21.58	0.28
2.497	22.34	0.30	2.727	25.58	0.30	2.727	25.07	0.31
2.894	27.61	0.31	2.894	27.77	0.30	3.115	30.94	0.38
3.115	31.20	0.34	3.343	35.88	0.33	3.343	36.02	0.36
3.555	41.03	0.35	3.761	44.66	0.39	3.765	44.57	0.45
3.989	49.32	0.41	4.820	68.29	0.28	4.821	68.26	0.26
5.028	74.47	0.27	5.028	74.00	0.26	5.434	87.31	0.29
5.435	88.01	0.27	5.832	100.2	0.3	5.832	100.1	0.3
6.407	122.9	0.4	6.408	123.4	0.4	6.572	128.9	0.4
6.573	128.5	0.3	7.026	151.1	0.4	7.026	151.4	0.4
7.204	156.5	0.5	7.204	158.2	0.5	7.703	186.3	0.5
7.703	187.0	0.5	7.908	197.8	0.5	8.443	232.6	0.6
8.444	234.8	0.5	9.269	290.1	0.7	9.269	291.7	0.7
10.160	360.7	0.8	10.160	360.7	0.8	10.739	413.6	1.1
10.743	410.2	0.9	11.781	510.9	1.2	12.918	637.1	1.2
12.918	639.7	1.2	14.172	801.4	1.5	15.516	993.5	1.6
15.521	994.2	1.8	79.962	16650	21	79.979	16747	21

Table A.4: Zero Field Calorimetry Data for a-Fe[29.92]Zr[70.08]

Temperature [K]	C_P $[\frac{\text{mJoule}}{\text{moleK}}]$	$\sigma[C_P]$ $[\frac{\text{mJoule}}{\text{moleK}}]$	Temperature [K]	C_P $[\frac{\text{mJoule}}{\text{moleK}}]$	$\sigma[C_P]$ $[\frac{\text{mJoule}}{\text{moleK}}]$	Temperature [K]	C_P $[\frac{\text{mJoule}}{\text{moleK}}]$	$\sigma[C_P]$ $[\frac{\text{mJoule}}{\text{moleK}}]$
1.808	14.81	0.08	1.809	15.09	0.10	1.811	15.07	0.11
1.813	14.99	0.10	1.815	15.15	0.11	1.845	15.50	0.11
1.846	15.40	0.11	1.847	15.44	0.11	1.850	15.40	0.09
1.950	16.34	0.11	1.950	15.89	0.10	1.951	15.95	0.10
1.953	15.94	0.12	1.957	15.82	0.13	2.050	16.99	0.13
2.061	16.95	0.13	2.076	17.45	0.14	2.300	20.04	0.13
2.301	20.08	0.15	2.502	22.45	0.15	2.502	22.69	0.15
2.674	24.62	0.15	3.200	32.62	0.16	3.201	32.66	0.16
3.201	32.89	0.16	3.203	33.11	0.18	3.376	34.99	0.17
3.377	35.21	0.15	3.380	35.68	0.17	3.381	35.60	0.15
3.555	38.83	0.18	3.562	38.45	0.18	3.562	38.73	0.18
3.743	41.91	0.25	3.757	41.58	0.21	3.954	45.41	0.24
3.987	46.04	0.25	4.227	51.71	0.26	4.227	51.98	0.40
4.406	54.74	0.28	4.406	55.15	0.28	4.610	59.94	0.23
4.610	59.99	0.26	4.963	69.18	0.29	4.963	69.19	0.31
5.449	83.02	0.32	5.524	85.32	0.28	5.524	85.42	0.34
5.987	100.8	0.4	5.987	102.2	0.4	6.568	123.6	0.4
6.607	124.7	0.4	6.607	125.0	0.4	6.630	126.4	0.4
6.631	126.9	0.4	7.201	152.9	0.6	7.201	153.2	0.5
7.904	190.9	0.6	8.661	233.8	0.8	8.661	234.9	0.8
9.493	292.8	0.8	10.407	363.3	0.9	10.407	364.7	1.0
11.018	415.4	1.2	11.018	407.0	1.4	11.408	453.3	1.2
11.408	453.4	1.2	12.196	525.5	1.4	12.196	534.6	1.3
13.495	674.7	1.6	13.495	678.7	1.4	14.914	867.8	1.7
16.512	1093	2	16.512	1094	2	18.282	1382	3
20.201	1733	3	20.207	1732	3	22.364	2181	4
24.411	2649	4	79.768	17303	20	79.786	16814	29

Table A.5: Zero Field Calorimetry Data for a-Fe[31.85]Zr[68.15]

Temperature [K]	C_P $\left[\frac{\text{mJoule}}{\text{moleK}}\right]$	$\sigma[C_P]$ $\left[\frac{\text{mJoule}}{\text{moleK}}\right]$	Temperature [K]	C_P $\left[\frac{\text{mJoule}}{\text{moleK}}\right]$	$\sigma[C_P]$ $\left[\frac{\text{mJoule}}{\text{moleK}}\right]$	Temperature [K]	C_P $\left[\frac{\text{mJoule}}{\text{moleK}}\right]$	$\sigma[C_P]$ $\left[\frac{\text{mJoule}}{\text{moleK}}\right]$
1.848	18.59	0.15	1.848	18.00	0.16	1.848	18.33	0.15
1.848	17.94	0.14	1.900	18.89	0.16	1.900	18.48	0.14
1.900	18.58	0.17	1.900	18.67	0.14	2.084	20.51	0.15
2.084	20.65	0.14	2.298	22.94	0.17	2.298	23.29	0.17
2.358	25.15	0.25	2.358	23.60	0.23	2.403	24.60	0.17
2.403	24.71	0.17	2.404	24.83	0.18	2.512	25.67	0.17
2.512	26.09	0.16	2.611	27.26	0.17	2.611	27.48	0.18
2.707	28.75	0.19	2.707	28.99	0.19	2.782	29.83	0.18
2.782	30.41	0.17	2.900	31.28	0.17	2.900	31.73	0.18
3.006	33.18	0.17	3.006	33.13	0.18	3.120	35.20	0.22
3.122	35.64	0.24	3.233	37.37	0.19	3.233	37.60	0.19
3.336	39.49	0.21	3.339	38.87	0.18	3.447	41.37	0.20
3.447	41.35	0.21	3.663	45.86	0.20	3.664	46.36	0.19
3.871	50.15	0.26	3.871	49.57	0.24	4.095	54.30	0.26
4.096	54.82	0.27	4.388	62.85	0.29	4.389	62.12	0.32
4.696	71.10	0.27	4.696	71.06	0.29	5.024	81.44	0.30
5.024	81.68	0.31	5.372	92.61	0.37	5.373	93.53	0.40
5.743	106.2	0.4	5.743	106.3	0.4	6.130	122.4	0.4
6.130	122.8	0.4	6.551	141.3	0.5	6.551	141.1	0.5
6.998	162.8	0.5	6.998	163.0	0.5	7.473	188.4	0.6
7.473	189.0	0.6	7.983	219.7	0.6	7.983	220.9	0.6
8.513	253.9	0.7	8.513	254.4	0.7	9.091	297.7	0.7
9.091	298.0	0.7	9.711	346.8	0.9	9.712	347.0	1.0
10.357	405.0	1.0	10.359	404.2	0.9	10.697	434.8	0.9
10.697	439.1	1.0	11.062	474.2	1.1	11.063	473.1	1.1
11.408	508.9	1.1	11.408	511.5	1.0	12.727	655.8	1.5
12.727	664.8	1.5	13.700	789.2	1.6	14.773	959.5	1.4
14.777	943.9	1.7	15.913	1134	2	17.138	1343	2
17.138	1343	2	18.487	1592	3	19.910	1877	3
19.910	1880	3	21.441	2211	4	23.082	2629	4
23.082	2633	4	24.442	2975	5	26.341	3456	6
26.354	3487	5	28.383	4057	6	28.396	4065	6
30.600	4691	7	30.614	4700	7	79.962	17623	18
79.962	18547	24						

Table A.6: Zero Field Calorimetry Data for a-Fe[31.92]Zr[68.08]

Temperature [K]	C_P $[\frac{\text{mJoule}}{\text{moleK}}]$	$\sigma[C_P]$ $[\frac{\text{mJoule}}{\text{moleK}}]$	Temperature [K]	C_P $[\frac{\text{mJoule}}{\text{moleK}}]$	$\sigma[C_P]$ $[\frac{\text{mJoule}}{\text{moleK}}]$	Temperature [K]	C_P $[\frac{\text{mJoule}}{\text{moleK}}]$	$\sigma[C_P]$ $[\frac{\text{mJoule}}{\text{moleK}}]$
1.795	17.00	0.14	1.894	17.62	0.14	1.894	17.86	0.13
1.895	17.86	0.14	1.895	18.21	0.13	1.995	19.09	0.14
1.996	19.03	0.14	1.997	18.74	0.15	1.997	18.81	0.14
2.098	19.72	0.14	2.098	20.29	0.13	2.099	19.98	0.14
2.209	21.62	0.15	2.209	21.23	0.14	2.209	21.51	0.14
2.211	21.49	0.14	2.295	22.77	0.14	2.295	22.49	0.14
2.401	23.58	0.14	2.401	23.61	0.15	2.401	23.70	0.15
2.553	24.06	0.16	2.553	25.46	0.16	2.783	27.94	0.15
2.783	28.18	0.15	3.002	31.28	0.16	3.002	31.16	0.14
3.002	30.70	0.16	3.226	34.03	0.14	3.228	34.03	0.16
3.229	33.53	0.16	3.451	37.92	0.29	3.451	37.47	0.18
3.654	40.64	0.48	3.655	40.59	0.45	3.655	40.81	0.48
3.867	44.26	0.47	3.869	45.07	0.47	4.051	47.43	0.51
4.058	47.94	0.50	4.066	48.49	0.16	4.072	48.73	0.18
4.233	51.52	0.72	4.234	50.84	0.64	4.403	54.16	0.20
4.404	54.85	0.21	4.501	56.83	0.44	4.501	57.18	0.53
4.755	62.04	0.23	4.756	62.34	0.23	4.997	67.24	0.57
4.998	68.69	0.68	5.128	70.96	0.25	5.128	71.37	0.26
5.238	73.08	0.48	5.533	82.24	0.29	5.533	82.42	0.28
5.537	81.50	0.68	5.537	83.21	0.64	5.969	95.34	0.30
5.969	96.01	0.31	6.131	100.9	0.7	6.132	101.6	0.8
6.438	111.0	0.4	6.439	112.0	0.4	6.930	129.4	0.4
6.930	130.1	0.4	7.469	154.4	0.5	7.469	154.4	0.5
8.041	181.7	0.6	8.041	182.5	0.5	8.667	215.9	0.6
8.667	215.7	0.7	9.327	256.0	0.7	9.327	257.6	0.7
9.884	294.6	0.9	9.885	294.5	0.9	10.031	306.6	0.9
10.032	305.0	0.9	10.053	307.7	0.8	10.053	306.8	0.9
10.798	363.3	1.0	10.798	364.7	1.0	10.823	364.6	1.1
10.823	364.9	1.0	11.236	399.9	1.1	11.241	400.0	1.0
11.641	436.7	1.3	11.641	437.0	1.1	11.670	437.2	1.0
11.670	439.0	1.1	12.532	522.7	1.4	12.532	523.1	1.4
13.513	626.4	1.7	13.517	626.5	1.7	14.556	753.7	1.9
14.556	754.8	2.2	15.674	893.9	2.3	15.674	900.5	2.3
16.831	1060	3	16.831	1062	3	18.125	1260	3
18.125	1264	3	19.515	1495	4	19.515	1495	4
21.015	1772	4	21.015	1773	4	22.686	2117	5
22.715	2124	5	24.417	2522	5	24.442	2515	6
26.485	3059	6	79.452	17009	16	79.452	17042	16
79.452	17080	26						

Table A.7: Zero Field Calorimetry Data for a-Fe[33.23]Zr[66.77]

Temperature [K]	C_P [mJoule/moleK]	$\sigma[C_P]$ [mJoule/moleK]	Temperature [K]	C_P [mJoule/moleK]	$\sigma[C_P]$ [mJoule/moleK]	Temperature [K]	C_P [mJoule/moleK]	$\sigma[C_P]$ [mJoule/moleK]
1.609	18.22	0.28	1.609	18.09	0.28	1.609	17.87	0.27
1.709	18.97	0.28	1.709	18.97	0.37	1.709	18.72	0.24
1.867	21.40	0.31	1.867	20.47	0.29	1.867	20.87	0.25
2.001	22.01	0.31	2.001	21.75	0.27	2.146	24.22	0.31
2.146	23.75	0.33	2.286	24.78	0.31	2.287	24.93	0.33
2.287	25.30	0.33	2.500	28.34	0.33	2.500	27.82	0.35
2.610	29.92	0.37	2.652	30.34	0.35	2.727	30.68	0.35
2.727	30.95	0.33	2.783	31.63	0.31	2.783	31.56	0.33
2.829	33.44	0.40	2.891	33.10	0.32	2.894	32.85	0.33
2.896	33.46	0.37	3.005	34.52	0.34	3.006	35.14	0.35
3.223	37.55	0.34	3.223	37.64	0.32	3.443	41.22	0.36
3.444	40.89	0.34	3.659	43.90	0.37	3.660	44.07	0.36
3.877	47.42	0.40	3.877	47.45	0.40	4.074	51.60	0.42
4.238	55.32	0.51	4.240	54.60	0.54	4.241	53.94	0.45
4.406	57.31	0.43	4.406	57.46	0.43	4.505	59.76	0.45
4.505	59.87	0.43	4.759	65.27	0.48	4.759	65.74	0.51
4.865	67.00	0.50	4.865	68.43	0.50	5.114	73.91	0.52
5.115	74.81	0.51	5.115	75.60	0.54	5.131	73.15	0.56
5.132	75.95	0.52	5.251	76.49	0.53	5.251	76.69	0.32
5.538	84.14	0.57	5.538	84.15	0.60	5.666	87.80	0.36
5.666	88.10	0.33	5.974	96.55	0.67	6.104	101.2	0.4
6.104	99.68	0.42	6.583	117.6	0.5	6.584	117.8	0.5
7.096	135.5	0.5	7.096	137.2	0.5	7.638	160.2	0.5
7.638	160.3	0.6	8.232	189.0	0.6	8.232	188.2	0.6
8.861	222.6	0.7	8.861	223.4	0.8	9.552	263.8	0.9
9.552	264.6	0.9	10.037	300.6	1.0	10.037	298.7	1.1
10.425	324.9	1.0	10.427	326.2	1.1	10.804	356.9	1.1
10.805	356.3	1.1	11.240	389.9	1.2	11.241	389.0	1.3
11.649	425.8	1.4	11.649	426.7	1.3	12.100	464.0	1.4
12.100	464.7	1.4	13.029	553.1	1.7	13.029	553.9	1.6
14.052	668.2	1.9	14.052	668.9	1.8	15.138	795.6	2.2
15.142	798.9	2.2	16.311	950.1	2.6	16.316	949.2	2.5
17.598	1132	3	17.602	1130	3	18.952	1325	3
18.952	1334	3	19.298	1388	4	19.298	1392	3
19.298	1398	3	19.669	1445	4	19.669	1447	3
20.815	1642	4	20.815	1652	4	20.815	1655	4
22.434	1960	4	22.451	1947	4	22.469	1971	5
24.207	2332	5	24.213	2339	5	24.225	2331	6
26.086	2736	6	26.093	2739	6	26.106	2744	6
28.161	3197	5	28.168	3201	7	28.182	3193	7
29.266	3434	7	29.294	3455	7	79.997	15971	164
80.032	16612	156						

Table A.8: Zero Field Calorimetry Data for a-Fe[34.42]Zr[65.58]

Temperature [K]	C_P $[\frac{\text{mJoule}}{\text{moleK}}]$	$\sigma[C_P]$ $[\frac{\text{mJoule}}{\text{moleK}}]$	Temperature [K]	C_P $[\frac{\text{mJoule}}{\text{moleK}}]$	$\sigma[C_P]$ $[\frac{\text{mJoule}}{\text{moleK}}]$	Temperature [K]	C_P $[\frac{\text{mJoule}}{\text{moleK}}]$	$\sigma[C_P]$ $[\frac{\text{mJoule}}{\text{moleK}}]$
1.986	27.26	0.26	1.988	27.51	0.27	2.109	28.48	0.27
2.110	28.44	0.26	2.110	28.66	0.26	2.225	29.61	0.28
2.225	30.16	0.29	2.225	29.67	0.29	2.319	30.61	0.27
2.326	30.95	0.28	2.342	30.80	0.26	2.342	30.86	0.25
2.436	31.76	0.24	2.437	32.33	0.25	2.437	32.72	0.27
2.497	32.91	0.26	2.498	33.06	0.24	2.556	33.61	0.28
2.556	33.60	0.28	2.781	36.58	0.27	2.781	36.53	0.27
2.786	36.33	0.27	2.787	36.72	0.28	3.004	39.10	1.23
3.005	39.92	0.27	3.005	39.45	0.27	3.006	39.85	0.25
3.227	43.55	0.27	3.228	43.49	0.28	3.433	45.99	0.28
3.445	46.81	0.27	3.448	47.45	0.27	3.632	51.29	0.27
3.633	50.21	0.29	3.872	55.85	0.29	3.876	55.46	0.29
3.886	55.54	0.29	4.093	61.23	0.32	4.093	59.09	0.38
4.093	61.41	0.32	4.233	63.32	0.35	4.627	71.17	0.37
4.627	71.15	0.37	5.029	82.15	0.40	5.029	83.03	0.41
5.111	83.48	1.93	5.456	94.55	0.46	5.456	95.51	0.48
5.924	111.0	0.4	5.925	110.1	0.5	6.431	130.8	0.5
6.432	128.7	0.5	6.969	152.4	0.6	6.969	152.6	0.5
7.560	180.2	0.7	7.560	180.4	0.6	8.189	216.1	0.7
8.189	217.4	0.7	8.870	254.7	2.5	8.870	257.6	2.8
9.558	304.8	0.9	9.558	305.2	0.9	9.621	310.7	3.0
9.622	306.7	2.9	10.477	377.4	1.1	10.477	379.6	1.0
11.485	466.8	1.3	11.489	469.1	1.2	12.600	581.4	1.6
12.604	583.2	1.4	13.823	724.4	1.7	13.823	730.0	1.8
15.165	909.1	2.1	15.165	913.2	2.2	16.633	1142	2
16.633	1146	2	18.247	1412	3	18.247	1419	3
20.017	1773	3	20.071	1667	4	22.132	2269	4
79.610	15241	33	79.627	14754	37	79.663	16178	46

Table A.9: Zero Field Calorimetry Data for a-Fe[35.22]Zr[64.78]

Temperature [K]	C_P [mJoule/moleK]	$\sigma[C_P]$ [mJoule/moleK]	Temperature [K]	C_P [mJoule/moleK]	$\sigma[C_P]$ [mJoule/moleK]	Temperature [K]	C_P [mJoule/moleK]	$\sigma[C_P]$ [mJoule/moleK]
1.803	30.48	0.26	1.805	30.28	0.28	1.808	30.13	0.29
1.888	30.67	0.22	1.891	31.00	0.22	1.895	30.77	0.21
1.909	30.64	0.23	2.077	32.65	0.27	2.077	32.66	0.25
2.203	34.63	0.28	2.203	34.37	0.27	2.325	35.72	0.25
2.325	36.16	0.24	2.441	36.59	0.26	2.441	37.00	0.25
2.523	38.96	0.31	2.560	38.52	0.31	2.560	38.78	0.30
2.614	39.50	0.25	2.614	39.38	0.25	2.742	40.65	0.32
2.743	41.21	0.33	2.787	41.76	0.22	2.787	42.02	0.24
2.901	43.66	0.28	2.901	44.04	0.30	2.953	44.35	0.29
2.953	43.93	0.26	3.013	43.63	0.27	3.013	44.54	0.27
3.014	44.93	0.29	3.014	45.03	0.29	3.121	45.79	0.27
3.230	48.45	0.23	3.230	48.29	0.24	3.327	50.34	0.25
3.327	50.69	0.27	3.445	51.77	0.25	3.445	51.74	0.25
3.538	52.54	0.29	3.538	53.26	0.29	3.658	55.30	0.26
3.658	55.92	0.28	3.760	56.93	0.28	3.760	57.62	0.27
3.874	59.82	0.28	3.875	59.66	0.27	3.952	61.78	0.25
3.993	61.36	0.27	4.083	63.33	0.28	4.085	63.38	0.30
4.236	66.90	0.30	4.237	67.12	0.28	4.343	68.40	0.31
4.343	69.03	0.30	4.405	71.40	0.30	4.405	70.75	0.29
4.462	71.26	0.36	4.462	71.75	0.36	4.693	77.27	0.35
5.115	87.14	0.37	5.116	88.04	0.40	5.525	101.1	0.4
5.528	100.3	0.4	5.564	101.5	0.4	5.836	110.2	0.4
6.057	117.8	0.5	6.058	118.0	0.5	6.137	120.9	0.5
6.541	134.3	0.6	6.585	137.3	0.5	6.848	148.7	0.5
7.103	154.0	0.8	7.144	161.6	0.6	7.164	161.1	0.6
7.173	161.1	0.7	7.424	173.7	0.6	7.620	183.5	0.6
7.782	191.5	0.7	7.918	198.4	0.7	8.019	205.1	0.7
8.453	228.5	0.8	8.453	229.8	0.7	8.690	242.5	0.8
9.102	271.7	0.8	9.195	275.9	0.8	10.061	337.3	1.1
11.008	414.4	1.2	11.806	483.9	1.3	11.810	487.4	1.2
13.898	717.0	1.5	15.340	903.5	1.9	16.865	1072	2
18.559	1511	12	19.674	1638	3	21.566	2028	4
79.715	16167	33	79.751	16658	19			

Table A.10: Zero Field Calorimetry Data for a-Fe[35.27]Zr[64.73]

Temperature [K]	C_P $\left[\frac{\text{mJoule}}{\text{moleK}}\right]$	$\sigma[C_P]$ $\left[\frac{\text{mJoule}}{\text{moleK}}\right]$	Temperature [K]	C_P $\left[\frac{\text{mJoule}}{\text{moleK}}\right]$	$\sigma[C_P]$ $\left[\frac{\text{mJoule}}{\text{moleK}}\right]$	Temperature [K]	C_P $\left[\frac{\text{mJoule}}{\text{moleK}}\right]$	$\sigma[C_P]$ $\left[\frac{\text{mJoule}}{\text{moleK}}\right]$
1.789	28.21	0.21	1.789	28.39	0.25	1.790	27.24	0.25
1.842	28.93	0.21	1.842	29.21	0.27	1.843	28.78	0.26
1.896	29.70	0.25	1.896	30.19	0.29	1.896	29.64	0.32
2.100	32.70	0.31	2.100	32.66	0.30	2.322	35.28	0.27
2.322	35.61	0.27	2.496	37.36	0.26	2.496	38.41	0.29
2.702	40.21	0.23	2.787	41.34	0.23	2.788	40.94	0.25
2.891	43.01	0.22	2.892	42.13	0.23	3.115	46.59	0.28
3.115	46.32	0.25	3.341	48.89	0.26	3.431	51.43	0.24
3.455	54.29	0.37	3.656	55.50	0.25	3.657	55.91	0.24
3.864	58.73	0.26	3.868	58.88	0.27	4.087	62.96	0.29
4.090	63.39	0.29	4.227	66.60	0.22	4.229	65.97	0.23
4.232	66.09	0.23	4.456	71.09	0.34	4.456	71.17	0.35
4.456	71.20	0.33	4.600	74.27	0.32	4.600	74.34	0.31
4.768	77.90	0.33	4.768	78.00	0.35	4.923	81.37	0.32
4.923	81.52	0.32	5.099	86.52	0.36	5.099	86.67	0.38
5.265	91.33	0.36	5.265	91.28	0.32	5.445	96.03	0.42
5.445	96.80	0.43	5.629	101.6	0.4	5.629	101.8	0.4
5.821	107.1	0.4	5.821	107.0	0.5	6.016	113.8	0.4
6.017	114.0	0.4	6.220	121.0	0.4	6.220	121.0	0.4
6.430	129.1	0.5	6.431	129.1	0.4	6.646	137.3	0.4
6.646	137.9	0.5	7.098	156.0	0.6	7.098	156.2	0.5
7.577	177.4	0.6	7.577	178.4	0.6	8.081	204.5	0.6
8.081	203.6	0.6	8.629	235.2	0.7	8.630	235.6	0.7
9.216	270.2	0.8	9.216	271.6	0.8	9.829	311.7	0.8
9.830	311.4	0.8	10.495	361.8	1.0	10.495	362.6	0.9
10.848	389.1	1.1	10.852	389.0	1.1	11.213	422.8	1.0
11.213	421.3	1.0	11.699	465.6	1.1	12.595	555.1	1.3
12.600	553.9	1.2	13.569	657.7	1.5	14.633	785.8	1.7
14.633	786.4	1.7	15.758	931.9	1.9	16.967	1107	2
16.967	1113	2	18.303	1320	3	19.712	1551	3
19.712	1555	3	21.222	1842	3	22.845	2187	4
22.845	2189	4	24.349	2526	4	26.262	2911	4
26.302	2978	5	28.355	3410	9	30.570	4033	6
30.909	4314	21	79.610	16420	14	79.645	16479	12

Table A.11: Zero Field Calorimetry Data for a-Fe[36.25]Zr[63.75]

Temperature [K]	C_P $[\frac{\text{mJoule}}{\text{moleK}}]$	$\sigma[C_P]$ $[\frac{\text{mJoule}}{\text{moleK}}]$	Temperature [K]	C_P $[\frac{\text{mJoule}}{\text{moleK}}]$	$\sigma[C_P]$ $[\frac{\text{mJoule}}{\text{moleK}}]$	Temperature [K]	C_P $[\frac{\text{mJoule}}{\text{moleK}}]$	$\sigma[C_P]$ $[\frac{\text{mJoule}}{\text{moleK}}]$
1.862	34.03	0.29	1.862	34.16	0.30	1.965	35.87	0.32
1.965	35.49	0.33	1.965	36.12	0.31	2.062	36.12	0.28
2.062	36.19	0.30	2.063	37.00	0.29	2.105	37.12	0.27
2.138	36.95	0.35	2.138	37.56	0.36	2.182	37.09	0.30
2.183	38.48	0.31	2.183	38.13	0.34	2.272	39.05	0.36
2.272	38.70	0.34	2.368	40.31	0.28	2.368	39.86	0.28
2.420	40.41	0.33	2.420	41.40	0.33	2.487	41.11	0.32
2.487	41.23	0.30	2.657	44.18	0.30	2.657	43.58	0.28
2.880	46.34	0.29	2.880	46.51	0.28	3.102	49.83	0.30
3.103	49.47	0.27	3.325	52.94	0.29	3.326	53.47	0.31
3.425	55.06	0.58	3.425	55.05	0.53	3.540	58.59	0.34
3.543	56.31	0.32	3.644	58.45	0.30	3.748	60.66	0.31
3.750	60.27	0.31	3.951	64.39	0.30	3.961	63.84	0.30
3.963	64.32	0.30	4.245	70.29	0.40	4.245	71.18	0.41
4.246	71.27	0.40	4.247	70.21	0.35	4.385	73.31	0.21
4.385	73.59	0.20	4.735	81.99	0.23	4.736	81.48	0.22
5.106	91.58	0.26	5.106	91.89	0.29	5.106	92.21	0.38
5.510	103.7	0.4	5.510	104.0	0.4	5.944	117.4	0.4
5.944	117.7	0.4	6.410	134.2	0.5	6.410	134.2	0.4
6.901	154.5	0.5	6.901	153.9	0.5	7.437	178.2	0.5
7.438	178.6	0.5	8.007	206.6	0.6	8.007	207.4	0.6
8.630	242.1	0.7	8.630	242.5	0.7	9.287	280.9	0.8
9.288	283.6	0.7	10.011	335.8	0.8	10.011	335.6	0.9
10.776	397.8	1.0	10.777	395.3	1.0	11.143	426.6	0.9
11.143	429.1	1.0	11.617	470.9	1.0	11.617	472.7	1.1
11.996	506.7	1.2	11.996	508.3	1.1	12.914	604.7	1.2
13.928	721.0	1.4	13.928	723.8	1.4	15.000	857.6	1.6
16.150	1021	2	16.150	1025	2	18.770	1435	2
18.770	1440	2	20.218	1697	3	21.765	2018	3
21.765	2019	3	23.471	2394	3	25.276	2827	4
25.276	2830	4	27.197	3294	5	29.266	3838	5
29.266	3846	6	31.536	4427	6	34.041	4816	6
34.081	5082	7	36.837	5785	9	38.388	6191	9
38.406	6179	10	41.456	6956	11	44.731	7827	12
44.752	7826	12	79.260	16834	13	79.277	16492	15
79.874	17903	48	81.097	17125	42			

Table A.12: Zero Field Calorimetry Data for a-Fe[37.60]Zr[62.40]

Temperature [K]	C_P $[\frac{\text{mJoule}}{\text{moleK}}]$	$\sigma[C_P]$ $[\frac{\text{mJoule}}{\text{moleK}}]$	Temperature [K]	C_P $[\frac{\text{mJoule}}{\text{moleK}}]$	$\sigma[C_P]$ $[\frac{\text{mJoule}}{\text{moleK}}]$	Temperature [K]	C_P $[\frac{\text{mJoule}}{\text{moleK}}]$	$\sigma[C_P]$ $[\frac{\text{mJoule}}{\text{moleK}}]$
1.849	30.55	0.34	1.849	29.64	0.39	1.849	30.40	0.31
1.849	30.99	0.42	1.849	30.00	0.37	1.849	30.57	0.40
1.850	29.98	0.36	1.850	30.45	0.34	1.850	29.97	0.43
1.913	30.41	0.39	1.914	30.67	0.39	1.914	31.26	0.42
1.914	31.83	0.41	2.027	32.66	0.40	2.027	32.80	0.43
2.027	32.06	0.43	2.138	33.42	0.38	2.138	34.46	0.44
2.139	34.16	0.37	2.289	36.24	0.38	2.289	36.06	0.36
2.381	36.98	0.35	2.382	36.87	0.35	2.382	36.88	0.37
2.465	38.00	0.32	2.575	40.28	0.38	2.576	39.72	0.39
2.714	41.89	0.37	2.715	41.99	0.33	2.715	42.18	0.36
2.770	42.49	0.29	2.885	44.60	0.37	2.886	45.36	0.40
2.988	46.33	0.28	2.988	45.56	0.28	2.989	46.89	0.33
3.209	52.10	0.34	3.209	50.79	0.33	3.326	53.62	0.35
3.326	52.96	0.34	3.428	56.23	0.33	3.429	57.10	0.33
3.534	59.14	0.36	3.634	61.11	0.37	3.634	61.27	0.37
3.638	62.09	0.35	3.642	62.21	0.37	3.850	67.32	0.38
3.853	66.50	0.40	4.036	72.30	0.44	4.212	75.51	0.21
4.213	75.12	0.19	4.384	79.24	0.51	4.384	79.70	0.47
4.735	87.55	0.52	4.735	88.44	0.49	5.509	110.9	0.7
5.509	111.0	0.7	5.942	126.6	1.0	5.942	127.3	1.0
6.408	143.1	0.9	6.900	167.3	0.8	6.901	163.1	1.0
7.436	188.0	1.1	7.437	191.1	1.0	8.005	225.9	1.3
8.627	264.9	1.2	8.628	265.3	1.4	9.285	304.9	1.6
9.285	311.6	1.6	10.007	358.6	1.8	10.772	426.6	2.1
10.772	417.1	1.7	10.937	454.0	2.3	10.937	468.8	1.9
11.777	536.0	2.3	12.693	618.5	2.6	12.693	626.7	2.7
13.665	731.8	2.8	14.714	863.5	3.0	14.719	881.7	3.0
15.871	1047	3	17.099	1258	4	17.104	1267	4
18.415	1502	5	19.861	1777	5	19.861	1795	5
21.385	2120	6	23.022	2518	6	23.022	2529	6
24.207	2812	6	26.047	3270	7	26.054	3307	8
28.024	3779	7	30.264	4386	7	30.293	4428	8
32.636	5038	9	35.257	5743	9	35.274	5733	9
38.086	6468	11	41.106	7299	12	41.143	7308	11
44.407	8218	14	79.137	18706	17	79.155	18406	34
79.452	18699	46	80.759	17243	49			

Table A.13: Zero Field Calorimetry Data for a-Fe[38.38]Zr[61.62]

Temperature [K]	C_P $[\frac{\text{mJoule}}{\text{moleK}}]$	$\sigma[C_P]$ $[\frac{\text{mJoule}}{\text{moleK}}]$	Temperature [K]	C_P $[\frac{\text{mJoule}}{\text{moleK}}]$	$\sigma[C_P]$ $[\frac{\text{mJoule}}{\text{moleK}}]$	Temperature [K]	C_P $[\frac{\text{mJoule}}{\text{moleK}}]$	$\sigma[C_P]$ $[\frac{\text{mJoule}}{\text{moleK}}]$
1.871	31.91	0.31	1.871	32.49	0.29	1.989	34.39	0.31
1.989	33.61	0.32	2.149	35.32	0.28	2.149	36.56	0.30
2.150	35.46	0.29	2.150	36.01	0.31	2.273	37.00	0.28
2.273	37.65	0.30	2.388	39.16	0.29	2.389	39.18	0.31
2.487	41.18	0.31	2.488	40.81	0.31	2.654	43.71	0.30
2.655	43.68	0.31	2.882	46.46	0.30	2.883	48.38	0.33
3.101	51.40	0.31	3.108	51.14	0.18	3.306	54.23	0.26
3.308	53.77	0.28	3.534	58.76	0.28	3.535	58.46	0.29
3.853	64.50	0.31	3.858	63.86	0.32	4.037	68.74	0.35
4.058	68.22	0.33	4.586	79.65	0.33	4.586	79.70	0.36
4.951	87.61	0.35	4.951	88.07	0.39	5.343	98.34	0.42
5.757	110.7	0.5	5.757	110.5	0.5	6.209	126.0	0.5
6.694	142.8	0.6	6.695	143.3	0.6	7.205	163.5	0.6
7.766	189.7	0.6	7.767	189.3	0.8	8.358	219.4	0.8
9.006	256.6	0.7	9.008	254.7	0.8	9.693	300.5	0.9
10.072	327.2	1.0	10.073	326.2	1.0	10.447	353.5	1.0
10.448	353.6	1.1	10.844	385.3	1.1	11.245	418.6	1.2
11.245	420.1	1.2	11.687	458.0	1.2	11.687	460.0	1.2
12.583	546.5	1.4	13.547	647.8	1.5	13.547	651.8	1.6
14.610	782.9	1.6	15.730	931.9	2.0	15.730	933.8	1.9
16.938	1112	2	18.272	1327	3	18.277	1326	3
19.690	1566	3	21.205	1872	3	22.839	2234	4
22.839	2238	4	24.207	2538	5	26.054	2980	5
26.054	2983	5	28.044	3489	7	30.271	4012	7
30.307	4057	7	32.651	4679	8	35.282	5368	10
35.299	5373	9	38.121	6086	11	38.450	6190	11
38.468	6219	11	41.514	6991	13	44.813	8022	26
44.904	8086	26	79.260	18087	24	79.294	18000	31
79.312	16898	47	79.312	17998	30			

Table A.14: Zero Field Calorimetry Data for a-Fe[38.99]Zr[61.01]

Temperature [K]	C_P $[\frac{\text{mJoule}}{\text{moleK}}]$	$\sigma[C_P]$ $[\frac{\text{mJoule}}{\text{moleK}}]$	Temperature [K]	C_P $[\frac{\text{mJoule}}{\text{moleK}}]$	$\sigma[C_P]$ $[\frac{\text{mJoule}}{\text{moleK}}]$	Temperature [K]	C_P $[\frac{\text{mJoule}}{\text{moleK}}]$	$\sigma[C_P]$ $[\frac{\text{mJoule}}{\text{moleK}}]$
1.797	27.02	0.20	1.797	27.56	0.21	1.901	28.77	0.26
1.902	29.25	0.28	1.902	28.64	0.30	2.098	32.25	0.22
2.098	31.70	0.23	2.158	33.24	0.28	2.297	35.54	0.25
2.298	34.92	0.28	2.397	37.28	0.24	2.397	36.62	0.26
2.499	39.19	0.27	2.499	38.60	0.29	2.608	40.38	0.28
2.609	40.32	0.27	2.704	42.06	0.29	2.704	41.57	0.30
2.896	45.45	0.29	2.896	45.24	0.30	3.007	48.04	0.29
3.221	52.22	0.30	3.223	52.41	0.29	3.424	56.39	0.33
3.663	62.02	0.32	3.666	62.47	0.32	3.876	67.88	0.39
3.879	67.18	0.40	4.094	73.87	0.41	4.221	77.15	0.40
4.221	77.69	0.39	4.221	77.94	0.43	4.355	80.22	0.37
4.355	80.26	0.37	4.661	88.79	0.43	4.661	90.75	0.42
4.985	98.86	0.47	4.985	99.66	0.46	5.331	112.2	0.5
5.332	110.7	0.5	5.699	123.8	0.5	5.699	124.9	0.5
6.091	139.6	0.6	6.092	139.4	0.6	6.501	157.5	0.7
6.501	159.0	0.7	6.943	180.2	0.7	6.944	180.1	0.7
7.417	206.0	0.8	7.418	204.4	0.8	7.922	232.8	1.0
7.922	232.9	0.9	8.448	264.2	1.0	8.448	267.0	1.0
9.022	302.1	1.0	9.022	302.9	1.0	9.637	347.4	1.2
9.637	351.2	1.1	10.277	393.6	1.3	10.278	403.8	1.2
10.977	453.1	1.3	10.977	468.9	1.4	11.404	513.4	1.6
11.405	524.7	1.6	11.980	590.6	1.5	11.984	603.2	1.5
13.021	693.2	1.8	14.172	812.6	2.1	14.172	855.6	2.0
15.405	1020	2	16.748	1229	2	16.753	1279	2
18.211	1542	3	19.792	1824	3	19.797	1895	3
21.515	2286	4	23.386	2655	5	23.392	2645	4
24.380	2862	5	26.650	3882	5	79.838	20039	25
79.856	19928	23						

Appendix B

Magnetocalorimetry Data for $a-Fe-Zr$

Conditions applying to the zero field calorimetry data (Appendix A) are true also for the magnetometry data. The absolute magnetocalorimetry data, for a given sample, were all taken on the same day in various magnetic fields, applied by an axial superconducting solenoid. The applied field values (B, given in Tesla) are shown in the table caption. Discrepancies occur between the data from the zero field runs (tables A.8 and A.11) and the magnetometry runs (tables B.4 and B.6) for the $a-Fe_{36.3}Zr_{63.7}$ and $a-Fe_{34.4}Zr_{65.6}$ samples. These discrepancies arise because the 10 μL syringe, used to dispense the silver paste, broke about the time that the magnetocalorimetry runs were started. The amount of silver paste used during the magnetocalorimetry runs (which were done last) had to be determined by eye. Furthermore, the silver paste was near the end of the bottle and was observed to be significantly densified. When the phonon specific heat is subtracted off the data (see sections 5.2.1 and 5.2.2), the discrepancies between the data sets disappear. This analysis suggests that during the run of table B.4 about 2mg more silver paste was on the addenda than during the run of table A.8. Similarly, during the run of table B.6 about 4mg more silver paste was on the addenda than during the run of table A.11.

Table B.1: Magnetocalorimetry for a-Fe[30.31]Zr[69.69]; B = 0 Tesla

Temperature [K]	C_P [mJoule/moleK]	$\sigma[C_P]$ [mJoule/moleK]	Temperature [K]	C_P [mJoule/moleK]	$\sigma[C_P]$ [mJoule/moleK]	Temperature [K]	C_P [mJoule/moleK]	$\sigma[C_P]$ [mJoule/moleK]
2.193	20.34	0.20	2.194	20.35	0.20	2.547	23.97	0.21
2.547	24.24	0.20	2.893	28.40	0.20	2.894	28.60	0.21
3.215	32.81	0.21	3.219	32.84	0.24	3.226	33.44	0.22
3.548	38.32	0.65	3.550	38.20	0.63	3.870	43.47	1.23
3.875	43.15	1.16	4.093	47.92	1.31	4.093	47.41	1.41
4.229	52.08	1.35	4.231	51.41	0.98	4.232	50.15	0.76
4.409	53.85	0.30	4.409	54.10	0.30	4.762	61.45	0.30
4.762	62.03	0.31	5.135	71.05	0.37	5.136	71.22	0.35
5.541	82.01	0.40	5.542	82.78	0.44	5.860	92.81	0.44
6.435	112.4	0.5	7.055	138.7	0.6	7.733	167.5	0.9
7.733	170.9	0.7	8.981	243.8	0.9	8.982	241.8	0.9
9.301	263.7	0.8	9.301	263.9	1.0	9.680	288.8	1.2
10.418	344.9	1.6	10.418	363.4	32.0	11.232	409.7	2.2
12.092	489.5	3.1	12.092	493.0	2.8	13.021	595.7	3.6
14.039	700.5	3.7	14.039	702.0	4.8	15.115	840.0	4.3
16.273	1005	4	16.273	1015	4	17.563	1217	5
18.910	1440	4	18.916	1445	5	19.685	1566	5
19.712	1605	5	21.719	2040	5	77.650	17070	15
77.667	17056	30	79.575	17782	416	79.610	16207	230
79.610	16601	243						

Table B.2: Magnetocalorimetry for a-Fe[30.31]Zr[69.69]; B = 3.50 Tesla

Temperature [K]	C_P [mJoule/moleK]	$\sigma[C_P]$ [mJoule/moleK]	Temperature [K]	C_P [mJoule/moleK]	$\sigma[C_P]$ [mJoule/moleK]	Temperature [K]	C_P [mJoule/moleK]	$\sigma[C_P]$ [mJoule/moleK]
2.887	28.70	0.29	2.901	28.77	0.27	3.219	33.28	0.37
3.219	33.95	0.37	3.548	38.83	0.38	3.867	43.46	0.43
3.875	43.60	0.40	4.088	48.21	0.41	4.234	51.29	0.37
4.236	50.57	0.38	5.056	67.65	19.27	5.333	73.26	20.13
5.852	96.21	48.60	6.131	101.5	0.7	6.428	102.0	24.7
6.429	119.9	26.8	7.048	141.5	31.7	7.127	142.2	0.9
7.726	168.7	34.8	7.726	170.7	1.0			

Table B.3: Magnetocalorimetry for a-Fe[30.31]Zr[69.69]; B = 5.00 Tesla

Temperature [K]	C_P [mJoule/moleK]	$\sigma[C_P]$ [mJoule/moleK]	Temperature [K]	C_P [mJoule/moleK]	$\sigma[C_P]$ [mJoule/moleK]	Temperature [K]	C_P [mJoule/moleK]	$\sigma[C_P]$ [mJoule/moleK]
2.189	20.03	0.29	2.189	20.12	0.26	2.546	23.90	0.34
2.547	23.67	0.26	2.878	27.92	0.37	3.221	33.03	0.50
3.225	32.44	0.38	3.231	33.26	0.36	3.841	42.95	0.54
3.844	43.32	0.41	4.077	47.42	0.44	4.232	50.41	0.84
4.232	51.26	0.51	4.403	53.67	0.38	4.403	53.82	0.46
4.839	64.32	0.67	5.321	76.60	0.69	5.322	73.32	2.06
5.842	92.48	0.67	6.417	113.6	0.8	6.418	113.7	0.8
7.038	140.6	1.0	7.716	174.5	1.2	7.716	174.7	1.0

Table B.4: Magnetocalorimetry for a-Fe[34.42]Zr[65.58]; B = 0 Tesla

Temperature [K]	C_P $[\frac{mJoule}{moleK}]$	$\sigma[C_P]$ $[\frac{mJoule}{moleK}]$	Temperature [K]	C_P $[\frac{mJoule}{moleK}]$	$\sigma[C_P]$ $[\frac{mJoule}{moleK}]$	Temperature [K]	C_P $[\frac{mJoule}{moleK}]$	$\sigma[C_P]$ $[\frac{mJoule}{moleK}]$
1.848	25.19	0.60	1.848	25.36	0.67	2.006	27.09	0.64
2.015	27.85	1.11	2.191	29.50	0.74	2.192	29.63	0.83
2.431	32.85	0.71	2.431	32.74	0.72	2.603	34.86	0.63
2.603	34.71	0.63	2.826	37.52	0.85	2.826	37.53	0.97
2.827	37.74	0.71	2.999	40.08	0.85	2.999	39.97	0.88
2.999	39.71	0.82	3.272	44.55	0.53	3.273	44.08	0.70
3.273	44.64	0.61	3.541	49.57	0.57	3.542	48.45	0.58
3.857	54.18	0.91	3.861	54.84	0.82	3.863	55.33	0.97
4.259	63.46	0.21	4.273	62.37	0.23	5.802	105.6	0.9
5.802	105.6	1.0	6.007	113.5	1.2	6.007	114.6	1.2
6.529	134.5	0.9	6.530	134.1	0.9	7.102	162.2	2.0
7.103	161.6	1.7	7.714	192.5	2.0	7.714	193.6	1.8
8.379	231.8	1.9	8.379	227.6	1.9	9.111	279.5	2.3
9.111	283.2	2.4	9.515	310.1	2.4	9.515	308.1	2.4
9.896	339.5	2.1	9.896	333.8	1.9	10.241	362.7	2.2
10.241	367.7	2.2	11.893	504.7	5.9	11.897	503.0	5.6
12.829	606.0	7.7	12.837	556.4	8.2	13.823	633.4	7.4
14.159	778.1	1.7	78.650	22438	68	78.667	22256	27
78.667	22582	27	78.667	22852	40	78.719	20865	108

Table B.5: Magnetocalorimetry for a-Fe[34.42]Zr[65.58]; B = 5.00 Tesla

Temperature [K]	C_P $[\frac{mJoule}{moleK}]$	$\sigma[C_P]$ $[\frac{mJoule}{moleK}]$	Temperature [K]	C_P $[\frac{mJoule}{moleK}]$	$\sigma[C_P]$ $[\frac{mJoule}{moleK}]$	Temperature [K]	C_P $[\frac{mJoule}{moleK}]$	$\sigma[C_P]$ $[\frac{mJoule}{moleK}]$
1.841	23.40	0.74	1.841	23.20	0.64	2.001	24.80	0.55
2.002	24.63	0.54	2.099	26.15	0.58	2.099	26.48	0.58
2.212	27.74	0.56	2.212	27.83	0.55	2.242	28.51	0.84
2.307	29.12	0.54	2.307	29.07	0.57	2.460	31.26	0.54
2.597	32.69	0.71	2.597	32.78	0.70	2.667	34.17	0.92
2.667	34.40	0.92	2.668	33.72	0.84	2.769	35.96	1.79
2.770	35.39	0.65	2.824	36.25	0.68	2.824	37.15	0.79
2.989	39.87	1.66	2.992	40.14	0.92	3.206	42.97	0.38
3.207	43.46	0.80	3.208	43.26	0.30	3.535	49.06	0.77
3.536	48.74	1.00	3.537	48.30	0.92	3.855	55.42	0.90
3.856	56.03	0.96	4.376	67.34	0.73	4.379	67.64	0.74
5.599	100.2	1.9	5.599	104.6	1.8	6.096	120.3	1.6
6.096	123.1	1.5	6.196	124.6	1.2	6.196	128.1	1.2
6.592	142.2	1.0	6.592	141.5	0.9	7.084	166.5	1.3
7.085	164.5	1.6	8.052	214.3	2.0			

Table B.6: Magnetocalorimetry for a-Fe[36.25]Zr[63.75]; B = 0 Tesla

Temperature [K]	C_P $[\frac{\text{mJoule}}{\text{moleK}}]$	$\sigma[C_P]$ $[\frac{\text{mJoule}}{\text{moleK}}]$	Temperature [K]	C_P $[\frac{\text{mJoule}}{\text{moleK}}]$	$\sigma[C_P]$ $[\frac{\text{mJoule}}{\text{moleK}}]$	Temperature [K]	C_P $[\frac{\text{mJoule}}{\text{moleK}}]$	$\sigma[C_P]$ $[\frac{\text{mJoule}}{\text{moleK}}]$
1.872	33.73	0.16	1.872	33.14	0.15	1.872	33.48	0.16
1.988	33.92	0.15	1.988	34.28	0.16	1.988	34.49	0.14
2.136	36.43	0.14	2.136	36.55	0.15	2.263	38.28	0.14
2.264	38.89	0.15	2.451	41.20	0.14	2.451	41.04	0.13
2.654	43.82	0.15	2.654	43.47	0.16	2.884	47.41	0.13
2.887	47.47	0.16	3.104	50.74	0.18	3.104	52.07	0.17
3.329	55.57	0.18	3.330	54.65	0.14	4.229	71.75	0.19
4.237	72.33	0.17	5.407	106.0	0.3	5.407	106.4	0.3
5.825	119.2	0.3	5.825	120.5	0.3	5.825	119.4	0.3
5.826	121.2	0.3	6.281	138.4	0.4	6.281	139.3	0.4
6.282	138.8	0.4	6.282	139.0	0.4	6.771	159.8	0.4
6.771	161.0	0.4	6.772	160.3	0.5	6.772	160.5	0.5
7.287	186.4	0.5	7.287	185.9	0.5	7.287	187.4	0.5
7.288	185.1	0.5	7.853	217.6	0.6	7.853	218.1	0.6
7.854	216.3	0.6	7.854	218.0	0.8	8.080	229.7	0.6
8.085	230.1	0.6	8.450	255.5	0.6	8.450	257.1	0.7
8.453	253.8	0.7	8.454	253.7	0.8	8.700	270.3	0.7
8.701	269.7	0.7	9.105	299.0	0.7	9.105	299.8	0.7
9.110	296.8	0.9	9.110	297.0	1.0	9.360	314.5	0.9
9.360	316.5	0.8	9.800	348.5	0.8	9.800	347.3	0.9
9.805	349.0	0.8	9.806	349.7	0.9	10.085	369.0	0.9
10.085	369.5	0.9	10.090	362.2	1.5	10.095	366.3	1.3
10.564	409.1	0.9	10.566	408.9	1.0	10.570	408.7	1.1
10.570	409.7	1.1	10.852	431.7	1.0	10.852	433.0	1.0
10.856	433.1	1.5	10.856	433.9	1.1	11.371	479.2	1.1
11.371	480.4	1.1	11.375	479.8	1.3	11.375	480.2	1.4
79.155	22455	32	79.155	22550	20	79.155	22690	19

Table B.7: Magnetocalorimetry for a-Fe[36.25]Zr[63.75]; B = 1.00 Tesla

Temperature [K]	C_P $[\frac{\text{mJoule}}{\text{moleK}}]$	$\sigma[C_P]$ $[\frac{\text{mJoule}}{\text{moleK}}]$	Temperature [K]	C_P $[\frac{\text{mJoule}}{\text{moleK}}]$	$\sigma[C_P]$ $[\frac{\text{mJoule}}{\text{moleK}}]$	Temperature [K]	C_P $[\frac{\text{mJoule}}{\text{moleK}}]$	$\sigma[C_P]$ $[\frac{\text{mJoule}}{\text{moleK}}]$
1.848	32.18	0.32	1.975	33.19	0.35	2.250	37.69	0.39
2.251	36.98	0.36	2.251	37.14	0.22	2.428	40.18	0.63
2.428	39.35	0.19	2.656	43.50	0.48	2.656	44.07	0.43
2.883	47.52	0.55	3.098	50.76	0.45	3.101	50.53	0.57
3.330	54.99	0.57	3.332	55.62	0.39	3.650	62.77	0.49
3.650	62.05	0.62	3.861	67.18	0.44	3.867	67.15	0.52
4.066	70.66	0.63	4.066	72.07	0.48	4.271	75.97	0.33
4.309	76.16	0.43	5.805	123.0	0.4	5.805	122.5	0.4
6.405	144.5	0.5	7.090	174.4	0.6	7.091	176.8	0.6
7.569	200.3	0.6	7.570	200.2	0.6			

Table B.8: Magnetocalorimetry for a-Fe[36.25]Zr[63.75]; B = 2.00 Tesla

Temperature [K]	C_P $[\frac{\text{mJoule}}{\text{moleK}}]$	$\sigma[C_P]$ $[\frac{\text{mJoule}}{\text{moleK}}]$	Temperature [K]	C_P $[\frac{\text{mJoule}}{\text{moleK}}]$	$\sigma[C_P]$ $[\frac{\text{mJoule}}{\text{moleK}}]$	Temperature [K]	C_P $[\frac{\text{mJoule}}{\text{moleK}}]$	$\sigma[C_P]$ $[\frac{\text{mJoule}}{\text{moleK}}]$
1.874	30.31	0.18	1.874	30.57	0.19	1.874	30.79	0.19
1.966	31.79	0.19	1.967	32.06	0.18	1.967	31.87	0.18
2.076	33.22	0.16	2.076	33.18	0.15	2.223	35.61	0.16
2.224	35.49	0.17	2.426	38.69	0.16	2.426	38.71	0.15
2.656	42.26	0.18	2.656	43.09	0.16	2.881	46.40	0.15
2.882	46.69	0.16	3.103	50.82	0.19	3.103	50.83	0.19
3.329	54.75	0.19	3.330	55.07	0.17	3.545	59.33	0.63
3.546	59.83	0.57	3.865	66.53	0.59	3.865	67.14	0.50
4.074	71.09	0.58	4.076	72.13	0.54	4.301	76.58	0.20
4.474	80.76	0.62	5.408	108.1	0.3	5.418	108.5	0.4
5.801	122.6	0.4	6.401	146.9	0.5	7.087	178.8	0.5
7.088	176.6	0.5	7.567	201.4	0.6	7.567	202.3	0.6

Table B.9: Magnetocalorimetry for a-Fe[36.25]Zr[63.75]; B = 3.50 Tesla

Temperature [K]	C_P $[\frac{\text{mJoule}}{\text{moleK}}]$	$\sigma[C_P]$ $[\frac{\text{mJoule}}{\text{moleK}}]$	Temperature [K]	C_P $[\frac{\text{mJoule}}{\text{moleK}}]$	$\sigma[C_P]$ $[\frac{\text{mJoule}}{\text{moleK}}]$	Temperature [K]	C_P $[\frac{\text{mJoule}}{\text{moleK}}]$	$\sigma[C_P]$ $[\frac{\text{mJoule}}{\text{moleK}}]$
1.747	26.65	0.47	1.748	26.82	0.45	1.748	26.97	0.39
1.829	28.02	0.39	1.830	28.08	0.39	1.945	29.73	0.37
1.946	29.57	0.35	2.082	31.94	0.40	2.082	32.28	0.41
2.308	35.07	0.23	2.543	39.34	0.34	2.769	43.29	0.50
2.769	43.09	0.41	2.876	44.89	0.18	2.877	44.90	0.19
2.989	47.04	0.20	2.990	47.34	0.33	3.099	49.26	0.18
3.101	49.26	0.17	3.206	50.45	0.29	3.209	50.92	0.27
3.325	54.09	0.17	3.327	53.84	0.16	3.423	55.33	0.41
3.429	55.32	0.31	3.530	58.90	0.31	3.542	58.52	0.20
3.542	59.21	0.45	3.739	62.49	0.27	3.744	62.35	0.27
3.918	67.02	0.31	3.927	67.00	0.33	4.251	75.02	0.42
4.377	76.89	0.20	5.093	98.61	0.72	5.404	109.4	0.3
5.405	110.0	0.3	5.698	119.6	0.8	5.698	119.1	0.6
6.293	142.7	0.8	6.535	153.9	0.5	6.979	174.8	1.0
6.979	175.9	0.8	7.551	207.1	1.1	7.553	208.9	1.0

Table B.10: Magnetocalorimetry for a-Fe[36.25]Zr[63.75]; B = 5.00 Tesla

Temperature [K]	C_P $\left[\frac{\text{mJoule}}{\text{moleK}}\right]$	$\sigma[C_P]$ $\left[\frac{\text{mJoule}}{\text{moleK}}\right]$	Temperature [K]	C_P $\left[\frac{\text{mJoule}}{\text{moleK}}\right]$	$\sigma[C_P]$ $\left[\frac{\text{mJoule}}{\text{moleK}}\right]$	Temperature [K]	C_P $\left[\frac{\text{mJoule}}{\text{moleK}}\right]$	$\sigma[C_P]$ $\left[\frac{\text{mJoule}}{\text{moleK}}\right]$
1.919	26.95	0.13	1.919	26.43	0.13	1.919	26.92	0.14
2.145	30.26	0.15	2.145	29.24	0.17	2.309	31.85	0.15
2.310	32.32	0.16	2.538	36.46	0.15	2.538	37.06	0.16
2.761	40.94	0.16	2.762	40.41	0.15	2.964	45.55	0.17
2.982	45.61	0.15	3.210	49.45	0.21	3.212	50.22	0.19
3.539	56.42	0.26	3.539	56.22	0.25	3.807	62.57	0.20
3.822	62.93	0.19	4.321	75.71	0.25	4.322	75.07	0.21
4.990	90.99	0.36	4.992	94.65	0.39	5.796	120.9	0.4
5.797	121.3	0.4	6.097	132.7	0.4	6.097	132.4	0.4
6.296	142.2	0.4	6.296	141.2	0.4	6.790	162.9	0.5
6.791	163.8	0.5	7.272	188.3	0.6	7.273	188.4	0.6

References

[1] E.P. Wohlfarth, *Proceedings of Intern. Conf. on Itinerant Electron Magnetism, 1976*, R.D. Lowde and E.P. Wohlfarth ed. (North Holland (Amsterdam), 1977), p. 305.

[2] K. Ikeda, S.K. Dhar, M. Yoshizawa and K.A. Gschneidner Jr., J. Magn. Magn. Mat. **100**, 292 (1991).

[3] D.C. Mattis, *Theory of Magnetism* (Harper and Row (New York), 1965).

[4] N. Ashcroft and D. Mermin, *Solid State Physics* (Saunders College (Philadelphia), 1976).

[5] D.H. Martin, *Magnetism in Solids* (M.I.T. Press (Cambridge, Mass.), 1967).

[6] B.I. Bleany and B. Bleany, *Electricity and Magnetism* (Clarendon Press (Oxford), 1957).

[7] J. Crangle, *The Magnetic Properties of Solids* (Edward Arnold (London), 1977).

[8] L. Taillefer, Spin Fluctuations in Itinerant Electron Ferromagnets, PhD. Thesis, Jesus College, Cambridge, 1986.

[9] E.P. Wohlfarth, J. Magn. Magn. Mat. **7**, 113 (1978).

[10] T. Moriya, *Spin Fluctuations in Itinerant–Electron Magnetism*, Vol. 56 (Springer–Verlag (Berlin), 1985).

[11] E.S.R. Gopal, *Specific Heats at Low Temperatures (New York)* (Plenum, 1966).

[12] E.C. Stoner, Proc. Roy. Soc. A **165**, 372 (1938).

[13] D.M. Edwards and E.P. Wohlfarth, Proc. Roy. Soc. A **303**, 127 (1968).

[14] G.G. Lonzarich and L. Taillefer, J. Phys. C **18**, 1 (1985).

[15] L. Taillefer, Class notes, Physics course 198-718B, McGill U., 1994.

[16] H.P. Wijn, *Magnetic Properties of Metals: d–Elements, Alloys and Compounds*, H.P.J. Wijn ed. (Springer–Verlag (Berlin), 1991).

[17] P. Mohn, D. Wagner and E.P. Wohlfarth, J. Phys. F **17**, L13 (1986).

[18] P. Mohn and E.P. Wohlfarth, J. Phys. F **17**, 2421 (1987).

[19] C. Herring, *Magnetism III*, G.T. Rado and H. Suhl ed. (Academic Press(New York), 1966), p. 120.

[20] T. Moriya, *Metallic Magnetism*, Vol. 42, H. Capellmann ed. (Springer–Verlag (Berlin), 1987), p. 15.

[21] T. Moriya, J. Magn. Magn. Mat. **14**, 1 (1979).

[22] N.F. Berk and J.R. Schrieffer, Phys. Rev. Lett. **17**, 433 (1966).

[23] W.F. Brinkman and S. Engelsberg, Phys. Rev. **169**, 417 (1968).

[24] S. Engelsberg, W.F. Brinkman and S. Doniach, Phys. Rev. Lett. **20**, 1040 (1968).

[25] S. Doniach and S. Engelsberg, Phys. Rev. Lett. **17**, 750 (1966).

[26] K. Hüller, J. Mag. Mag. Mat. **61**, 347 (1986).

[27] N.R. Bernhoeft, G.G. Lonzarich, P.W. Mitchell and D.McK. Paul, Phys. Rev. B **28**, 422 (1983).

[28] T. Moriya and A. Kawabata, J. Phys. Soc. Japan **34**, 639 (1973).

[29] T. Moriya and A. Kawabata, J. Phys. Soc. Japan **35**, 669 (1973).

[30] G.G. Lonzarich, J. Mag. Mag. Mat. **54-57**, 612 (1986).

[31] G.P. Felcher, J.S. Kouvel and A.E. Miller, Phys. Rev. B **16**, 2124 (1977).

[32] F.R. de Boer, C.J. Schinkel, J. Biesterbos and S. Proost, J. Appl. Phys. **40**, 1049 (1969).

[33] G.D. Mahan, *Many Particle Physics* (Plenum Press (New York), 1990).

[34] C. Kittel, *Quantum Theory of Solids* (John Wiley and sons (New York), 1973).

[35] D. Pines, *Elementary Excitations in Solids* (W.A. Benjamin (New York), 1963).

[36] R.K. Pathria, *Statistical Mechanics* (Pergamon Press (Oxford), 1972).

[37] R.M. White, *Quantum Theory of Magnetism* (McGraw–Hill (New York), 1970).

[38] K.H. Bennemann, Phys. Rev. **167**, 564 (1968).

[39] C.J. Pethick and G.M. Carneiro, Phys. Rev. A **7**, 304 (1973).

[40] G.R. Stewart, J.L. Smith, A.L. Giorgi and Z. Fisk, Phys. Rev. B **25**, 5907 (1982).

[41] S.K. Dhar and K.A. Gschneidner Jr., Phys. Rev. B **39**, 7453 (1989).

[42] S.K. Dhar, K.A. Gschneidner Jr., L.L. Miller and D.C. Johnston, Phys. Rev. B **40**, 11488 (1989).

[43] R.J. Trainer, M.B. Brodsky and H.V. Culbert, Phys. Rev. Lett. **34**, 1019 (1975).

[44] K. Ikeda and K.A. Gschneidner Jr., Phys. Rev. Lett. **45**, 1341 (1980).

[45] G.R. Stewart, Rev. Mod. Phys. **56**, 755 (1984).

[46] J.A. Chilton, B.R. Coles, M.J. Mortimer and R.O.A. Hall, J. Magn. Magn. Mat. **76**, 171 (1988).

[47] M.T. Béal–Monod, S.K. Ma and D.R. Fredkin, Phys. Rev. Lett. **20**, 929 (1968).

[48] T.Y. Hsiang, J.W. Reister, H. Weinstock, G.W. Crabtree and J.J. Vuillemen, Phys. Rev. Lett. **47**, 523 (1981).

[49] W. deDood and P.F. deChatel, J. Phys. F **3**, 1039 (1973).

[50] R.L. Falge Jr. and N.M. Wolcott, J. Low Temp. Phys. **5**, 617 (1971).

[51] N. Rivier and V. Zlatic, J. Phys. F **2**, L99 (1972).

[52] J.S. Dugdale, *The Electrical Properties of Metals and Alloys* (Edward Arnold (London), 1977).

[53] Z. Altounian, S.V. Dantu and M. Dikeakos, Phys. Rev. B **49**, 8621 (1994).

[54] H. Sasakura, K. Katsuhiko and Y. Masuda, J. Phys. Soc. Japan **53**, 352 (1984).

[55] C.J. Fuller, C.L. Lin, T. Mihalistin, F. Chu and N. Bykovetz, Solid State Comm. **83**, 863 (1992).

[56] J. Ström–Olsen, Z. Altounian, R.W. Cochrane and A.B. Kaiser, Phys. Rev. B **31**, 6116 (1985).

[57] E. Batalla, Z. Altounian and J.O. Ström–Olsen, Phys. Rev. B **31**, 577 (1985).

[58] D.H. Ryan, J.M.D. Coey, E. Batalla, Z. Altounian and J.O. Ström–Olsen, Phys. Rev. B **35**, 8630 (1987).

[59] E.P. Wohlfarth, *Amorphous Metallic Alloys*, F.E. Luborsky ed. (Butterworth (London), 1983), p. 299.

[60] Z. Altounian and J.O. Ström–Olsen, Phys. Rev. B **27**, 4149 (1983).

[61] V.L. Moruzzi, P. Oelhafen, A.R. Williams, R. Lapka, H.–J. Güntherodt and J. Kúbler, Phys. Rev. B **27**, 2049 (1983).

[62] K.M. Unruh and C.L. Chien, Phys. Rev. B **30**, 4968 (1984).

[63] B. Gaulin, private communication, 1994.

[64] M. Trudeau, R.W. Cochrane, D.V. Baxter, J.O. Ström–Olsen and W.B. Muir, Phys. Rev. B **37**, 4499 (1988).

[65] D.G. Onn, L.Q. Wang and K. Fukamichi, Solid State Comm. **47**, 479 (1983).

[66] D.G. Onn, L.Q. Wang, Y. Obi and K. Fukamichi, J. Non–Cryst. Sol. **61**, 1149 (1984).

[67] M. Matsuura, U. Mizutani and K. Fukamichi, Proceedings of the Fifth International Conference on Rapidly Quenched Metals, Würzburg, Germany, September 3-7, 1984, North Holland, Amsterdam, (S. Steeb and H. Warlimont eds.), Volume 1, pg. 1019.

[68] T.B. Massalski, *Binary Alloy Phase Diagrams*, T.B. Massalski ed. (American Society for Metals (Ohio), 1986).

[69] D. Arias and J.P. Abriata, Bulletin of Alloy Phase Diagrams **9**, 597 (1988).

[70] 99.98% pure iron flake – available from Johnson–Mathey, Seabrook, New Hampshire.

[71] 99.94% pure Zr bar – available from Teledyne Wah Chang, Albany, Oregon.

[72] Samples generously donated by Zaven Altounian.

[73] Z. Altounian, T. Guo–hua and J.O. Ström–Olsen, J. Appl. Phys. **57**, 1777 (1985).

[74] A. Guinier, *X-ray Diffraction* (W.H. Freeman and company, 1963).

[75] M.W. Zemansky and R.H. Dittman, *Heat and Thermodynamics* (McGraw–Hill (New York), 1981).

[76] R. Bachman, F.J. diSalvo, T.M. Geballe, R.L. Greene, R.E. Howard, C.N. King, H.C. Kirsch, K.N. Lee, R.E. Schwall, H.U. Thomas and R.B. Zubeck, Rev. Sci. Instrum. **43**, 205 (1972).

[77] G.R. Stewart, Rev. Sci. Instrum. **54**, 1 (1983).

[78] R.E. Schwall, R.E. Howard and G.R. Stewart, Rev. Sci. Instrum. **46**, 1054 (1975).

[79] M. Regelsberger, R. Wernhardt and M. Rosenberg, J. Phys. E **19**, 523 (1985).

[80] E.M. Forgan and S. Nedjat, Rev. Sci. Instrum. **51**, 411 (1980).

[81] 0.003 inch diameter (40 Ga.) manganin wire with Formvar insulation – available from Pelican Co., Naples, Florida.

[82] Y.S. Touloukian, *Thermal Conductivities: Metalllic Elements and Alloys*, Y.S. Touloukian ed. (Plenum (New York), 1986).

[83] Lakeshore Product Catalog, Lakeshore Cryogenics Inc., Westerville, Ohio

[84] Carbon Composite resistors – available from Stackpole Electronics, El Paso, Texas.

[85] E.M. Forgan, Cryogenics , 207 (1974).

[86] Labmaster DMA data acquisition board – available from Scientific Solutions, Solon, Ohio.

[87] 1 inch diameter, 1mm thick sapphire slabs– available from Crystal Systems, Salem, Mass.

[88] Y.S. Touloukian, *Specific Heats: Nonmetalllic Solids*, Y.S. Touloukian ed. (Plenum (New York), 1986).

[89] Y.S. Touloukian, *Thermal Conductivities: Nonmetalllic Solids*, Y.S. Touloukian ed. (Plenum (New York), 1986).

[90] 0.003inch diameter Au–7%Cu wire – available from California Fine Wire, Grover City, California.

[91] Chobond–584 Silver Epoxy – available from Chromerics, Woburn, Mass.

[92] RCWP-154J 150KΩ thick film resistors – available from Dale Electronics, Tempe, Arizona.

[93] 0.003inch diameter Chromel wire – available from Omega Engineering Inc., Stamford, Conn.

[94] Eccobond 286 general purpose epoxy – available from Emerson and Cumings, Woburn, Mass.

[95] L.G. Rubin, B.L. Brandt and H.H. Sample, Cryogenics , 491 (1982).

[96] Potentiometric Conductance Bridge – no longer available from S.H.E corporation.

[97] Q. Li, C.H. Watson, R.G. Goodrich, D.G. Haase and H. Lukefahr, Cryogenics **26**, 467 (1986).

[98] W.A. Bosch, F. Mathu, H.C. Meijer and R.W. Willekers, Cryogenics **26**, 3 (1986).

[99] M. Benzaquen and D.W. Walsh, Phys. Rev. B **30**, 7287 (1984).

[100] 1.2Ah 12V rechargeable Gel Cell batteries – available from Johnson Controls, Milwaukee, Wisconsin.

[101] P.K. Dixon and L. Wu, Rev. Sci. Instrum. **60**, 3329 (1989).

[102] X. Wang, Rev. Sci. Instrum. **61**, 1999 (1990).

[103] Manual on the Use of Thermocouples in Temperature Measurement, ASTM Special Technical Publication, 1987.

[104] J. Harper, Thermal Properties of Metals with Low Temperature Structural Instabilities, PhD. Thesis, Stanford University, Stanford, 1975.

[105] J.R. Anderson and D.R. Zrudsky, Rev. Sci. Instrum. **44**, 316 (1971).

[106] R.K. Kirschman, Cryogenics **25**, 115 (1985).

[107] 391A single phase lock–in–amplifier – Ithaco, Ithaca, New York.

[108] Y.S. Touloukian, *Specific Heats: Metalllic Elements and Alloys*, Y.S. Touloukian ed. (Plenum (New York), 1986).

[109] Flexible Silver 16 conductive adhesive – available from Engelhard, East Newark, New Jersey.

[110] D.L. Martin, Can. J. Phys. **65**, 1104 (1987).

[111] A.J. Bevolo, Cryogenics , 661 (1974).

[112] A.LeR. Dawson and D.H. Ryan, Phys. Rev. B **45**, 1034 (1992).

[113] E.T. Swartz, Rev. Sci. Instrum. **57**, 2848 (1986).

[114] J. Xu, C.H. Watson and R.G. Goodrich, Rev. Sci. Instrum. **61**, 814 (1990).

[115] R. Bachman, H.C. Kirsch and T.M. Geballe, Rev. Sci. Instrum. **41**, 547 (1970).

[116] M. Seki and K. Sanokawa, Cryogenics , 121 (1982).

[117] D.L. Martin, L.L.T. Bradley, W.J. Cazemier and R.L. Snowdon, Rev. Sci. Instrumen. **44**, 675 (1973).

[118] D.L. Martin, Phys. Rev. B **8**, 5357 (1973).

[119] A5020–1 5 Tesla superconducting solenoid – available from American Magnetics Inc., Oak Ridge, Tenn.

[120] P. Horowitz and W. Hill, *The Art of Electronics* (Cambridge Univ. Pr. (Cambridge), 1980).

[121] Lakeshore Technical Publication, Lakeshore Cryogenics Inc., Westerville, Ohio

[122] Oleh Baran, private communication, 1994.

[123] D.G. Onn, *Amorphous Metallic Alloys*, F.E. Luborsky ed. (Butterworth (London), 1983), p. 451.

[124] D.G. Onn, L.Q. Wang, Y. Obi and K. Fukamichi, Solid State Comm. **46**, 37 (1983).

[125] K. Binder and A.P. Young, Rev. Mod. Phys. **58**, 801 (1986).

[126] I.S. Jacobs and C.P. Bean, *Magnetism III*, G.T. Rado and H. Suhl ed. (Academic Press (New York), 1963), p. 271.

[127] A.LeR. Dawson and D.H. Ryan, J. Appl. Phys. **75**, 6837 (1994).